UNIVERSITY OF CALIFORNIA,
IRVINE

Development and Translation of Multimodal Microscopic and Endoscopic Biomedical Imaging Technologies

THESIS

submitted in partial satisfaction of the requirements
for the degree of

DOCTOR OF PHILOSOPHY

in Biomedical Engineering

by

Yan Li

Dissertation Committee:
Professor Zhongping Chen, Chair
Professor Matthew Brenner
Professor William Tang

2020

DEDICATION

To

Mom, Dad, my husband, and my younger sister

TABLE OF CONTENTS

LIST OF FIGURES

LIST OF TABLES

TABLE OF ABBREVIATIONS

ARF	Acoustic radiation force
CT	Computed tomography
CRC	Colorectal cancer
OCT	Optical coherence tomography
FDOCT	Fourier domain optical coherence tomography
FFT	Fast Fourier Transform
FWHM	Full width at half maximum
FPS	frames per second
FDML	Fourier domain mode locking
GRIN	Gradient refractive index
H&E	Hematoxylin and eosin
IVUS	Intravascular ultrasound
IVOCT	Intravascular optical coherence tomography
ICG	Indocyanine green
MRI	Magnetic resonance imaging
OCTA	Optical coherence tomography angiogram
OCE	Optical coherence elastography
OPD	Optical path difference
PA	Photoacoustic
PMN-PT	Lead magnesium niobate-lead titanate
PZT	Lead zirconate titanate

SSOCT	Swept source optical coherence tomography
SDOCT	Spectrometer-based optical coherence tomography
SNR	Signal-to-noise ratio
SD	Sprague Dawley
TCFA	Thin cap fibroatheroma
ThCFA	Thick cap (>65 μm) fibroatheroma
TDOCT	Time domain optical coherence tomography
US	Ultrasound
NIRF	Near-infrared fluorescence
NIR	Near-infrared
2D	Two-dimensional
3D	Three-dimensional

ACKNOWLEDGMENTS

I would like to express the deepest appreciation to my supervisor, Professor Zhongping Chen for his mentorship. Dr. Chen provided me with an opportunity to study in his lab as a visiting scholar before enrolled as a PhD student. Without his support, my dream—studying in the USA—may not have come true. During the past five years, Dr.Chen has tirelessly taught me and encouraged me. He has also given me the freedom and support to conduct the research that I am interested in. I am forever grateful.

I thank my committee members, Professor Matthew Brenner, Professor William Tang, Professor Chang Liu, and Professor Ozdal Boyraz for their insight and feedback throughout my graduate work.

In addition, I would like to thank our collaborators from UCI and USC: Professor Qifa Zhou and Professor Pranav Patel. The projects would not have been possible without their expertise and dedication. I thank Dr. Teng Ma, Dr. Mingyue Yu, Mr. Runze Li, and Mr. Gengxi Lu from Dr. Zhou's group for providing ultrasound transducer and technical support. I also thank Dilbahar Mohar and Mr. Earl Steward from Dr. Patel's Cardiology division for assisting me with all the animal studies.

I am grateful to my colleagues in Dr. Chen's research groups for all of their support throughout my graduate studies. Dr. Joseph Jing taught me everything I know about OCT, including the principles, probe making, system optimization, and writing data acquisition in c++. He was always there whenever I needed help. I would like to thank Dr. Rachel Qu for teaching me how to make the dual-modality probe, histology, gold coating as well as conduct animal experiment. I would like to thank Dr. Jiang Zhu for his deliciated instruction of the OCE system. I also want to thank Junxiao Yu, Jason Chen, Youmin He, Yusi Miao, Buyun Zhang, Zhikai Zhu, Saijun Qiu, Fengyi Zhang for their companionship and support.

I appreciate the help of Mr. Michael Dhuy of the willed body program for helping me to collect artery samples. I would like to thank Leacky Liaw and Chung-ho Sun for their patient lesions in histology, tissue analysis, and safety training. I thank Elaine Kato for her wonderful editing of my papers and thesis.

I would like to express my deepest gratitude to my family. To my mon and dad, everything I have accomplished in my life is all due to the work and sacrifices that you have made in yours. Thank you for raising me with the values and principles that shaped me into who I am today.To my younger sister, I thank you for companionship during hard times, and selflessly looking out for and taking care of our parents in China. To my husband, I cannot

thank you enough for everything you've done for me. Thanks for driving 6 hours back to Irvine to accompany me biweekly. Thanks for drawing amazing schematics of probes for my papers. Thanks for comforting me during the hard times and all the life lessons that you have taught me. Thanks for all the sacrifices you have made and the support you have given me. I love you all.

Finally, I want to thank American Heart Association to provide me a two-year predoctoral fellowship. Through this fellowship, I have gained insights into a wide array of biological and photonic research fields in Cardiology. In addition, I would like to express my sincere gratitude for the funding provided by the National Institutes of Health through Projects R01HL-125084, R01HL-127271, R01EY-026091, and R01EY-028662.

CURRICULUM VITAE

Yan Li

2018-2020 Doctor of Philosophy in Biomedical Engineering
University of California, Irvine

2016-2018 Master of Science in Biomedical Engineering
University of California, Irvine

2011-2014 Master of Science in Optical Engineering
University of the Chinese Academy of Sciences, China

2007-2011 Bachelor of Science in Electrical Science and Technology
Tianjin University, China

FIELD OF STUDY

Biomedical Imaging and Biophotonics

PUBLICATIONS

1. **Yan Li**, Sucbei Moon, Jason J. Chen, Zhikai Zhu & Zhongping Chen. Ultrahigh-sensitive optical coherence elastography Light Sci Appl 9, 58 (2020). Link
2. Xuejun Qian, Runze Li, **Yan Li**, Gengxi Lu, Youmin He, Mark S Humayun, Zhongping Chen, and Qifa Zhou. In vivo evaluation of posterior eye elasticity using shaker based optical coherence elastography. Experimental Biology and Medicine, 1535370219897617(2020). Link
3. Neha Talreja, Yusi Miao, **Yan Li**, Jason Chen, Joseph Jing, Jiang Zhu, Yona Tadir, Zhongping Chen, and Felicia Lane. Optical Vaginal Biopsy Using Optical Coherence Tomography. Female Pelvic Med. Reconstr. Surg..26(2):155-158 (2020). Link
4. **Yan Li**, Jason Chen, and Zhongping Chen. Advances in Doppler Optical Coherence Tomography and Angiography, Translational Biophotonics, e201900005 (2019). Link
5. **Yan Li**, Jason Chen, and Zhongping Chen. Multimodal Intravascular Imaging Technology for Characterization of Atherosclerosis, Journal of Innovative Optical Health Sciences ,2030001(2019). Link
6. **Yan Li**, Jiang Zhu, Jason Chen, Junxiao Yu, Zi Jin, Yusi Miao, Andrew Browne, Qifa Zhou, Zhongping Chen. Simultaneously Imaging and Quantifying in vivo Mechanical Properties

of Crystalline Lens and Cornea Using Optical Coherence Elastography with Acoustic Radiation Force Excitation, APL Photonics 4, 106104 (2019). Link.

7. **Yan Li**, Gengxi Lu, Jason Chen, Joseph Jing, Tiancheng Huo, Ruimin Chen, Laiming Jiang, Qifa Zhou, Zhongping Chen. PMN-PT/Epoxy 1-3 Composite Based Ultrasonic Transducer for Dual-Modality Photoacoustic and Ultrasound Endoscopy, Photoacoustics, 100138(2019). Link
8. **Yan Li**, Zhikai Zhu, Jason J. Chen, Joseph C. Jing, Chung-Ho Sun, Sehwan Kim, Phil-Sang Chung, Zhongping Chen. Multimodal endoscopy for colorectal cancer detection by optical coherence tomography and near-infrared fluorescence imaging, Biomedical Optics Express. 10(5): 2419-2429(2019). Link Top Download
9. **Yan Li**, Zhikai Zhu, Joseph C Jing, Jason J Chen, Andrew Emon Heidari, Youmin He, Jiang Zhu, Teng Ma, Mingyue Yu, Qifa Zhou, Zhongping Chen. High-Speed Integrated Endoscopic Photoacoustic and Ultrasound Imaging System, IEEE JSTQE. 25(1):1-5(2019). Link
10. Zi Jin, Reza Khazaeinezhad, Jiang Zhu, Junxiao Yu, Yueqiao Qu, Youmin He, **Yan Li**, Tomas E. Gomez Alvarez-Arenas, Fan Lu, and Zhongping Chen. In-vivo 3D corneal elasticity using air-coupled ultrasound optical coherence elastography. Biomed. Opt. Express 10, 6272-6285 (2019). Link
11. Tiffany T. Pham, Lily Chen, Andrew E. Heidari, Jason J. Chen, Alisa Zhukhovitskaya, **Yan Li**, Urja Patel, Zhongping Chen, Brian J.F. Wong, Computational analysis of six optical coherence tomography systems for vocal fold imaging: A comparison study. Lasers Surg Med (2019). Link
12. Zhaodong Du, Runze Li, Xuejun Qian, Gengxi Lu, **Yan Li**, Youmin He, Yueqiao Qu, Laiming Jiang, Zeyu Chen, Mark S. Humayun, Zhongping Chen, and Qifa Zhou. Quantitative confocal optical coherence elastography for evaluating biomechanics of optic nerve head using Lamb wave model. Neurophotonics 6 (4), 041112 (2019). Link
13. Jiang Zhu, Junxiao Yu, Yueqiao Qu, Youmin He, **Yan Li**, Qiang Yang, Tiancheng Huo, Xingdao He, Zhongping Chen. Coaxial excitation longitudinal shear wave measurement for quantitative elasticity assessment using phase-resolved optical coherence elastography. Optics Letters 43 (10), 2388-2391(2018). Link
14. Qiang Yang, Yusi Miao, Tiancheng Huo, **Yan Li**, Emon Heidari, Jiang Zhu, Zhongping Chen, Deep imaging in highly scattering media by combining reflection matrix measurement with Bessel-like beam based optical coherence tomography, Applied physics letters 113 (1), 011106(2018). Link
15. **Yan Li**, Riqiang Lin, Chengbo Liu, Jianhua Chen, Huadong Liu, Rongqin Zheng, Xiaojing Gong, Liang Song, In vivo photoacoustic/ultrasonic dual-modality endoscopy with a

miniaturized full field-of-view catheter, Journal of biophotonics, e201800034 (2018). Link. Inside Cover.

16. **Yan Li**, Neha T. Sudol, Yusi Miao, Joseph C. Jing, Jiang Zhu, Felicia Lane, and Zhongping Chen.1.7 micron optical coherence tomography for vaginal tissue characterization in vivo, Lasers Surg Med (2018). Link. ASLMS Journal Highlights.
17. **Yan Li**, Joseph Jing, Junxiao Yu, Buyun Zhang, Tiancheng Huo, Qiang Yang, and Zhongping Chen. Multimodality endoscopic optical coherence tomography and fluorescence imaging technology for visualization of layered architecture and subsurface microvasculature, Optics Letter, 43(9): 2074-2077(2018). Link
18. **Yan Li**, Zhongping Chen. Multimodal intravascular photoacoustic and ultrasound imaging. Biomedical Engineering Letters, 1-9 (2018). Link
19. **Yan Li**, Joseph Jing, Emon Heidari, Jiang Zhu, Yueqiao Qu, and Zhongping Chen. Intravascular Optical Coherence Tomography for Characterization of Atherosclerosis with a 1.7 Micron Swept-Source Laser. Scientific Reports, 7 :14525 (2018). Link. Featured by OCT News.
20. **Yan Li**, Joseph Jing, Yueqiao Qu, Yusi Miao, Buyun Zhang, Teng Ma, Mingyue Yu, Qifa Zhou, Zhongping Chen. Fully integrated optical coherence tomography, ultrasound, and indocyanine green-based fluorescence tri-modality system for intravascular imaging. Biomedical Optics Express. 2017, 8(2):1036-1044. Link
21. **Yan Li**, Xiaojing Gong, Chengbo Liu, Riqiang Lin, Xiaosong Bai, Liang Song. High-speed intravascular spectroscopic photoacoustic imaging at 1000 A-lines per second with a 0.9-mm diameter catheter. J Biomed Opt. 2015 Jun; 20(6):065006. Link
22. **Yan Li**, Bao Zhang, Yongfeng Hong. Design of Large Zoom Ratio Middle Wavelength Infrared Zoom Optical System. ACTA OPTICA SINICA. 2013.33(4)2. Link. F5000 Frontrunner.
23. **Yan Li**, Bao Zhang, Yongfeng Hong. Optical Design of Harmonic Diffractive Infrared Dual-Band and Dual-Field System. ACTA OPTICA SINICA. 2013,33(11). Link
24. **Yan Li**, Bao Zhang, Yongfeng Hong. Miniaturization design of large zoom ratio MWIR zoom optical system. Journal of Applied Optics. 2013,34(2). Link
25. **Yan Li**, Bao Zhang, Yongfeng Hong. Athermalization of dual field of view infrared system. Journal of Applied Optics. 2013,34(3). Link
26. **Yan Li**, Bao Zhang, Yongfeng Hong. Compact and multispectral off-axial three-mirror reflective optical system. Journal of Applied Optics, 2014,35(3). Link

CONFERENCE PRESENTATIONS

1. **Yan Li**, Zhikai Zhu, Jason J. Chen, Joseph C. Jing, Chung-Ho Sun, Zhongping Chen, "Multimodal endoscopy for colorectal cancer detection by optical coherence tomography and near-infrared fluorescence imaging," SPIE Photonics West, San Francisco, CA, Oral Presentation (2020)
2. **Yan Li**, Zhikai Zhu, Joseph C Jing, Jason J Chen, Andrew Emon Heidari, Youmin He, Jiang Zhu, Teng Ma, Mingyue Yu, Qifa Zhou, Zhongping Chen, "High speed in vivo endoscopic photoacoustic and ultrasound dual-modality imaging," SPIE Photonics West, San Francisco, CA, Oral Presentation (2019)
3. **Yan Li**, Jiang Zhu, Jason Chen, Junxiao Yu, Zi Jin, Yusi Miao, Andrew Browne, Qifa Zhou, Zhongping Chen, "Imaging and Quantifying in vivo Mechanical Properties of Crystalline Lens Using Acoustic Radiation Force Optical Coherence Elastography," BMES 2019, Philadelphia, PA, Oral Presentation (2019)
4. **Yan Li**, Joseph Jing, Emon Heidari, Jiang Zhu, Yueqiao Qu, and Zhongping Chen,"Intravascular optical coherence tomography for characterization of atherosclerosis with a 1.7 micron swept-source laser," SPIE Photonics West, San Francisco, CA, Oral Presentation (2018)
5. **Yan Li**, Joseph Jing, Yueqiao Qu, Jiang Zhu, Jason Chen, and Zhongping Chen, "Intravascular Optical Coherence Tomography for Characterization of Atherosclerosis with a 1.7 Micron Swept-Source Laser," Gordon Research Conferences, Stonehill College, Easton, MA, United States, Poster (2018).
6. **Yan Li**, "1.7-micron optical coherence tomography for characterization in gynecology," Korean Society for Laser Medicine and Surgery, Oral Presentation (2018).
7. **Yan Li** and Zhongping Chen, "Multimodality endoscopic imaging technology for visualization of layered architecture and vasculature," The 3rd International Conference on Photonics and Optical Engineering (icPOE 2018), Chinese, Invited talk (2018).
8. **Yan Li**, Joseph C. Jing, Yueqiao Qu, Yusi Miao, Teng Ma, Mingyue Yu, Qifa Zhou, Zhongping Chen, "Fully integrated optical coherence tomography, ultrasound, and indocyanine green based fluorescence tri-modality system for intravascular imaging," SPIE Photonics West, San Francisco, CA, Oral Presentation (2017)
9. **Yan Li**, Xiaojing Gong, Chengbo Liu, and Liang Song, "High-speed intravascular spectroscopic photoacoustic imaging at two spectral bands," Optics in cardiology, Thorax Center, Erasmus MC, Rotterdam, Poster (2015)

ABSTRACT OF THE THESIS

Development and Translation of Multimodal Microscopic and Endoscopic Biomedical Imaging Technologies

By

Yan Li

Doctor of Philosophy in Biomedical Engineering

University of California, Irvine

Professor Zhongping Chen, Chair

Each endoscopic imaging technique, including optical coherence tomography, fluorescence, ultrasound, or photoacoustic, has unique features as well as limitations. Presently, since no single technique can provide a complete assessment of biological tissue, such as plaque and colorectal wall, several imaging methods are often performed in sequence to achieve a comprehensive evaluation. While the sequential imaging approach can compensate for limitations of each individual technique, the increased X-ray exposure, procedure length, and associated risks cannot be overlooked. As multiple imaging probes are required, repeated probe insertions to the arteries are required, and the associated costs (e.g., guide wires, sterilization, etc.) also increase significantly. In addition, since data acquisition is performed individually, image co-registration is necessary, which is often performed off-line manually or semi-automatically. Not only is image co-registration a tedious and time-consuming task, it also has limited accuracy due to human error and interobserver variances. Therefore, a technique that can simultaneously perform multiple imaging technologies through a single imaging probe would greatly improve clinical

outcomes in clinical applications. Here, we present different kinds of multimodal imaging modalities for cardiology and gastrointestinal tract. *In vivo* and *ex vivo* studies using rabbit and rat were performed for system validation. The results show that multimodal technology is able to overcomes the limitations of individual intravascular imaging modality, providing more comprehensive information on morphology and/or composition for better characterization.

Since the first demonstration of Doppler OCT in 1997, several functional extensions of Doppler OCT have been developed, including velocimetry, angiogram, and optical coherence elastography (OCE). OCT Angiogram (OCTA) is able to reconstruct the microvasculature by detecting fluctuations in the amplitude and phase of the interference signal induced by moving blood cells and plasma. Here, we developed a 1.7-micron OCT/OCTA system for characterization of skin cancer. The use of the longer wavelength allows for a ~25% improvement in penetration depth as well as better identification of microvasculature in the deeper layers of the skin tissue. The feasibility and performance of our system were tested and validated in vivo in human subjects. The developed 1.7-micron OCT/OCTA system has the capability of providing more structural and vascular information at greater skin depths than previous OCT systems, and it has great potential to bring new insights in diagnosis as well as management of skin cancer.

OCE possesses micron-level resolution and an axial displacement sensitivity on the order of a few nanometers and, therefore has become an attractive research tool for ophthalmology, dermatology, cardiology, and oncology. Here, we developed an OCE system, which is able to perform a simultaneous evaluation of elasticity in both cornea and

crystalline lens. In vivo rabbit experiments were performed to verify the performance as well as investigate the relationship between elasticity of ocular tissue and intraocular pressure and between elasticity and age. In addition, we developed an ultrahigh sensitivity OCE system using a common-path configuration to further improve the system performance. The system has a phase stability of 4.2 mrad without external stabilization or extensive post-processing, such as averaging. We validated the SS-OCE$_{CP}$ performance in a tissue-mimicking phantom and an in vivo rabbit model, and the results demonstrated significantly improved phase stability compared to conventional SS-OCE. The significant improved capability suggests that the developed OCE system has great potential to advance ophthalmic research in disorders affecting the lens and the cornea.

Chapter 1 – Introduction

1.1 Introduction

Biomedical imaging is able to create visual representations of the internal structure and function of biological tissue, such as blood velocity and chemical composition, which allows for a comprehensive characterization of organs or tissues. Many of the techniques were developed for biomedical imaging, such as magnetic resonance imaging (MRI), radiography, nuclear medicine, ultrasound (US), elastography, optical coherence tomography (OCT), photoacoustic (PA) imaging, and near-infrared fluorescence (NIRF) imaging, which have been widely applied in clinical and research settings. In our studies, we focused on US, NIRF, PA imaging, OCT, and functional extensions of OCT, such as OCT angiogram (OCTA) and optical coherence elastography (OCE) [1-8].

US applies time delay between acoustic pulse echoes reflected by different surfaces of biological tissue to reconstruct the internal structure of the target which is commonly used in many different fields, such as cardiology, gastroenterology, and gynecology. US can provide cross-sectional structural images of the biological tissue with a high resolution and a large penetration depth. For example, intravascular US (IVUS) is often used to visualize lumen geometry and layered architecture of the arterial wall as well as to classify plaque with a resolution of ~100 μm and a imaging depth of ~7 mm [9].

As the light analogue to US, OCT is an imaging technique that is based on low coherence interferometry that can provide cross-sectional images of the arterial wall with a superior resolution of 1-15 μm [10, 11]. Benefiting from micron-scale resolution, OCT is able to detect

small internal details in structures and tissues, such as neo-vessels, thin fibrous caps, and microphage accumulations in atherosclerotic plaque, which are the main characteristics of vulnerable plaque. Based on the Doppler principle, Doppler OCT is a functional imaging technique that allows for identifying and quantifying movements of biological tissue with high spatial resolution and sensitivity. Doppler OCT methods have been extended to different functional imaging techniques, such as OCTA and OCE. OCTA is able to reconstruct the microvasculature by detecting micromotions induced by the moving blood cells and plasma in biological tissue. OCE allows for mapping of arterial wall elasticity by measuring the localized tissue displacement induced by an external excitation force [12-15].

Near-infrared fluorescence (NIRF) is capable of providing molecular contrast with high sensitivity [2, 9, 16-18]. In NIRF, a contrast agent is often required to mark specific molecules. For example, indocyanine green (ICG), which is able to bind to lipoproteins and accumulate at the sites of the inflamed tissues, can be combined with intravascular NIRF for the detection of lipid content and inflammatory reaction. Recently, differentiation of plaque types has been demonstrated via autofluorescence with a 633-nm excitation wavelength.

Photoacoustic (PA) imaging utilizes a nanosecond laser to excite biological tissues for the generation of acoustic signals caused by localized thermal expansion [19-21]. PA imaging is based on tissue absorption contrast and has the ability to visualize depth-resolved composition of biological tissue. Additionally, multiple wavelengths of laser pulse excitation can also be applied to differentiate different compositions of biological tissue.

Each imaging technique has unique features as well as limitations. For example, although US provides a large penetration depth, it cannot visualize micro-features of the tissue because of

resolution limitations. OCT has micrometer-scale resolution, but it only allows for visualization of superficial morphology (1~2 mm). In addition, both US and OCT have limited sensitivity for identifying chemical composition of biological tissue. Presently, since no single technique can provide a complete assessment of biological tissue, several imaging methods are often performed in sequence to achieve a comprehensive evaluation [22]. While the sequential imaging approach can compensate for the limitations of each individual technique, the increased procedure length and associated risks cannot be overlooked. As multiple imaging probes are required, the associated costs (e.g., guide wires, sterilization, etc.) also increase significantly. In addition, since data acquisition is performed individually, image co-registration is necessary which is often performed off-line manually or semi-automatically. Not only is image co-registration a tedious and time-consuming task, it also has limited accuracy due to human error and interobserver variances. Therefore, a technique that can simultaneously perform multiple imaging technologies would greatly improve clinical outcomes [23, 24]. In our studies, we focus on the development of multimodal imaging technologies, including OCT, OCTA, OCE, US, NIRF, and PA, which were translated to different fields, including cardiology, gastroenterology, ophthalmology and dermatology.

1.2 Atherosclerosis

Atherosclerosis is a progressive disease in which plaques build up within the lining of an artery [25, 26]. A plaque is made up of lipids, cholesterol, calcium, fibrous constituents, monocytes, and various other inflammatory cells in the arterial wall, and it is typically classified as a stable plaque or a vulnerable plaque, as shown in Figure 1.1. A typical vulnerable plaque is characterized by a thin fibrous cap, a large lipid pool, increased inflammatory cells, and reduced smooth muscle volume [27-29]. Over time, a plaque may not only harden and narrow the blood vessel but also—if ruptured in the case of vulnerable plaques—trigger a blood clot or thrombus, which is the major cause of heart attacks (86%) and brain aneurysms (45%) [27, 30, 31]. These high-risk plaques often remain clinically silent, and the initial manifestation of the disease could result in death [32]. Detection methods that aim for early recognition of vulnerable plaques are, first and foremost, of critical importance for preventing lethal consequences [30].

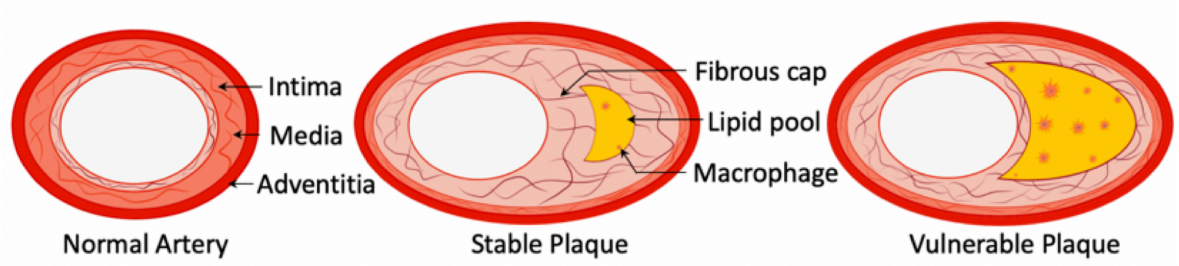

Figure 1.1 Cross-sectional views of normal artery, artery with a stable and vulnerable plaque.

In clinical practice, computed tomography (CT) angiography is routinely performed to identify the stenotic region caused by plaque formation via visualization of coronary arteries in two dimensions although it lacks the spatial resolution to resolve tissue-level information of the arterial wall: hence, the inadequacy in studying vulnerable plaques [33-35]. The development of interventional techniques aims to address this limitation. Intravascular ultrasound (IVUS) and

intravascular optical coherence tomography (IVOCT) are currently the most significant clinical adaptations. The main advantage of IVUS and IVOCT lies in their capability of providing cross-sectional information of the arterial wall, revealing the underlying layered structure of the vascular tissue. The large penetration depth of IVUS enables full-depth visualization of the coronary lumen, blood vessel wall, and atherosclerotic plaque formation and, therefore, has been routinely utilized in clinical practices [36-39]. Benefiting from its micron-scale resolution, IVOCT has been proven as a sensitive method for measuring fibrous cap thickness [40, 41]. Nevertheless, IVOCT suffers from shallow penetration depth and cannot completely visualize larger plaques, and IVUS lacks the resolution for microstructure identification. In addition, both IVUS and IVOCT have limited sensitivity for studying chemical composition and quantifying tissue biomechanical properties [12, 42-44].

In recent years, several other methods have been explored for assessing plaque in the chemical and biomechanical domains. Intravascular near-infrared fluorescence or spectroscopy (NIRF or NIRS) is capable of providing molecular contrast with high sensitivity for characterizing the intra-lesion lipid content, but depth information is lacking, hence, the limited capability of plaque characterization [2, 9, 16-18]. Intravascular photoacoustic (IVPA) is based on tissue absorption contrast and has the ability to visualize depth-resolved composition of atherosclerotic plaque; however, it lacks the sensitivity for biomechanical properties [19-21]. Intravascular optical coherence elastography (IVOCE) is a functional extension of IVOCT, and it allows for the point-by-point mapping of arterial wall elasticity by measuring the localized tissue displacement with sub-micrometer/nanometer detection sensitivity of phase-resolved OCT [12-15]. In addition, the plaque type can be identified based on the composition-dependent biomechanical property [12]. Each imaging technique can provide important plaque characteristics, but all have certain

limitations, and these are summarized in Table 1.1. Presently, since no single technique can provide a complete assessment of the plaque, several imaging methods are often performed in sequence to achieve a comprehensive evaluation [22]. While the sequential imaging approach can compensate for the limitations of each individual technique, the increased X-ray exposure, procedure length, and associated risks cannot be overlooked. In addition, since data acquisition is performed individually, image co-registration is necessary, which is often performed off-line manually or semi-automatically. Not only is image co-registration a tedious and time-consuming task, it also has limited accuracy due to human error and interobserver variances. Therefore, a technique that can simultaneously perform multiple imaging technologies through a single intravascular imaging probe would greatly improve clinical outcomes in cardiology [23, 24].

Table 1.1 Comparison of different imaging modalities: ** indicates excellent performance, and * indicates moderate performance.

	Thin fibrous cap	Large lipid pool		Mechanical property
		Composition	Dimension	
IVOCT	**	*		
IVUS		*	**	
NIRF		*		
NIRS		**		
IVPA		**	**	
IVOCE	**	*		**

1.3 Colorectal Cancer

Colorectal cancer (CRC) is also known as colon cancer or rectal cancer. In the United States, about 1 in 21 men and 1 in 23 women will develop CRC during their lifetime according to the American Cancer Society. CRC is the third most common type of cancer, consisting of about 10% of all cancer cases globally [45]. In 2012 alone, approximately 1.4 million new cases of (and almost 0.7 million deaths from) CRC were reported [46]. CRC is a cancer that starts in the rectum or the colon, in which a growth, termed polyps, on the inner lining of the rectum or colon can be found. Polyps often include hyperplastic polyps and adenomatous polyps. Hyperplastic polyps are a growth of extra cells that projects out from colorectal tissues which are more common and not pre-cancerous generally. Doctors generally remove hyperplastic polyps anyway, just to be safe. Adenomatous polyps (adenomas) are gland-like growths that develop on the mucous membrane that lines the large intestine. Two-thirds of colon polyps are the precancerous type which may progress to cancer with a 5% possibility after 7- 10 or more years. Figure 1.2 shows a progression from polyps to cancer.

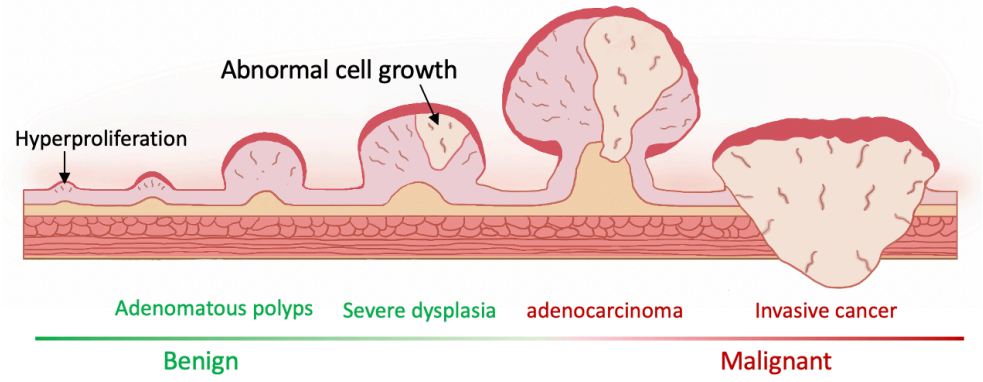

Figure 1.2 Colorectal cancer progression.

Colonoscopy (i.e., white light endoscopy, as shown in Figure 1.3) is the gold standard for CRC diagnostics as it provides visualization of abnormal tissue growth on the mucous membrane

in the colon or rectum, known as colorectal polyps [47]. In addition to CRC screening, physicians also utilize colonoscopy to excise small polyps and biopsy larger polyps or tumors for further diagnosis in a minimally invasive manner. However, several disadvantages of colonoscopy exist. While being the standard imaging technique, colonoscopy provides only surface morphology of the rectal wall and cannot resolve the abnormal layer architecture and subsurface microvasculature which are highly associated with CRC. Hence, cancer staging often requires biopsy which not only is more invasive and time-consuming but also has diminishing accuracy limited by the sample number (four and six biopsy specimens yield accuracies of 68% and 78%, respectively) [48, 49]. The size of the polyp also affects the accuracy of CRC diagnostics. The miss rate increases significantly in smaller sized polyps and the estimated miss rate is as high as 26% for polyps size less than 5 mm [50]. An imaging system that provides a high sensitivity and specificity for differentiating all kinds of polyps is therefore necessary.

Figure 1.3 A flexible endoscope.

To address the limitations of conventional colonoscopy, many endoscopic imaging modalities, such as endoscopic ultrasound (US), OCT, Doppler OCT, photoacoustic (PA), and near-infrared

(NIR) fluorescence imaging [51-65], have been applied in the GI tract to visualize the layered architecture or subsurface vascular network for better CRC staging and management. Each modality has its own strengths and limitations, as shown in Table 1.2. Endoscopic ultrasound (EUS) [52, 56] imaging allows a clinician to obtain images of the GI tract and the surrounding tissue and organs with an imaging depth of ~7 mm and a resolution of ~150 μm. However, many disorders of the GI tract, cancer in particular, arise within the mucosa. Therefore, limited by the resolution of the EUS, it is difficult to detect changes in the early stage of GI disease. Recently, endoscopic OCT [51, 57, 58, 66, 67], which is capable of providing high-resolution cross-sectional images of cellular-tissue microstructure, has been widely applied to image the esophagus, stomach, small and large intestine, and biliary and pancreatic ducts. In addition, endoscopic Doppler OCT technology [51, 68, 69] has been applied in endoscopic imaging to visualize vascular networks without any exogenous fluorescent agent. However, limited by the phase stability of the system and movement from the imaging probe, the reconstructed Doppler OCT images often contain motion artifacts and have relatively low sensitivity for microvasculature due to random and slow flow speed of the capillary. Another endoscopic angiography technology is NIR fluorescence imaging [53, 70-73] with indocyanine green (ICG) which provides high resolution microvasculature imaging and has been used clinically to observe a variety of vascular lesions, such as detecting abnormal submucosal vascularization in tumor lesions. Endoscopic photoacoustic (PA) imaging is a non-invasive imaging modality that provides molecular contrast with depth-resolved information [4, 74-76]. Integrated with US imaging, this multimodal endoscopic PA/US imaging technology is able to provide both structural and chemical compositions of colorectal walls for diagnosis of GI cancer at an early stage.

Table 1.2 Comparison of different modalities.

	Image	Structure	Vasculature	oxygen saturation
OCT [77]	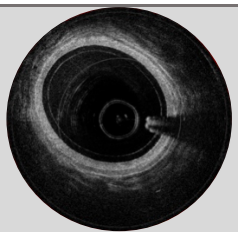	Resolution: 1-15 μm	N	N
Doppler OCT [59, 78]	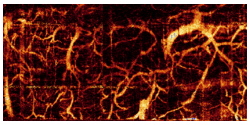	N	Resolution: 1-15 μm	N
US	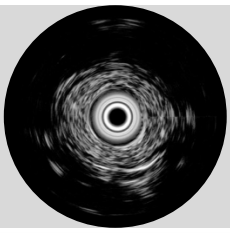	Resolution: ~100 μm	N	N
NIRF	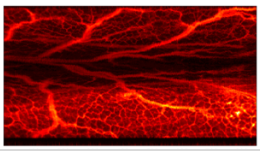	N	Resolution: 1-15 μm	N
PA	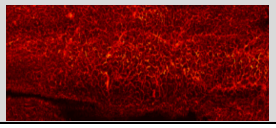	N	Resolution: >1 μm	Y

1.4 Ocular Disease

The eye is a complex organ consisting of several mutually interacting components with each part bearing biomechanical properties which are closely related to its respective anatomic functionality. Changes in the biomechanical properties are associated with a number of ocular diseases [79, 80]. The cornea and the crystalline lens, like a Keplerian telescope, focus light onto the retina through a series of refractions, allowing us to perceive a sharp image of objects. The light first enters the eye through the cornea, whose curvature contributes approximately 60% of the focusing power of the eye. Thereafter, the biconvex lens provides the remaining refractive power [as shown in Figure 1.4]. In youth, the lens can have its curvature dynamically adjusted to allow adjustment of focal distance through a process known as accommodation [81]. With age, the lens loses its malleability, and its dynamic range of adjustable focus evanesces. With advancing age and in many disease states, the lens becomes more rigid and more opaque and is described as a cataract [82]. Therefore, the biomechanical properties of the lens are essential to understand the development of refractive disorders. Other disorders, including myopia, hyperopia, and astigmatism, within this optical system may also cause refractive errors [83-85]. In severe cases, vision quality can be significantly affected, resulting in serious reduction in quality of life.

Contemporary clinical ophthalmic imaging techniques include optical coherence tomography (OCT), scheimpflug imaging, and confocal microscopy [86-89]. These techniques enable the study of corneal and lens morphology and clarity. The biomechanical properties of the cornea have been investigated by many research groups [90-95] because of the superficial location and ease of accessibility. However, knowledge of lens biomechanics in vivo is limited by its less accessible intraocular locations. Therefore, a need exists for a noninvasive approach to study lens biomechanics in vivo.

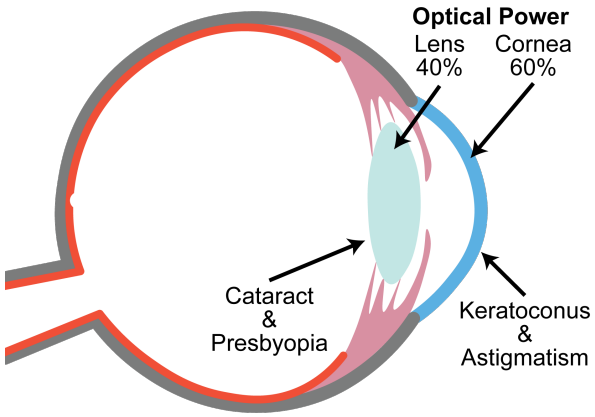

Figure 1.4 Schematic of the crystalline lens and cornea. The eye optical power provided by the lens is about 40% and that by the cornea, approximately 60%. Common diseases affecting the functionalities of lens and cornea include astigmatism, cataract, keratoconus, and presbyopia.

Elastography detects tissue elasticity by visualizing the tissue deformation induced by an external force stimulation as a function of time (i.e., elastic wave propagations) [96]. Several elastography modalities have been developed, including those based on magnetic resonance imaging, ultrasonography, Brillouin microscopy, and optical coherence tomography (OCT), each with its own advantages and limitations [91, 94, 97-101]. Magnetic resonance elastography provides a large penetration depth and a wide field of view, but ophthalmology applications are hindered by low spatial resolution, long imaging time, and cost [99]. Ultrasound elastography has an improved resolution (~100 μm) but is still insufficient for accurate elasticity evaluation in ocular tissue [100]. While Brillouin microscopy has also been proposed to investigate the age-related elasticity change in lenses, the correlation between Brillouin shifts and Young's modulus is still unclear because of the uncertainty of Poisson's ratio [101-103]. Optical coherence elastography (OCE), benefiting from OCT technique, possesses micron-level resolution and an axial displacement sensitivity on the order of a few nanometers, and it has been applied in ophthalmology to provide quantitative assessment of tissue biomechanical properties with high resolution and sensitivity [8, 94, 104-109].

1.5 Skin Cancer

In the United States, skin cancer is the most common cancer, and more than 9,500 people are diagnosed with skin cancer every day [110]. Skin cancer is the out-of-control growth of abnormal cells in the epidermis, the outermost skin layer, caused by unrepaired DNA damage that triggers mutations. These mutations cause the skin cells to multiply rapidly and form malignant tumors. The main types of skin cancer are basal cell carcinoma (BCC), squamous cell carcinoma (SCC), and melanoma [111, 112], as shown in Figure 1.5.

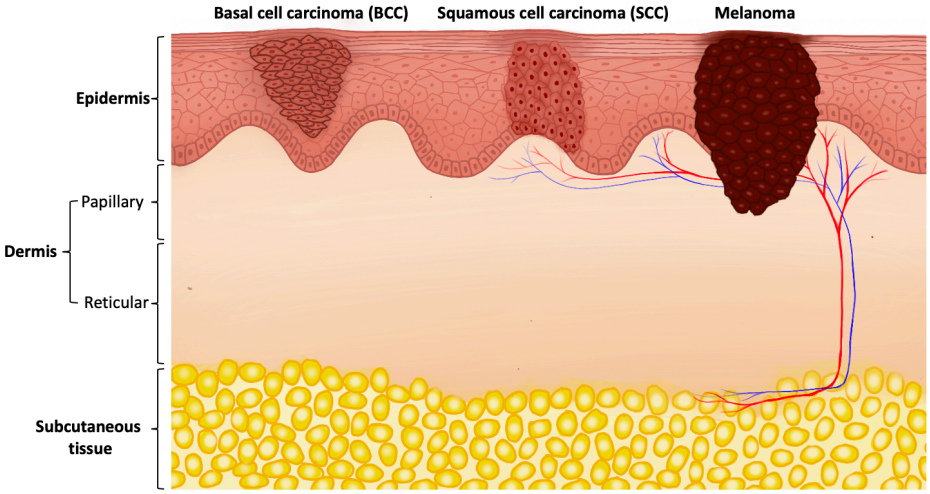

Figure 1.5 Schematic of the main types of skin cancer. Left: Basal cell carcinoma. Middle: Squamous cell carcinoma. Right: Melanoma.

The mortality rate of basal-cell and squamous-cell carcinoma is around 0.3%, causing 2,000 deaths per year in the U.S. The mortality rate of melanoma is 15–20%, and it causes 6,500 deaths per year [113-115]. The survival rate for people with skin cancer depends upon when they start treatment. The cure rate is very high when skin cancer is detected at an early stage. The traditional diagnosis of skin cancer is limited to dermascopy, which is able to help the dermatologist to visualize small and weakly contrasted morphologic features [116, 117]. However,

the accuracy of diagnosis highly depends on the skills and clinical experience of the examiners. To obtain an accurate diagnosis, skin biopsies are often needed in the majority of cases, which is considered as the gold standard for detection and staging skin cancer. Nevertheless, several disadvantages of skin biopsies exist. It is invasive and time consuming. In addition, accuracy is also limited due to limited sample number because usually it does not allow for repetitive measurements. To address the above issues, there is strong demand for noninvasive, high sensitivity, in vivo real time imaging techniques. In recent decades, imaging techniques, such as high frequency ultrasound (US) imaging, magnetic resonance imaging (MRI), confocal microscopy (CM), multiphoton tomography (MPT) and optical coherence tomography (OCT), have been developed for improving the diagnostic accuracy of skin cancer [118-130]. Despite diagnostic advantages, in vivo real time imaging allows dynamic visualization that plays an important role in monitoring and optimizing treatment where histopathological examinations are of very limited use. US imaging provides cross-sectional images with an imaging depth of ~7 mm and a resolution of ~150 μm. However, its low spatial resolution limits its clinical application in dermatology. MRI has an increased resolution of 80 μm, but it cannot be used to detect early stage cancer due to an inability to provide histological level information. CM and MPT, in contrast, are able to visualize biological tissue with cellular resolution and high contrast, but they have superficial imaging depth (~200 μm), small fields of view (0.5 ×0.5 mm^2) and long acquisition time which hinder the clinical application, such as border delineation. Another equally promising technology is optical coherence tomography (OCT). OCT is able to provide high-resolution (1-15 μm) cross-sectional real time images with a penetration depth of 1-2 mm that are comparable to the histopathological level. Furthermore, Doppler OCT and OCT angiography (OCTA) have been developed to visualize the vascular network and tumor angiogenesis [131, 132]. Therefore,

integrated OCT and Doppler OCT imaging has the capability to provide information with respect to the layer architecture and microvasculature. In the clinic, OCT and Doppler OCT have also been shown to be useful in tumor margin delineation and preoperative treatment planning.

1.6 Summary of Chapters

In this dissertation, multimodal endoscopic and microscopic biomedical imaging technique, including intravascular tri-modality OCT/US/NIRF, 1.7-micron intravascular OCT, endoscopic PA/US, microscopic OCE, and 1.7-micron OCT/OCTA, are developed for cardiovascular, ocular, gastrointestinal, and dermatological applications and has been translated from benchtop testing to *ex vivo* and *in vivo* animal or human studies. The systems are able to map morphology, molecular contrast, vasculature, or mechanical elasticity of tissues, which address current unmet need in clinic applications. Brief summaries of the chapters are given below.

Chapter 1 provides a brief background of atherosclerosis, CRC, ocular disease, and skin cancer. The features and limitations of current imaging methods are introduced.

Chapter 2 introduces OCT, Doppler OCT, and OCE in detail. First, the principles of time-domain and Fourier-domain OCT are discussed, and the methods of k calibration, dispersion compensation are described. In addition, the extensions of OCT, Doppler OCT and OCE are introduced. Finally, the principle of PA is discussed.

Chapter 3 presents two intravascular imaging systems for atherosclerosis characterization. First, a novel IVOCT system with a 1.7-micron center wavelength swept light source that can readily penetrate deeper into the tissue is presented. A human cadaver coronary artery is imaged to validate the performance. Then, a tri-modality imaging system that is able to simultaneously acquire OCT, US, and NIRF is introduced. A male New Zealand white rabbit was imagined *ex vivo* to evaluate the performance.

Chapter 4 discusses two different endoscopic multimodal imaging systems for the early detection of CRC. First, we introduced a high-speed imaging system that integrated PA and US

into a miniature probe to visualize vasculature and morphology of colorectal wall. In addition, an US transducer fabricated using PMN-33%PT/epoxy 1-3 composite was incorporated into a probe to further enhance sensitivity of system. An *in vivo* healthy rat experiment was performed for system verification. Then, we described another imaging system that combined OCT and NIRF together to simultaneously visualize vasculature and morphology of colorectal wall. We performed the image experiment in an animal model of rat with CRC to demonstrate that the integrated system can detect CRC better than individual imaging technique alone.

Chapter 5 introduces two microscopic OCE systems for elasticity quantification of ocular tissue. First, we demonstrated an OCE system which is able to simultaneously map and quantify the elasticity in both cornea and crystalline lens. The correlations between elasticity and intraocular pressure and between elasticity and age were investigated using the proposed OCE system. Then, we presented an ultrahigh sensitive OCE system which is based on swept-source optical coherence tomography (SS-OCT) with a common-path configuration. *Ex vivo* phantom and *in vivo* rabbit experiments were performed to quantify phase stability and validate the performance of system.

Chapter 6 introduces a microscopic 1.7-micron OCT/OCTA system for the characterization of skin cancer which allows for the visualization of both structure and vascular morphology in a deeper skin depth compared to the 1.3- micron OCTA system. Furthermore, we presented the imaging results from six human subjects with different types of lesions and described the features in OCT and OCTA images.

Chapter 7 summarizes the above developed imaging systems and corresponding imaging results and discusses future directions.

Chapter 2 – Biomedical Imaging Technologies

In this chapter, we first introduce the principles of OCT, including a time domain OCT system and Fourier domain OCT system. Mathematic derivations of OCT system's spatial resolution, sensitivity, imaging range, k space calibration, and dispersion compensation will be described. In addition, as a functional extension of OCT, Doppler OCT and OCE will be introduced. Last, the principle and application of photoacoustic imaging are discussed.

2.1 Optical Coherence Tomography

OCT is an imaging technique that utilizes low-coherence light to capture structural images of biological tissue with high resolution of 1-15 μm in the micrometer scale [11, 133, 134]. OCT was first developed in the early 1991, and first *in vivo* OCT images which show retinal structures were published in 1993 [11, 135, 136]. In OCT systems, a scanning reference mirror was applied to vary optical path length in a Michelson interferometer with broad band light source in order to retrieve the structural information of the sample from different depths, termed as time domain OCT (TD-OCT). The main limitation of TD-OCT is the slow mechanical scanning speed of the reference arm, which causes a limited imaging speed (typically an A-line rate of 1-5 kHz) [137]. In 2003, Fourier domain (FD-OCT) was developed with the aim of achieving high-speed OCT in which the broadband interference is spectrally separated, either by encoding the optical frequency in time with a spectrally sweeping source or in space with a spectrometer, which allows for simultaneous acquisition of entire depth of the sample [138, 139]. In contrast to TD-OCT, FD-OCT has faster imaging speed and higher sensitivity. Currently, OCT has brought great impact to diagnosis and management of diseases in many fields of medicine, such as ophthalmology,

cardiology, gastroenterology, urology, and otolaryngology, by enabling the visualization, hence the quantification, of morphological changes caused by the disease [140-142].

2.1.1 Time Domain OCT

OCT is based on low-coherence interferometry, in which a broadband light source is applied. The output of the light source is split into two beams: a reference arm and a sample arm. The back-scattered light from the sample arm is superimposed with the back reflected light from the reference arm interferometer to generate interference. During imaging, the optical path length of the refence arm will be changed in order to obtain the interference fringe from the difference depths of the sample. Figure 2.1 shows a schematic of the OCT system.

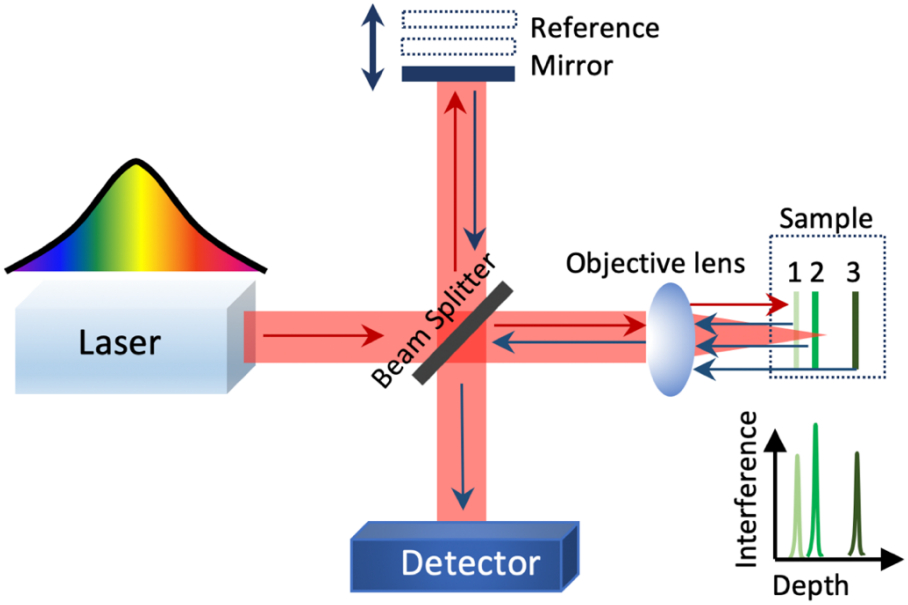

Figure 2.1 Schematic of TD-OCT system.

For a low coherence light source, the interference fringe can be observed only when optical path lengths match within the coherence length of the light source. Figure 2.2 shows the interference signal of one reflector in the sample arm with different light source. If the light source

is a laser diode [as shown in Figure 2.2 (a)-(c)], the interference fringe is a uniform sinuous function. As the wavelength number increases, the interference fringe gets enhanced at zero optical path difference (OPD), as shown in Figure 2.2 (d)-(f). With a broadband light source, the two sides are eliminated so the interference fringe is only obtained around zero OPD.

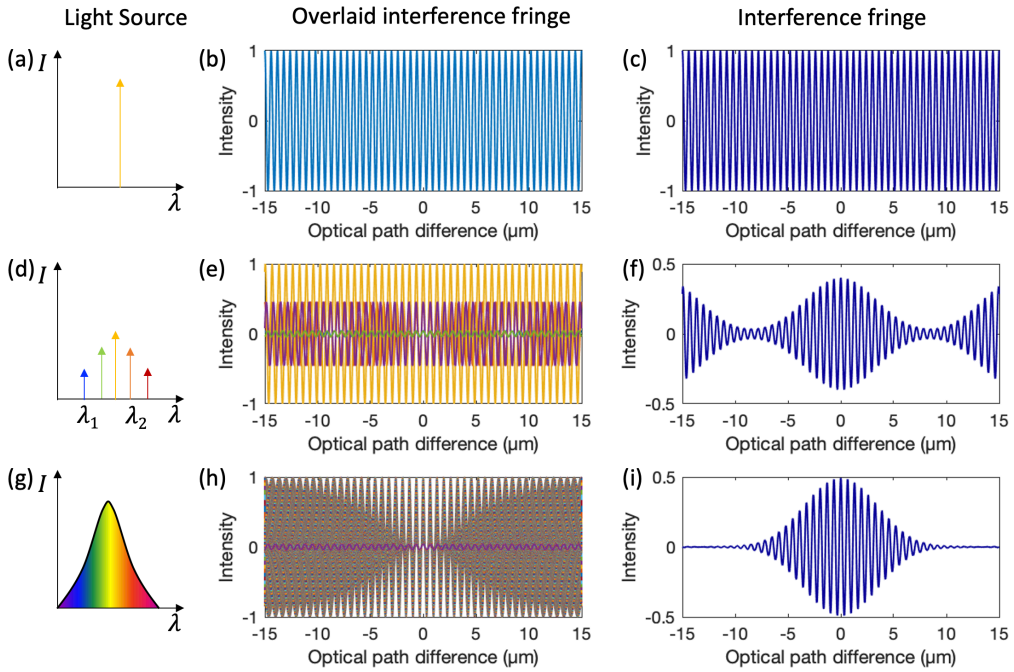

Figure 2.2 Interference fringe signal with different light sources. (a), (d), and (g) Spectrum of light sources. (b), (e), and (h) Overlaid interference fringes with single one wavelength. (c), (f), and (i) Integration of interference fringes over the entire wavelength.

Principle: Assuming that the interference fringe is generated with a broadband light source and single reflector in the sample, the illuminating wave from the light source can be described by its electric field:

$$E_i(k,\omega) = s(k,\omega)e^{i(kz-\omega t)} \tag{2.1}$$

where $s(k,\omega)$ is the electric field amplitude as a function of wavenumber $k = 2\pi/\lambda$ and angular frequency $\omega = 2\pi\nu$. The electric field of back reflected light from sample and reference can be expressed as:

$$E_s(k,\omega) = \frac{s(k,\omega)}{\sqrt{2}} r_s e^{i(2kz_s-\omega t)} \tag{2.2}$$

$$E_r(k,\omega) = \frac{s(k,\omega)}{\sqrt{2}} r_r e^{i(2kz_r-\omega t)} \tag{2.3}$$

where r_s and r_r are the electric field defectivities from the sample and reference arms, respectively; z_s and z_r are the optical path length of sample and reference arm, respectively. The factor of 2 presents a round-trip propagation. The generated interference signal can be described as $E_s(k,\omega) + E_r(k,\omega)$. Photodetectors are only able to measure intensity rather than electric field, so the signal detected by the photodetector can be expressed as:

$$I_D(k,\omega) = \frac{\rho}{2}\langle|E_s + E_r|^2\rangle = \frac{\rho}{2}\langle(E_s + E_r)(E_s + E_r)^*\rangle \tag{2.4}$$

where $\langle\ \rangle$ represents integration over the response time of the photodetector, ρ is the responsibility of the detector. Substituting equations (2.2) and (2.3) into (2.4), the interference can be expressed as:

$$I_D(k,\omega) = \frac{\rho}{2}\left\langle\left|\frac{s(k,\omega)}{\sqrt{2}} r_r e^{i(2kz_r-\omega t)} + \frac{s(k,\omega)}{\sqrt{2}} r_s e^{i(2kz_s-\omega t)}\right|^2\right\rangle \tag{2.5}$$

The detector response time is ~10^{-9}s, so <sin(ωt)> is equal to 0. Equation (2.5) can be simplified:

$$I_D(k) = \frac{\rho}{2}\left\langle\left|\frac{s(k,\omega)}{\sqrt{2}} r_s e^{i(2kz_s)} + \frac{s(k,\omega)}{\sqrt{2}} r_r e^{i(2kz_r)}\right|^2\right\rangle \tag{2.6}$$

Expanding equation (2.6) yields:

$$I_D(k) = \frac{\rho}{4}\left\{S(k)\cdot(R_s + R_s) + 2\left(S(k)\cdot\sqrt{R_r R_s}\right)\left(e^{i2k(z_s-z_r)} + e^{-i2k(z_s-z_r)}\right)\right\} \tag{2.7}$$

$$=\frac{\rho}{4}\{S(k)\cdot(R_s+R_s)+2S(k)\cdot\sqrt{R_rR_s}\cos 2k(z_s-z_r)\}$$

where $S(k)=\langle|s(k,\omega)|^2\rangle$ and $R_i=|r_i|^2$. In real OCT imaging, the sample often consists of multiple depth dependent reflectors. Considering that, the reflectivity of the sample can be expressed as an integration:

$$r_s(z)=\sum_{n=1}^{N} r_{s_n}\,\delta(z-z_{s_n}) \tag{2.8}$$

Plugging (2.8) into (2.6) yields:

$$\begin{aligned} I_d(k) &= \frac{\rho}{2}\langle\left|\frac{s(k,\omega)}{\sqrt{2}}r_r e^{i(2kz_s)}r+\frac{s(k,\omega)}{\sqrt{2}}\sum_{n=1}^{N} r_{s_n}e^{i(2kz_{s_n})}\right|^2\rangle \\ &= \frac{\rho}{4}\left[S(k)\cdot\left(R_r+\sum_{n=1}^{N}R_{S_n}\right)\right] \quad \text{"DC Terms"} \\ &+\frac{\rho}{2}[S(k)\cdot\sum_{n=1}^{N}\sqrt{R_rR_{S_n}}\left(\cos 2k\left(z_{S_n}-z_r\right)\right) \quad \text{"Cross}-\text{correlation Terms"} \\ &+\frac{\rho}{4}[S(k)\cdot\sum_{n\neq m=1}^{N}\sqrt{R_{S_n}R_{S_m}}\left(\cos 2k\left(z_{S_n}-z_{S_m}\right)\right) \quad \text{"Auto}-\text{correlation Terms"} \end{aligned} \tag{2.9}$$

From equation (2.9), three distinct components can be found. The first term is the DC terms from the reference and sample reflectivity. The second term is the cross-correlation between the reference and sample arms which contains the information of the depth dependent reflectivity of sample $\sqrt{R_s(z)}$. The third term is the autocorrelations term which is the self-interferences between the reflectors in the sample arm. The intensity of each term is proportional to the power reflectivity. Typically, the power reflectivity of the sample is far less than that of the reference mirror, so the third term can be omitted. The interference signal can be expressed as:

$$I_d(k) \propto \frac{\rho}{2}[S(k) \cdot \sum_{n=1}^{N} \sqrt{R_r R_{S_n}} \left(\cos 2k\left(z_{S_n} - z_r\right)\right) \tag{2.10}$$

In Time Domain OCT, depth scanning is achieved by changing the optical path length of the reference arm to generate an interference fringe. If the source spectral distribution is a Gaussian function, $S(k)$ can be expressed as:

$$S(k) = e^{-4\ln 2[\frac{(k-k_0)}{\Delta k}]^2} \tag{2.11}$$

where Δk is full width at half maximum of the spectrum, and $S_0 = \int S(k)dk$. The output detector signal $I_d(z)$ is equal to the wavenumber dependent detector $I_d(k)$ integrated over all k:

$$\begin{aligned} I_d(Z_r) &\propto \sum_{n=1}^{N} \int \frac{\rho}{2}[S(k) \cdot \sqrt{R_r R_{S_n}} \left(\cos 2k\left(z_{S_n} - z_r\right)\right) dk \\ &\propto \sum_{n=1}^{N} S_0 \sqrt{R_r R_{S_n}}\ e^{\frac{-[2(z_r - z_{S_n})]^2 \Delta k^2}{16\ln 2}} \left(\cos 2k_0\left(z_{S_n} - z_r\right)\right) \end{aligned} \tag{2.12}$$

From equations (2.10), (2.11), and (2.12), we can find that $I_d(Z_r)$ and $I_d(k)$ are Fourier transform pair.

2.1.2 Fourier Domain OCT

In TD-OCT, depth information in the sample is achieved by changing OPD through a mechanically scanning reference mirror. Therefore, the imaging speed is often slow due to the mechanical scanning of the reference arm. In 1995, Fercher et al. proposed Fourier Domain OCT (FD-OCT); the interference spectrum was measured as a function of wavenumber from the sample instead of the scanning reference mirror [143-145]. Previous studies demonstrated that the image

speed of FD-OCT was 2-6 orders of magnitude faster, and the sensitivity of FD-OCT was 20 dB or greater over TD-OCT system [138, 139, 146, 147]. Two kinds of FD-OCT systems are often used to achieve interference spectrum measurement; spectral domain OCT (SD-OCT) and swept-source OCT (SS-OCT). In SD-OCT, a broadband continuous wave (CW) laser is often applied as the light source, and the interference fringe with different wavenumbers can be spatially separated by a grating and then detected through a multi-pixel camera, as shown in Figure 2.3. In SS-OCT, a swept source laser which is able to output different wavenumbers as a function of time is utilized as the light source, and the interference fringe with different wavenumbers can be temporally separated and then detected through a photodetector, as shown in Figure 2.4.

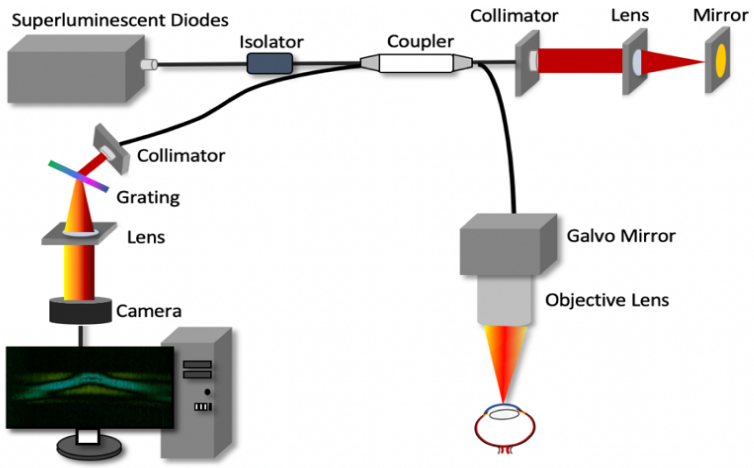

Figure 2.3 Schematic of SD-OCT system.

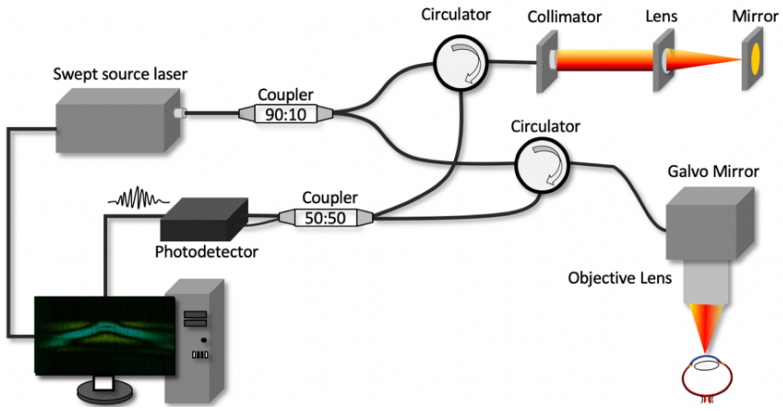

Figure 2.4 Schematic of SS-OCT system

In FD-OCT, the interference fringe at different depths presents different frequencies which increase with depth. Figure 2.5 shows the simulation of interference fringes at different depths and corresponding Fourier transforms. Therefore, the depth information can be reconstructed by performing Fourier transform for interference fringe.

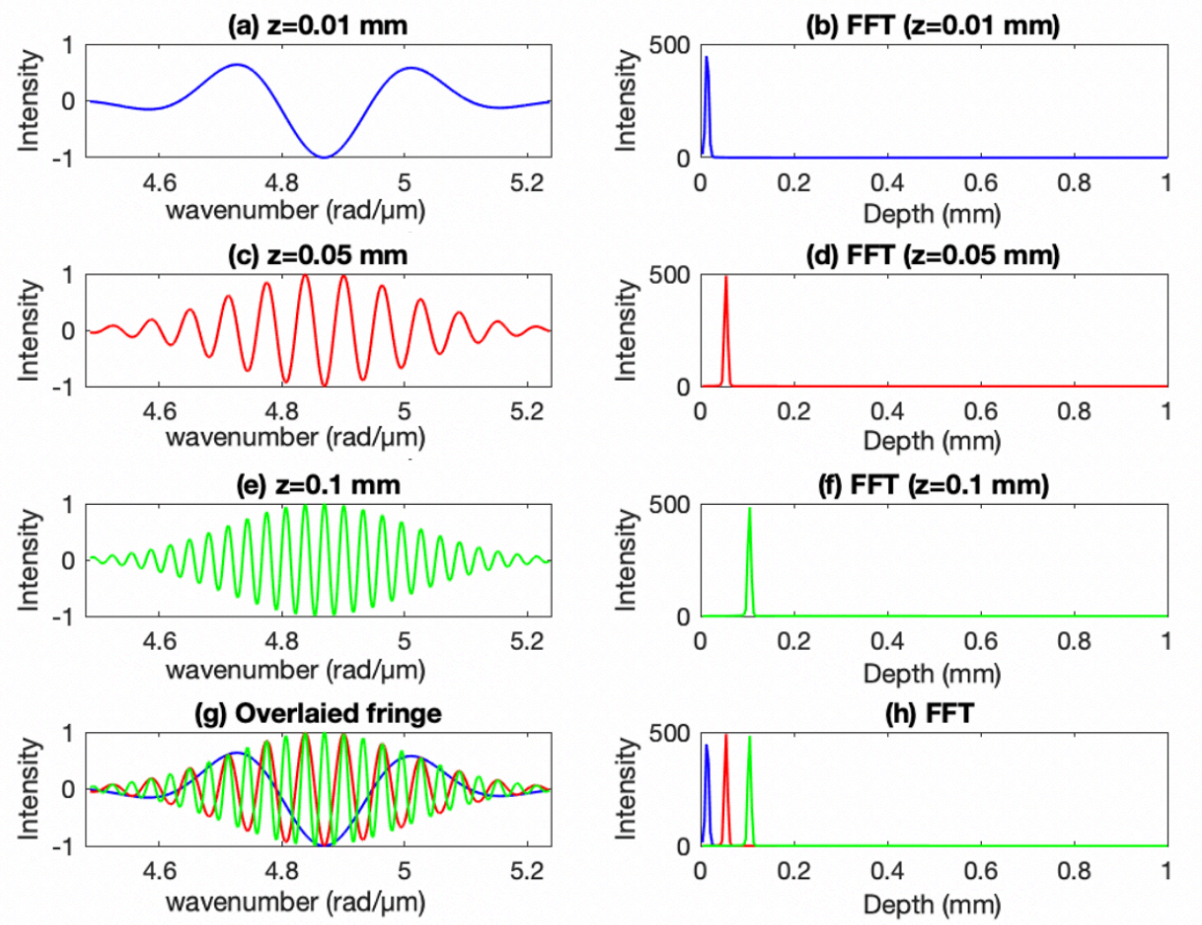

Figure 2.5 Schematic of FD-OCT system.

Principle: According to equation (2.9) and (2.12), the sample reflectivity profile $r_s(z_s)$ is inverse Fourier transform of $I_d(k)$. Taking the inverse Fourier transform of (2.9) and (2.12) using Convolution theorem and Fourier transform pair $\int_{-\infty}^{\infty} e^{-ikx}\,dx = 2\pi\delta(k)$ yields:

$$
\begin{aligned}
I_d(z) &= \mathcal{F}^{-1}\left[\frac{\rho}{2}\left\langle\left|\frac{s(k,\omega)}{\sqrt{2}} r_r e^{i(2kz_s)} r + \frac{s(k,\omega)}{\sqrt{2}}\sum_{n=1}^{N} r_{s_n} e^{i(2kz_{s_n})}\right|^2\right\rangle\right] \\
&= \frac{\rho}{4}\left[S'(z)\otimes\left(R_r + \sum_{n=1}^{N} R_{S_n}\right)\right] \quad \text{"DC Terms"} \\
&+ \frac{\rho}{4}\left[S'(z)\otimes\sum_{n=1}^{N}\sqrt{R_r R_{S_n}}\left(\delta\left[z \pm 2\left(z_r - z_{S_n}\right)\right]\right)\right] \quad \text{"Crosscorrelation Terms"} \\
&+ \frac{\rho}{8}\left[S'(z)\otimes\sum_{n=1}^{N}\sqrt{R_r R_{S_n}}\left(\delta\left[z \pm 2\left(z_{S_n} - z_{S_m}\right)\right]\right)\right] \quad \text{"Autocorrelation Terms"}
\end{aligned}
\tag{2.13}
$$

Where $S'(z) = \mathcal{F}^{-1}(s(k)) \propto e^{-(z)^2\Delta k^2/16/\ln 2}\cos(k_0 z)$. Due to the shifting property of delta function, equation (2.13) can be converted to:

$$
\begin{aligned}
I_d(z) &= \frac{\rho}{4}\left[S'(z)\cdot\left(R_r + \sum_{n=1}^{N} R_{S_n}\right)\right] \quad \text{"DC Terms"} \\
&+ \frac{\rho}{4}\left[\sum_{n=1}^{N}\sqrt{R_r R_{S_n}}\left[S'\left[2\left(z_r - z_{S_n}\right)\right] + S'\left[-2\left(z_r - z_{S_n}\right)\right]\right]\right] \text{"Cross} - \text{correlation Terms"} \\
&+ \frac{\rho}{8}\left[\sum_{n=1}^{N}\sqrt{R_r R_{S_n}}\left[S'\left[2\left(z_{S_n} - z_{S_m}\right)\right] + S'\left[-2\left(z_{S_n} - z_{S_m}\right)\right]\right]\right] \text{"Auto} - \text{correlation Terms"} \\
&\propto \frac{\rho}{4}\left[e^{-(z)^2\Delta k^2}\cdot\left(R_r + \sum_{n=1}^{N} R_{S_n}\right)\right] \quad \text{"DC Terms"} \\
&+ \frac{\rho}{2}\left[\sum_{n=1}^{N}\sqrt{R_r R_{S_n}}\left[e^{\frac{-\left[2\left(z_r - z_{S_n}\right)\right]^2\Delta k^2}{16\ln 2}}\right]\cos\left[2k_0\left(z_r - z_{S_n}\right)\right]\right] \quad \text{"Cross} - \text{correlation Terms"} \\
&+ \frac{\rho}{4}\left[\sum_{n=1}^{N}\sqrt{R_r R_{S_n}}\left[e^{\frac{-\left[2\left(z_{S_n} - z_{S_m}\right)\right]^2\Delta k^2}{16\ln 2}}\right]\cos\left[2k_0\left(z_{S_n} - z_{S_m}\right)\right]\right] \text{"Auto} - \text{correlation Terms"}
\end{aligned}
\tag{2.14}
$$

From equation (2.13), it can be found that the sample filed reflectivity profile $r_s(z)$ is embedded in the "Cross-correlation Terms." Figure 2.6 shows simulation results according to "Cross-correlation Terms" in equation (2.14). Assuming that the sample consists of three reflectors (d=0.01, 0.4, and 0.8 mm), the corresponding reflectivities are 0.1, 0.2, and 0.3.

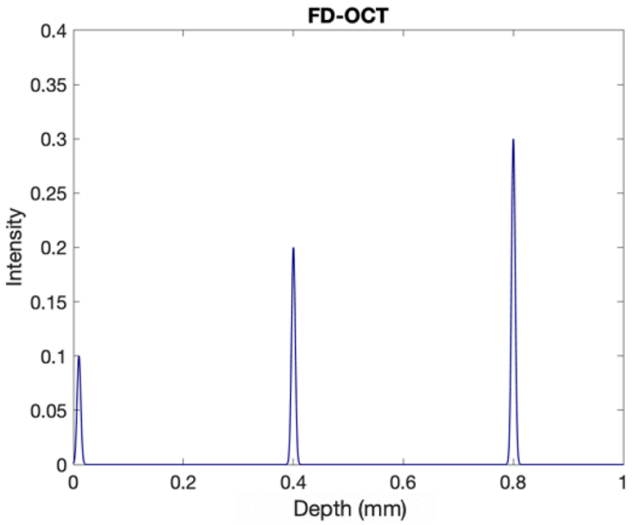

Figure 2.6 Simulation of FD-OCT.

2.1.3 Spatial Resolution

(1) Axial resolution

An interference fringe between the back reflected light and backscattered light from the reference and sample arms is only present when the OPL is within the coherence length of the laser source, which corresponds to the axial resolution. Here, we define full width of half maximum of interference fringe of the single reflector as the coherence length. According to the "Cross-correlation Terms" in equation (2.14), the interference fringe is proportional to $e^{\frac{-[2z]^2\Delta k^2}{16\ln 2}}$, so the coherence length L_c defined as full width at half maximum of interference signal can be calculated by:

$$\frac{1}{2} = e^{\frac{-\left[2\cdot\frac{L_c}{2}\right]^2 \Delta k^2}{16\ln 2}} \tag{2.15}$$

Taking logarithm yields:

$$\ln 2 = \frac{-\left[2\cdot\frac{L_c}{2}\right]^2 \Delta k^2}{16\ln 2} \tag{2.16}$$

Therefore,

$$Lc = \frac{4\ln 2}{\Delta k^2} = \frac{2\ln 2}{\pi}\frac{{\lambda_0}^2}{\Delta\lambda} \approx 0.44\frac{{\lambda_0}^2}{\Delta\lambda} \tag{2.17}$$

where λ_0 and $\Delta\lambda$ are the center wavelength and bandwidth of the light source, respectively. From equation (2.12) and (2.17), it can be concluded that axial resolution can be improved by using a shorter center wavelength and/or a broader bandwidth.

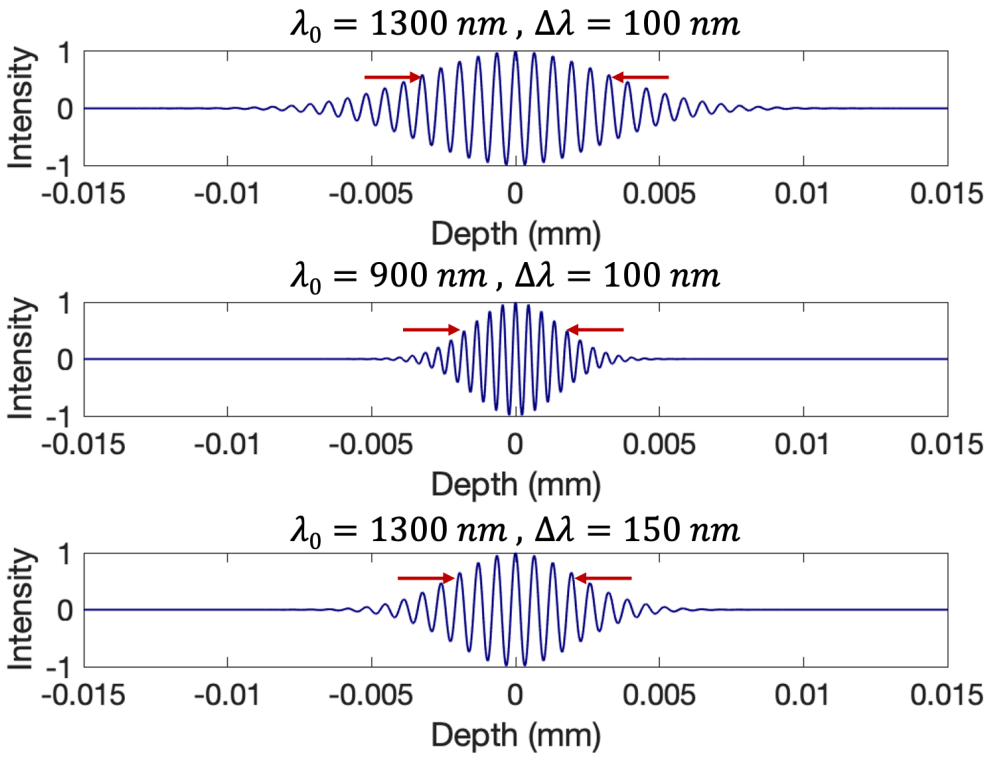

Figure 2.7 Simulation of FD-OCT.

(2) Lateral resolution

Lateral resolution of an OCT image is determined by numerical aperture (NA) of the objective lens, which can be expressed as:

$$\Delta x = \frac{2\lambda}{\pi}\frac{1}{NA} = \frac{4\lambda}{\pi}\left(\frac{f}{d}\right) \tag{2.18}$$

where d is diameter of the Gaussian beam, f is the focal length of the objective lens. From equation (2.18), it can be found that lateral resolution can be improved by increasing the NA of the objective lens. However, it should be noted that increased lateral resolution will cause decreased depth of focus ($d=\pi \Delta x^2 / \lambda$).

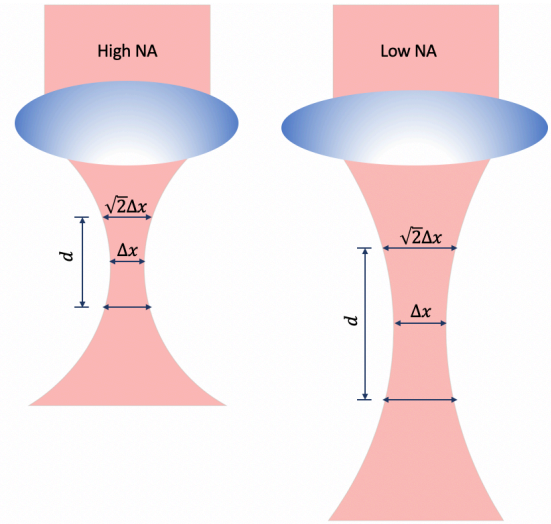

Figure 2.8 Relationship between focus spot size and depth of field for objective lens.

2.1.4 Sensitivity

(1) TD-OCT

The sensitivity of a TD-OCT system is defined as the ratio of the signal power of a perfect reflector (such as a mirror) and noise power. The noise in TD-OCT is mainly from shot noise I_{SH} due to inherent variance in the arrival and detection of photons, relative intensity noise I_{RIN}

in the light source, and thermal noise I_{TH} from detector. The overall noise is the sum of the square of three noises because only the noise power is additive, which can be expressed as:

$$I_N{}^2 = I_{SH}{}^2 + I_{RIN}{}^2 + I_{TH}{}^2 \tag{2.19}$$

An ideal OCT system has minimal detection and intensity noise, and the short noise dominates. The noise power can be calculated by its variance:

$$I_N{}^2 = \sigma_{SH}{}^2 = \rho e P_{TD} R_r B_{TD} \tag{2.20}$$

where P_{TD} is the instantaneous source power, e is the electron charge, R_r is the reference reflectivity, and B_{TD} is the FWHM signal power bandwidth. Regarding TD-OCT, depth scanning is achieved by changing OPL of the reference arm, which causes a Doppler shift (Δf) of the reference light frequency. The FWHM signal power bandwidth can be calculated as:

$$\Delta f = \frac{\Delta k_{FWHM} Z_{max}}{\pi \Delta t} \tag{2.21}$$

where Z_{max} is the imaging range of the system, Δt is the acquisition time for one A-scan. Using Nyquist sampling theorem, the optimal sampling bandwidth is equal to twice of Δf:

$$B_{TD} = 2\Delta f = \frac{2\Delta k_{FWHM} Z_{max}}{\pi \Delta t} \tag{2.22}$$

The peak detector I_d can be expressed as：

$$\langle I_d \rangle_{TD}^2 = \frac{\rho^2 S_{TD}^2}{2} [R_r R_s] \tag{2.23}$$

The signal-to-noise ratio (SNT) of TD-OCT system can be obtained by:

$$SNR_{TD} = \frac{\langle I_d \rangle_{TD}^2}{\sigma_{TD}{}^2} = \frac{\rho P_{TD} R_s}{2 e B_{TD}} \tag{2.24}$$

From equation (2.24), it can be found that SNR is related to the responsivity of the detector (ρ), back-scattered light from the sample arm (R_s), and FWHM signal power bandwidth (B_{TD}).

(2) FD-OCT

According to equation (2.10), the interference signal at a specific wavenumber k can be expressed as:

$$I_d[k_m] = \frac{\rho}{2} P_{FD}[k_m]\left[\sqrt{R_r R_s}\left(\cos 2k(z_s - z_r)\right)\right] \tag{2.25}$$

assuming the case $z_s - z_r$=0 (zero OPD) and the spectral power of light source are evenly distributed as a function of wavenumber. Then the interference signal can be expressed as:

$$I_d[z_s - z_r = 0] = \frac{\rho}{2}\sqrt{R_r R_s}\sum_{m=1}^{M} P_{FD}[k_m] = \frac{\rho}{2}\sqrt{R_r R_s} P_{FD}[k_m] \cdot M \tag{2.26}$$

where M is the spectral sampling interval (δk) number and $\Delta k = M \cdot \delta k$, which is typically determined by sampling rate of data acquisition system in SS-OCT or the physical size of the pixels in the camera in SD-OCT. Noise in FD-OCT can be described as additive, uncorrelated white noise which has a Gaussian shape with zero mean and a standard deviation of $\sigma_{TD}[k_m]$. FD-OCT noise can also be shot noise and calculated by equation (2.20).

Therefore, the total noise variance of two channels can be expressed as:

$$\sigma_{FD}{}^2 = 2\sum_{m=1}^{M} \sigma_{FD}{}^2[k_m] = 2\rho e P_{FD}[k_m] R_r B_{FD} \cdot M \tag{2.27}$$

Regarding swept source OCT, $P_{FD}[k_m] = P_{TD}$ and $B_{FD} = B_{TD}$. For spectral domain OCT, $P_{FD}[k_m] = P_{TD}/M$ and $B_{FD} = B_{TD}/M$. Utilizing equations (2.26) and (2.27), sensitivity can be obtained by:

$$\mathrm{SNR_{FD}} = \frac{\langle \mathrm{I_d} \rangle_{\mathrm{FD}}^2}{{\sigma_{\mathrm{FD}}}^2} = \frac{\rho \mathrm{P_{FD}[k_m]R_s}}{4\mathrm{eB_{FD}}} \cdot \mathrm{M} = \mathrm{SNR_{TD}} \cdot \frac{\mathrm{M}}{2} \tag{2.28}$$

From equation (2.28), it can be found that sensitivity of FD-OCT is M/2 times more than that of TD-OCT. Typically, spectral sampling interval (δk) number is larger than 1000, which results in at least a 20-30 dB sensitivity increase of FD-OCT over TD-OCT.

2.1.5 Imaging Range

(1) TD-OCT

Imaging range is defined as how depth OCT signals can be observed. For TD-OCT systems, reconstruction of depth information relies on the scanning of a reference mirror so the imaging range is completely dependent on the scanning range of the reference arm. A longer scanning range of reference contributes to a larger OCT imaging range. Typically, piezoelectric scanners and translational motors are utilized to perform reference arm scanning [11, 148] which are generally slow in scanning and result in slow imaging speed. To improve imaging speed, several faster scanning methods were proposed [149-151], such as rapid-scanning optical delay and grating-based phase control delay line. However, a faster scanning speed and scanning range result in an increase of the required detection bandwidth, thereby reducing the sensitivity of the system for a given axial resolution.

(1) FD-OCT

In the FD-OCT system, depth information corresponds to the frequency of the interference signal. Several factors restrict the retrieval of the frequency of the interference signal. First, to obtain the depth information, the inverse Fourier transform is often used to retrieve the depth-dependent sample reflectivity profile which generates mirror terms and halves the imaging range. In addition, spectral resolution ($\delta_r k$) affects the imaging range, which is determined by the

narrowness of the instantaneous linewidth of the laser source in SS-OCT and the number of pixels of the camera in SD-OCT. Mathematically, the effect of the spectral resolution by convolving the ideal spectral interferogram [equation (2.14)] with a Gaussian function in which FWHM is equal to δk is shown in equation (2.29)

$$\mathrm{I}(\hat{z})' = \mathrm{I_d}(\hat{z}) \cdot \left[\mathrm{e}^{\frac{-(\hat{z})^2 \delta_r k^2}{4\ln 2}}\right] \tag{2.29}$$

where $\hat{z} = 2z$. The exponential falloff of sensitivity with depth can be understood as decreasing intensity of interference fringe with frequency. Here, we define the one-sided depth where the sensitivity falls off by a factor of ½ as the imaging range ($\mathrm{e}^{\frac{-(\hat{z}_{6dB})^2 \delta_r k^2}{4\ln 2}} = \frac{1}{2}$):

$$\hat{z}_{6dB} = \frac{2\ln 2}{\delta_r k} = \frac{\ln 2}{\pi} \frac{{\lambda_0}^2}{\delta_r \lambda} \tag{2.30}$$

The third factor in imaging depth is sampling rate of data acquisition system or the physical size of the pixels in the camera. We assume the interferogram acquired with a spectral sampling interval of δk and Δk= M· $\delta_s k$. Therefore, the sampling interval in z domain ($\delta_s \hat{z}$) is equal to 2π/(2Δk), where the extra factor of 2 is due to the use of $\hat{z} = 2z$. Therefore, we can have:

$$\mathrm{z}_{max} = \frac{M}{2} \cdot \delta_s \hat{z} = \frac{\pi}{2 \cdot \delta_s k} \tag{2.31}$$

Overall, imaging range of FD-OCT is affected by Fourier transform, spectral resolution ($\delta_r k$) and sampling interval ($\delta_s k$).

2.1.6 OCT Calibration

For the FD-OCT system, an inverse Fourier transform was applied to convert the data from k-domain to z-domain. To obtain an accurate axial reflectivity profile, the interference fringe

should be uniformly sampled in k-space. However, most FD-OCT systems perform uniform sampling in time (such as SS-OCT) or space (such as SD-OCT), which cause a broadening of the axial PSF function with increasing imaging depth. Figure 2.9 shows the simulation results of Fourier transform in lambda space and k space in which three discrete mirrors with a depth of 0.01 mm, 0.1 mm and 0.2 mm as the imaging targets. From the simulation results, it can be found that the OCT signal maintains high axial resolution as depth increases after FFT in k space. However, the PSF profile gets broader as the depth increases.

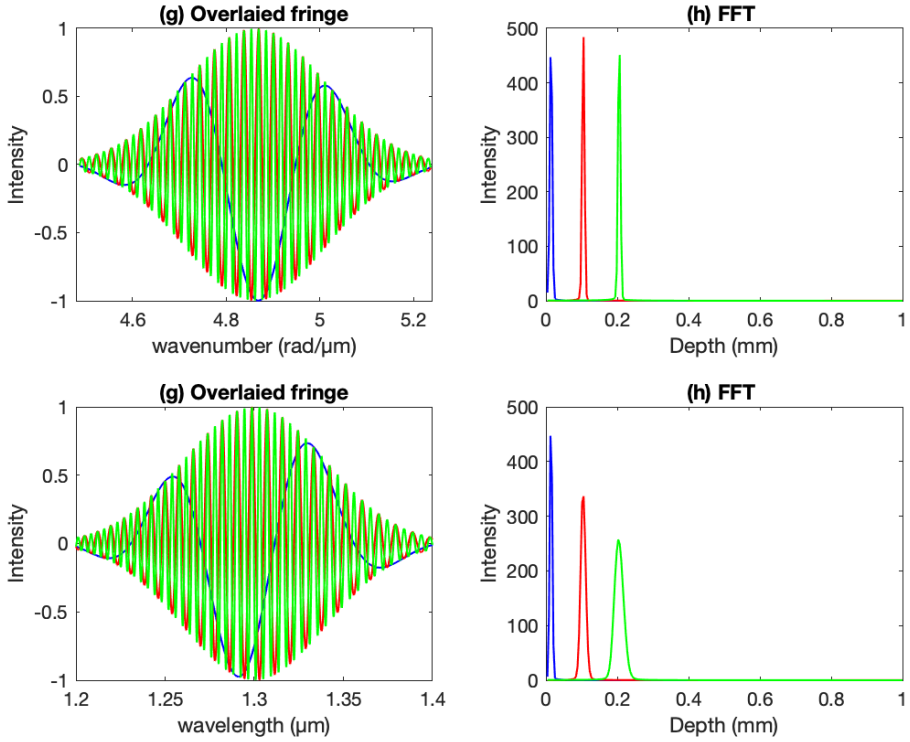

Figure 2.9 Calibration simulation. (a) and (c) Overlaid fringes with even wavenumber and wavelength, respectively. (b) and (d) FFT in lambda space and k space.

Several methods can be applied to address this issue. One approach is to utilize a laser which has a "k-clock" output. K-clock output will provide a clock signal with a uniform k. Even though this approach is convenient, k-clock is not always available in the OCT light source. The second way is to build a k-clock signal through an external Mach-Zehnder interferometer (MZI).

The OPD of MZI is constant so the interferogram is the shape of the light source power spectrum modulated by a cosine function that oscillates as a function of wavenumber [I=S(k)(cos2k(Δt))]. Therefore, the peaks, valleys, or zero crossings from this cosine function correspond to the even wavenumber and can be used to acquire OCT fringe as an external clock [152, 153], which is able to provide robust calibration but at the cost of additional system complexity. The third method is to generate a calibration file to resample acquired OCT fringe through a common-path configuration MZI which provides more accurate measurement because it is dispersion-free. First, the acquired OCT data are processed by Hilbert transform in order to convert the real OCT data set to a complex data set. Then the phase of interference fringe which is proportional to the wavenumber can be extracted, as shown in equation (2.32). Then the phase function is unwrapped to obtain a total overall phase of the system vs. discrete time or space [equation (2.33)].

$$\varphi[\mathrm{t}] = \mathrm{phase}(\mathrm{Hilbert}(I_d(\mathrm{k}))) = 2(\mathrm{k}[\mathrm{t}])\Delta\mathrm{z} \tag{2.32}$$

$$\varphi'[\mathrm{t}] = \mathrm{unwarp}(\varphi[\mathrm{t}]) \tag{2.33}$$

Using linear interpolation, we can obtain the calibration vector of rational time points (t') that correspond to equidistant discrete spacing of wavenumbers. Then, this calibration vector can be used to resample the OCT fringe before performing Fourier transform. Figure 2.10 shows a brief summary of the calibration process. Figure 2.10 (a) and (b) are original OCT fringe and OCT images with FFT. Using equations (2.32) and (2.33), phase of fringe can be acquired, as shown in Figure 2.10 (c). Then, a linear interpolation is applied to calculate the new time (or space) points, as shown in Figure 2.10 (d). Figure 2.10 (e) and (f) are OCT fringe and OCT images with FFT after calibration. The peak in Figure 2.10 (f) becomes sharper and higher after the calibration.

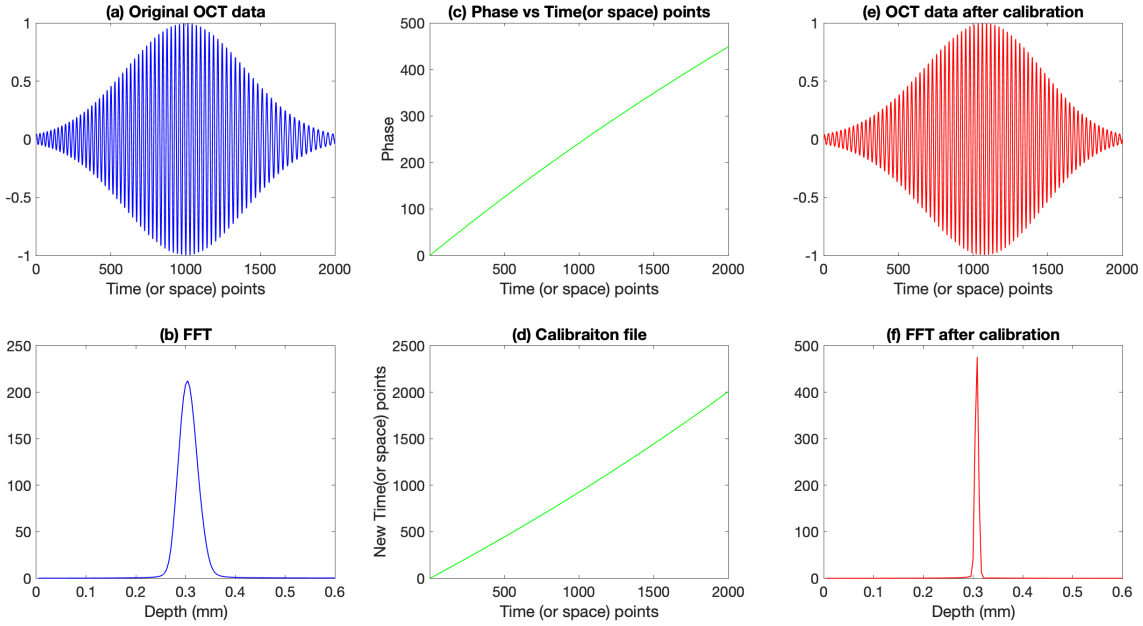

Figure 2.10 Calibration. (a) Original interference fringe. (b) FFT of original fringe. (c) Phase of OCT data. (d) New time or space points. (e) Resampled interference fringe using rational time points. (f) FFT of resampled fringe.

2.1.7 Dispersion Compensation

Due to the use of broad bandwidth laser sources in OCT, chromatic dispersion is caused by a difference in speed of individual wavenumbers of light because the index of refraction is wavenumber dependent in most optics components (such as collimators, objective lens, and optical fibers), which alters optical path length of reference and sample arms. The total amount of dispersive effects in the OCT system is determined by optical path length mismatch between the reference and samples arms. Uncorrected dispersion in an OCT system leads to both worse axial resolution as well as lower peak intensities [154]. To avoid dispersion in OCT, the additional dispersive media, such as water or glass, can be added to the sample or reference arm to compensate for the unequal chromatic dispersion. However, this approach requires the knowledge of the index profile of optical components as well as an accurate measure of the OPL difference between the two arms.

Chromatic dispersion can also be corrected by postprocess. Mathematically, the addition of chromatic dispersion introduces a phase shift $\Delta\varphi(\mathrm{k})$. The dispersion can be compensated by multiplying $e^{-i\Delta\varphi(\mathrm{k})}$ with OCT data $\mathrm{A(k)}e^{-i\varphi(\mathrm{k})}$. The phase of OCT data can be described by its Taylor series expansion [155]:

$$\varphi(\mathrm{k}) = \varphi_0 + \left.\frac{\partial\varphi(\mathrm{k})}{\partial\varphi}\right|_{\mathrm{k}_0} \cdot (\mathrm{k}-\mathrm{k}_0) + \frac{1}{2}\cdot\left.\frac{\partial\varphi(\mathrm{k})^2}{\partial\varphi^2}\right|_{\mathrm{k}_0} \cdot (\mathrm{k}-\mathrm{k}_0)^2 + \cdots + \frac{1}{n!}\cdot\left.\frac{\partial\varphi(\mathrm{k})^n}{\partial\varphi^n}\right|_{\mathrm{k}_0} \cdot (\mathrm{k}-\mathrm{k}_0)^n \qquad (2.34)$$

The first term is a constant phase shift, which is equal to $2\,\pi/\lambda_0$ and λ_0 is the center wavelength of OCT light source, and the second term represents the group velocity, which won't cause dispersion. The third term represents the group velocity dispersion (GVD) caused by altering speeds of light based on the index of refraction of a medium which is the main cause of dispersive broadening. Other higher order terms can also result in undesirable broadening of axial resolution. Therefore, we can compensate for the dispersion by subtracting the third term and other higher order terms from the phase of interference fringe.

First, an OCT interferogram is obtained using a mirror as a sample. A Hilbert transform is performed to extract the phase, which is then unwrapped. Second, a polynomial fitting with a degree ($n \geq 2$) is applied to calculate the coefficients of each term, as shown in equation (2.35).

$$\varphi(\mathrm{k}) = \mathrm{A}_0 + \mathrm{A}_1\cdot\mathrm{k} + \mathrm{A}_2\cdot\mathrm{k}^2 + \mathrm{A}_3\cdot\mathrm{k}^3\cdots + \mathrm{A}_n\cdot\mathrm{k}^n, \qquad (n \geq 2) \qquad (2.35)$$

Then, the phase change caused by dispersion can be expressed as:

$$\Delta\varphi(\mathrm{k}) = \mathrm{A}_2\cdot\mathrm{k}^2 + \mathrm{A}_3\cdot\mathrm{k}^3\cdots + \mathrm{A}_n\cdot\mathrm{k}^n, \qquad (n \geq 2) \qquad (2.36)$$

Therefore, the dispersion compensated data set is equal to $\mathrm{A(k)}e^{-i[\varphi(\mathrm{k})-\Delta\varphi(\mathrm{k})]}$. Figure 2.11 shows simulation of dispersion. Figure 2.11 (a) and (b) shows interference fringe with dispersion and corresponding FFT, respectively. Figure 2.11 (c) shows the entire phase profile and phase

profile only with constant phase shift and the group velocity. The blue curve in Figure 2.11 (c) shows the entire phase profile and phase profile only with constant phase shift. The red curve in Figure 2.11 (c) shows the entire phase profile and phase profile only with constant phase shift and the group velocity.

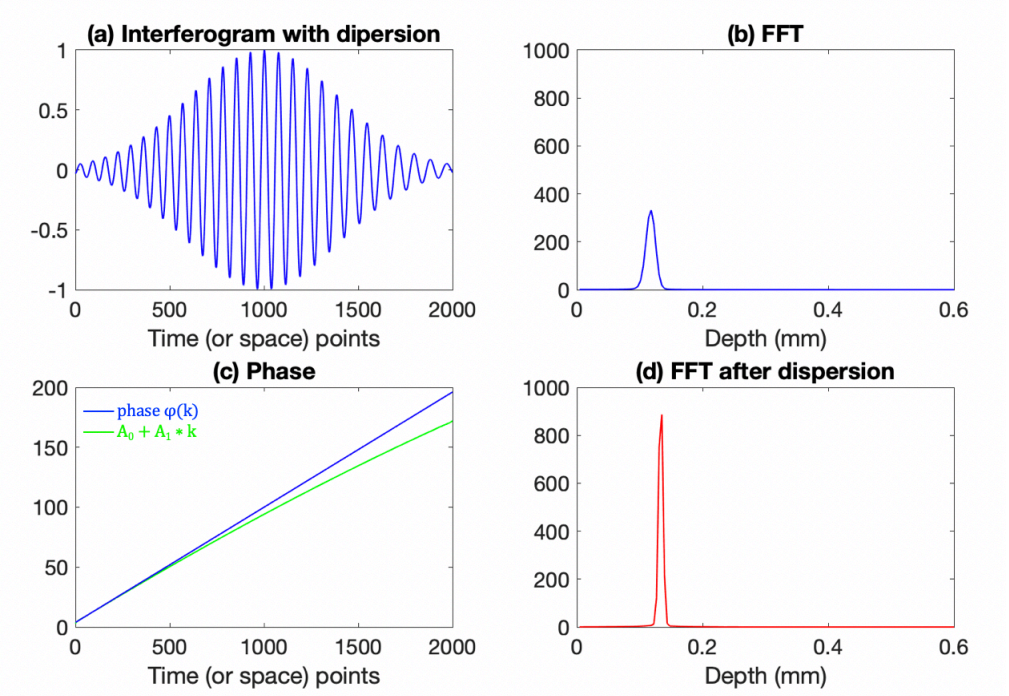

Figure 2.11 Dispersion. (a) Interference fringe with dispersion. (b) FFT of the fringe in (a). (c) Phase of OCT data. (d). (f) FFT of resampled fringe.

2.2 Doppler OCT and Optical Coherence Elastography

Based on the Doppler principle, Doppler OCT is a functional imaging technique that allows for quantifying the speed of moving particles with high spatial resolution and sensitivity in addition to structural imaging [6, 7, 68, 156-159]. Doppler OCT was first demonstrated in 1997 [68, 156, 160] in which a spectrogram method was applied to obtain Doppler frequency shift based on time domain OCT. However, the long acquisition time as well as the conflict between spatial resolution and velocity sensitivity limited its application [161, 162]. The development of Fourier domain OCT significantly increased the imaging speed of OCT [144, 145]. In 2000, a phase-resolved method was proposed and demonstrated to image and quantify blood flow in which the Doppler shift could be calculated by observing the phase change between sequential A-lines in a B-scan or C-scan [6]. With the phase-resolved method, a high imaging speed, high spatial resolution, and high velocity sensitivity could be achieved. Chen et al. demonstrated the first in vivo imaging of vasculature and blood flow in patients using phase-resolved Doppler OCT [163, 164]. However, this method is sensitive to the orientation and pulsatile nature of blood flow, and the results are the most optimal when the flow direction is aligned with the probe beam. The phase-resolved Doppler variance method was developed in 2000 to address this issue, which allows quantification of transverse flow [165, 166]. In addition, Doppler variance methods also enable visualizing small vessels down to the capillary level, making it ideal for OCT angiography (OCTA) applications [165, 167]. Based on the Doppler variance method, a number of extensions have been developed, including intensity-based Doppler variance, amplitude decorrelation, speckle variance, standard deviation, intensity-based differentiation, phase variance, and intensity and phase-based differentiation [6, 7, 157, 159, 167-181].

OCTA has the capability to visualize the microvasculature with high resolution (1-15 μm) and a moderate penetration depth (1-2 mm). It has become an attractive tool for angiography in ophthalmology, cancer, and cerebral brain research due to advantages over conventional imaging methods: fast acquisition time, high spatial resolution, depth-resolved information, absolute flow measurement, and non-invasiveness. The qualitative comparison with the current angiography modalities is summarized in Table 2.1. In addition to angiography and flowmetry, Doppler OCT has also been extended to elastography application: namely, optical coherence elastography (OCE). Benefiting from the optical resolution enabled by phase-resolved OCT, OCE provides high spatial resolution at the micrometer-level and an axial displacement sensitivity on the order of subnanometer [96, 104, 182-185]. As such, it has been widely applied in biomedical research to provide quantitative assessment of tissue biomechanical properties [12, 105, 106, 186-193].

Table 2.1 Summary of current angiography methods. ●●●: Excellent; ●●： Good; ●: Moderate.

Performance / Method	Lateral Resolution	Axial Resolution	Flow velocity sensitivity	Invasiveness
ICG angiogram[194, 195]	●●	None	None	Yes
Laser Doppler flowmetry [196, 197]	●●	None	●	None
Doppler ultrasound[198]	●	●	●●	None
Laser speckle[199, 200]	●●	None	●	None
Doppler OCT [6, 7, 157, 159, 167-180].	●●	●●	●●	None

2.2.1 Spectrogram

Doppler OCT was first proposed for blood flow quantification in 1997 [68, 156]. Based on the Doppler principle, the frequency shift of the backscattered light from a moving particle can be generated, as shown in Figure 2.12, and calculated using equation *(2.37)* [6, 156]:

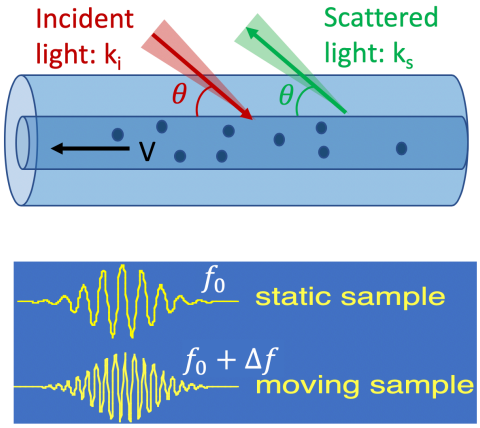

Figure 2.12 The principle of Doppler OCT: k_i and k_s are wave vectors of incoming and scattered light, respectively. V is the velocity vector of the moving particles; f_0: center frequency of signal from static sample; Δf: Doppler frequency shift caused by moving particles. θ is the angle between the incident light and flow direction. Since OCT detects only back-scattered light, θ is identical for both the incident and back-scattered light.

$$\Delta f = \frac{1}{2\pi}(\boldsymbol{k_s} - \boldsymbol{k_i}) \cdot \boldsymbol{V} \tag{2.37}$$

where $\boldsymbol{k_i}$ and $\boldsymbol{k_s}$ are wave vectors of incoming and scattered light, respectively, and $\boldsymbol{V}$ is the velocity vector of the moving particles. Given the Doppler angle, θ (between the incident light beam and the flow direction), equation (2.37) is simplified to:

$$\Delta f = \frac{2 \times n \times V \times \cos(\theta)}{\lambda} \tag{2.38}$$

where n is the tissue refractive index, and λ is the central wavelength of the light. In order to extract Doppler frequency shift, Δf, which is the difference between the carrier frequency from optical phase modulation, f_0, and the centroid, f_c, of the measured power spectrum, a short-time fast Fourier transformation (STFFT) or wavelet transformation can be applied to calculate the power spectrum of OCT signals [156]. A detailed signal processing is shown in Figure 2.13. With the spectrogram method, structural and velocity images can be obtained simultaneously, but the velocity sensitivity will be compromised by the increased spatial resolution or imaging speed.

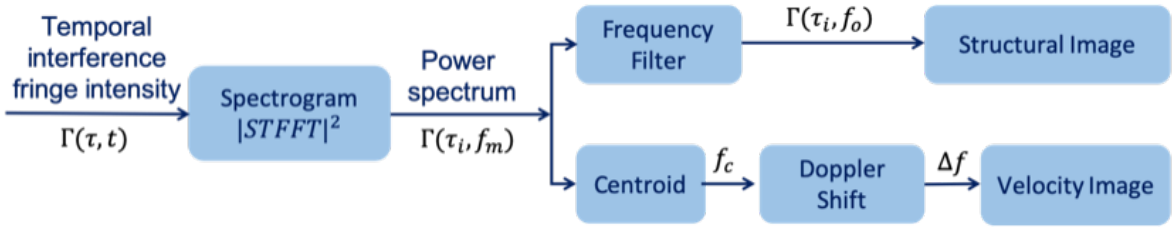

Figure 2.13 Signal processing for structural and velocity images.

2.2.2 Phase-Resolved Doppler OCT

To overcome the limitation of the spectrogram method, the phase-resolved Doppler OCT method was proposed in 2000 [6]. The Doppler frequency shift can be extracted by calculating the phase change in sequential A-lines in inter-A-line or inter-frame. Deriving Δf through phase change can be achieved through equation (2.39):

$$\Delta f = \frac{\Delta\varphi}{2 \times \pi \times \Delta T} \tag{2.39}$$

where ΔT is the time interval between sequential A-lines, and Δφ is the phase change. Δφ can be calculated using OCT complex data (F_m and F_{m+1}), as shown in equation (2.40).

$$\Delta\varphi = tan^{-1}\left[\frac{Im(F_m \times F_{m+1}^*)}{Re(F_m \times F_{m+1}^*)}\right] \tag{2.40}$$

where F_m and F_{m+1} are the OCT complex data from same location but at a different time. Therefore, the longitudinal flow velocity can be determined by measuring the phase of the OCT signals as a function of time, as demonstrated by combining equations (2.39) and (2.40) :

$$V \times \cos(\theta) = \frac{\lambda \times \Delta\varphi}{4 \times \pi \times n \times \Delta T} = \frac{\lambda}{4 \times \pi \times n \times \Delta T} \times tan^{-1}\left[\frac{Im(F_m \times F_{m+1}^*)}{Re(F_m \times F_{m+1}^*)}\right] \tag{2.41}$$

The signal processing of phase-resolved Doppler OCT is shown in Figure 2.14 [201, 202]. With the phase-resolved Doppler OCT method, high velocity sensitivity, high spatial resolution, and high imaging speed can be achieved simultaneously, enabling real-time visualization and

quantification of blood flow. Since the phase-resolved Doppler OCT method is sensitive to the orientation and pulsatile nature of blood flow, determining the Doppler angle plays an important role in accurate quantification of blood flow. Furthermore, this method cannot be applied when the Doppler angle is near 90°, which limits its application, such as for ocular blood flow imaging.

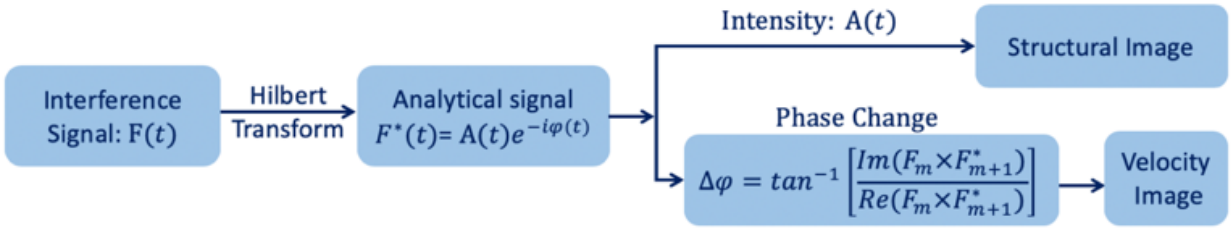

Figure 2.14 Phase-resolved Doppler OCT method.

2.2.3 Doppler Variance

To address the limitations of phase-resolved Doppler OCT to image transverse flow, a Doppler variance method based on the bandwidth of Doppler frequency shift was proposed [165, 166]. OCT incident probe-beam geometry causes a broadening of the Doppler frequency shift spectrum which can be used to quantify blood flow when the flow direction is near perpendicular to the probe beam. The principle is shown in Figure 2.15, where Doppler bandwidth, B, is approximated by the differences between the Doppler shift generated by the red and blue beam. Therefore, the transverse flow velocity, $V_T = V \sin\theta$, can be quantified by equation (2.42) [166]:

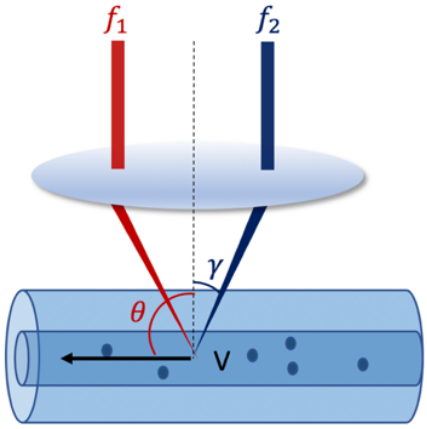

$$f_1 = 2V\cos(\theta - \gamma)/\lambda$$

$$f_2 = 2V\cos(\theta + \gamma)/\lambda$$

$$B = f_1 - f_2 = \frac{4V \sin\theta\, NA_{eff}}{\lambda}$$

$$\sigma = \frac{\pi V \sin\theta\, NA_{eff}}{8\lambda}$$

Figure 2.15 Phase-resolved variance Doppler OCT.

$$V \times \sin(\theta) = \frac{8 \times \lambda \times \sigma}{\pi \times n \times \mathrm{NA}_{eff}} \tag{2.42}$$

where NA_{eff} is the effective numerical aperture of the scan lens. The standard deviation, σ, of the Doppler bandwidth can be determined by:

$$\sigma^2 = \frac{\int g(f)\,(f-\bar{f})^2 df}{\int g(f) f^2 df} = \frac{1}{(2\pi\Delta T)^2}\left(1 - \frac{2 \times |F_m \times F_{m+1}^*|}{|F_m|^2 + |F_{m+1}|^2}\right) \tag{2.43}$$

where f is the Doppler shift, $\bar{f}$ is averaged Doppler shift, and $g(f)$ is the Doppler power spectrum. While Equations (2.42) and (2.43) provide the backbone for high-sensitivity flow measurement, the velocity range is limited due to phase wrapping and phase washout, which are the main challenges of Doppler OCT in flow velocity quantification. To address this, several phase calculation algorithms, such as the fast phase unwrapping method proposed by Schofield et al. have been developed [158, 203, 204].

2.2.4 Angiogram

OCTA is an extension of Doppler OCT that reconstructs the microvasculature by detecting the micromotions in biological tissue. These motions induced by the moving blood cells and plasma can generate fluctuations in the amplitude and phase of the interference signal that correspond to the flow velocity. The first OCTA based on Doppler variance OCT was demonstrated in 2001[164, 165], and since then, various OCTA algorithms based on the detection of fluctuations in the amplitude and/or phase have been developed for the visualization of blood vessels. OCTA can be categorized into: (1) amplitude, including intensity-based Doppler variance, amplitude decorrelation, speckle variance, standard deviation, and intensity-based differentiation; (2) phase, including phase variance; and (3) both amplitude and phase, including phase-resolved

Doppler variance, and intensity and phase-based differentiation. These algorithms are summarized in Table 2.

In most cases, these algorithms have similar performances although each is designed to utilize a particular scanning protocol for a specific application in a subfield of medicine whose requirements vastly differ. In ophthalmology, for instance, the phase variance method is a more favorable approach for achieving a higher contrast-to-noise ratio than the amplitude decorrelation and speckle variance approaches [172] whereas in mouse brain imaging, intensity-based Doppler variance is a more suitable technique for mapping vasculature than phase-resolved Doppler variance [205].

Table 2.2 Summary of current algorithms of optical coherence tomography angiography.

Method	Algorithm	
Doppler variance	Intensity-based[157]	$\sigma^2 = 1 - \frac{2 \times \sum_{m=1}^{M-1}(\lvert F_m \rvert \times \lvert F_{m+1} \rvert)}{\sum_{m=1}^{M-1}\lvert F_m \rvert^2 + \sum_{m=1}^{M-1}\lvert F_{m+1} \rvert^2}$
	Phase-resolved[6, 165]	$\sigma^2 = 1 - \frac{2 \times \left\lvert \sum_{m=1}^{M-1}(F_m \times F_{m+1}^*) \right\rvert}{\sum_{m=1}^{M-1}\lvert F_m \rvert^2 + \sum_{m=1}^{M-1}\lvert F_{m+1} \rvert^2}$
Amplitude decorrelation[168]	$\sigma^2 = 1 - \frac{1}{M-1} \times \sum_{m=1}^{M-1} \frac{2 \times \lvert F_m \rvert \times \lvert F_{m+1} \rvert}{\lvert F_m \rvert^2 + \lvert F_{m+1} \rvert^2}$	
Speckle variance[176]	$\sigma^2 = \frac{1}{M} \times \sum_{m=1}^{M-1} \left(\lvert F_m \rvert - \frac{1}{M} \sum_{m=1}^{M} \lvert F_m \rvert \right)^2$	
Standard deviation[177]	$R = \frac{\sqrt{\frac{1}{M-1} \times \sum_{m=1}^{M} \left(\lvert F_m \rvert - \frac{1}{M} \sum_{m=1}^{M} \lvert F_m \rvert \right)^2}}{\frac{1}{M} \sum_{m=1}^{M} \lvert F_m \rvert}$	
Differentiation	Intensity-based[169]	$I = \frac{1}{M-1} \times \sum_{m=1}^{M-1} \left\lvert \lvert F_m \rvert - \lvert F_{m+1} \rvert \right\rvert$
	Intensity and phase-based[178]	$I = \frac{1}{M-1} \times \sum_{m=1}^{M-1} \lvert F_m - F_{m+1} \rvert$
Phase variance[179, 180]	$PV_v = \frac{1}{M-1} \sum_{m=1}^{M-1} \left(\Delta\varphi_m - \frac{1}{M-1} \sum_{m=1}^{M} \Delta\varphi_m \right)^2 \qquad \Delta\varphi_m = \varphi_{m+1} - \varphi_m$	
F_m and F_{m+1}: OCT complex data from the same location but at different time points. M: time repeated at one location. $\Delta\varphi$: phase change. σ^2: variance. R: standard deviation. I: intensity of OCT signal.		

OCTA acquires multiple images in sequence to reveal the portion with fluctuations. Since this principle involves temporal imaging, the imaging protocol which determines the time interval between successive fluctuations plays a key factor in the signal-to-noise ratio (SNR) and dynamic range of OCTA. The two conventional imaging protocols are inter-frame and inter-A-line, as depicted in Table 2.3. In the inter-frame imaging protocol, neighboring B-scans are compared to extract vascular information. This protocol has a longer time interval ΔT as it utilizes the slow scan of the scanning apparatus. While this provides high sensitivity for the blood vessel with slow flow, prolonged time intervals may cause more motion-induced artifacts and phase wrapping as well as signal saturation for the blood vessel with fast flow. On the contrary, neighboring A-lines are correlated in the inter-A-line method by using the fast scan of the scan setup to achieve a shorter time interval, and this allows for accurate quantification of fast flow while sacrificing the sensitivity for capillaries. For both imaging protocols, the scanning step needs to be much smaller with respect to lateral resolution (i.e., the beam size) in order to achieve accurate angiography.

Table 2.3 Summary of scanning protocols.

	Inter-A-lines	Inter-Frames
Principle	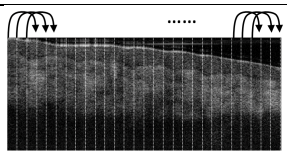	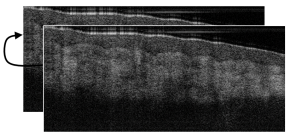
Advantage	Less motion artifact	High sensitivity for slow velocity
Disadvantage	Low sensitivity for slow velocity	More motion artifact

Several averaging methods have also been incorporated in imaging protocols to enhance the sensitivity of OCTA with split spectrum and volume averaging most predominantly used, as shown in Table 2.4. The split spectrum method divides the interference spectrum into several narrow spectra using a Gaussian window to generate several OCT images by performing Fourier transform for each sub-spectrum [168]. These OCT images are post-processed using an

angiography algorithm and then averaged to improve the SNR. This method is computationally inexpensive but sacrifices spatial resolution. The split spectrum method improves the image contrast and continuity of vessels [168]. Conversely, volumetric averaging maintains the image spatial resolution and, therefore, can greatly improve the image quality, but it reduces the imaging speed. Nonetheless, volumetric averaging is particularly advantageous in visualizing the outer capillary plexus [172].

Table 2.4 Summary of current average methods.

		Methods	Advantage	Drawback
Averaging method	Split spectrum	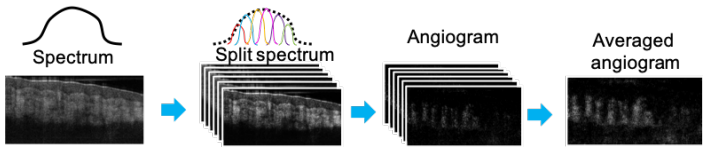	High speed	Low axial resolution
	Volumetric	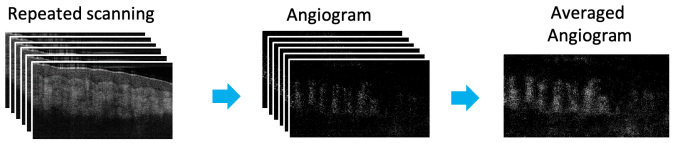	High sensitivity	Long acquisition time

2.2.5 Optical Coherence Elastography

Optical coherence elastography (OCE) is an emerging functional imaging technique that quantifies the elasticity of biological tissue using Doppler optical coherence tomography (OCT) to measure local tissue displacement as a function of applied stress [182, 193]. Compared with conventional elastography, such as magnetic resonance elastography, ultrasound elastography, and Brillouin microscopy [99, 100, 102, 105, 206], OCE possesses micron-level resolution and an axial displacement sensitivity on the order of a few nanometers and, therefore, has become an attractive research tool for ophthalmology, dermatology, cardiology, and oncology [12, 91, 94, 106, 186, 187, 190, 207, 208].

OCE determines tissue elasticity through measuring localized sample deformation, and the most common approaches are compression, resonant frequency, and elastic wave propagation.

(1) Compression

The compression approach is one of the most classic techniques in mechanical testing in which the localized deformation is induced by a compressional pressure, and the displacement is measured. In OCE applications, an ultrasound transducer or a piezoelectric transducer (typically lead zirconate titanate, or PZT) is commonly used as the external force excitation to generate acoustic waves, which is modulated with a low frequency (~1 kHz) to avoid damaging the transducer from continuous high-power emission. Proper modulation should provide a maximum phase difference while avoiding the resonant frequency of the sample and phase wrapping. The compression approach only determines relative Young's moduli; to obtain the absolute values, knowledge of the corresponding local stress applied to the biological tissue is required, as shown in Equation (2.44) [185]. This can also be achieved by calibration in which OCE is performed on several calibration phantoms with known stiffness to generate a calibration map (i.e., displacement versus Young's modulus) given the external force. The compression approach allows for a high frame rate, but additional force measurement or calibration steps are necessary. Furthermore, it requires a uniform excitation, which is often achieved by placing an unfocused ultrasound transducer or a PZT in contact with the sample, making it less ideal for clinical applications:

$$E = \frac{\sigma}{\varepsilon} = \frac{\mathrm{F/S}}{\Delta \mathrm{z}/z_0} \tag{2.44}$$

where σ is the stress, ε is the strain, F is the applied force, S is the area of force application, Δz is the length change in the sample, z_0 is the initial length of the sample.

(2) Resonant Frequency

The calibration process or force measurement for the compression approach is laborious and inconvenient. To address this, the mechanical resonant frequency of the sample can be utilized to quantify Young's modulus without knowing the external force applied. This can be attained by repeatedly B-scanning an area while varying the modulation frequency to create a frequency response spectrogram which can then be used to determine the resonant frequency of the sample. The Young's modulus can be calculated using Equation (2.45) [184] :

$$E = \frac{4\pi^2 \times M \times z_o}{S} \times f \tag{2.45}$$

where M is the mass of the sample, z_o is the thickness of the sample, and S is the area where the force is applied. This approach can quantify the elasticity without the need of calibration, but it lengthens the imaging time as it requires repeating B-scans to capture all the varying modulation frequencies. While this approach is non-contact, it often has a limited imaging area which is deterred by the beam width of the ultrasound transducer.

(3) Elastic Waves

Unlike the compression and resonant frequency approaches where the excitation has to be spatially uniform, an elastic wave can be generated by a focused excitation. The propagation speed of an elastic wave is associated with the mechanical properties of the sample and therefore can be used to determine the corresponding Young's modulus. In contrast to the compression approach, no calibration process is required. Since the calibration process does not consider other factors that may exist in actual experiments, the elastic wave approach can provide a more direct and more accurate measurement. The type of elastic waves generated depends on the different boundary

conditions. In the eye, for example, Lamb waves and surface waves are considered in cornea and lens, respectively. In a homogenous isotropic medium, shear waves are often considered.

Measuring the elastic wave propagation via OCE commonly relies on either M-B mode or B-M mode scanning protocol, as shown in Table 2.5, among which the M-B mode is more frequently used. In M-B mode, continuous A-line scanning (i.e., M-mode) is performed at a given location to record the displacement induced by a single excitation over time. Upon completion of the scanning at one location, the OCT detection beam is moved to the next neighboring location, and the M-mode scan (including the excitation) is repeated while maintaining the focal point of the excitation force at the same place. As such, a B-scan image of displacement over time can be reconstructed to visualize elastic wave propagation and thus determine the propagation speed. OCE based on M-B mode scanning has been utilized in several medical applications, such as ophthalmology and cardiology [12, 188]. While M-B mode is advantageous in achieving high temporal resolution, multiple excitations are necessary as each M-scan requires one. This brings more challenges for real-time elasticity mapping due to the lengthened imaging time, which also makes the imaging more prone to bulk motion artifacts. Additionally, multiple excitations may also cause measurement errors in a sample with a long relaxation time.

Table 2.5 Imaging protocols of OCE

	B-mode	M-B mode	B-M mode
	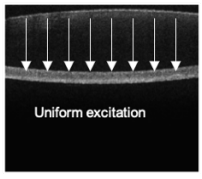	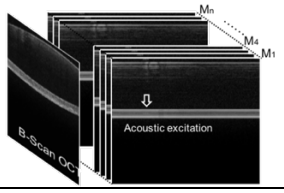	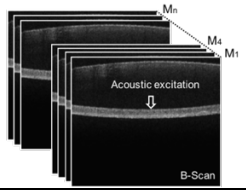
A-line rate	~1.6 MHz [209]	~100 kHz[210]	~1.6 MHz [209]
Advantage	Fast imaging	High temporal resolution High lateral resolution	Fast imaging High sensitivity
Disadvantage	Pre-calibration is needed	Slow imaging speed Sensitive for bulk motion	Low temporal resolution Low lateral resolution

To overcome the limitation of M-B mode scanning, B-M mode has been proposed and has recently become more available through the advancement of the speed of swept source laser. In B-M mode, given a single shot of excitation, the induced elastic wave propagation is captured by consecutive B-scans. Currently, a repetition rate as fast as ~1.6 MHz FDML laser has been applied to perform B-M mode OCE [209] in which a four-dimensional elasticity map of porcine cornea was acquired within 100 ms. As only a single shot of excitation is needed to create a volumetric elasticity map, the excitation force delivered and imaging time required is greatly reduced, making it possible for clinical application. Nevertheless, the current imaging speed is still insufficient to resolve the wave propagation in harder biological tissues [191], such as the optic nerve head. Further improvement in laser speed can enable elasticity measurement of harder tissue as well as achieve higher spatial resolution.

2.3 Photoacoustic and Ultrasound

Photoacoustic (PA) imaging is an emerging biomedical imaging modality based on the photoacoustic effect which is able to provide extremely high molecular contrast while maintaining the large imaging depth of ultrasound (US) imaging [5, 211-215]. In photoacoustic imaging, the biological tissue is irradiated by a nanosecond laser pulse. A portion of the optical energy is absorbed and converted into heat which leads to a transient pressure rise. This initial pressure acts as an acoustic source that generates an acoustic wave propagating through the tissue. An ultrasonic transducer is used for detecting the acoustic wave to form PA images, as shown in Figure 2.16. The unique optical absorption of different tissues when excited at a specific wavelength can be used to characterize the tissue type. With multi-wavelength laser excitation, spectroscopic PA imaging based on unique optical absorption spectrum of different tissues can be performed to identify different components in biological tissue with high sensitivity and specificity. The prime benefit of PA imaging is that it provides high chemical specificity of optical and comparable penetration depth with US images. In addition, due to the usage of an ultrasonic transducer, PA is able to automatically incorporate US imaging technology to perform multimodal imaging.

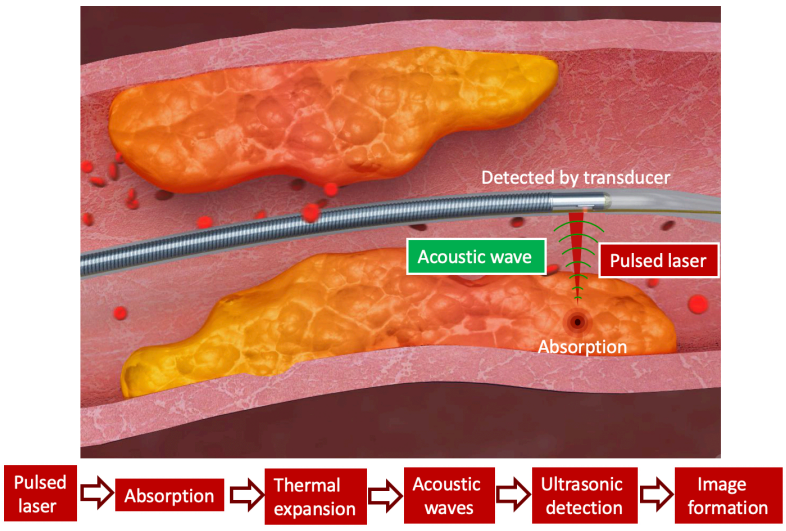

Figure 2.16 Schematic of IVPA imaging.

Several types of PA imaging systems, photoacoustic computed tomography (PACT), photoacoustic microscopy (PAM), and photoacoustic endoscopic imaging have been developed [4, 5, 19, 216-218]. In a PACT system, an unfocused ultrasound transducer is often used to acquire the PA signals, and the PA image is reconstructed by inversely solving the PA equations. Regarding a PAM system, a spherically focused ultrasound transducer with 2D point-by-point scanning is typically applied for PA signal detection, hereby requiring no reconstruction algorithm. For PA endoscopic imaging, a miniature imaging probe that contains optical components used for delivering the laser pulse onto tissue and an ultrasonic transducer for the detection of generated photoacoustic signals is applied to image the tissue wall. The miniature imaging probe is designed such that the excitation laser beam and ultrasound detection region overlap, and the region of overlap determines the imaging range of PA imaging.

PA signal originates from optical absorption, so PA readily takes advantage of endogenous and exogenous optical contrasts. For example, endogenous oxy- and deoxy-hemoglobin can be used as anatomical and functional contrasts for visualization of vasculatures, hemoglobin oxygen saturation, the velocity of blood flow, and the metabolic rate of oxygen [218-220]. For intravascular application, various IVPA imaging systems have been reported to image arterial wall, lipid, and calcium in human atherosclerotic aorta [19-21, 212, 217, 221-224]. Over the past ten years, PA has been widely applied in vascular biology, oncology, neurology, ophthalmology, dermatology, gastroenterology, and cardiology [19, 217, 224-234].

Chapter 3 – Intravascular Imaging

3.1 1.7-Micron Intravascular Imaging System

Coronary artery disease is the most common type of heart disease in developed countries with high mortality caused by ruptured atherosclerotic plaques. Accurate assessment of vulnerable atherosclerotic plaque characteristics is essential for choosing proper interventional techniques. Various imaging technologies, such as IVOCT, intravascular ultrasound (IVUS) and a combined multimodality imaging system, have been developed to detect vulnerable plaques with the hope of guiding therapy and monitoring response for intervention [19, 55, 76, 234-236]. IVOCT, the latest development in intravascular coronary imaging, offers cross-sectional images of human arteries with a superior spatial resolution of ~15 μm that enables the detection of micrometer-scale features of atherosclerosis, such as the intimal cap layers associated with vulnerable plaques [237-240].

In the clinic, an IVOCT system based on a swept source laser with a center wavelength of 1.3 μm is often used for identifying the thin fibrous cap [55]. However, because of the limited depth penetration of the typical IVOCT system, it is difficult to visualize a large lipid pool. Therefore, IVUS with an imaging depth of ~7 mm and a resolution of ~150 μm is utilized to image both the lumen geometry and structure of the arterial wall that may contain large lipid pools [76, 241, 242]. The IVOCT system with a center wavelength at 1.7 μm has several advantages compared to the IVOCT system at 1.3 μm. First, the contrast between lipid and normal tissue will be more obvious, based on stronger lipid absorption [243]. In addition, the light at a wavelength of 1.7 μm can penetrate deeper into tissue; thus, more structural information can be obtained, enabling the visualization of a large lipid pool. Here, we present a novel IVOCT system with a 1.7 μm swept source laser for identification of atherosclerosis. We performed imaging in phantom

and human coronary artery specimens. Our results indicate that the IVOCT system with a center wavelength of 1.7 μm increases imaging depth and allows for better identification of the morphology and chemical composition of atherosclerotic plaque.

3.1.1 Methods

(1) High speed scanning laser

We have collaborated with Santec, Inc., to develop a novel 1.7 μm swept laser. The high-speed scanning laser is a key component. Table 3.1 shows the parameters of this laser; Figure 3.1 shows the output power over time. For characterization of atherosclerosis, this laser has several advantages. First, its tuning range is from 1600 nm to 1770 nm which covers the absorption peak of lipids, the main content of vulnerable plaque. Therefore, the 1.7 μm IVOCT system will provide a high sensitivity for lipid content. In addition, the long wavelength range and high output power will contribute to a large penetration depth and better signal-to-noise ratio which makes the visualization of the whole plaque possible. All of these make the 1.7 μm IVOCT system a better tool for the characterization of atherosclerosis.

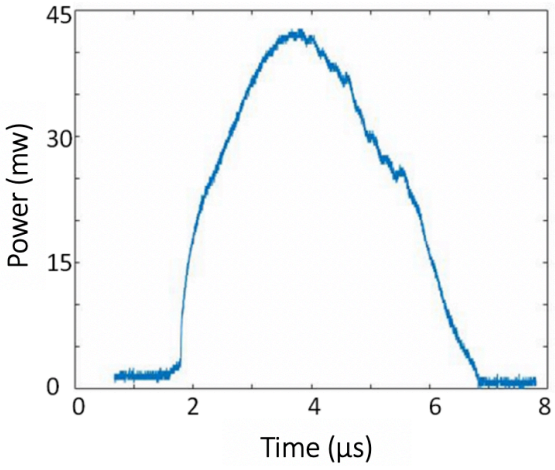

Figure 3.1 Output power of the 1.7 μm swept source laser.

Table 3.1 Parameters of the high-speed scanning laser

Parameter	Units	Min	Max	Measured
Maximum Optical Output Power	mW	35	-	42.8
Scan Range	nm	135	-	173.8
Center Wavelength	nm	1665	1725	1684.9
Coherence Length	mm	8	-	10.0
Scan Rate	kHz	89.9	90.1	90.0

(2) System setup and imaging probe

The novel IVOCT system was built based on a 1.7 μm swept source laser with a sweep rate of 90 kHz as shown in Figure 3.2. Because there is no commercial coupler and detector specifically designed for the 1.7 μm wavelength band, we used couplers (90:10 and 50:50) with a center wavelength of 1310 nm and circulators with a center wavelength of 1550 nm in the proposed IVOCT system. The mismatch between the couplers, circulars, and swept source laser caused a decrease of laser power. In order to demonstrate the performance of the novel IVOCT, we also built a typical 1.3 μm IVOCT system with the same optical components except circulators. A swept source (Santec, Inc., HSL-2100) with a center wavelength of 1310 nm and a sweeping rate of 20 kHz were used in the 1.3 μm OCT system. In both IVOCT systems, the output light was split by a 90-10 coupler into the sample and reference arms, respectively. A balanced photodetector (800 nm-1700 nm) and a 12 bit data acquisition board were used to detect and record the interference signal. The IVOCT software was written entirely in C++ for data acquisition, image processing and display in real-time using GPU.

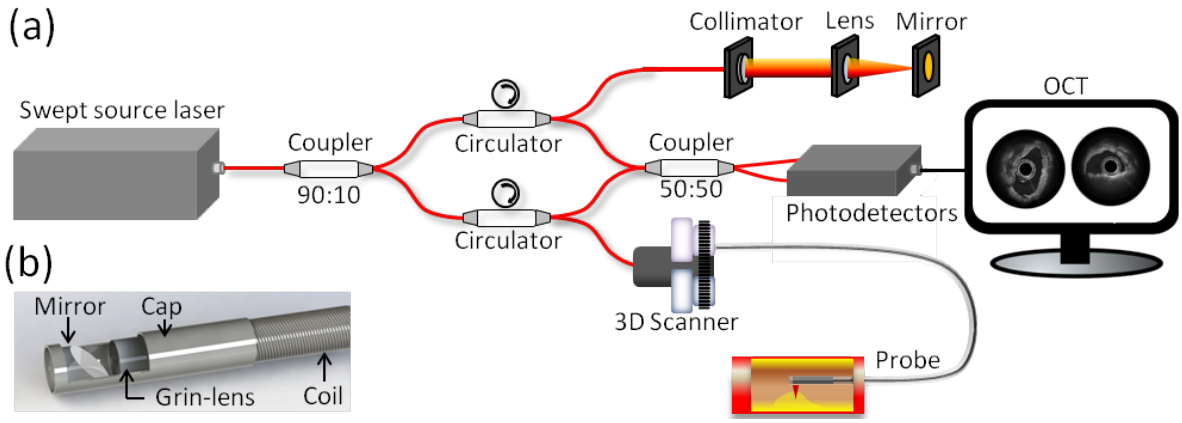

Figure 3.2 Schematic of the 1.7 µm IVOCT system (a) and the imaging probe (b).

A 1.2 mm proximal scanning endoscopic OCT probe [244] was developed for 3-D imaging as shown in Figure 3.2. The OCT laser beams propagated through the single mode core fiber, focused by a GRIN lens and reflected to the tissue surface by a rod mirror at an angle of 45°. The spot size at a 1.5 mm working distance (1700 nm and 1310 nm) was around 15 µm. All the elements were housed in a metal cap and fixed by epoxy. The cap was connected to a double-wrapped torque coil (ASAHI INTECC USA). A custom-made DCF rotary joint was used to propagate the two wavelength laser beams while rotating the probe. Two motors were used for driving the rotating/pullback catheter assembly. The pullback speed was set to be 1 mm per second with a frame rate of 40 images (the 1.7 µm OCT system) and 20 images (the 1.3 µm OCT system) per second.

For all the experiments, the output power of the 1.3 µm OCT system was attenuated to the same energy with the 1.7 µm OCT system. The energy from the probe tip was measured around 6 mw for both IVOCT systems. Under the same conditions as much as possible, we performed the experiments and analyzed the results. The two OCT systems had similar sensitivity (1.3 µm: 101 dB, 1.7 µm: 102 dB) and resolution (1.3 µm: 17.9 µm, 1.7 µm: 22.6 µm). In addition, a logarithm

transform was applied to the OCT signal in all the figures and plots to make low-reflective layers visible.

3.1.2 Imaging Results

(1) Phantom preparation and imaging

In order to demonstrate the performance of the novel IVOCT system, a vessel-mimicking gelatin phantom was imaged. A solution containing 5% gelatin and 2% silica particles with an average particle diameter of 5 μm was molded into a hollow cylindrical shape. Figure 3.3 (a – d) show IVOCT images of the phantom with novel (1.7 μm) and conventional (1.3 μm) IVOCT systems. Figure 3.3 (a) and (b) show the phantom imaged in air. Figure 3.3 (c) and (d) demonstrate the phantom imaged in water. Between Figure 3.3 (a) and (b), the penetration depth is deeper for the 1.7 μm OCT system compared to the 1.3 μm OCT system. Figure 3.3 (e) is a quantitative analysis of imaging depth that shows the relationship between depth and OCT signal intensity from the area indicated by the yellow dash line in Figure 3.3 (a) and (b). From Figure 3.3 (e), we can conclude that the penetration depth of the 1.7 μm IVOCT system is around two times more than the 1.3 μm IVOCT system. In consideration of the strong absorption from water at the 1.7 μm wavelength, the experiments were also performed in water for more accurate estimation. The corresponding IVOCT images are shown in Figure 3.3 (c) and (d). Figure 3.3 (f) is a quantitative analysis from the area indicated by the yellow dash line in Figure 3.3 (c) and (d), which also shows an increase in penetration depth for the 1.7 μm OCT system compared to the 1.3 μm OCT system. By comparing the penetration depth result in water and air, we can infer that the absorption from water does not influence penetration depth significantly, the reason being that the volume of the phantom's hollow cylinder is relatively small. With regards to an *in vivo* clinical application, the

lumen's coronary artery diameter is often about 2-3 mm which is small enough such that the influence from the absorption from water is negligible.

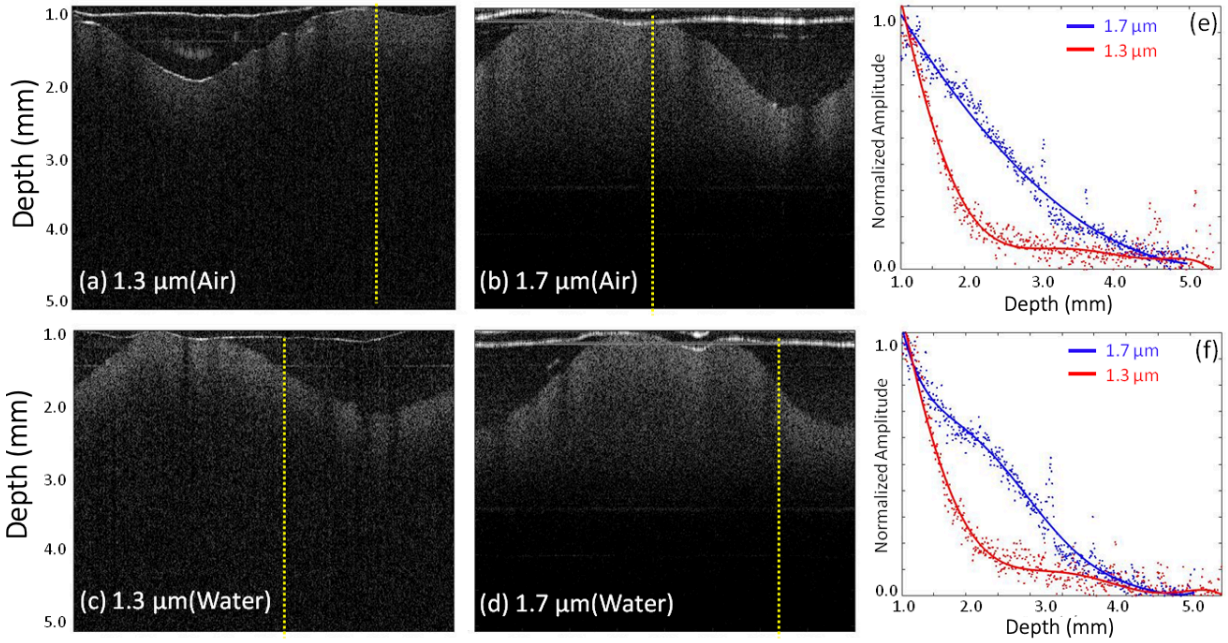

Figure 3.3 IVOCT images of phantom and quantitative analysis of penetration depth. (a) and (c) IVOCT images with conventional IVOCT system in air and water, respectively. (b) and (d) IVOCT images with the 1.7 μm IVOCT system in air and water, respectively. (e) and (f) Quantitative analysis of penetration depth for two IVOCT systems in air and water.

(2) Human coronary artery imaging

Fresh human carotid artery samples were obtained from cadavers and frozen in a -19 degree freezer. After the imaging system was set up, the tissue was imaged with the 1.7 μm IVOCT system and 1.3 μm IVOCT system in air and water. After imaging, the region of interest was marked with pins. The tissue was decalcified, embedded, and sectioned to 6 μm-thick slides. Then the slides were stained with H&E, and images were taken with a microscope with 4x magnification to find a match with the experimental region of interest. All methods were carried out in accordance with the University of California, Irvine (UCI) Institutional Review Board (IRB) and the Institutional Biosafety Committee (IBC). IRB granted an exemption to the protocol requirement since the

activities do not constitute Human Subject Research. Informed consent was deemed unnecessary because confidentiality of the deceased cadaver tissues is protected and coded. All experimental protocols were approved by the UCI IBC under protocol #2016-1570.

To further verify the capability of large penetration depth with the 1.7 μm IVOCT system, a healthy human coronary artery was imaged. Figure 3.4 (a) and (c) show IVOCT images obtained by the 1.3 μm IVOCT system in air and water, respectively. Figure 3.4 (b) and (d) show IVOCT images obtained by the 1.7 μm IVOCT system in water and air, respectively. Comparing Figure 3.4 (a) and (b) and (c) and (d), it can be seen that more information was obtained along the axial direction with the 1.7 μm IVOCT system. Figure 3.4 (e) and (f) are the quantitative analysis of penetration depth for the two IVOCT systems in air and water, which also demonstrates the larger penetration depth achievable with the 1.7 μm IVOCT system. These results agree well with the phantom experiment.

To demonstrate the capability of differentiating plaque from normal tissue, the atherosclerotic coronary arteries were imaged by using the two IVOCT systems. Groups (I-IV) are IVOCT images at different artery sites with different pathological features. Figure 3.5 (a-d) were obtained at similar sites by the 1.3 μm and 1.7 μm IVOCT systems in both air and water. Figure 3.5 (Ie-IVe) are corresponding hematoxylin and eosin (H&E) histology for each group. For group I, a low-density signal region (denoted by the yellow arrow) can be found in Figure 3.5 (Ia-Ie), which indicates the existence of calcium plaque. The classification of plaque type is validated by the corresponding histology images, which matches the four IVOCT images well. For groups II and IV, a large low-density signal region was also found, which indicates the existence of thick-cap (>65 μm) fibroatheroma (ThCFA). The corresponding H&E histology [Figure 3.5 (II e) and (IVe)] all verified the results. For group III (a-d), a thin fibrous cap and a large low-density signal

region behind the thin fibrous cap were found, indicating thin-cap (<65 μm) fibroatheroma (TCFA). Figure 3.5 (IIIe) histology verified these results. Comparing the IVOCT images of the 1.3 μm IVOCT system and the 1.7 μm IVOCT system, it is clearly seen that the 1.7 μm IVOCT system images have a larger penetration depth compared to the 1.3 μm IVOCT system images which demonstrates the capability of the 1.7 μm IVOCT system to visualize the whole plaque. Analyzing the results in water and air, we can find that the absorption of water is almost negligible for the atherosclerotic coronary artery due to the small lumen. These IVOCT images and H&E histology illustrate the capability of the 1.7 μm system to identify plaque with large imaging depth and high sensitivity.

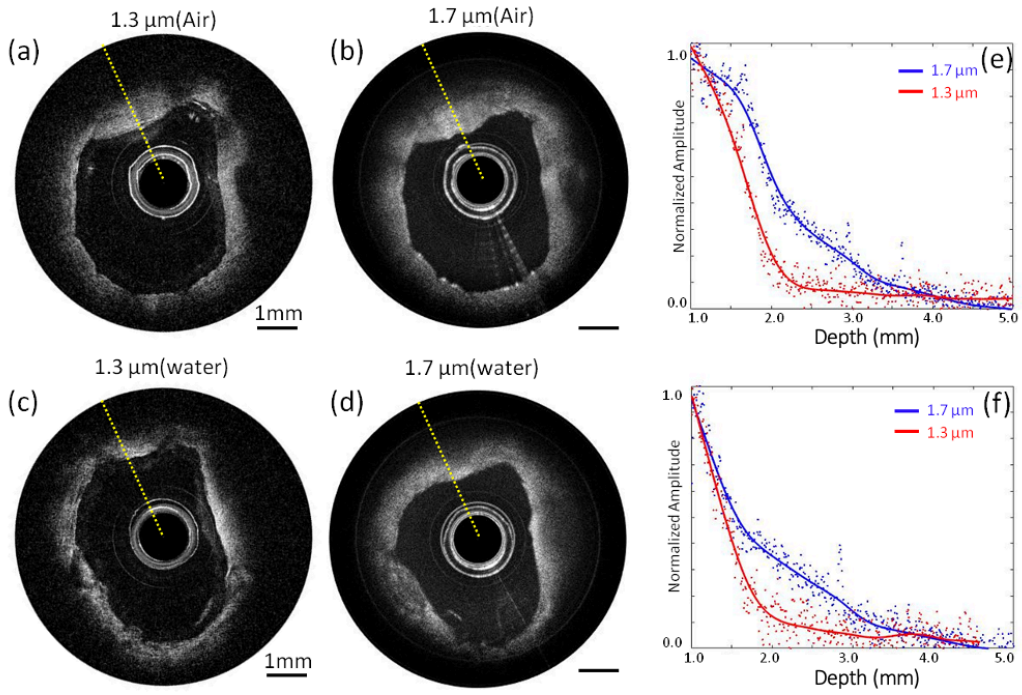

Figure 3.4 IVOCT images of healthy human and quantitative analysis of penetration depth. (a) and (c) IVOCT images with the 1.3 μm IVOCT system in air and water, respectively. (b) and (d) IVOCT images with the 1.7 μm IVOCT system in air and water, respectively. (e) and (f) Quantitative analysis of penetration depth for two IVOCT systems in air and water. Scale bars are 1 mm.

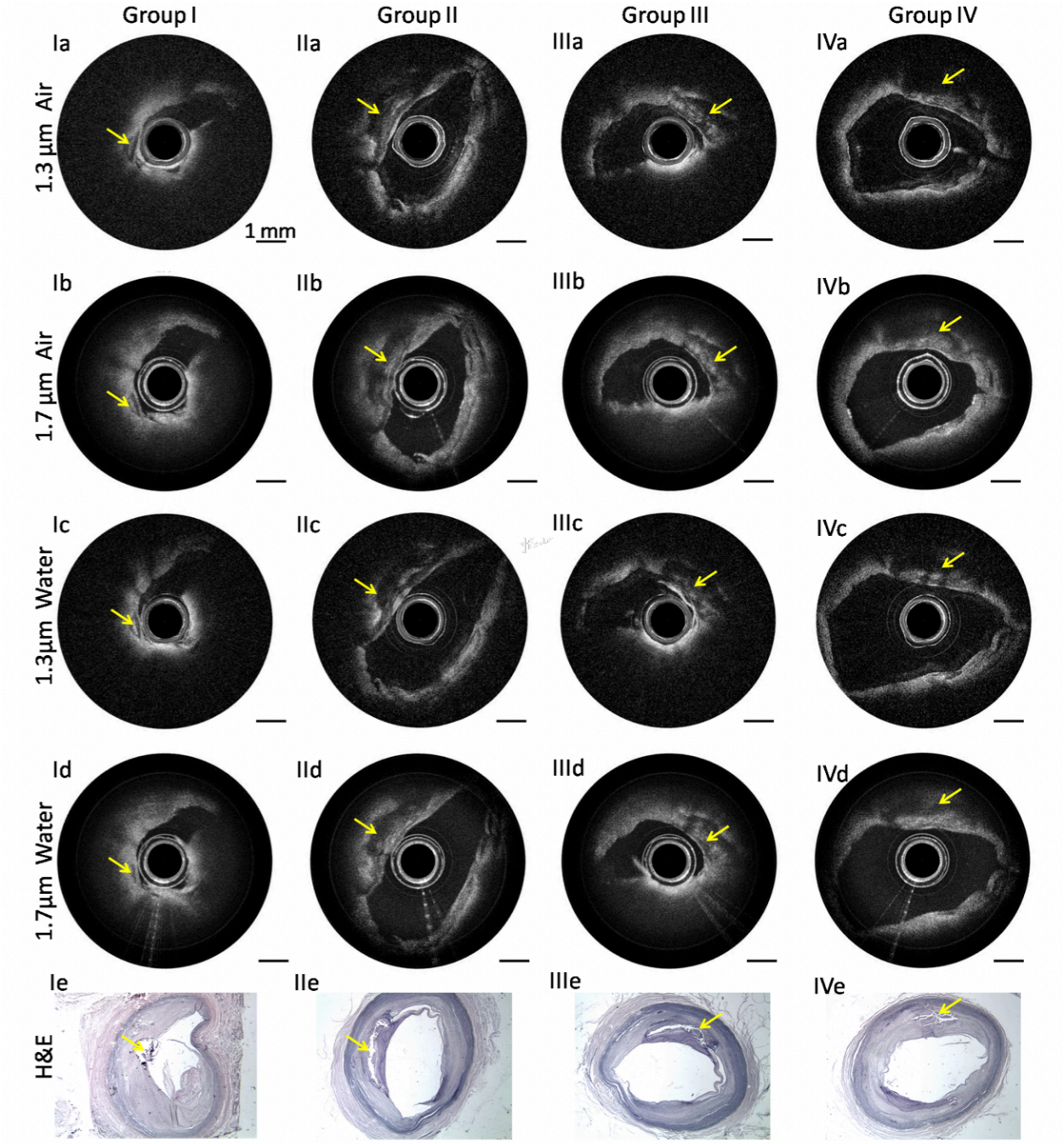

Figure 3.5 IVOCT images of atherosclerotic artery. (Ia-IVa) IVOCT images obtained by the 1.3 µm IVOCT system in air. (Ib-IVb) IVOCT images obtained by the 1.7 µm IVOCT system in air. (Ic-IVc) IVOCT images obtained by the 1.3 µm IVOCT system in water. (Id-IVd) IVOCT images obtained by the 1.7 µm IVOCT system in water. (Ie-IVe) Hematoxylin and eosin (H&E) histology. Scale bars are 1 mm.

3.1.3 Conclusion

IVOCT, a minimally invasive, non-ionizing imaging methodology, is the gold standard to detect the thin fibrous cap of vulnerable plaques. Due to the shallow penetration depth of 1.3 μm IVOCT systems, the capability of identifying a large lipid pool is often limited. Here, we utilized a 1.7 μm swept source laser for the IVOCT system that realized a higher sensitivity based on the lipid absorption spectrum and an improved depth penetration based on a longer wavelength band. The results from human coronary artery in-vitro experiments with corresponding histopathology verified the performance of the 1.7 μm IVOCT system.

Although our results clearly demonstrate the advantages of the 1.7 μm IVOCT system, the current 1.7 μm IVOCT system is far from optimal. The reason is that our current couplers work at a center wavelength of 1.3 μm or 1.5 μm, which reduces the output energy of the light source. In addition, the detector used in the 1.7 μm IVOCT system has a wavelength sensitivity range of 800-1700 nm and is optimized at 1310 nm, which decreases the detection efficiency significantly. If custom-made couplers and detector optimized for the 1.7 μm IVOCT system are implemented, the performance of the 1.7 μm IVOCT system will be significantly improved.

In summary, the novel IVOCT system with the 1.7 μm swept source laser provides a new insight into the pathology of coronary artery disease *in vivo* and is a powerful tool to assess the immediate and long-term outcomes of percutaneous coronary intervention. Moreover, by combining with other imaging modalities, such as ultrasound imaging and elastography [109, 245], it will provide the physician with a powerful tool for imaging, diagnosing, and managing vulnerable plaques. Furthermore, a spectroscopic IVOCT system can also be developed to increase contrast for lipid identification.

3.2 Tri-modal Imaging System

Identifying plaque type helps the diagnosis and plays an important role in choosing proper interventional techniques. According to clinical studies, three characteristics of plaques are used as criteria to estimate the presence of vulnerable plaques (1) large lipid pool, (2) thin fibrous cap, and (3) major inflammatory reaction [31, 246, 247]. So far, intravascular imaging is regarded as the most accurate method for characterizing plaques *in vivo*. In the clinic, intravascular ultrasound (IVUS) can image both the lumen geometry and structure of the arterial wall with an imaging depth of ~7 mm and a resolution of ~150 μm, which can be used to image large lipid pools [248]. On the other hand, intravascular optical coherence tomography (IVOCT) offers a superior spatial resolution of ~15 μm, which has enabled the detection of thin fibrous caps [61, 249, 250]. Near-infrared fluorescence imaging is able to obtain specific molecular information by using different contrast agents. For intravascular imaging, near-infrared fluorescence (NIRF) imaging can be used to identify inflammatory reaction, which is one of the main characteristics of vulnerable plaques [251]. However, most imaging systems focus on one or dual-modality imaging [76, 212, 252-254] which are not enough for an accurate estimation of these characteristics (large lipid pool, thin fibrous cap, and major inflammatory reaction). For example, it is difficult to identify whether there is a thin fibrous cap or not by using a combined NIRF and IVUS system. Recently, a few tri-modality imaging systems have been reported [255-257], and these works represent a significant step forward for the estimation of atherosclerotic plaques. However, the tri-modality system [257] that combined OCT, US, and photoacoustic (PA) can only obtain imaging by moving the probe instead of rotating, and thus the system cannot truly perform endoscopic imaging such as intravascular imaging. Moreover, the diameter of the probe presented in this study is 5 mm, which is too big to achieve intravascular imaging. Another tri-modality system [258] that combined OCT,

US, and fluorescence was also reported by our group. This system is able to get tri-modality imaging simultaneously. However, the diameter of the probe used in this system is around 1.2 mm, which is still too big for clinical applications. Furthermore, for fluorescence imaging, Cy5.5 dye was applied as a contrast agent in that work. Cy 5.5 dye is not FDA-approved which impedes the clinical translation of this technology. For the tri-modality system [255], only phantom experiments were conducted so the performance of the imaging plaque is unknown. In addition, the imaging speed of PA is relatively lower (~1 frame per 13 seconds) for clinical application.

For accuracy assessment of plaques, it is critical to obtain all the information of the main characteristics of vulnerable plaques. In our study, we developed a tri-modality system with a fully integrated miniature probe. We have reduced the diameter of the probe to 1.06 mm. When inserted in a catheter sheath, it has an outer diameter of 1.3 mm, which is small enough to fit in a 5 French introducer. The system is able to acquire OCT, US, and fluorescence imaging simultaneously. US imaging has a large penetration depth and can be used for identifying the lipid pool. High-resolution OCT can contribute to the identification of the thin fibrous cap. For fluorescence imaging, FDA-approved ICG dye is used as a contrast agent to indicate the local accumulation of macrophages which normally corresponds to inflammatory reaction [259]. *Ex vivo* experiments of rabbit aortas were performed to validate the performance of our tri-modality system. H&E histology results of the rabbit aorta were also presented to check assessment accuracy.

3.2.1 Methods

(1) System design

In order to obtain OCT, US, and fluorescence images, the three imaging technologies need to be fully integrated. In our study, we applied a trigger signal from the swept source laser as the

main trigger to synchronize the US and fluorescence imaging. In addition, a wavelength division multiplexer was used to combine the OCT and fluorescence imaging systems. For the fluorescence imaging system, we used a double clad fiber (DCF) coupler (Thorlabs, DC1300LEB) to collect the emission light instead of a free space optical path which enabled a compact and stable tri-modality system. Figure 3.6 illustrates the overall setup of the tri-modality system, which consists of a 1310 nm- swept-source OCT (SS-OCT) system, ultrasound imaging system, and fluorescence imaging system. For OCT, the swept source (Santec, HSL- 2100) with a center wavelength of 1310 nm and a sweeping rate of 20 kHz was used. For fluorescence imaging, a 785-nm semi-conductive CW laser (IS785-50 IR, Meshtel) was used as the excitation source, which corresponds to the excitation peak of ICG, and a DCF coupler was incorporated to transmit excitation light and collect emission light. For transmission, the combined beams went through the single mode core of the DCF from port A to port S, and the small diameter of the single mode core contributes to high fluence on surface tissue, which enables a high efficiency excitation. The emission light came back from the first clad of the DCF and core (port S) to a multimode fiber (port B) whose larger diameter and higher NA enhance the capability of collecting emission light, which was filtered by a bandpass filter of 814 to 851 nm (Semrock, Rochester, NY), and then detected by a photomultiplier tube (PMT, Hamamatsu, Photosensor module: H10722-20). The beams of the SS-OCT and laser diode were combined with a custom-made wavelength division multiplexer (Thorlabs: WDM coupler785/1310). For ultrasound imaging, a JSR Ultrasonics DPR500 DUAL Pulser/Receiver was used to generate and detect ultrasound signal.

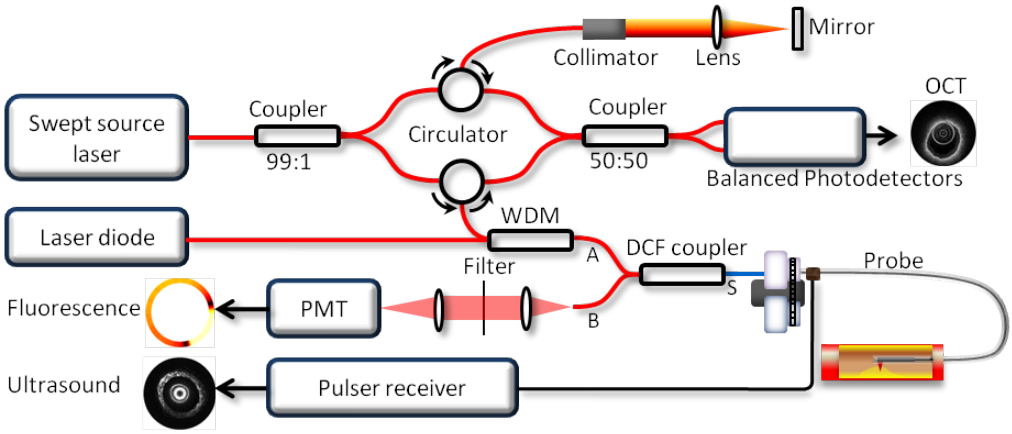

Figure 3.6 Schematic of the tri-modality system. PMT: photomultiplier tube. DCF: double clad fiber. WDM: wavelength division multiplexer.

Considering there were three channels (OCT, US and fluorescence), two synchronized data acquisition cards (Alazar Technologies Inc., Canada) were used. The C++ program was able to display OCT, ultrasound, and fluorescence imaging in real-time using GPU.

(1) Probe design

For tri-modality imaging, we designed and implemented a fully integrated miniature probe, as shown in

Figure 3.7(a). The combined beams propagate through the single mode core of the DCF, focused by a 0.5 mm GRIN lens and reflected by a rod mirror with a diameter of 0.5 mm at an angle of 43°, to the tissue surface. The spot size at a 1.5 mm working distance (1310 nm) is around 20 μm. A custom-made single-element ultrasonic transducer (dimension: 0.4×0.4×0.4 mm) (University of Southern California) with a center frequency of 40 MHz was sequentially aligned with the optical components and tilted at a slight angle in order to obtain optimum overlap between the optical beams and ultrasound, which contributes to obtaining colocalized tri-modality images. All the elements were housed in a metal cap and fixed by epoxy. The cap was connected to a double-wrapped torque coil (ASAHI INTECC USA). The outer diameter of the element was 1

mm. A custom-made DCF rotary joint was used to propagate the two optical beams and a slip ring was used to deliver electronic signals while rotating the probe. Two motors were used for driving the rotating/pullback catheter assembly. The pullback speed was set to be 1 mm per second with a frame rate of 20 images per second.

We imaged the target at different distances to acquire basic performance characterizations of the developed probe. For OCT images, the sensitivity, lateral resolution, and depth range were 115 dB, 25 μm, and 3-5 mm, respectively. For US images, sensitivity, lateral resolution, and depth range were 72 dB, 200 μm, and 5-6 mm, respectively. For fluorescence images, the minimum concentration of ICG that can be identified was 0.01 μmol/L under 5-mW laser power, and lateral resolution and depth range were 30 μm and 3-5 mm, respectively.

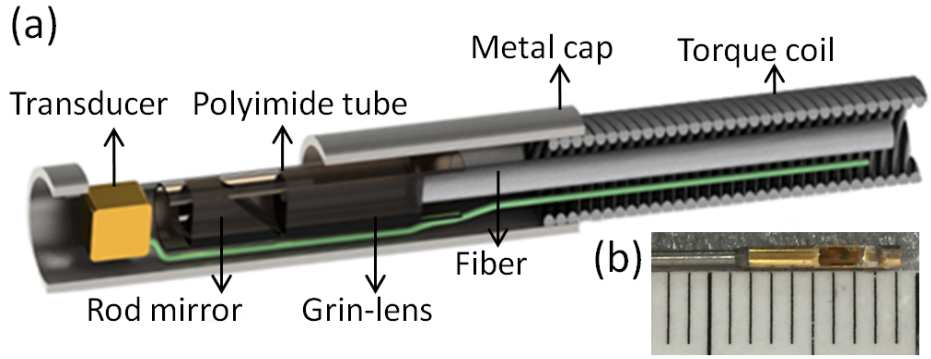

Figure 3.7 Tip of the probe. (a) Overall schematics. (b) Top view of the probe.

3.2.2 Imaging Results

(1) Phantom experiment

In order to demonstrate the performance of the tri-modality imaging system, a lipid-mimicking phantom was fabricated by injecting 0.1 μmol/L of ICG into a healthy pig artery to stain selective regions with ICG while other areas remained unchanged. Figure 3.8 (I –IV) show tri-modality images of the phantom at different sites. Figure 3.8 (Ia-IVa), (Ib-IVb), and (Ic-IVc) are the

combined OCT (inner, SNR: 61 dB) and fluorescence (outer, SNR: 113 dB), ultrasound (SNR: 51 dB), and tri-modality images, respectively. Figure 3.8 (I), (III) and (IV) show tri-modality images at the sites without injecting ICG. From Figure 3.8 (Ia), (IIIa), and (IVa), it can be seen that the signal amplitude of fluorescence is significantly lower and homogenous, corresponding to the sites without ICG. From OCT and ultrasound images, the whole structural and micro-structural information can be obtained. From Figure 3.8 (IIa), it can be found that the signal amplitude of fluorescence (indicated by the white arrow) is significantly higher than other regions with no ICG, corresponding to the site with ICG. Figure 3.9 (I) and (II) show the reconstructed 3D tri-modality images. Figure 3.9 (Ia)/(IIa), (Ib)/(IIb), and (Ic)/(IIc) represent 3D fluorescence, OCT, and ultrasound images, respectively. These results demonstrate that the tri-modality system has the capability of getting three modalities images at the same time and the location.

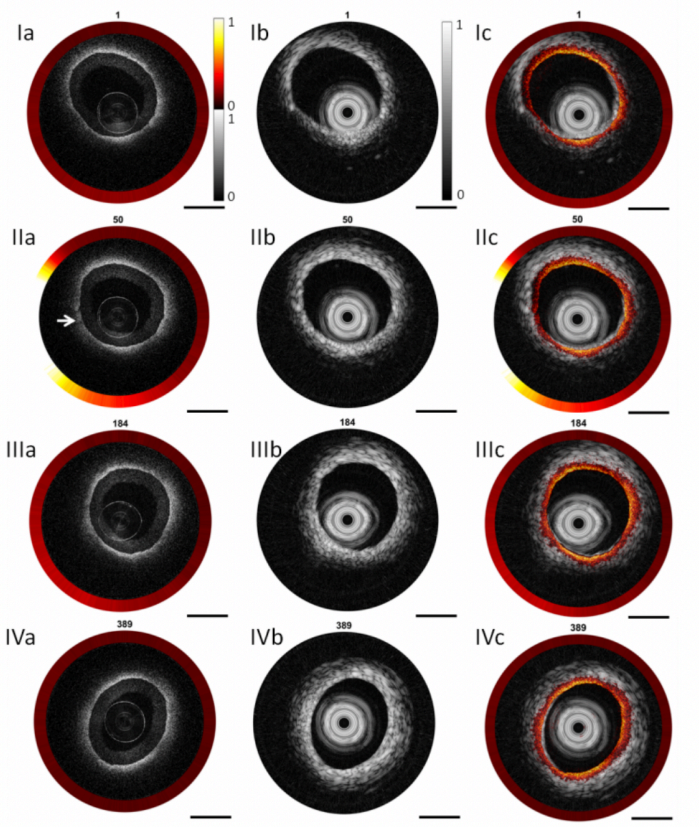

Figure 3.8 Tri-modality images of phantom. (Ia-IVa) Combined OCT and fluorescence, (Ib-IVb) US, (Ic-IVc) fused tri-modality and (Id-IVd) hematoxylin and eosin(H&E) histology. (I), (III) and (IV) Healthy artery. (II) Healthy artery with ICG. Scale bars are 1 mm.

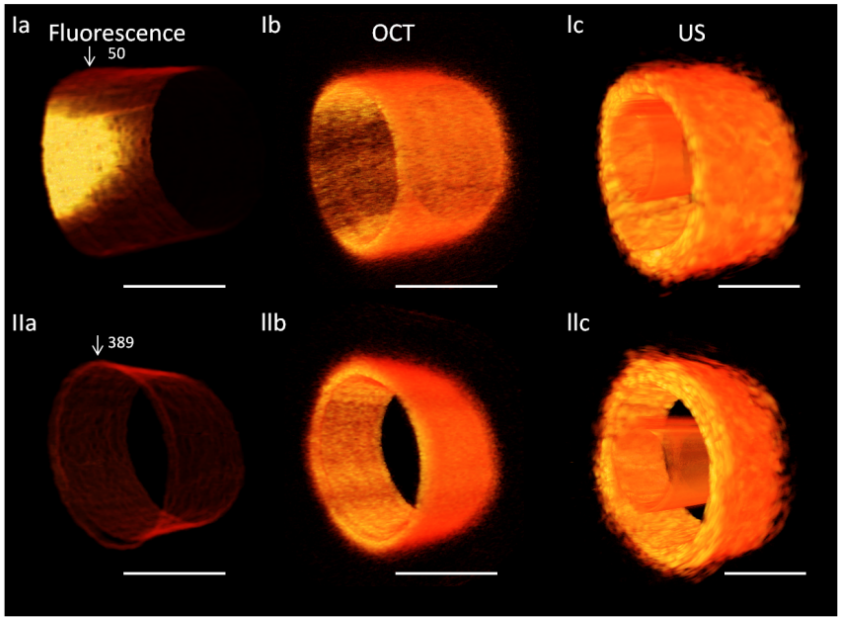

Figure 3.9 3D tri-modality images of lipid-mimicking phantom. (Ia) and (IIa) Fluorescence, (Ib) and (IIb) OCT, (Ic) and (IIc) US. Scale bars are 1 mm. The high signal region (in Ia) indicates the existence of ICG.

(2) Rabbit aorta experiment

To demonstrate the capability of accurately assessing vulnerable plaques, an aorta from an atherosclerotic rabbit was imaged. First, lesions were created by balloon injury and 16 weeks of a high-cholesterol diet in a male New Zealand white rabbit, and lesions were similar to those of human atherosclerotic plaques. Then the experimental rabbit was anesthetized and ICG (2.25mg/kg) was injected. Twenty minutes after injection, the rabbit was sacrificed. The aorta was excised and conserved in 4% formaldehyde for *ex vivo* experiments.

Representative OCT (SNR: 63 dB), IVUS (SNR: 50 dB), and fluorescence images (SNR: 84 dB) and corresponding H&E staining of coronary artery segments with different pathological features are shown in Figure 3.10. IVUS is used as the first step for identifying plaque since IVUS

enables the visualization of the layered structures of the artery wall. Due to low soft-tissue contrast, it only provides initial identification of the lipid plaque. Fibrosis and the lipid pool can be differentiated by OCT images based on its relatively higher soft tissue contrast. Inflammatory region can be identified by fluorescence images to further characterize the stability of the plaque.

From Figure 3.10 (IIb) and (IIIb), intimal thickening and a low-density acoustic signal region (denoted by the white arrow) can be found which demonstrates the existence of plaque. At the same site in the OCT image [Figure 3.10 (IIIa)], a homogenous high signal region also indicates intimal thickening. Moreover, the high signal region is also found at the same site in the fluorescence images, which indicates inflammatory reaction. From the combined tri-modality images, it can be concluded that this aorta shown in Figure 3.10 (III) is in the early stage of plaque formation. The classification of plaque type is validated by the corresponding histology photos which match the tri-modality images well. From Figure 3.10 (IIa), the diffuse boundary and weak signal region under the high signal region indicates the existence of a lipid pool. The thickness of the fiber cap is 150 μm according to Figure 3.10 (IIA). Furthermore, the high signal at the same site in the fluorescence images indicates an inflammatory reaction. A lipid pool can be found in the corresponding H&E histology photo which agrees well with the tri-modality images. Therefore, we can conclude that the aorta shown in Figure 3.10 (IIa) is thick-cap (>65 μm) fibroatheroma (ThCFA) in the stage of plaque progression. In Figure 3.10 (Ib), some low echo signals can be found which means that this region may have plaque. However, based on the combined OCT and fluorescence results, it can be concluded that this aorta is normal. Histology further supports this conclusion. From Figure 3.10 (IV), the tri-modality images and the H&E histology all show that this aorta is healthy. These images and H&E histology illustrate the

capability of the tri-modality system to determinate the plaque type. 3D OCT, US, and ICG-based fluorescence images are shown in Figure 3.11.

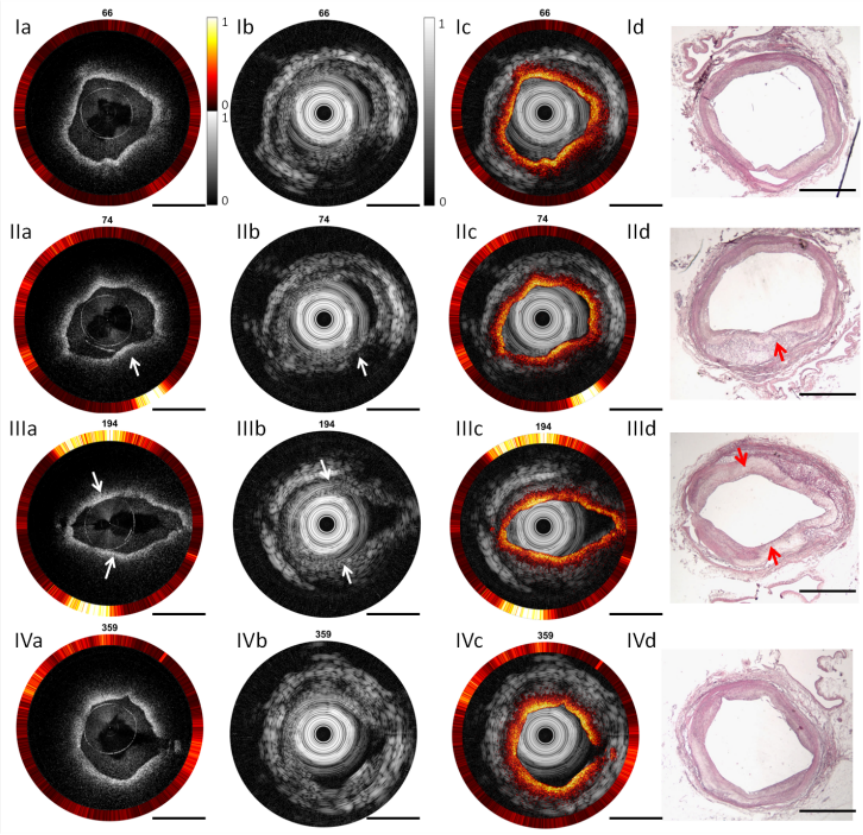

Figure 3.10 Tri-modality images of atherosclerotic aorta of rabbit. (Ia-IVa) Combined OCT (inner) and fluorescence (outer), (Ib-IVb) US, (Ic-IVc) Combined tri-modality and (Id-IVd) hematoxylin and eosin (H&E) histology. The artifact circles in the IVUS images are caused by the ultrasound pulse ring-down effect and the reflection of the catheter sheath. (II) and (III) Aorta with plaque, indicated by white arrows; (I) and (IV) are healthy aorta. Scale bars are 1 mm.

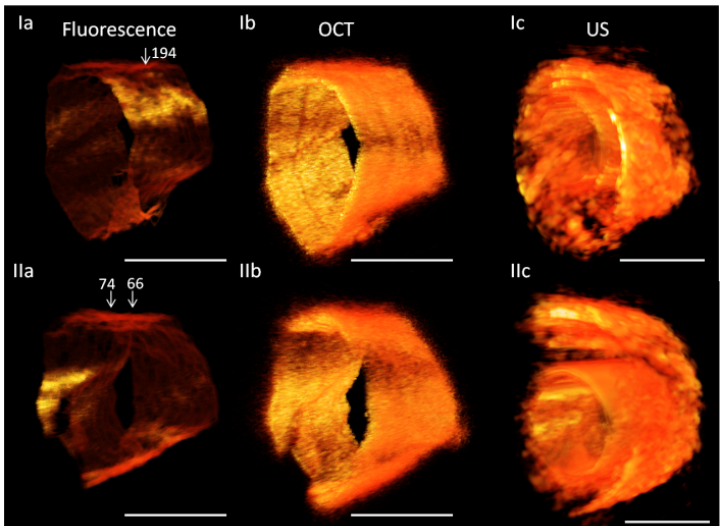

Figure 3.11 3D tri-modality images of atherosclerotic rabbit. (Ia) and (IIa) Fluorescence, (Ib) and (IIb) OCT, (Ic) and (IIc)US. Scale bars are 1 mm.

3.2.3 Conclusion

In this paper, a tri-modality imaging system with a fully integrated tri-modality intravascular probe was presented. The system has the capability of simultaneously obtaining OCT, ultrasound, and fluorescence data and displaying images in real-time. The diameter of the probe is 1mm, which means that it has great potential for clinical applications. This system may lead to a more accurate assessment of vulnerable plaques. Both phantom and *ex vivo* experiment demonstrate that this tri-modality system is capable of obtaining a high-resolution OCT cross-section, deep-penetration ultrasound structure, and molecular-specific ICG-based fluorescence images. Furthermore, H&E staining further validates the *ex vivo* results. The initial results have shown that the tri-modality system has potential for plaque detection and characterization. The tri-modality system and fully integrated tri-modality imaging probes, in the near future, may make the identification of lipid-rich, inflamed plaques that are likely to rupture possible and provide a powerful tool for clinical management of cardiovascular diseases.

Chapter 4 – Endoscopic Imaging Techniques

4.1 High Speed Endoscopic Photoacoustic and Ultrasound

Endoscopic photoacoustic (PA) imaging is a non-invasive imaging modality that provides molecular contrast with depth-resolved information [4, 74-76]. Integrated with ultrasound (US) imaging, this multimodal endoscopic PA/US imaging technology is able to provide both structural and chemical compositions of colorectal walls for diagnosis of GI cancer at an early stage. Several groups have reported different designs of an integrated endoscopic PA/US imaging system [213, 217, 260-262] that represent a significant step forward for the characterization of GI cancer. However, these imaging systems are still not adequate for *in vivo* clinical translation due to insufficient field-of-view, large probe diameters, and slow imaging speed. For example, the systems [213, 263] reported by Xing et al. and Li et al. were limited due to oversized probes which are incompatible with a clinical endoscope. Yang et al. developed a series of endoscopic photoacoustic imaging systems [261, 264] based on a distal scanning method with much smaller catheters. However, only part of the cross-sectional images could be obtained due to the partial blocking of the view from the electric wires of the micromotor. In addition, the probes were rigid and had slow imaging speeds (<10 Frame/s) which limited the clinical applications.

In this section, we demonstrate a high speed integrated endoscopic PA and US imaging system. Utilizing a high repetition rate pulsed laser with an optimized rotary joint as well as a proximal scanning method, this integrated imaging system is able to obtain morphological tissue information and vasculature of the GI tract simultaneously at a high imaging speed up to 50 frames/s (the fastest speed reported to date). We conducted *in vivo* animal studies to demonstrate the performance of our imaging system for evaluating the GI tract.

4.1.1 Methods

One of the key determining factors of clinical translation is the imaging speed. To acquire quality images for accurate disease detection, high speed imaging is essential as it can minimize the motion artifact caused by breathing and rectal peristalsis. In addition, increasing imaging speed, hence improving the imaging area, helps physicians visualize larger sections of GI tract in a shorter period of time. Currently, the imaging speed of an endoscopic PA/US system is what limits translation to clinical application. In this study, several improvements to an endoscopic PA/US imaging system were made to achieve a higher imaging speed with good imaging quality. Most current endoscopic probes for GI application utilize distal scanning with a micromotor which makes it difficult to achieve a high rotation speed in water [261, 264]. To address this issue, a proximal scanning method utilizing a torque coil to transmit the torque from a rotary motor was applied to drive the imaging probe, providing a rotation speed up to 100 revolutions per second in water. A 10 W pulsed laser with a repetition rate up to 300 kHz was used as the excitation source to perform photoacoustic imaging. In consideration of the laser energy loss caused by high speed rotation, we customized the optical rotary joint to maintain a high transmission efficiency of laser energy for a rotation speed up to 50 revolutions per second. High speed rotation also generated a higher noise level that degraded the sensitivity of the imaging system; hence, the slip ring, motor driver, and motor were covered by magnetic shielding foils to enhance electromagnetic shielding. Additionally, instead of the conventional B-scan averaging which greatly decreases the imaging speed, an algorithm was developed for residual electrical noise removal. Lastly, a gradient index (GRIN) lens was used to collimate the illumination light, providing improved image resolution and system sensitivity.

Figure 4.1 illustrates the overall setup of the integrated endoscopic PA/US imaging system (a), schematic (b), and photograph (c) of our imaging probe. In the system, a 532-nm nanosecond laser (DCH-532-10, Photonics Industries International Inc.) with a repetition rate up to 300 kHz is utilized for PA signal excitation. The output laser beam is focused by a condenser lens into the multimode fiber (MMF) of the imaging probe. The MMF is used to deliver the laser energy. A custom-made, single-element transducer ($0.7 \times 0.7 \times 0.5\ mm^3$ with an active element area of $0.5 \times 0.5\ mm^2$, 45 MHz center frequency) is used to detect the photoacoustic and ultrasound signals from the biological tissue. The trigger signal from the pulsed laser is used as the main trigger to synchronize data acquisition and laser emission. Simultaneously, the main trigger signal is delayed by 5 μs to trigger the ultrasound pulser/receiver (DPR500, JSR Ultrasonics) to emit acoustic waves for ultrasound imaging. The generated PA and US signals are band-pass filtered, amplified, and digitized with a data acquisition (DAQ) card (ATS9350, Alazar Technologies Inc.) in a personal computer. In order to obtain cross-sectional images (B-scans), we applied a proximal scanning method in which the imaging probe is rotated through a rotary joint. The rotary joint is assembled with a custom-made electric slip ring (Hangzhou Prosper Electric Co.), a fiber optic rotary joint (Princetel, Inc.) and a rotary motor (MicroMo Electronics, Inc.) which allow the laser beam and electrical signal to pass across rotating interfaces. In consideration of increased electrical noise and laser energy loss caused by high speed scanning, we customized a fiber optic rotary joint which is able to keep high transmission efficiency of laser energy with a rotation speed up to 50 revolutions per second. Furthermore, we made improvements to enhance electromagnetic shielding and developed an algorithm to remove electrical noise instead of taking an average which greatly decreases the imaging speed. The algorithm separates the noise and the signal by correlating two adjacent B-scan images in which the noise is differentiated by its randomness, and

thus, the signal can be extracted from the original data. In addition, spiral three-dimensional (3D) images can be obtained by a pull-back imaging probe using a translation stage. The software is written entirely in C++ for data acquisition, image processing, and display in real-time using a graphics processing unit.

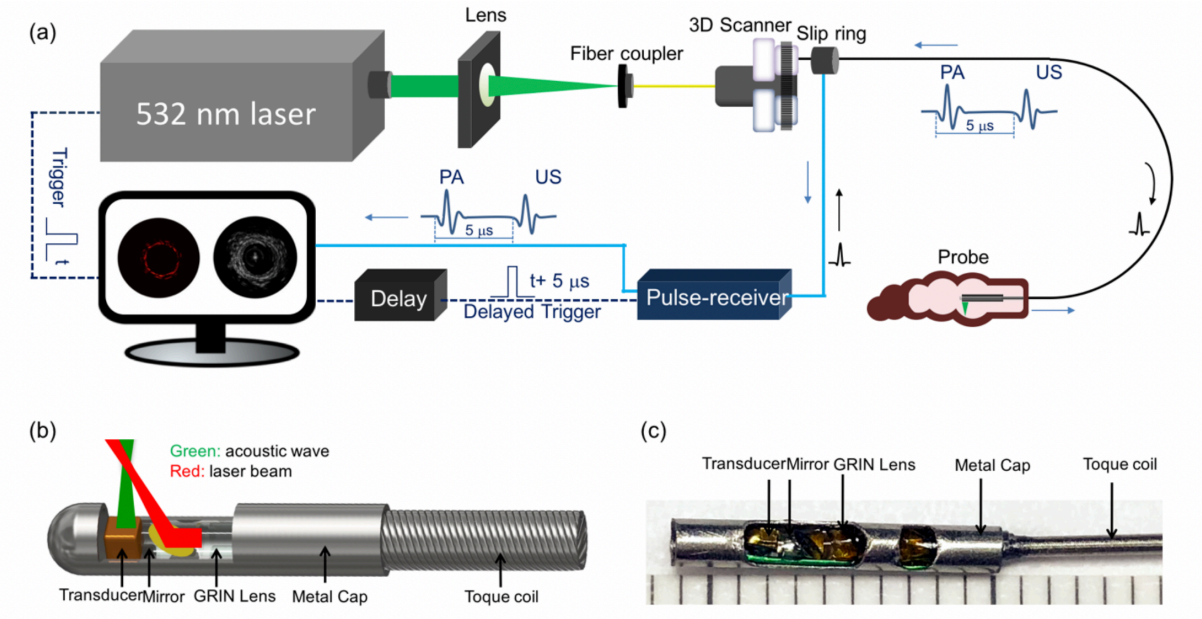

Figure 4.1 Integrated PA/US imaging system (a), schematic (b), and photograph (c) of our imaging probe. 3D scanner consists of fiber optic rotary joint, slip ring, motor, and pull-back translation stage

In the probe, the laser beam propagates through the MMF, collimated by a 1-mm GRIN lens (Aviation Magneto Optical Sensor Corp.), and reflected by a rod mirror (Aviation Magneto Optical Sensor Corp.) with a diameter of 1 mm at an angle of 45° towards the tissue surface. The laser pulse energy emitted from the imaging probe is maintained to be ~30 µJ throughout the study. In consideration of water absorption and astigmatism caused by the sheath, the corresponding fluence on the rectum is 15 mJ/cm^2, which is well within the American National Standard Institute (ANSI) safety standard (20 mJ/cm^2) in the visible spectrum (400–700 nm) [265]. A miniature custom made single-element ultrasonic transducer is used to detect the PA waves from the sample

as well as to perform pulse-echo US imaging. Both transducer and rod mirror are tilted at a small angle in order to obtain optimized overlap between optical and acoustic beams. The outer diameter and rigid length of the imaging probe are 1.5 mm and 11 mm, respectively. The length of the imaging probe is 50 cm. A double-wrapped torque coil (ID: 0.4 mm, OD: 0.8 mm, Asahi Intecc USA, Inc.) is connected to the distal end of the imaging probe to transmit the torque from the rotary motor to perform cross-sectional images (B-scans) with a high imaging speed up to 50 revolutions per second (RPS). Compared with the distal scanning method that applies a micromotor to drive the mirror, the proximal scanning method has full field of view imaging, improved flexibility and high imaging speed for the endoscopic PA/US system.

4.1.2 Imaging Results

In order to demonstrate the performance of our integrated endoscopic PA/US imaging system, we conducted an *in vivo* experiment to image the rectum of a Sprague Dawley (SD) rat. The rat was placed under general anesthesia by IP injection of ketamine hydrochloride (87 mg/kg) and xylazine (10 mg/kg) through a 29 G needle. After the rat was anesthetized, we performed enemas to clean the rectum and then inserted our imaging probe with sheath for *in vivo* imaging. All methods were carried out in accordance with the University of California, Irvine (UCI) Institutional Review Board (IRB) and the Institutional Biosafety Committee (IBC). All experimental protocols were approved by the UCI IBC under protocol #2016-3198.

Figure 4.2 shows the representative PA and US images. The transverse resolution of the PA imaging is ~250 μm which is determined by the optical beam size. For the US imaging, the transverse resolution is ~ 300 μm which is mainly governed by the ultrasound transducer size. The axial resolutions of the PA and the US systems both depend on the bandwidth of the ultrasound transduce and are approximately 50 μm. The imaging depth is ~4 mm, determined by the

overlapping range between the optical beam and the acoustic wave. At the optimum imaging depth in which the optical beam and acoustic wave are fully overlapped, the signal-to-noise ratio (SNR) of the PA and US systems are ~45 dB and ~42 dB, respectively. The detailed methods for measuring these parameters are described previously [65]. We acquired ~ 500 B-scan images with a pullback speed of 0.5 mm/s. For groups I, II, and III, a 20 frame per second (FPS) was used to perform B-scan imaging. For group IV, a 50 FPS was applied to perform imaging. From the US images of the four groups [Figure 4.2 (Ia), (IIa), (IIIa), and (IVa)], the typical layered architecture indicated by the white dashed box and seminal vesicles that correspond to low echo in US images indicated by the white arrow can be identified. From the PA images [Figure 4.2 (Ib), (IIb), (IIIb), and (IVb)] of the four groups, the signal of blood vessels present in different layers can be found. Fused PA and US images [Figure 4.2 (Ic), (IIc), (IIIc), and (IVc)] provide the co-registration images, which are advantageous over either modality alone to supplement lesion evaluation. These results demonstrate that this integrated endoscopic imaging system has the capability to visualize the layered architecture and vasculature of the rectum wall simultaneously.

Figure 4.3 (I), (II), and (III) show representative 3D PA, US, and fused images, respectively, of the rectum. Figure 4.4 shows unwrapped images from Figure 4.3; the pattern of vasculature can be observed. The entire process of imaging only takes ~ 10 seconds, and no averaging was applied. From the 3D US images [Figure 4.3 (IIa), (IIb) and Figure 4.4 (IIa), (IIb)], morphology of the rectum wall and surrounding organ can be identified. The white dashed box indicates the typical layered architecture, and the white arrow indicates the seminal vesicles. From 3D PA images [Figure 4.3 (Ia), (Ib) and Figure 4.4 (Ia), (Ib)], vasculature of the rectum wall can be clearly visulized.

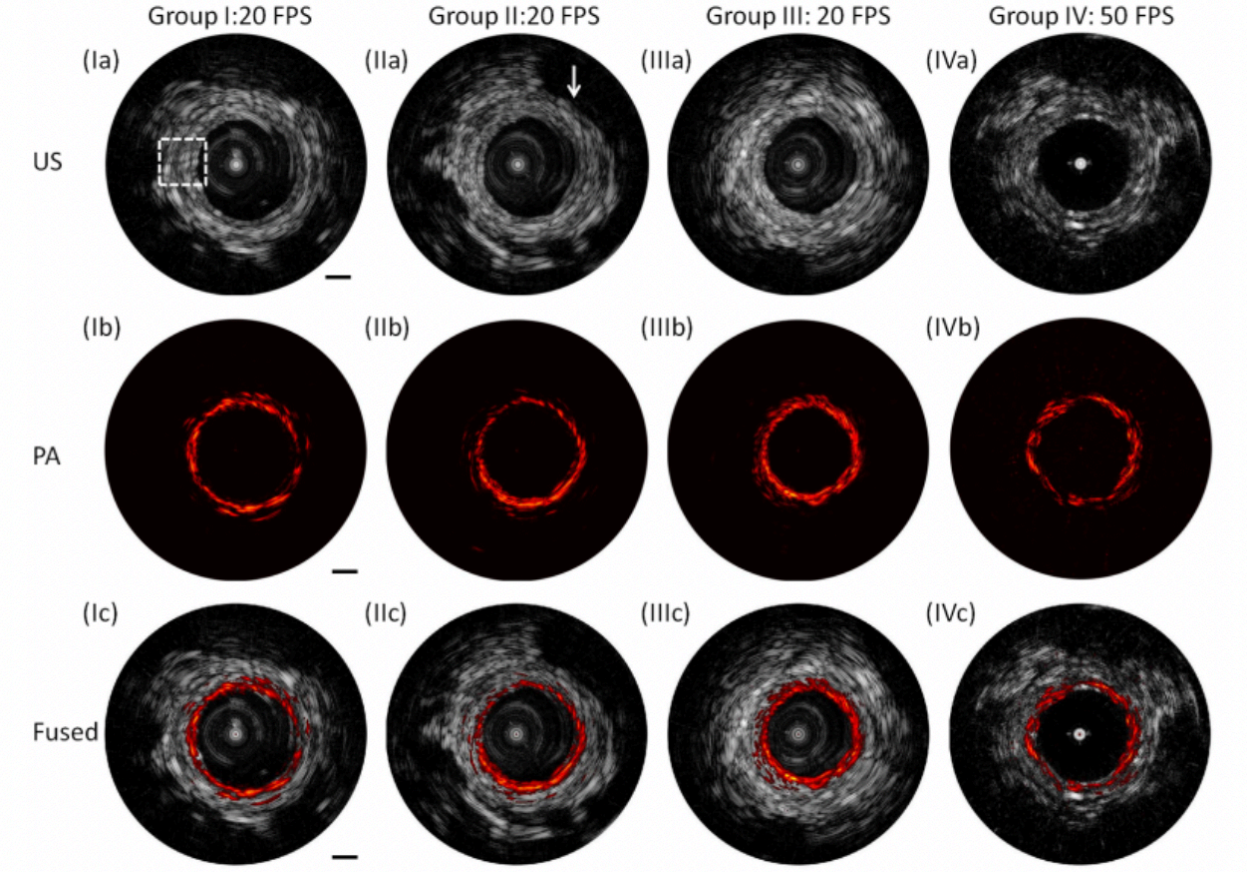

Figure 4.2 Cross-sectional PA, US, and fused images with different locations along pullback direction. (a) US images. (b) PA images. (c) Fused images. White dashed box: typical layers of rectum wall. Groups I, II, and III were obtained with 20 frames per second (FPS). Group IV was obtained with 50 frames per second. White arrow: surrounding organ. Scale bar: 1 mm.

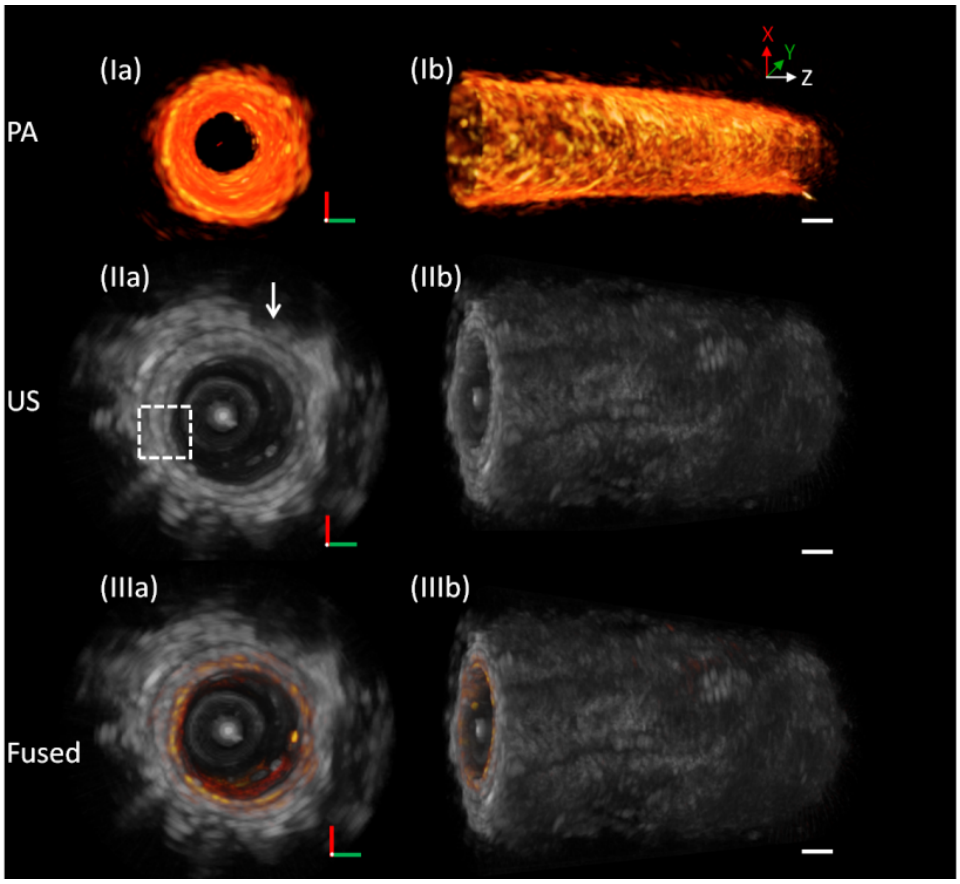

Figure 4.3 3D endoscopic PA, US, and combined images of rat rectum. (Ia) and (Ib) PA images. (IIa) and (IIb) US images. (IIIa) and (IIIb) Fused images. White arrow: surrounding organ. Scale bar: 1 mm.

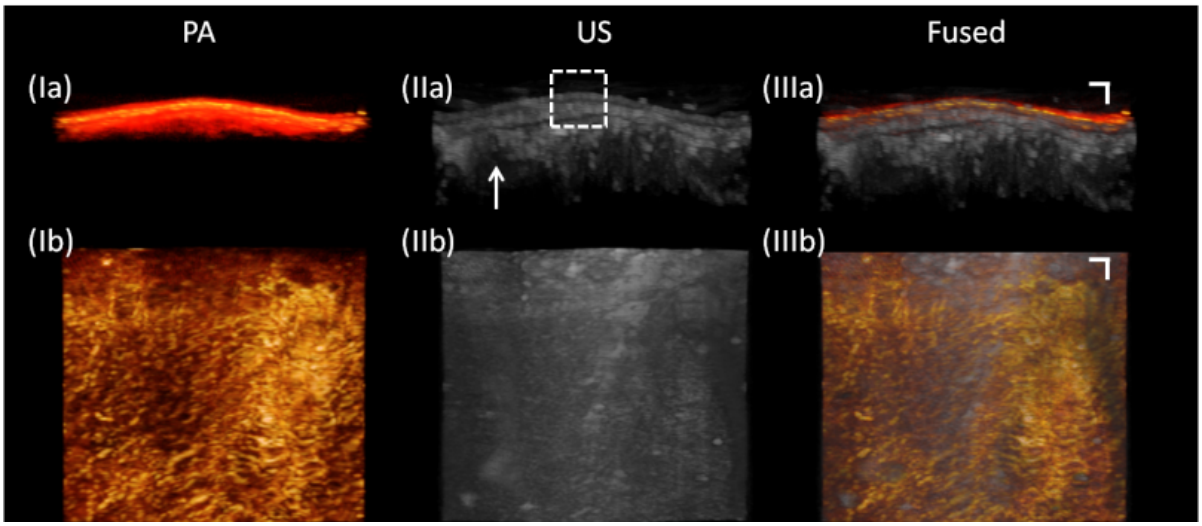

Figure 4.4 3D endoscopic PA, US, and fused images of rat rectum. (I) PA images. (II) US images. (III) Fused images. White arrow: surrounding organ. Scale bar: 1 mm.

4.1.3 Conclusion

Endoscopic integrating of PA and US imaging is a minimally invasive non-ionizing imaging technology that has the potential for the diagnosis and classification of GI disease. Here, we reported on an integrated endoscopic PA/US imaging system which is able to provide information of tissue structure and vasculature of GI tissues simultaneously. Utilizing a high repetition rate pulsed laser with an optimized rotary joint as well as a proximal scanning method, a high speed integrated endoscopic PA/US imaging system was obtained. The outer diameter of the imaging probe is around 1.5 mm, which is accessible through the accessory channel of the commercial endoscope. The results obtained from the *in vivo* rat experiment demonstrated that the typical layered architecture and vasculature can be identified by this integrated imaging system. While our PA/US imaging system has laid the groundwork for clinical imaging, several challenges still need to be addressed for clinical integration. (1) Resolution: to visualize the microvasculature of the rectal wall, the transverse resolution of the PA imaging needs to be improved. Furthermore, to accurately demarcate the tissue layers, axial resolution of both modalities has to be improved as well which may be achieved by employing a higher frequency acoustic transducer. (2) Probe form factor: for deeper GI tract imaging (e.g., small intestine), the diameter and the rigid length of the imaging probe need to be further minimized to ensure a smooth insertion. This may be achieved by using a GRIN fiber with better flexibility and a smaller diameter to focus the optical beam. (3) Sensitivity: for higher speed imaging (> 50 RPS), the performance of the fiber optic rotary joint and slip ring will also need to be further optimized. In addition, the overlap between the optical beam and the acoustic wave can be further improved to enhance the detection efficiency through the entire imaging depth, and this may be accomplished by employing coaxial imaging. Lastly, a diseased animal model with *in vivo* imaging is needed for further verification.

4.2 High Sensitivity Endoscopic Photoacoustic and Ultrasound

Photoacoustic (PA) imaging is an emerging imaging modality that has been applied in a wide variety of biomedical applications, such as brain lesion detection and breast cancer diagnosis [5, 216, 266]. The advantage of PA imaging lies with its ability to reveal molecular information as organic molecules vary in absorption efficiency. In brief, PA imaging utilizes a non-ionizing nanosecond laser to deliver pulsed light into the biological tissue. When the pulsed laser energy is absorbed by the tissue sample, it is converted to heat which causes a transient thermoelastic expansion that emits wideband ultrasonic waves. A piezoelectric transducer or all-optical ultrasound sensor can be used to detect these generated ultrasonic waves, or the PA signals, and each has its own advantages and limitations. An all-optical ultrasound sensor, such as a Fabry-Pérot interferometer and microresonator, is able to provide wide detection bandwidth, resonance-free acoustic detection spectrum, and high resolution [267-274]. However, it still presents challenges for ultrasound detection. First, it requires a cost-intensive read-out system. In addition, with an all-optical ultrasound sensor, it is incapable of generating ultrasound waves to perform ultrasound imaging which is often preferable in clinical applications using a multimodality endoscope. Regarding the piezoelectric transducer, it can provide ultrasound detection with large penetration depth and high sensitivity. In addition, a piezoelectric transducer is able to emit and receive the US signal simultaneously. Therefore, the integration of PA imaging with US imaging is seamless since PA imaging relies on the use of ultrasonic transducers. With the capability to simultaneously resolve molecular (PA) and structural information (US) in depth, dual-modality PA/US imaging has been used in various applications, including the detection of cancer and characterization of vulnerable plaque [20, 21, 217, 224, 255, 261, 275-277]. In our study, a

piezoelectric transducer was applied for PA signal detection and to perform US imaging simultaneously.

The key factor of the performance of a PA/US imaging system is the ultrasonic transducer. For the PA/US transducer, the widely used materials include: lithium niobate ($LiNbO_3$) [264, 278, 279], lead magnesium niobate-lead titanate (PMN-PT) [261, 280], and lead zirconate titanate (PZT) composite [20, 217, 275, 281, 282]. LiNbO3, as the conventional single crystal, has stable and strong electro-mechanical coupling capabilities but exhibits inferior piezoelectric performance compared to PZT [283]. PZT is advantageous due to its high performance and ease of manufacture, yet it has a limited application in highly attenuative materials. Recently developed PMN-PT as a new class of signal-crystal piezoelectric material has gained much interest in the research field and has demonstrated improved piezoelectric performance. Its piezoelectric strain constant (d_{33}) ranging from 1500 to 2500 (pC/N) is approximately five times higher than that of PZT, and its electromechanical coupling coefficient k_t of ~0.58 is also superior [284, 285]. In addition, it has been reported that the PMN-PT single crystal ultrasonic transducer shows improved performance over both the PZT and PZT-based 1-3 composite ultrasonic transducers [286]. On top of the PMN-PT's advantages, the PMN-PT/epoxy 1-3 composite material has further benefits. As one of the most promising in frontier transducer technology, piezoelectric rods embedded in a low-density polymer lower the acoustic impedance and highly enhance the electromechanical coupling coefficient. For PMN-PT, the electromechanical coupling coefficient increases from 0.58 to 0.94, which inherently contributes to better acoustic impedance matching between transducers and water along with higher sensitivity and improved image resolution [287].

In this section, we report on a 32-MHz single-element ultrasonic transducer with an aperture size of 0.5 mm fabricated using PMN-33%PT/epoxy 1-3 composite. A miniature PA/US

endoscopic probe (OD: 1.45 mm) was fabricated based on this material for PA/US imaging. The manufacture process of the transducer, imaging probe design, and imaging system setup are described herein. The performance of the transducer was quantified using a reflector and tested in the rat gastrointestinal tract *in vivo*. The results demonstrated an enhanced sensitivity over the conventional transducer.

4.2.1 Methods

(1) Design and fabrication of PMN-33%PT/epoxy 1-3 composite ultrasonic transducer

Figure 4.5 (a) illustrates the fabrication process of the PMN-PT/epoxy 1-3 composite. (1) Polished PMN-PT crystal plate was first diced along one direction using an automatic dicing saw (K&S 982-6, Kulicke and Soffa Industries, Inc., Willow Grove, PA). (2) The kerfs were filled with epoxy (EPO-TEK 301, EPOXY Technology, Inc., Billerica, MA). (3) After the epoxy was cured, the plate was diced again in the direction perpendicular to the kerfs. (4) The new kerfs were filled with the same epoxy and allowed to cure. (5) Last, the composite plate was flapped to the final thickness and coated with Cr/Au on both sides as electrodes. For endoscopic application, we fabricated an ultrasonic transducer with a $0.5 \times 0.5\ mm^2$ effective detection area, as shown in Figure 4.5 (b).

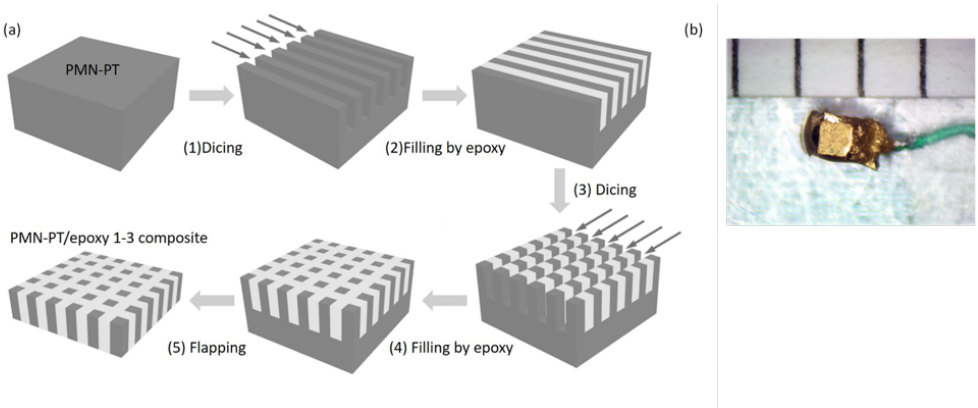

Figure 4.5 PMN-PT/ epoxy 1-3 composite ultrasonic transducer. (a) Fabrication process of PMN-PT/ epoxy 1-3 composite material. (b) Photo of ultrasonic transducer.

(2) System design and probe design

We applied the same system for the feasibility test, as described in section 4.1.1. Regarding the probe, we also applied the same design to replace the conventional transducer with a PMN-33%PT/epoxy 1-3 composite ultrasonic transducer.

4.2.2 Imaging Results

(1) Performance of ultrasonic transducers

A glass mirror was used as an imaging target in the pulse-echo test to measure the frequency spectrum of three representative ultrasonic transducers made of PMN-PT/epoxy 1-3 composite, PMN-PT, and PZT composite (Figure 4.6). In Figure 4.6, the blue curves represent the pulse-echoes of the ultrasonic transducers, and the red curves show the frequency responses. In the plot, the pulse echo on the left is the initial pulse from the ultrasonic transducer, and the one on the right is from the mirror. As shown in Figure 4.6, the PMN-PT-based transducer has a center frequency of around 35 MHz and a 78% frequency bandwidth (at -6dB), and those of the PZT composite based transducer are 40 MHz and 47%, respectively. In contrast, the transducer made of the PMN-PT/epoxy 1-3 composite material has a center frequency at 32 MHz with a 91% bandwidth which shows a better electro–mechanical performance compared with the other two ultrasonic transducers. The characterization of the three types of ultrasound transducers including the center frequency, bandwidth, SNR, and insert loss (IL) are demonstrated in Table 4.1.

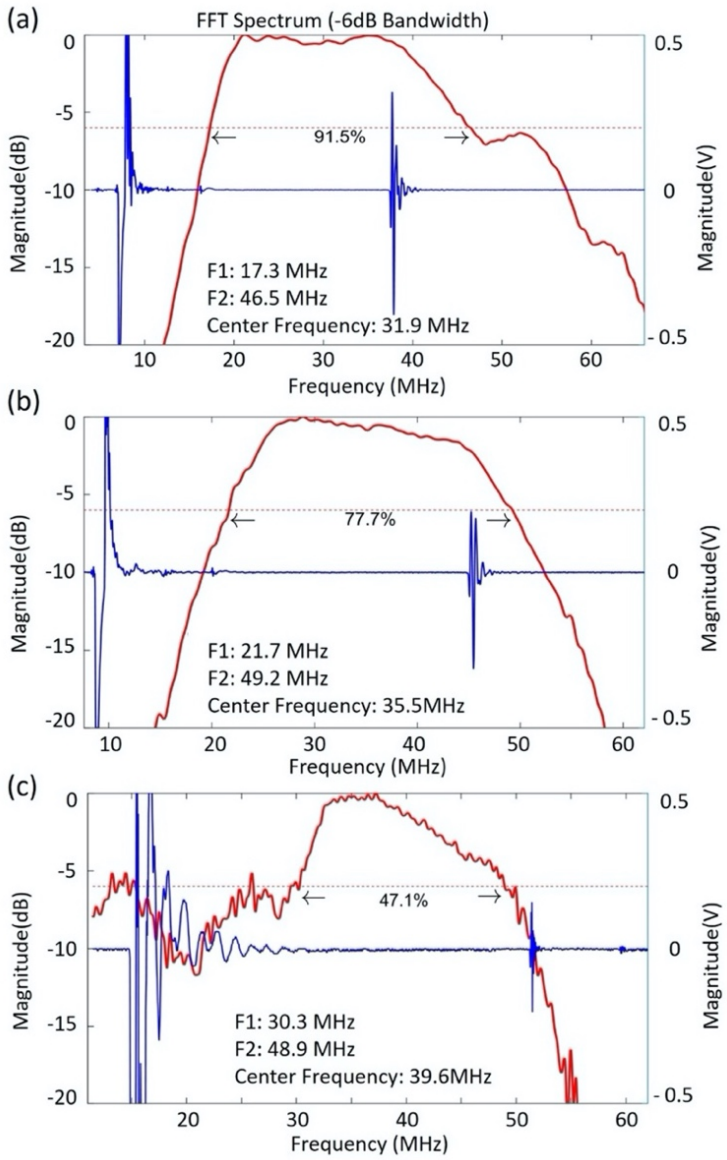

Figure 4.6 Pulse-echo measurements and respective frequency spectra. (a) PMN-PT/epoxy 1-3 composite, (b) PMN-PT, and (c) PZT composite. Blue curve: US pulse echo. Red curve: spectrum.

Table 4.1 Performance comparisons of PMN-PT/ epoxy 1-3 composite, PMN-PT, and PZT composite transducers.

Material	Center Frequency (MHz)	Bandwidth (-6dB)	SNR (dB)	Insert Loss (dB)	Noise equivalent pressure (P)
PMN-PT/epoxy 1-3 composite	31.9	91.50%	44.27	16	2.6
PMN-PT	35.5	77.70%	40.61	17	3
PZT composite	39.6	47.10%	30.8	21	1.7k

(2) Performance of ultrasonic transducers

Imaging probes were fabricated using each of the transducers, and the SD rats were imaged with each of the probes. The representative images are shown in Figure 4.7. Figure 4.7 (a), (b), and (c) show the US images from PMN-PT/epoxy 1-3 composite, PMN-PT, and PZT composite, respectively. The signal-to-noise ratios (SNRs) of US are reported in Table 4.2. The US images acquired using the probe made of PMN-PT/epoxy 1-3 composite demonstrate significant improvement in SNR compared to the PMN-PT and PZT composite. This agrees with the reported study [286, 287].

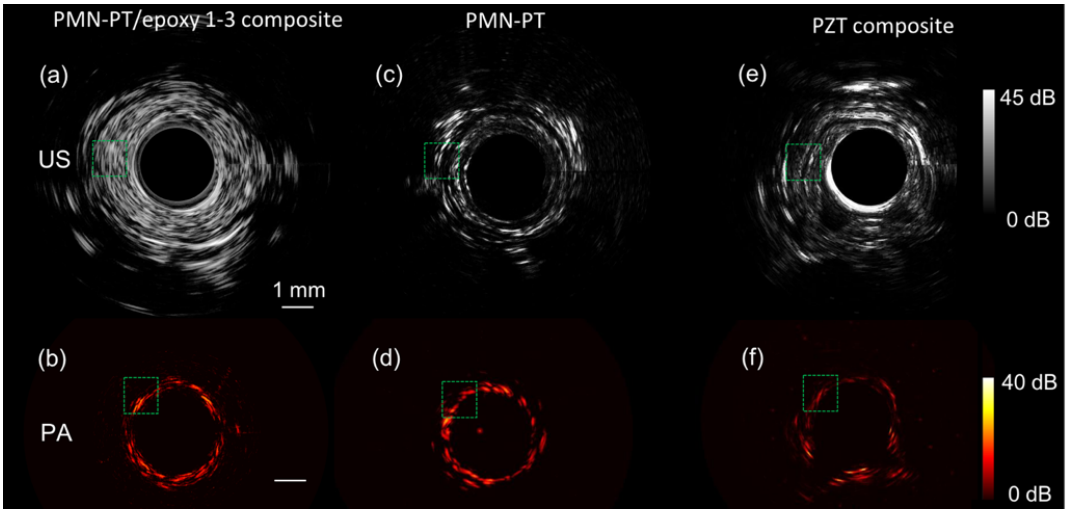

Figure 4.7 US and PA images of *in vivo* imaging of rat rectum. (a) and (b): PMN-PT/epoxy 1-3 composite. (c) and (d): PMN-PT. (e) and (f): PZT composite.

Table 4.2 SNR of PA and US images of *in vivo* imaging of rat rectum. The regions for SNR calculation are marked by green dashed boxes in Figure 4.7.

Material	SNR [dB]	
	US	PA
PMN-PT/epoxy 1-3 composite	46.7	32.4
PMN-PT	32.2	31.8
PZT composite	33.4	31.5

(3) *In vivo* Imaging of the Rat Rectum

To demonstrate its clinical application, *in vivo* imaging utilizing a PMN-PT/epoxy 1-3 composite PA/US probe was performed in the rectum of a SD rat. With a pullback speed of 1 mm/s using a motorized translation stage, 500 cross-sectional PA/US images were acquired sequentially. The representative images of different longitudinal positions are shown in Figure 4.8. From the US images [Figure 4.8(a-d)], the colorectal wall and surrounding connective tissue can be identified clearly (the boundary between them with a low intensity signal, indicated by dashed yellow circle). In Figure 4.8 (e-h), the PA images show the depth-resolved blood vessel distribution which is advantageous over fluorescence imaging. Co-registered images, shown in Figure 4.8 (i-l), provide helpful supplementary information for lesion evaluation and is advantageous over either modality alone. Figure 4.9 shows representative 3D PA and US images, respectively, of the rectum. The pattern of vasculature can be observed in Figure 4.9 (a). The morphology of the rectum wall can be identified in Figure 4.9 (b) and (d).

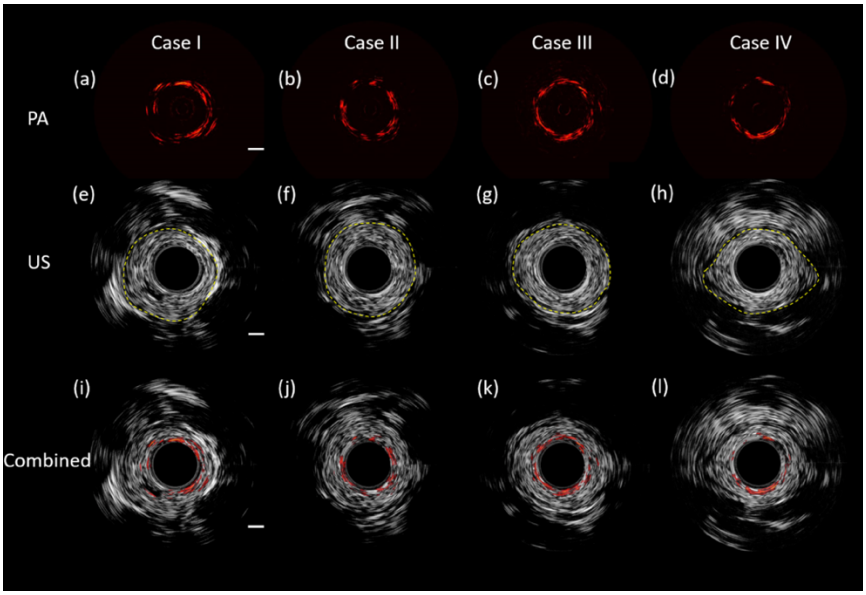

Figure 4.8 PA, US, and combined images of *in vivo* imaging of rat rectum (a-d): PA images. (e-h): US images. (i-l): combined PA and US images. Scale bar: 1mm. Cases I, II, III, and IV: different longitudinal positions of rat rectum.

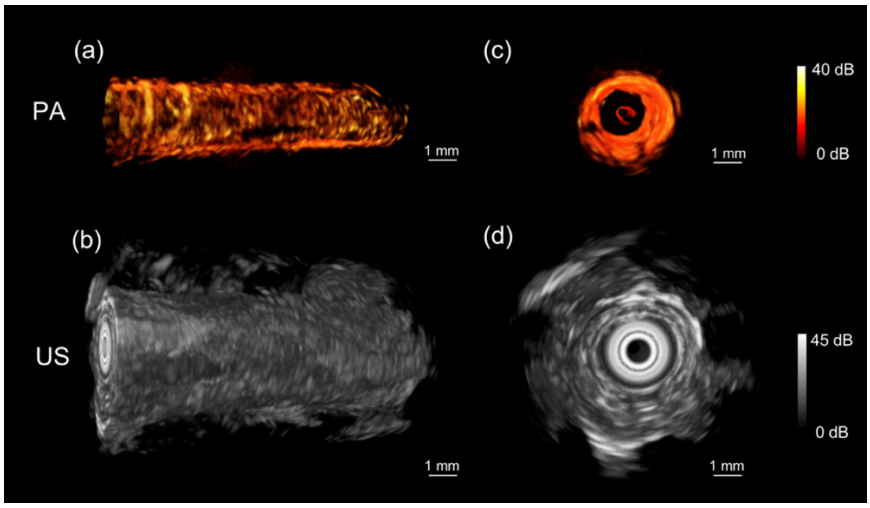

Figure 4.9 3D endoscopic PA and US images of rat rectum. (a) and (c) 3D PA images. (b) and (d) 3D US images. Scale bar: 1 mm.

4.2.3 Conclusion

Endoscopic dual-modality PA/US imaging is a minimally invasive imaging modality that has the capability of visualizing the morphology and vasculature of the rectal wall. With the integration of a PMN-PT/epoxy 1-3 composite-based ultrasonic transducer which has been demonstrated to have high piezoelectric coefficients d_{33}, high coupling coefficients k_{33}, and low dielectric loss, we further improved the sensitivity of the conventional PA/US imaging system. The results obtained from the reflector and *in vivo* rat experiments have shown its enhanced sensitivity compared to the two conventional transducers (PMN-PT and PZT composite) based imaging systems. In the obtained PA/US images, the layered architecture and vasculature can be identified. With its small form factor (probe outer diameter < 1.5 mm), the multimodal imaging probe can access the colon through the accessory channel of a commercial endoscope so it can be easily integrated into clinical practice to provide additional subsurface information.

Despite the superior performance of the PMN-PT composite, there are a few drawbacks. The first is the higher cost compared to conventional piezoelectric ceramics. However, the cost

can be further reduced with the development of new manufacturing methods. Another disadvantage of PMN-PT composite is that its Curie temperature is relatively low, (T_C~130 ° C), which limits its potential in high-power applications. To address this issue, a new piezoelectric single crystal material, PIN-PMN-PT, has recently been proposed and is being investigated for its higher Curie temperature [288]. In addition, the PMN-PN composite based PA/US imaging system can be further improved, including achieving higher resolution of PA/US images for visualizing the microvasculature of the rectum wall by using a single mode fiber and higher frequency ultrasonic transducer, and precise assembly of the imaging probe with help of 3D printing (resolutions: 10 μm for XY-axis and 50 μm for Z-axis). The improved performance of the PA/US transducer is a critical step to translate this technology to clinical application.

4.3 High Speed Endoscopic OCT and NIRF

For improving diagnostics accuracy, many groups focus on developing multimodality imaging systems (such as combined OCT/US, PA/US, and OCT/NIR fluorescence). Among them, integrated OCT and NIR fluorescence allows cross-sectional visualization of the tissue morphology and vasculature with high spatial resolution and sensitivity, providing a powerful tool to monitor the hallmarks of CRC (i.e., morphological abnormality and angiogenesis). Additionally, integrated OCT/NIR fluorescence imaging decreases the procedure cost and time as only one imaging probe is used to acquire both OCT and NIR fluorescence data in one session. Several multimodal OCT/NIR fluorescence systems [54, 63, 289-292] have been reported, demonstrating their capability of visualizing tissue morphology and molecular composition simultaneously. However, a successful clinical adaptation for CRC diagnostic imaging requires a combination of miniaturized endoscopic packing, FDA approved contrast agent, high-speed and high-resolution 3-dimensional (3D) imaging, and animal model validation. Currently, none of the reported systems has achieved all of the above prerequisites.

In this section, we present a multimodal endoscopic system with simultaneous co-registered OCT and NIR fluorescence imaging. By introducing a contrast agent into the vascular network, NIR fluorescence is able to highlight the cancer-suspected area based on significant change of tumor vascular density and morphology caused by angiogenesis. With the addition of co-registered OCT images to reveal subsurface tissue layer architecture, the suspected regions can be further investigated by the altered light scattering resulting from the morphological abnormality. Using this multimodal imaging system, an *in vivo* animal study was performed using a F344-ApcPirc^{Uwm} rat in which the layered architecture and microvasculature of the colorectal wall at different time points were demonstrated. The co-registered OCT and NIR fluorescence images

allowed the identification and differentiation of normal colon, hyperplastic polyp, adenomatous polyp, and adenocarcinoma. This multimodal imaging strategy using a single imaging probe has demonstrated the enhanced capability of identification and classification of CRC compared to using any of these technologies alone, thus having the potential to provide a new clinical tool to advance gastroenterology practice.

4.3.1 Methods

(1) Contrast agent

Indocyanine green (ICG) is a fluorescent dye used in medical imaging as an indicator substance and was approved by the FDA in 1959. ICG binds 98% to plasma proteins and accumulates in the tumor region more than in normal tissue after intravenous injection due to the "enhanced permeability and retention" effect caused by angiogenesis [293, 294]. For this reason, ICG is widely used for angiogram and tumor border delineation [295, 296]. Because tumor vasculature is more dense and highly tortuous, the morphology and density of tumor vasculature can be used as biomarkers for tumor detection. In this study, ICG was used to perform the angiogram and identify the suspected tumor region based on the altered density and morphology of vasculature. ICG has a short half-life (~ 3 minutes) and is cleared from circulation exclusively by the liver to bile juice quickly. Therefore, the imaging will be performed right after the intravenous injection and finished in 3 minutes.

(2) Animal model

Male rats from the F344-ApcPircUwm strain were used for this study. The rat model carries a knockout allele in the gatekeeper gene adenomatous polyposis coli (Apc) and has been designated the polyposis in the rat colon (Pirc) kindred which can develop spontaneous intestinal

lesions starting at 45 days of age which then eventually expand to the colon and rectum [297]. This model has been widely used in longitudinal analysis of colorectal tumor biology, chemoprevention, microbiome effects, chemotherapy, and early detection.

(3) Multimodal OCT and NIR fluorescence imaging system

Figure 4.10 (a) shows the schematic of the integrated multimodal OCT and NIR fluorescence imaging system. A wavelength division multiplexer (WDM) and a double clad fiber (DCF) are utilized to fully integrate OCT and NIR fluorescence together. Figure 4.10 (b) shows a micromotor-based imaging probe which is able to perform stable and fast 3D scanning. The system setup and probe design have been described previously [298]. In comparison to our previous design, the outer diameter of the imaging probe is smaller with an outer diameter of 1.6 mm to readily access the colon. In addition, an upgraded micromotor and correction algorithm were applied to provide stable cross-sectional OCT/NIR fluorescence images. All of the software was written entirely with a C++ graphics processing unit which allows fast data processing and real-time display during the rat imaging.

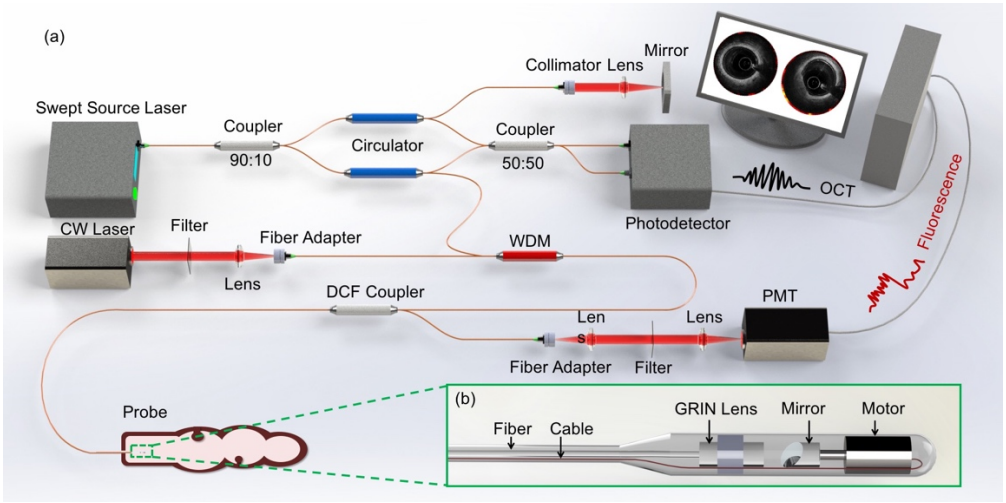

Figure 4.10 (a) Overall design of endoscopic multimodality OCT and NIR fluorescence system. (b) Multimodality imaging probe. WDM: wavelength division multiplexer. PMT: photomultiplier tube. DCF coupler: double clad fiber coupler. OCT: optical coherence tomography. CW: continuous wavelength. GRIN: gradient index.

(4) Imaging protocol

The male rats with a certified report were purchased from Rat Resource & Research Center. The rats were kept on a normal diet upon arrival and were imaged at weeks 1 (after 1 week of acclimatization), 4, and 8 to track the development of the colorectal tumor. To anesthetize the rat for the imaging procedure, the rat was first placed in a hermetically sealed plexiglass chamber for general anesthesia induction and was then removed from the chamber for an intraperitoneal injection of a ketamine-xylazine mixture (87 mg/kg and 10 mg/kg, respectively). After the rat was anesthetized, an enema was performed to remove fecal matter from the rectum. Then, a plastic tube was inserted to inflate the rectum. After gently warming the rat tail, ICG (1.5 mg/kg) was then administrated intravenously through either of the lateral tail veins, followed by immediate imaging in consideration of the fast-hepatic uptake and the short half-life of ICG (3-4 minutes). The entire imaging was performed and finished within less than 3 minutes after the ICG injection; 1,200 cross-sectional OCT/fluorescence images were acquired in each experiment by a 4-cm longitudinal scan. The rat was sacrificed for hematoxylin and eosin (H&E) staining right after the last imaging (at week 8). All procedures were reviewed and approved by the Institutional Animal Care and Use Committee at the University of California, Irvine, under protocol #2016-3198.

4.3.2 Imaging Results

Using our multimodal imaging system, the disease progression of CRC can be visualized by NIR fluorescence with co-registered OCT images. For NIR fluorescence imaging, the signal intensity was determined by the concentration of ICG and the distance from probe. A calibration map (intensity-to-distance) was obtained by measuring the intensity of the fluorescence signal of a plastic tube filled with ICG at different distances. Then the NIR fluorescence image was

calibrated using this calibration map according to the distance extracted from corresponding OCT images.

Figure 4.11 shows the representative fluorescence imaging results obtained at weeks 1, 4, and 8 from one of the mutation rats. Well-defined microvasculature without abnormality was demonstrated in the fluorescence images of week 1 [Figure 4.11 (a)] and week 4 [Figure 4.11 (b)]. No lesion was identified at these two time points. At week 8, several abnormal masses were found in the fluorescence image, indicative of lesions [indicated by white arrows in Figure 4.11 (c)]. Figure 4.11 (d) shows the excised rectum that corresponded to these lesions.

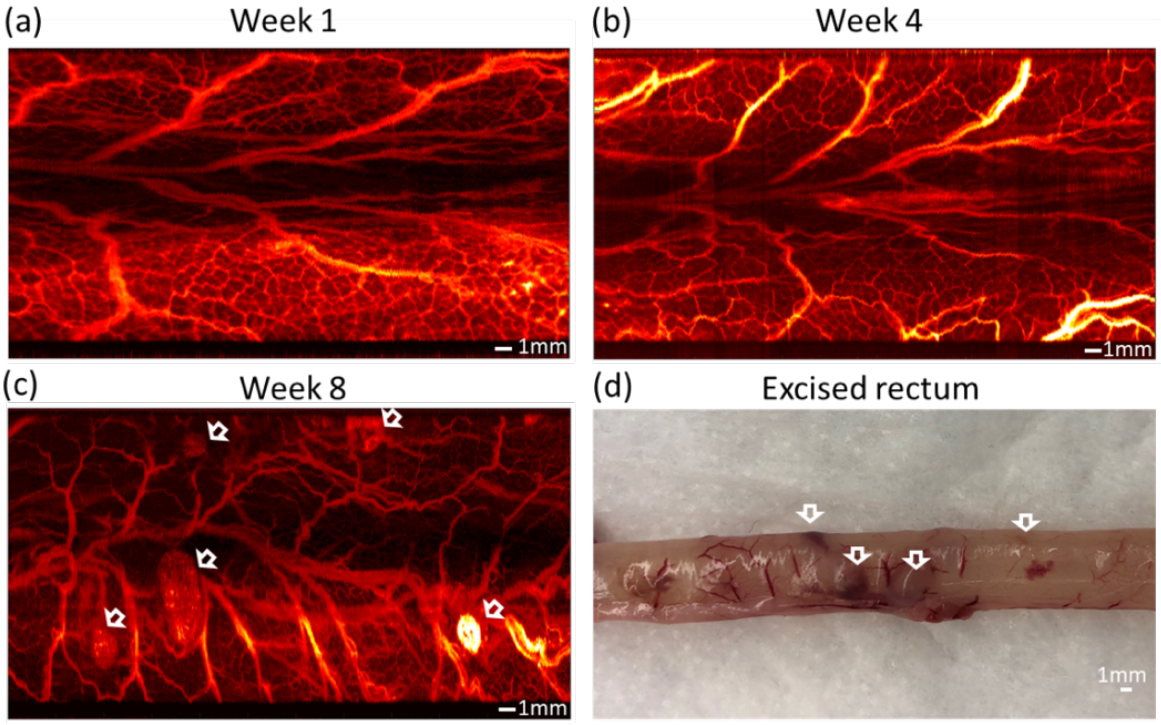

Figure 4.11 Unfolded NIR fluorescence images of rectal wall with different time points. (a) Week 1. (b) Week 4. (c) Week 8. (d) Photo of the excised rectum. Scale bar: 1mm

Figure 4.12 shows the corresponding cross-sectional co-registered OCT (inner) and NIR fluorescence (outer) images of the rat rectum at three time points. At week 1, the layer definitions were well delineated and easily observed [Figure 4.12 (Ia) and (Ib)]. At week 4, the boundary

between different layers indicated by the green dashed box in Figure 4.12 (IIb) became blurred. In addition, several small gaps, indicated by the yellow arrows between the layers can be found in Figure 4.12 (IIa). At week 8, a large polyp [Figure 4.12 (IIIa)] and suspected adenocarcinoma [Figure 4.12 (IIIb)] were observed.

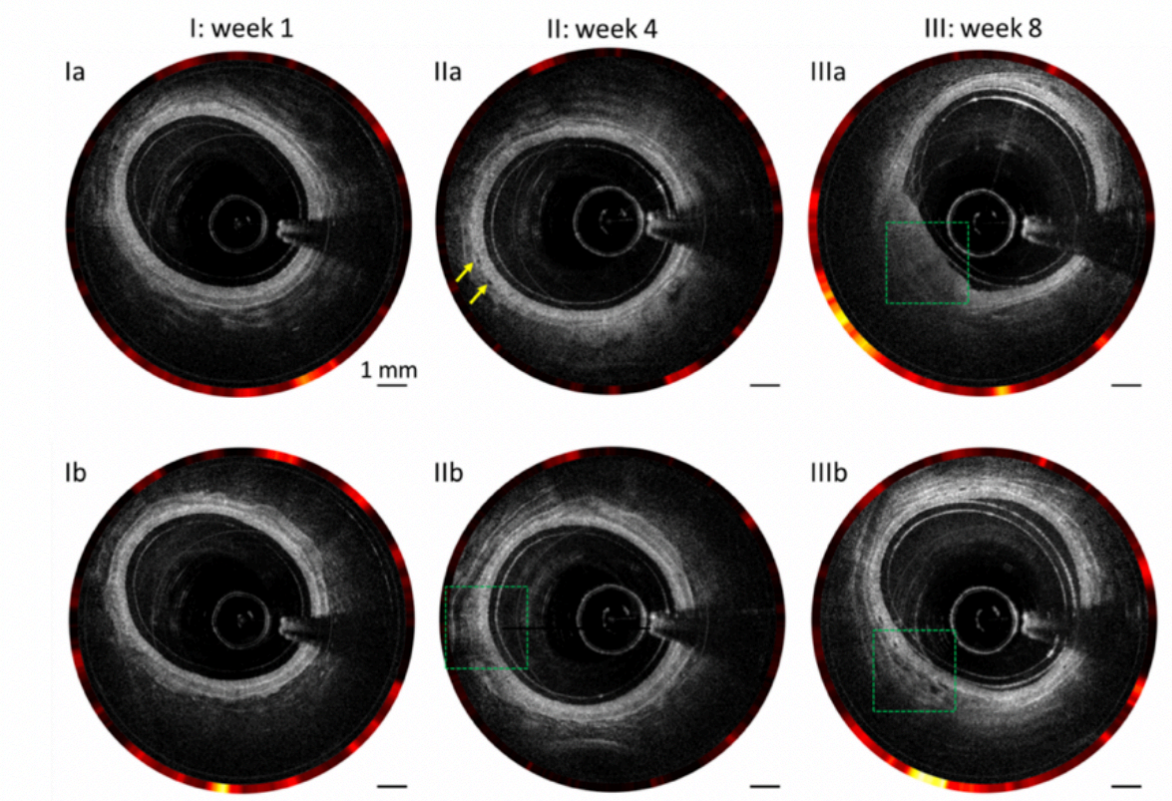

Figure 4.12 Combined OCT and NIR fluorescence B-scan images of colorectal wall with different time points: (I) week 1, (II) week 4, (III) week 8. Green dashed boxes: abnormal lesions. Yellow arrows: small gaps between different layers.

To demonstrate the benefit of dual modality imaging, Figure 4.13 shows the en face 2D NIR fluorescence image and the corresponding cross-sectional co-registered OCT and NIR fluorescence images with abnormal morphology. From these 2D fluorescence images, polyps can be identified clearly, but the polyp types (raised or flat) cannot be determined due to the lack of depth information. The white arrows in Figure 4.13 (g) indicate lesions, and each corresponds to a cross-sectional OCT image for better visualization of the abnormality. Figure 4.13 (a), (c), (d),

and (e) show the polyps in varying sizes. In Figure 4.13 (c), a region of low intensity with a disrupted layer structure can be observed, indicative of adenoma/adenocarcinoma. In Figure 4.13 (f), layer detachment can be found as indicated by the yellow arrows. In the NIR fluorescence image, the density of vasculature is much higher in abnormal regions (i.e., adenoma and hyperplastic polyps) and thus can help identify lesions and abnormalities quickly as the first step. In contrast, a healthy layered architecture is accompanied by a more homogenous NIR fluorescence signal in [Figure 4.13 (b)].

Figure 4.14 shows the 3D OCT, NIR fluorescence and combined images of the colorectal wall. 3D reconstruction of OCT provides information on the shape of the lumen, and the fluorescence data is transformed and morphed into a 3D rendering according to the lumen shape. The fluorescence images shown in 3D allow visualization and identification of polyp types (flat polyp or raised polyp). In Figure 4.14, several polyps indicated by white arrows can be clearly identified from both 3D OCT and NIR images. With respect to the small polyps and flat polyps indicated by green arrows which are often missed by conventional colonoscopy, they can also be visualized by 3D NIR fluorescence images. Although 3D OCT images show limited capability of finding small and flat polyps, they can be clearly imaged by cross-sectional OCT images as shown in Figure 4.12 and Figure 4.13.

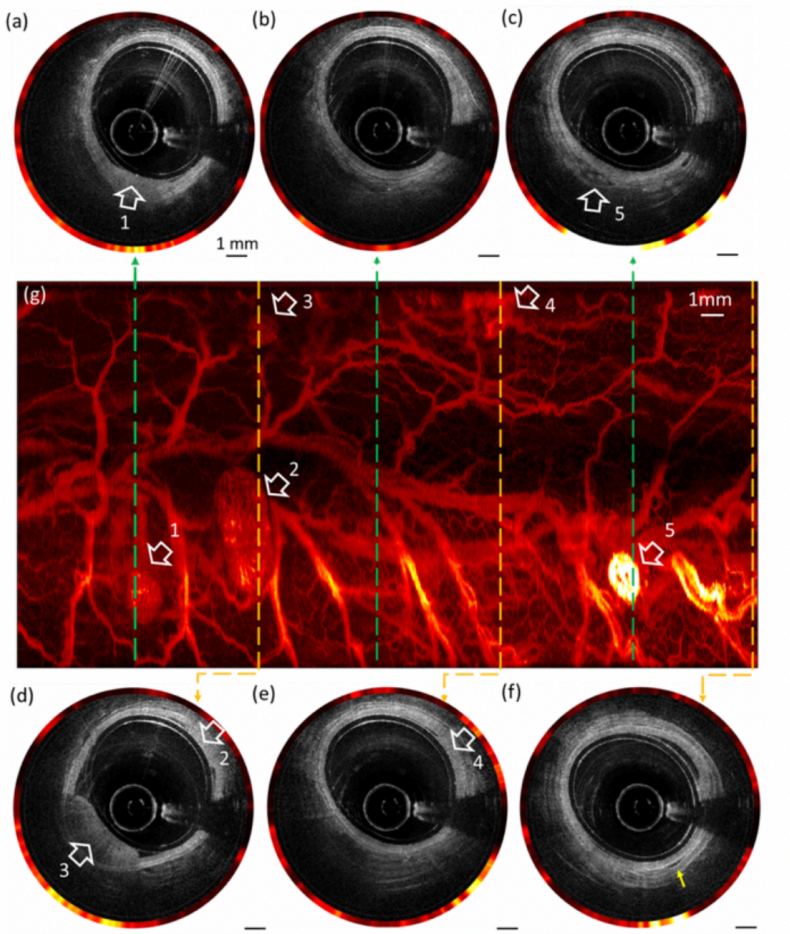

Figure 4.13 Combined OCT and NIR fluorescence images of the colorectal wall. (a)-(f) Combined OCT and NIR fluorescence images at different longitudinal positions. (g) *En face* NIR fluorescence images. Scale bar: 1mm.

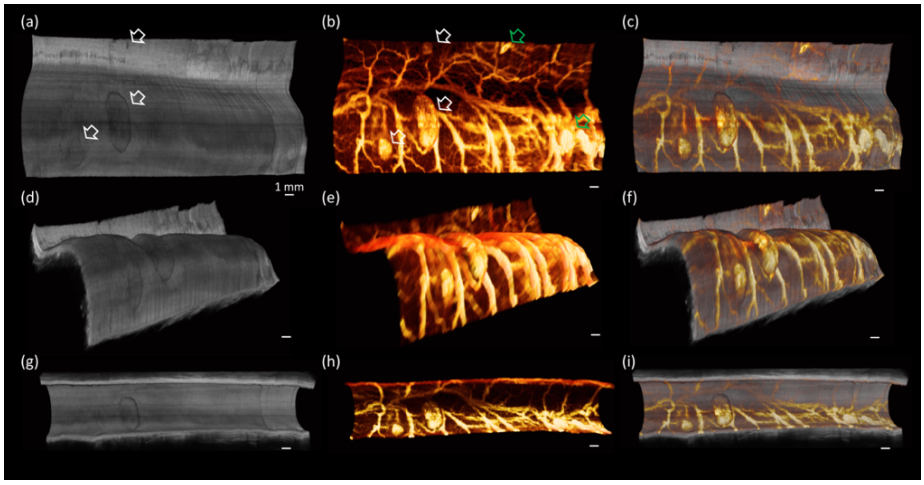

Figure 4.14 3D OCT and NIR fluorescence images. (a)-(f) *En face* 3D images of colorectal wall with different views (field of view: 0°-360°). (g)-(h) Volumetric 3D images of colorectal wall (field of view: 0°-250°). Scale bar: 1mm.

Histology of the sample was obtained and compared with the images obtained from the dual modality system for histological confirmation. All histology photos were read by a histopathologist. Cases of a healthy rectum, a hyperplastic polyp, an adenoma, and adenocarcinoma are representatively presented as follows.

Healthy rectum: As demonstrated in Figure 4.15, the OCT image shows well-defined layer structures and allows the differentiation of mucosa, submucosa, and muscularis propria [Figure 4.15 (b)] which is confirmed by histology [Figure 4.15 (c)]. In Figure 4.15 (a), the intensity of the NIR fluorescence signals is shown at the circumference of the OCT image, and the discrete brightness corresponds to the presence of the blood vessels.

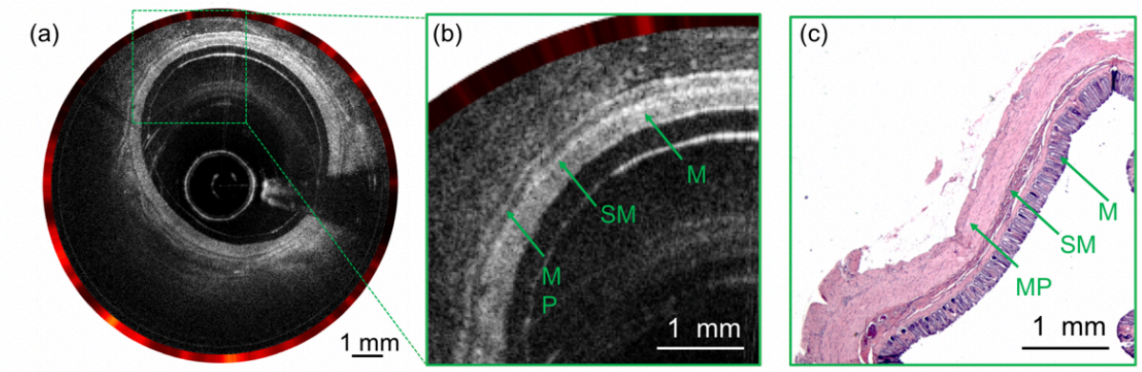

Figure 4.15 Normal rectum. (a) Combined OCT and NIR fluorescence image. (b) Enlarged view of the dashed box in (a). (c) Histology. M: mucosa; SM: submucosa; MP: muscularis propria.

Hyperplastic polyp: Figure 4.16 shows the results from a hyperplastic polyp. In the OCT image, the thickening in the mucosal layer can be observed, accompanied by a slight increase in the NIR fluorescence data. This thickened mucosa exhibits similar intensity with the adjacent healthy tissue, suggestive of a hyperplastic polyp (HP). Corresponding histology supportive of finding a hyperplastic polyp with the dual modality data is shown in Figure 4.16.

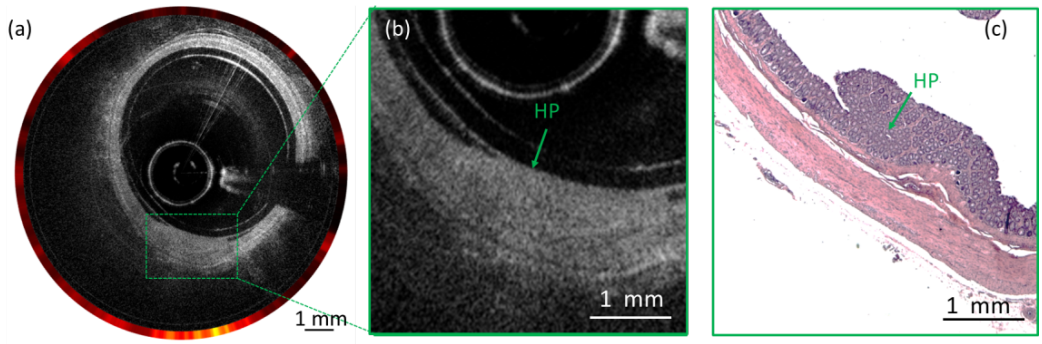

Figure 4.16 Hyperplastic polyp. (a) The combined OCT and NIR fluorescence image. (b) Enlarged view of the dashed box in (a). (c) Histology. HP: hyperplastic polyp.

Adenomatous polyp: In comparison to the hyperplastic polyp, adenoma exhibits further thickening in the mucosal layer [Figure 4.17 (b)]. In addition, due to the increased thickening, lower intensity in the deeper tissue layers with respect to the neighboring healthy tissue is also observed. In addition, in that area, several black pools can be found which correspond to the presence of mucus because sometimes tumor cells are able to secrete mucus, and mucus is optically transparent. The NIR fluorescence signal is also further increased [Figure 4.17 (a)]. The corresponding histological evidence is shown in Figure 4.17 (c) in which the tubular structure can be clearly visualized.

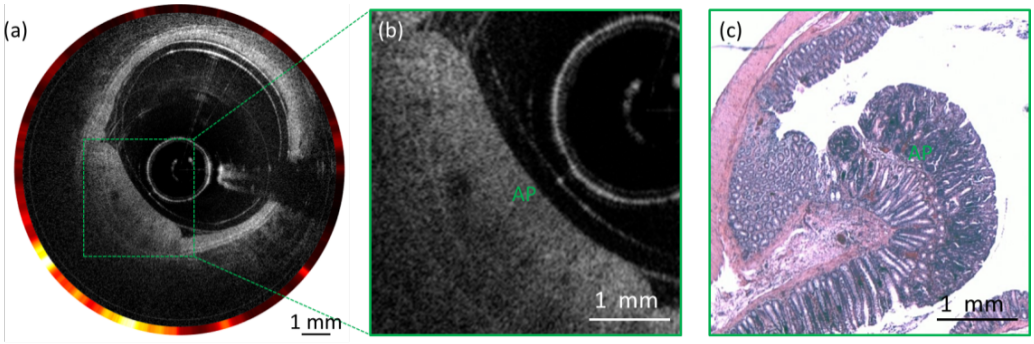

Figure 4.17 Adenomatous polyp. (a) The combined OCT and NIR fluorescence image. (b) Enlarged view of the dashed box in (a). (c) Histology. AP: adenomatous polyp.

Adenocarcinoma: Figure 4.18 shows a combined OCT and NIR fluorescence image of a rectum with adenocarcinoma. The OCT image shows the thickening mucosal layer and uneven dark areas which are caused by high signal absorption in the necrotic tissue. Furthermore, the corresponding NIR fluorescence images show increased intensity. From the histology, a darker area, thickened mucosa, and large numbers of cancer cells can be identified that match the images well.

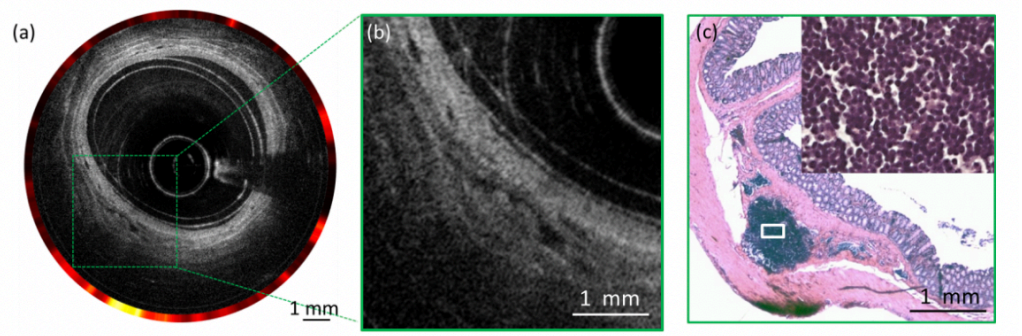

Figure 4.18 Adenocarcinoma. (a) The combined OCT and NIR fluorescence image. (b) Enlarged view of the dashed box in (a). (c) Histology.

4.3.3 Conclusion

While OCT and NIR fluorescence imaging each can individually provide clinical valuable information to supplement conventional white-light colonoscopy, combining these two imaging modalities further enhances the practicality of this dual-modality system. Colonoscopy allows viewing of the colorectal surface morphology and is intuitive for the surgeon, but because of lower sensitivity and specificity, it cannot access information from subsurface tissue layers. With the multimodal imaging system, NIR fluorescence imaging can be used to identify the suspect lesions rapidly, and OCT endoscopy helps visualize the microanatomy of the subsurface layer structures with microscopic detail for further diagnosis, allowing better staging and diagnosis of GI tract disorders.

With histological confirmation, our results demonstrated the capability of the multimodal imaging system to identify and differentiate healthy tissue, hyperplastic polyps, adenomatous polyps, and adenocarcinoma. In NIR fluorescence images, the contrast is from the vascular network. The vascular density gradually increases, and vascular morphology becomes more tortuous with disease progression. In OCT images, tissue layered architecture alters as the disease progresses. We observed that different types of polyps exhibit unique patterns which can be used for differentiating polyps. In a healthy colorectal wall, well-defined layers can be visualized. The intensity of each layer is uniform, and boundaries are well-demarcated. In hyperplastic polyps, mucosal thickening is observed, and the OCT signal intensity of the thickened mucosa is similar to the neighboring healthy tissue. In adenomatous polyps, mucosal thickening is also visualized, but the OCT signal intensity is reduced in contrast with the surrounding normal tissue due to lowered light scattering. For adenocarcinoma, boundaries are blurred and intensity of OCT images are non-uniform (e.g., the uneven dark areas in Figure 4.18).

The endoscopic multimodal imaging is minimally invasive and can be performed in real time. With its small size (probe outer diameter < 3 mm), the multimodal imaging probe can access the colon through the accessory channel of a commercial endoscope. This approach can be easily integrated into clinical practice as surgeons can still rely on intuitive colonoscopy guidance but also gain additional subsurface information provided by the multimodal imaging system. Such integration can help differentiate polyps observed by colonoscopy to provide a better diagnostic yield.

Future studies will focus on determining sensitivity and specificity of the proposed multimodal imaging system with respect to colorectal cancer. A larger sample size will be proposed for quantitative analysis. Additionally, it is also possible to utilize autofluorescence

rather than NIR fluorescence, which can eliminate the need of a contrast agent, further reducing the invasiveness of our multimodal approach.

Chapter 5 – Microscopic OCE

5.1 Simultaneous Quantifying Elasticity of Anterior Eye

The crystalline lens and cornea comprise the eye's optical system for focusing light in human vision. The changes in biomechanical properties of the lens and cornea are closely associated with common diseases, including presbyopia and cataract. Mapping and characterizing *in vivo* mechanical properties of cornea using OCE have been reported by several groups [90, 92, 94, 299-303]. Our group has recently demonstrated the feasibility of *in vivo* imaging of retina and choroid mechanical properties using an OCE system with acoustic radiation force excitation (ARF-OCE) [14, 15, 106, 187]. Although the lens elasticity has been investigated *ex vivo*, *in vivo* imaging and quantification of lens mechanical properties remain challenging [186, 304, 305]. Furthermore, the cornea and the lens collectively are an optical system, and simultaneous measurements of cornea and lens mechanical properties will yield clinical endpoints for studying tissue biomechanics in health, disease and treatment.

To better understand the anterior segment of the eye, we developed an optical coherence elastography system utilizing acoustic radiation force excitation to simultaneously assess the elasticities of the crystalline lens and the cornea *in vivo*. A swept light source was integrated into the system to provide an enhanced imaging range that covers both the lens and the cornea. Additionally, the oblique imaging approach combined with orthogonal excitation also improved the image quality. We first demonstrated the feasibility of ARF-OCE for lens elasticity measurement by comparing *ex vivo* healthy rabbit whole-globes to those with cold cataract. Simultaneous *in vivo* measurements were then performed on both lens and cornea in a rabbit

model. Lastly, we investigated the *in vivo* elasticity changes in the lens with respect to intraocular pressure (IOP) and age.

5.1.1 Methods

(1) ARF-OCE System Setup

A customized phase-sensitive swept-source OCT system was constructed to image the elastic waves of the anterior eye. The laser has a repetition rate of 100 kHz and a center wavelength of 1310 nm. A 90:10 optical fiber coupler splits the output light into the sample and the reference arms, respectively. In the sample arm, the illuminating light propagates to the sample through a circulator, collimator, and objective scan lens. A dual-axis Galvo system is incorporated to enable volumetric scanning. In the reference arm, the light propagates through a circulator, collimator, and mirror. The back-reflection and back-scattering light from the reference and the sample arms are collected through the exiting ports of the corresponding circulators into a 50:50 coupler to generate the interference signals, which are then detected by a balanced photodetector. The signal from the detector is digitized using a waveform digitizer (Alazar Technologies Inc, QC, Canada) and stored in a computer for data processing.

To provide the excitation force, a custom-built 4.5 MHz ultrasound transducer with a focal length of 35 mm is incorporated. The transducer is placed approximately orthogonally to the OCT scan lens. The trigger signal from the swept-source laser is utilized to synchronize a function generator to generate a 4.5 MHz sine wave with an amplitude of 800 mV and a duration of 200 μs. The generated wave is amplified by approximately 42 dB and then applied to the focused ultrasound transducer for tissue excitation. The ARF-OCE setup is shown in Figure 5.1(a).

For the *in vivo* experiment, the rabbit eye is proptosed within a rubber drape that serves as a container to immerse the eye in sterile phosphate-buffered saline (PBS), shown in Figure 5.1(b). In consideration of the strong optical absorption of water at 1310 nm, the OCT detection beam is rotated by 10° to minimize the required PBS level as well as to avoid a strong reflection from air-liquid interface, shown in Figure 5.1(b).

The schematic of the custom-built IOP control system is depicted in Figure 5.1(c). A sterile saline reservoir is connected to the eye through a 22-gauge needle, and a pressure sensor is integrated to monitor the IOP. Different IOPs of the eye globe can be achieved by adjusting the height of the saline reservoir while monitoring the pressure transducer output.

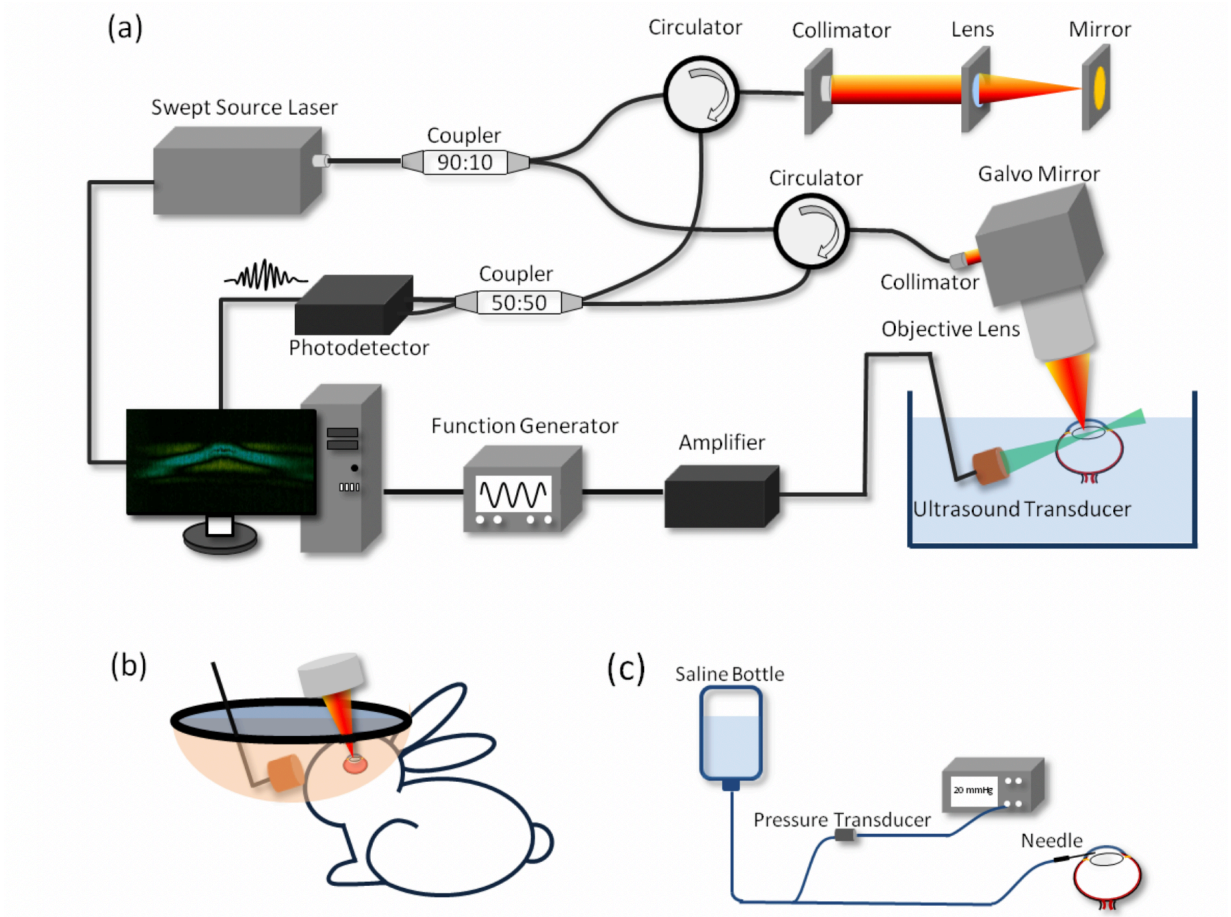

Figure 5.1 Schematics of (a) the ARF-OCE system, (b) the *in vivo* experiment setup, and (c) the custom-built IOP control system.

(2) System Synchronization

To visualize elastic waves propagation in ocular tissue, an M-B scan protocol is utilized to acquire data. At each position, 500 A-lines are acquired to record the phase change over time (M-mode acquisition). The ultrasound transducer generates the excitation force between the 101st and the 120th A-line scans. After one M-mode data acquisition, the galvanometer scanner moves the detection beam to the next position, and the same M-mode scan is repeated. The scanning protocol is summarized in Figure 5.2. The λ trigger signal from the laser is used to synchronize the laser sweeps, data acquisition, ARF excitation, and galvanometers. Using the λ trigger instead of the normal swept trigger provides precise synchronization with the phase of the laser, which is critical for Doppler imaging.

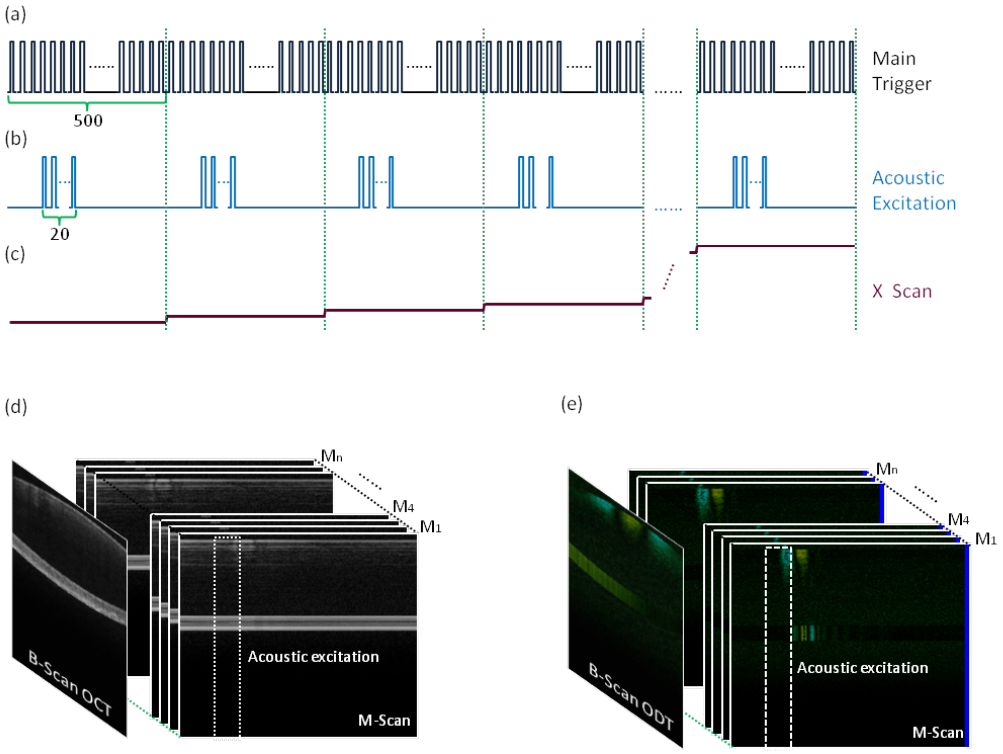

Figure 5.2 Scanning scheme of OCE system. (a) Trigger signals from laser for synchronization of data acquisition; 500 A-lines consist of one image. (b) Trigger signals for synchronizing the

ARF excitation. (c) Signals for the x-axis galvanometer scanner to employ M-B mode scan. (d) OCT image with M-B mode scan protocol. (e) OCE images with M-B mode scan protocol.

(3) Mechanical Characterization

With M-mode OCT images, a temporal phase profile at the lens can be obtained using Equation (5.1) [306, 307]:

$$\Delta\varphi = tan^{-1}\left[\frac{Im(F_m \times F_{m+1}^*)}{Re(F_m \times F_{m+1}^*)}\right] \quad (5.1)$$

where Im() and Re() are the imaginary and real parts of the OCT complex signal, respectively, F_m is the complex signal captured at a given position (i.e., M-mode), F_{m+1} is F_m at the next time point, and F^* is the complex conjugate of F. Then, the temporal phase change, $\Delta\varphi$, can be converted to temporal displacement change, Δd, by Equation (5.2):

$$\Delta d = \frac{\lambda_0}{4\pi n}\Delta\varphi \quad (5.2)$$

where λ_0 is the center wavelength of the laser source, and n is the refractive index. With M-B mode OCT images, Δd as a function of time on the lens can be visualized, and the elastic wave velocity V can be determined by finding the slope of $\Delta d(t, s)$.

When the excitation focus is near or on the sample surface, the detected elastic wave in the lens can be considered as a Rayleigh wave. For a homogeneous isotropic sample, the Young's modulus E can be calculated based on the Rayleigh wave velocity V_R using Equation (5.3) [308]:

$$E = \frac{2\rho \times (1+\nu)^3}{(0.87+1.12\nu)^2} \times {V_R}^2 \quad (5.3)$$

where the Poisson's ratio ν is 0.5, the lens density ρ is 1183 kg/m^3, and V_R is the detected wave velocity [309, 310].

The elastic wave propagation in the cornea is partly guided by the top and the bottom boundaries of the cornea with consecutive reflections, known as the Lamb wave. In a vacuum, Lamb wave velocity can be calculated using Equation (5.4) [311]:

$$V_{L\_vacuum} = \sqrt{\frac{2\pi \times f \times h \times V_s}{\sqrt{3}}} \tag{5.4}$$

where f *is* the frequency of the Lamb wave, h is the cornea thickness, and V_s is the shear wave velocity. Since the cornea is submerged by liquid, the corresponding Lamp wave velocity can be corrected by multiplying a factor of $1/\sqrt{2}$ due to a total leakage of compressional wave and total reflection of shear wave at both boundaries[($V_L = V_{L\_vacuum}/\sqrt{2}$). Given that $E = 3\rho \times V_s^2$, the corresponding Young's modulus can be calculated based on the Lamb wave velocity using Equation (5.5).

$$E = \frac{9\rho \times V_L^4}{(\pi \times f \times h)^2} \tag{5.5}$$

where the corneal density is 1062 kg/m^3 and V_L is the detected wave velocity [312].

(4) *Ex vivo* rabbit experiment preparation

A whole eye globe from a healthy rabbit was obtained within 3 hours of euthanasia. One one percent agar was molded around the globe to secure it for imaging. The mounted globe and the ultrasound transducer were submerged in PBS during imaging. After imaging the normal globe, the globe was immersed in iced saline for 15 minutes to induce a cold cataract for diseased model imaging.

(5) *In vivo* rabbit experiment preparation

For the induction of general anesthesia, the rabbit (male, New Zealand white rabbit) was administrated a ketamine-xylazine mixture (35 mg/kg and 5 mg/kg, respectively) for initial

anesthesia. Two drops of proparacaine HCI were applied topically for further local anesthesia. After conforming the proper depth of anesthesia, the rabbit was placed on a stage for position adjustment. Its eye was then carefully proptosed, and a latex drape with an aperture was put through the globe to serve as a container. In the latex drape container, sterile PBS was filled to submerge the eye and the ultrasound transducer. Additional ketamine (17.5 mg/kg) was administered via subcutaneous injection as needed. The IOP control system was used to regulate the IOP of the globe. After imaging, the rabbit was euthanized via intravenous pentobarbital overdose. Five rabbits were imaged in total. All procedures were reviewed and approved by the Institutional Animal Care and Use Committee at the University of California, Irvine, under protocol #2016-3199.

5.1.2 Imaging Results

An experiment based on a cold cataract model was performed *ex vivo* to test the proposed ARF-OCE system. Figure 5.3 (a) shows the time-lapse OCT B-scan images of a rabbit crystalline lens. At 0.1 ms, fringe washout caused by acoustic radiation can be observed in the center of the OCT images, in which an elastic wave was induced. To visualize the wave propagation, the Doppler OCT images were obtained using Equations (5.1) and (5.2) to display the localized axial displacement [Figure 5.3 (b)]. At 0.1 ms of Figure 5.3 (b), a significant displacement was observed at the center of the lens, where the focus of the ultrasound transducer was applied. Over time, the wave propagating bilaterally outwards was observed [Figure 5.3 (b)]. After the initial imaging, the lens was immersed in ice water to induce cataract. The corresponding Doppler OCT images are shown in Figure 5.3 (c). In order to quantify the Young's modulus change, quantitative analysis was performed to visualize spatiotemporal Doppler OCT images of the lens at a selected depth [Figure 5.3 (d) and (e)], indicated by the yellow dashed line in Figure 5.3 (a). The elastic

wave velocities were determined by calculating the ratio of travel distance to travel time, which were 2.65 m/s and 2.79 m/s in normal and cold cataract lens, respectively. The corresponding Young's moduli were calculated to be 27.4 kPa and 30.4 kPa, respectively, using Equation (5.3). These results demonstrate the increased Young's modulus of the lens in the cold cataract model, which was supported by a previous study [186].

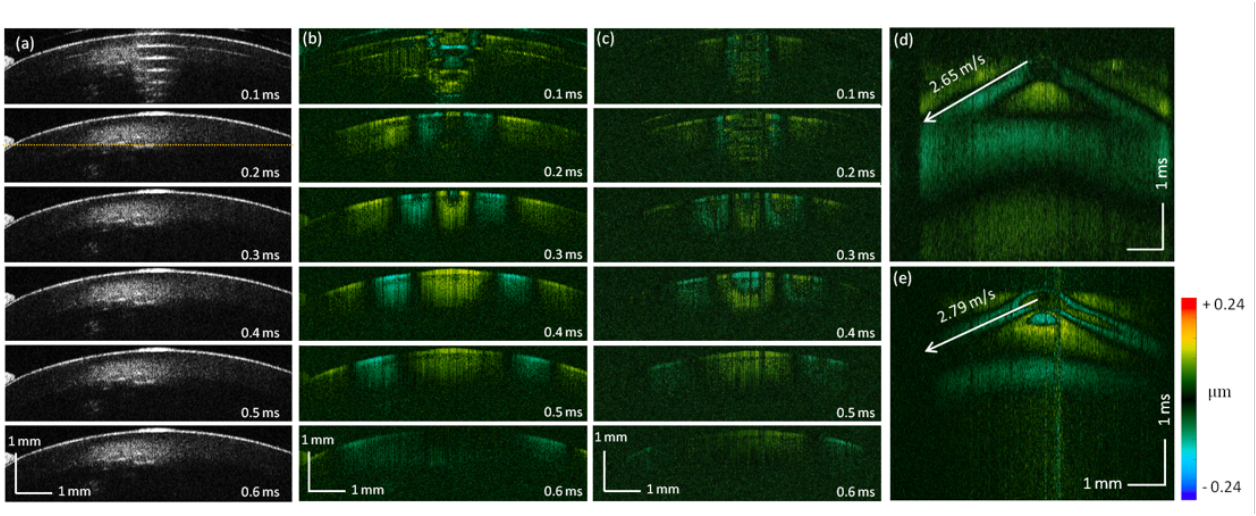

Figure 5.3 *Ex vivo* cold cataract lens results. (a) Time-lapse OCT B-scan images of a normal lens. (b) Time-lapse Doppler OCT B-scans of a normal lens. (c) Time-lapse Doppler OCT B-scans of a cold cataract lens. (d) and (e) Spatiotemporal Doppler OCT of normal and cataract lens at a depth indicated by yellow dashed line in (a).

To study the elasticities of the lens and the cornea as a complete optical system, we performed an *in vivo* experiment to simultaneously measure the elastic waves of the lens and cornea in a rabbit model (~5 kg, n = 2). The ARF-OCE system has a sufficient imaging penetration depth to visualize both the cornea and the lens [Figure 5.4 (a)]. Figure 5.4 (b)-(d) demonstrate the propagations of the elastic waves in the cornea and the lens at different time points after a single ARF excitation. Figure 5.4 (e) and (f) show the corresponding spatiotemporal images at two selected depths, indicated by yellow dashed lines shown in Figure 5.4 (a). The elastic wave velocity in cornea was measured to be 15.20 m/s in the proptosed eye, which was faster than the

previously reported velocities of the *ex vivo* cornea [313, 314]. The elastic wave velocity in the lens was 3.01 m/s, which was similar to the velocity obtained from our *ex vivo* rabbit experiment.

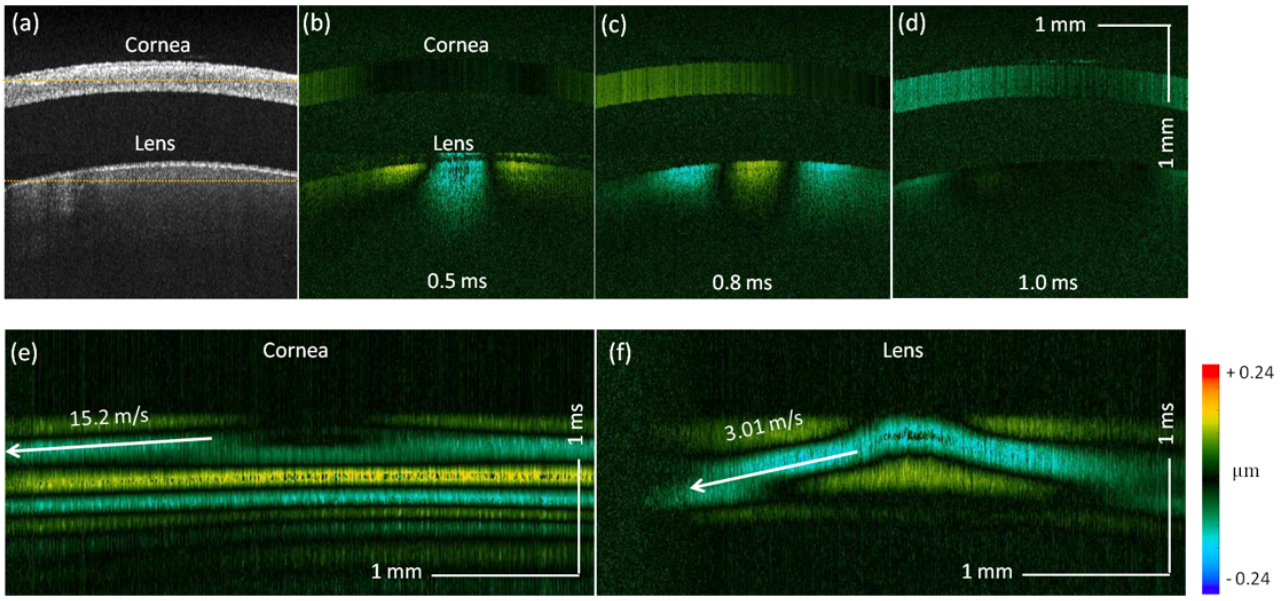

Figure 5.4 Simultaneous measurements of the lens and cornea in an *in vivo* rabbit model. (a) OCT B-scan images of the lens and the cornea. (b-d) Doppler OCT B-scans of lens and cornea at 0.1 ms, 0.4 ms, and 0.7 ms after ARF excitation, respectively. (e-f) Spatiotemporal Doppler OCT of the cornea and lens, respectively, at the depth indicated by yellow dashed lines in (a).

Age-related loss of lens elasticity (i.e., presbyopia) is a common condition resulting in the decreased ability of the eye to focus on nearby objects. To further validate the ARF-OCE system, we performed *in vivo* elastography on 2-kg (~8 weeks, n = 1), 2.5-kg (~12 weeks, n = 1), and 5-kg (~52 weeks, n = 1) male rabbits to evaluate the changes in lens elasticity with respect to aging. The spatiotemporal Doppler images of the three ages are shown in Figure 5.5 (a)-(c). The youngest rabbit exhibited the slowest wave velocity whereas the oldest one had the fastest. The measurements of the elastic wave velocity and Young's modulus were repeated 5 times, and the means and standard deviations are shown in Figure 5.5 (d) and (e). A significant increase in lens stiffness with aging was observed, which is consistent with the reported studies [100, 315].

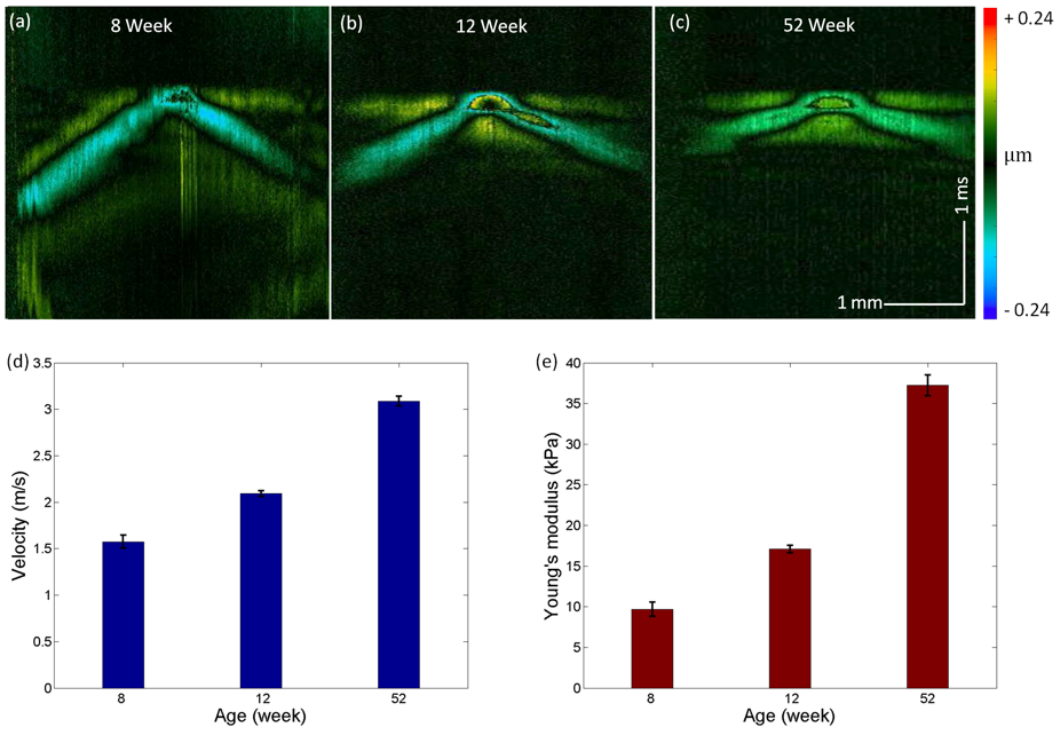

Figure 5.5 Results of the *in vivo* presbyopia rabbit experiment. (a-c) Spatiotemporal Doppler OCT of the lenses of 8-week, 12-week, and 52-week rabbits, respectively. (d-e) Elastic wave velocities and Young's moduli, respectively, of the corresponding ages.

The positive correlation between corneal elasticity and IOP has been previously reported; here, we further investigated the change in lens elasticity with increasing IOP. A custom-built IOP monitoring and control system was integrated into the rabbit experiment, and ARF-OCE was performed at different IOPs. Figure 5.6 (a) and (b) show the spatiotemporal cornea and lens Doppler images of the 12-week rabbit (n=2) with different IOPs, respectively. Five measurements were taken from each rabbit, and the means and standard deviations were reported. Figure 5.6 (c) and (d) demonstrate the increased wave velocity and Young's modulus of the cornea with increasing IOPs. For the lens [Figure 5.6 (c) and (e)], although a minimal increase in the velocity and Young's modulus is noted, the correlation between Young's modulus and IOP is much weaker than in the cornea.

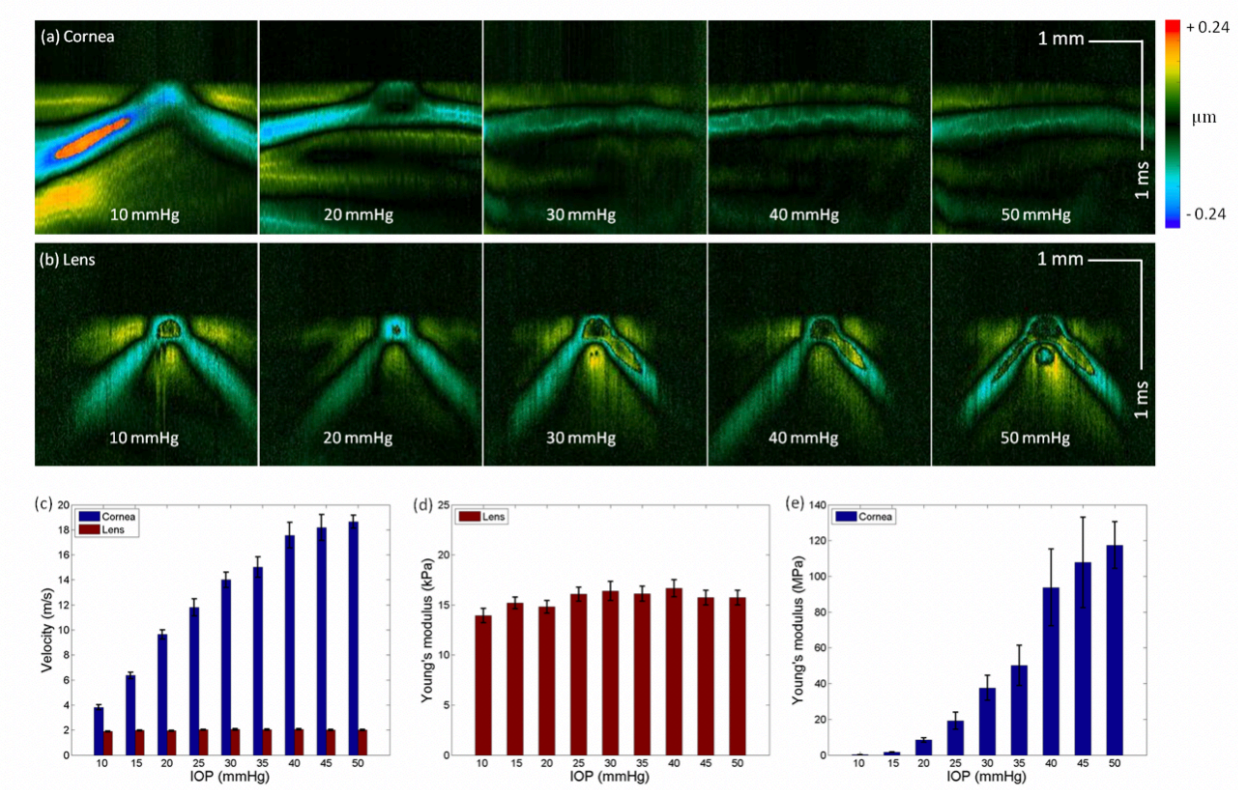

Figure 5.6 In vivo IOP experiments using a 12-week rabbit. (a-b) Spatiotemporal Doppler OCT of the cornea and lens, respectively, at different IOPs. (c) Elastic wave velocities in the cornea and lens. (d) Young's modulus of cornea as a function of IOP. (e) Young's modulus of lens as a function of IOP.

The lens is an inhomogeneous solid tissue with location-dependent stiffness. Three-dimensional (3D) visualization of elastic wave propagation will allow for accurate characterization of the lens biomechanical capacity and heterogeneity. Figure 5.7 shows representative time-lapse 3D Doppler images. ARF excitation was employed at 0.15 ms, indicated by fringe washout at the center of the field of view. The outward propagation of the spherical wave traveling at an average speed of 3 m/s was observed.

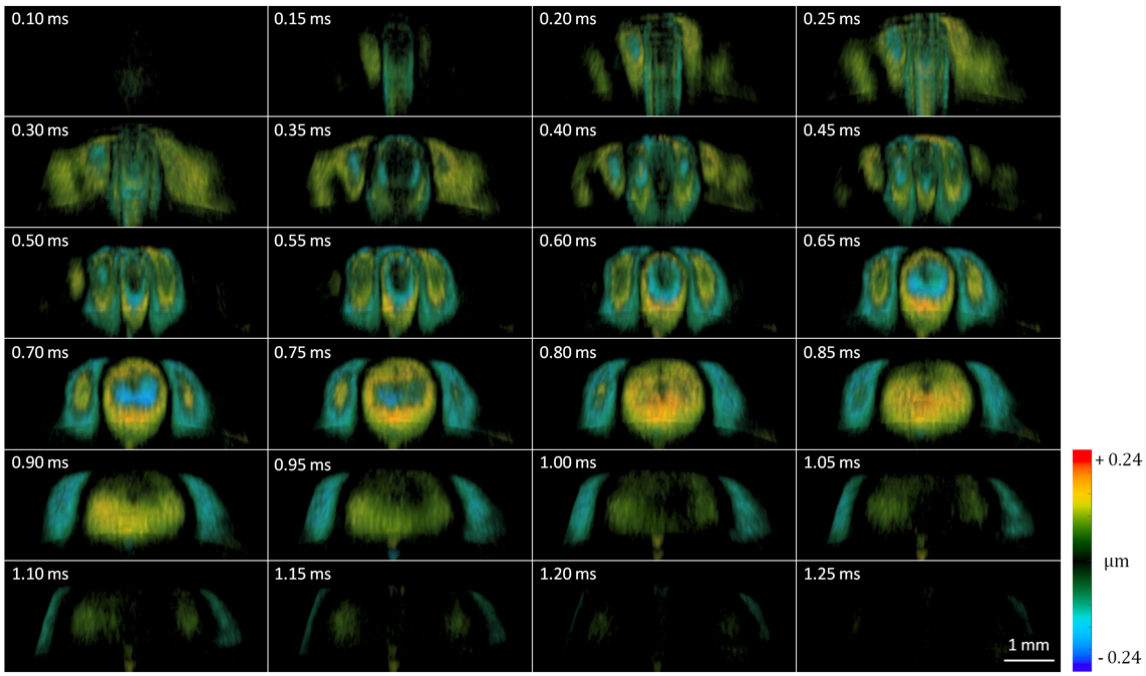

Figure 5.7 Time-lapse 3D Doppler OCT of the 12-week-old rabbit lens.

5.1.3 Conclusion

The crystalline lens and the cornea as a complete optical system are the crucial elements in human vision. Understanding the biomechanical capacity that facilitates the eye accommodation process to focus near and far objects will advance not only our knowledge in vision science but also in developing better clinical management for relevant ocular diseases. Previous *in vivo* studies of anterior eye elasticity focused on the easily accessible cornea, but *in vivo* lens elasticity studies remain challenging. Our ARF-OCE system, which incorporated a swept-source light with oblique illumination, provides improved performance and thus enables real-time simultaneous *in vivo* measurements of the lenticular and corneal Young's moduli.

We first tested the ARF-OCE system through an *ex vivo* cold cataract model in which the increase in lens elasticity was detected. Through an *in vivo* rabbit model, we demonstrated the system capability to simultaneously quantify lens and cornea elasticity, and lastly, the

dependencies of age and IOP with respect to lens elasticity were investigated. We confirmed the age-related lens hardening which was consistent with previous work [315]. We also identified an overall positive trend of lens elasticity in the IOP experiment, but the influence on lens elasticity from changes in IOP was insignificant compared with the cornea. Lens experiencing weak deformation with increasing IOP compared to other ocular tissue, such as cornea and sclera, has been previously observed [304].

While the proposed ARF-OCE system is a promising *in vivo* imaging method for quantifying anterior eye elasticity, a few challenges still need be addressed in order to successfully translate this technology for clinical applications. First, a faster imaging speed is necessary to minimize artifacts induced by bulk motion of the body, especially for animal models whose respiratory and heart rates are much higher than humans. Additionally, high-speed imaging will enable 3D volumetric imaging of the anterior eye with a single-shot ARF excitation, which will reduce the procedure time and hence minimize the light and ARF exposures. Recently, Fourier domain mode locking (FDML) lasers providing laser repetition rates in the MHz range have been commercialized and can be utilized to improve the imaging speed. Additionally, the current imaging protocol for the rabbit model in our experiment utilizes orthogonal ARF excitation that requires proptosis of the eye, which increases the IOP up to 50 mmHg and affects the OCE results. Ideally, a normal IOP (ranging from 12-22 mm Hg) should be maintained during elastography measurement. Although this can be achieved by our IOP controller system, it increases the procedure invasiveness and risks and is clinically impractical. An alternative method is a fluid bath, which is clinically used in anterior segment ultrasound to couple the transducer; this may eliminate the required eye proptosis and better facilitate clinical translation. Furthermore, the mechanical index (MI) of the applied ARF in our study is approximately 1.5, which is much higher

than the FDA ophthalmic MI standard of 0.23 [316]. In our experiment, the displacement induced by the ARF is hundreds of nanometers while the phase sensitivity of our system is less than 1 nm. Therefore, decreasing the excitation force by 10-fold is feasible to achieve safety MI. Our future study will focus on determining the minimal excitation force while maintaining adequate mechanical properties. Lastly, elasticity quantification in 3D is essential for the heterogeneous tissue. In this study, we have presented the visualization of elastic wave propagation in 3D to demonstrate the feasibility of 3D quantification of elasticity. In the future, more ocular tissues will be tested to provide 3D quantitative elasticity mapping.

In summary, we have reported the first *in vivo* lens elasticity measurement. Additionally, the ARF-OCE system allows for mapping and quantification of the mechanical properties of lens and cornea simultaneously, and our technique was validated in an *in vivo* rabbit model. Ophthalmic anterior segment elastography enabled by the proposed OCE system is able to identify the important biomechanical parameters that have great potential to help advance vision science research and improve clinical management of patients with refractive vision disorders.

5.2 Ultrahigh Sensitive Optical Coherence Elastography

Since OCE relies on measuring phase via Doppler OCT, the phase stability of the imaging system is the key determining factor for its performance [6, 317, 318]. Most OCE systems utilizing acoustic radiation force (ARF) as a tissue excitation method are reported to have the capability of detecting displacements in the range of hundreds of nanometers. Common-path configuration as an optical method addresses the phase instability caused by environmental vibration that leads to a fluctuating optical path difference (OPD) between reference and sample arms. Additionally, the common-path configuration provides intrinsic compensation for polarization mismatch and dispersion mismatch between the sample and reference arms [319-321]. In 2017, Lan *et al.* reported a high phase stability OCE system using common-path spectral-domain OCT (SD-OCT) to achieve a subnanometer displacement sensitivity, demonstrating the feasibility of common-path OCE; however, only a phantom experiment was performed [322]. In addition, SD-OCT is based on a static operation principle that provides phase-stable detection [186, 187, 190, 323-325], but their performance is limited by the groove density of the diffraction grating, the center wavelength of the light source, and the resolution of the line-scan camera: hence, the inherent disadvantages of phase washout, low imaging speed, shallow penetration depth, and short imaging range [326, 327].

In contrast, swept-source optical coherence tomography (SS-OCT) that can be operated with much narrower instantaneous linewidth, longer center wavelength, higher repetition rate, and balanced detection has the capability of providing long imaging range, deep penetration depth, high imaging speed, and reduced fringe wash-out effects. Nevertheless, the phase stability of SS-OCT suffers from the fluctuations in the mechanical movement of the sweeping laser so a proper synchronization between data acquisition and laser sweep is crucial in achieving high phase

stability in a swept-source system [328]. A lambda (λ) trigger using a fiber Bragg grating (FBG) as well as k-clock generated by a Mach-Zehnder interferometer (MZI) has been introduced to improve the phase stability, making SS-OCT a more attractive setup in OCE application [329]. In recent years, several OCE systems based on conventional SS-OCT (SS-OCE_{COV}) have been proposed [189, 207, 210, 330-334], and their feasibilities have been validated through *ex vivo* and *in vivo* experiments, demonstrating great potential towards clinical translation. Although these studies have reported subnanometer displacement sensitivities in their SS-OCE_{COV} systems, the quantification of phase stability is typically obtained through a simple common-path configuration (e.g., adding a glass plate) while measurements of the actual experiments are acquired using a SS-OCE_{COV} setup. Although such a setup has been used to characterize system phase stability, the system performance is degraded when performing measurement because the phase fluctuation between the sample and reference arms is not negligible in conventional OCE. Furthermore, the reported SNR and phase stability is usually from the average of several measurements [335]. Despite current advancement in SS-OCT, achieving a phase sensitivity on the order of subnanometer from the actual experiments using SS-OCE remains challenging.

In our study, we designed and implemented a high phase stable OCE system using a common-path SS-OCT configuration (SS-OCE_{CP}). A 3-mm thick, 30-arcmin wedged glass window was incorporated distal to the scan lens to generate two reference signals, each from one of the surfaces of the window. This allowed for the simultaneous generation of two OCT interference signals in two different frequency domains which can be averaged for an enhanced SNR and reduced speckle. This average method is not achievable in SD-OCT due to the limited imaging range. Furthermore, the common-path configuration minimized the differences between the sample and the reference arm, thereby providing stable phase information for precision

displacement measurement. In addition to the optical method, data acquisition and synchronization were optimized to accurately retrieve the phase information. In this report, we first compared the phase performance of SS-OCE$_{CP}$ and SS-OCE$_{COV}$. Then, a tissue-mimicking phantom model and an *in vivo* rabbit model were imaged to validate the SS-OCE$_{CP}$ performance.

5.2.1 Materials and Methods

(1) **Reference arm design**

To accomplish a common-path OCT, we place a 30-arcmin wedged glass window in the sample arm to act as a reference arm, shown in Figure 5.8. The aim of the 30-arcmin angle on the front surface is to effectively reduce the autocorrelation fringe patterns generated within the window cavity. During the experiment, the differences in the refractive indices and in the corresponding incident angles contribute to the discrepancy in reflectance of the two surfaces, but this can be compensated for by adjusting the position of the wedged window relative to the scan lens because the collected power of the focusing back-reflected light is spatially dependent. Below, the equation, table, and figure describe the achievement of equalized power of two reference arms in detail.

Assuming unpolarized light, the reflectance, R, of an interface can be calculated using the Fresnel equations:

$$R = \left[\frac{n_i \cos(\theta_i) - n_t \cos(\theta_t)}{n_i \cos(\theta_i) + n_t \cos(\theta_t)}\right]^2 \tag{5.6}$$

where n_i is the incident refractive index, n_t is the transmitted refractive index, θ_i is the incident angle, and θ_t is the transmitted angle. The refractive indices and the corresponding reflection coefficients are reported in Table 5.1:

Table 5.1 Reflectance of two interfaces of wedged window

Interface	n_i	n_t	θ_i	θ_t	R
Air-glass	1.0	1.50	0.5°	0.33°	4%
Glass-gel	1.50	1.34	0.33°	0.37°	0.32%

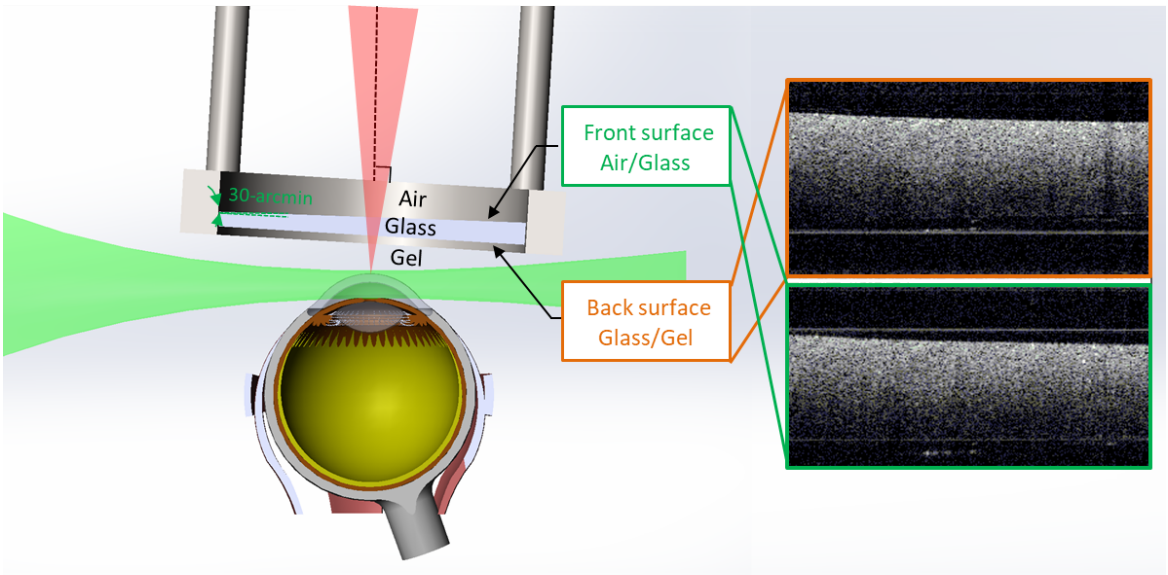

Figure 5.8 Schematics of the SS-OCE$_{CP}$ system.

We note that R of the air-glass interface is approximately 10 times greater than that of the glass-gel interface. In order to equalize the reflective power from the two interfaces, we offset the difference in the collection efficiency of back-reflected power through defocusing. In Figure 5.9, we report the back-reflected power through the scan lens from a flat mirror as a function of distance from the focal point where distance = 0 represents the focal point of the scan lens. To balance the collected back-reflected power from the two interfaces, we placed the wedged window so that its air-glass and glass-gel interfaces were positioned at "A" and "B" of Figure 5.9, respectively. Because the collection efficiency of back-reflected power at A is about 10 times less than that at B, we can expect the signals collected from the two interferences are approximately balanced.

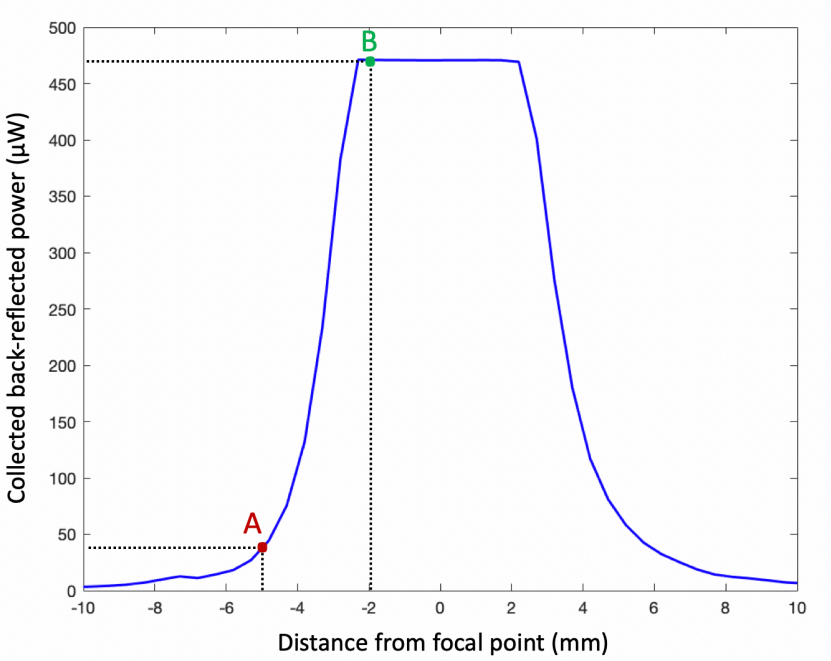

Figure 5.9 Collected back-reflected power vs. distance from focal point

(2) System setup

A SS-OCE$_{CP}$ system was designed and constructed. The swept laser (SL1310V1-10048, Thorlabs, Inc., NJ) has a repetition rate of 100 kHz, a center wavelength of 1310 nm, and a bandwidth of 100 nm. The system has an imaging range of 11 mm which makes the generation of 2 OCT images in different frequency domains possible. The output light from the laser source is split by a 90:10 optical fiber coupler with 90% of the light propagating to the sample through a circulator, collimator, objective scan lens (LSM04, Thorlabs, Inc., NJ), and wedged window, shown in Figure 5.10. The common-path configuration is achieved through the 30-arcmin wedged window. In contrast to a flat window, the 30-arcmin window effectively reduces the autocorrelation fringe patterns generated within the window cavity as well as compensates for the difference in the reflection coefficients of each of the interfaces to equalize the power of the back-reflected light, shown in Figure 5.10. In this setup, two interfaces exist, which consist of the air-

glass front surface and the glass-gel back surface. The indices of refraction of air, glass (the wedged window), and ultrasound gel are 1.0, 1.5, and 1.34, respectively. The back surface of the wedged window is perpendicular to the OCT scanning beam while the front surface is shifted by 30-arcmin from the normal. The differences in the refractive indices and in the corresponding incident angles contribute to the discrepancy in reflectance of the two surfaces, but this can be compensated for by adjusting the position of the wedged window relative to the scan lens because the collected power of the focusing back-reflected light is spatially dependent. As such, two back-reflected reference signals of similar power are interfered with the backscattered sample signal to generate two distinct fringes corresponding to the top and the bottom image, respectively. The two interferences are then delivered to one channel of the balanced photodetector. The wedged window has a thickness of 3 mm which corresponds to a 3.4-mm axial separation of the generated OCT images calculated based on the ultrasound gel reflective index of 1.34. Additionally, the two images can be averaged to enhance the SNR and minimize speckles. The remaining 10% of the light propagates through a compensation arm consisting of a circulator, collimator, adjustable slit and mirror. The back-reflected light from the compensation arm is detected by the second channel of the balanced photodetector to offset the DC component of the generated interference fringes. A balanced photodetector with a bandwidth from 30 kHz up to 1.6 GHz was selected to minimize timing jitters for enhancing phase stability as well as to enable long imaging range for retrieving the two OCT interference fringes from different frequency domains.

For the displacement excitation, a custom-built 4.5-MHz ultrasound transducer with a focal length of 35 mm is placed approximately orthogonal to the scan lens. A function generator is synchronized with the λ trigger signal to generate a 4.5-MHz sine wave (amplitude: 800 mV; duration: 200 μs) that is then amplified by approximately 42 dB to drive the ultrasound transducer

for tissue excitation. The space between the wedged window, the ultrasound, and the sample is filled with ultrasound gel to couple ARF.

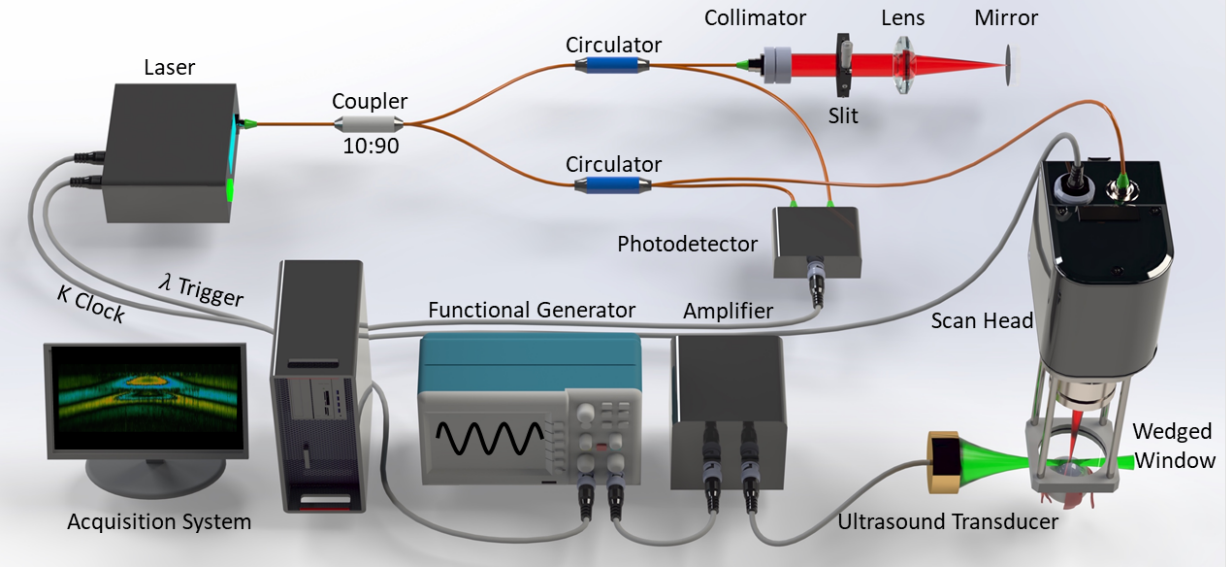

Figure 5.10 Schematics of SS-OCE$_{CP}$ system.

For comparison, the SS-OCECP can be quickly converted to SS-OCECOV during the experiments while maintaining the exact location of the sample and the ultrasound transducer relative to the OCT detection beam (as shown in Figure 5.11). A 50:50 coupler was inserted between the balanced photodetector and Port 3 of circulators in which the back-reflected light from the reference arm and the back-scattered light from the sample arm interfere to generate the signal. Additionally, a small amount of water was added onto the front surface of the window shown in Figure 5.11 (b). Because the scan head was tilted by a small angle, the water surface is oblique with the OCT beam which reduces the reflection from the water and window effectively, hence minimizing the autocorrection. The use of a balanced photodetector can remove the residual autocorrection.

.

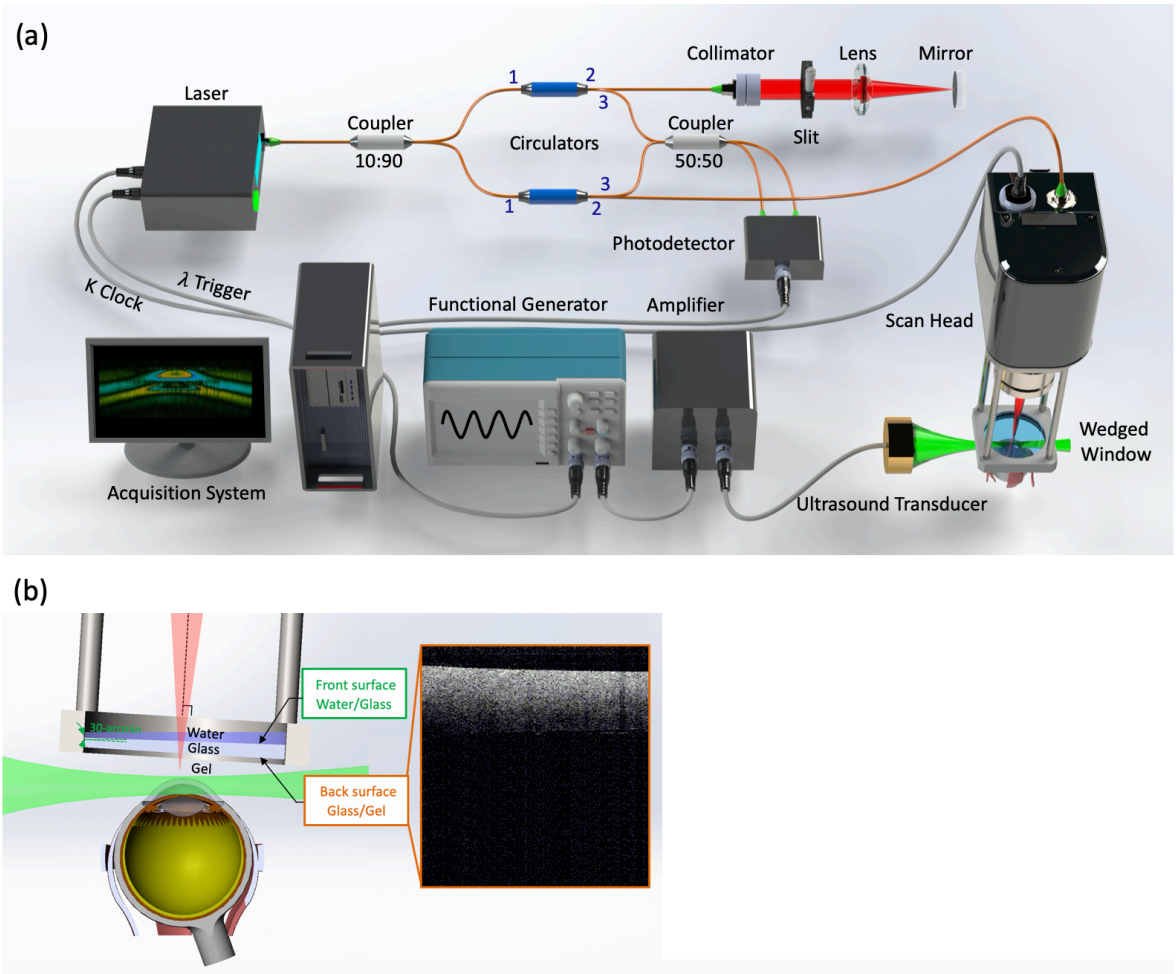

Figure 5.11 Schematics of SS-OCE$_{COV}$ imaging system. (a) System setup. (b) Wedged window.

(3) Data Acquisition, Synchronization, and Signal Processing

Two timing signals produced by the swept source laser were utilized for data acquisition and synchronization. The k-clock signal generated by the internal MZI provides timing of equal wavenumber spacings and the λ trigger signal was produced by the internal FBG to give a temporal mark for each wavelength sweeping. In the conventional SS-OCT or SS-OCE imaging systems, a series of OCT signal points are digitized starting by the edge of the λ trigger while the signal digitization is clocked by the k-clock signal for k-linear signal sampling. However, in this

mode of operation, random timing errors of the signal edges can be magnified to significant timing fluctuations between the k-clock and λ trigger through a process termed edge collision [336]. To achieve best stability, the signal delays were adjusted to be optimal for the k-clock, λ trigger and OCE signals. The previous study on the phase stability with the same type of swept lasers suggested that a very high stability could be obtained using this method [336].

The propagation velocity of the elastic wave provides a direct measurement of the biomechanical property as pre-calibration is not necessary to convert the displacement to elasticity. To visualize elastic waves propagation, an M-B protocol was utilized to induce and detect the displacement. At each lateral position, 500 A-lines were acquired to record the phase change over time (M-mode). The ultrasound transducer was excited after a trigger delay of 1 ms to generate ARF with a duration of 200 μs for each M-mode acquisition. After one M-mode acquisition, the galvanometer scanner moved the detection beam to the next lateral position, and the same step was repeated; 3000 M-mode images were acquired for each dataset to convert to B-mode images. The scanning protocol is summarized in Figure 5.2 in section 5.1. A phase-resolved Doppler algorithm was applied to extract the temporal phase information. With a time interval of 50 μs, inter-A-line analysis was performed to obtain time-lapse Doppler OCT B-scans and spatiotemporal Doppler OCT images. The Young's modulus then can be calculated by determining the propagation velocity using the spatiotemporal Doppler images. As the different boundary conditions yield to different propagation modes of elastic wave, a specific equation was used to calculate the elasticity based on the sample types [159, 191]. In our experiment, Young's modulus, E, was calculated based on Rayleigh wave velocity, V_R, and Lamb wave velocity, V_L, for tissue mimicking phantom and rabbit cornea, respectively. The detailed data processing steps and key equations for elasticity calculation are depicted in Figure 5.12.

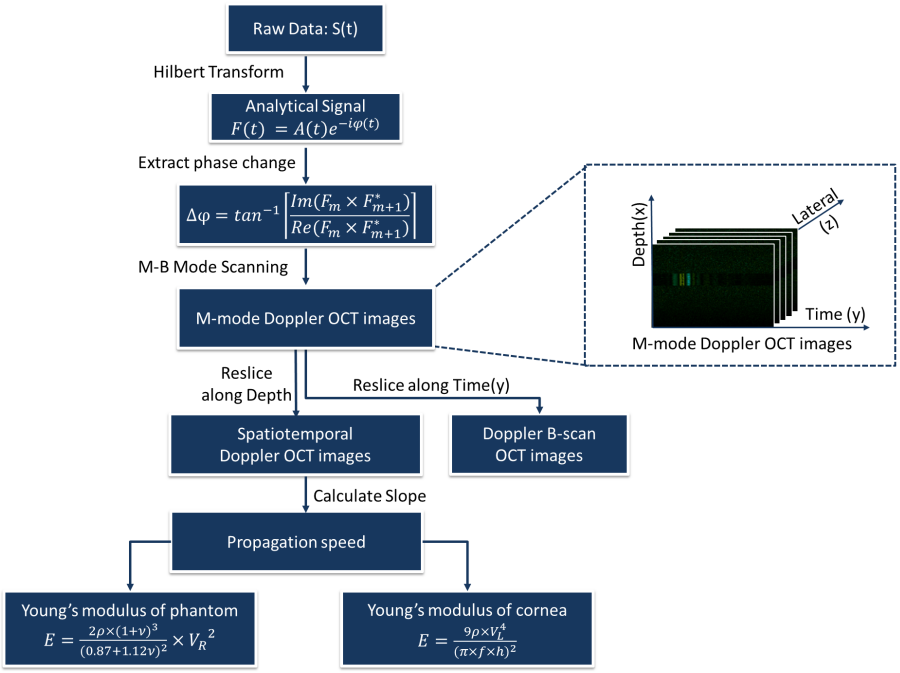

Figure 5.12 Flow chart of signal processing for calculating elasticity

(4) Phantom Preparation

To fabricate the silicone-based phantom that mimics tissue biomechanical properties, 2 g of titanium dioxide was added for every 100 g of silicone rubber base (P4 – Part B, Eager Polymers, Inc., IL) and mixed using an ultrasonic cleaner. Then, 1 part of the silicone rubber base with well-mixed titanium dioxide was added into 16 parts of silicone activator (P4 – Part A, Eager Polymers, Inc., IL). After gently mixing the base with the activator using a stirring rod, the mixture was placed into a vacuum chamber until all air bubbles trapped inside the mixture were removed. The mixture was then poured into a container for molding and let cure for 24 hours. The final phantom had a dimension of 40 mm by 40 mm by 10 mm.

(5) *In vivo* Rabbit Experiment Preparation

To induce the initial anesthesia, the rabbit (New Zealand white rabbit, male, ~3 kg) was administrated a ketamine-xylazine mixture (35 mg/kg and 5 mg/kg, respectively) subcutaneously.

Two drops of 2.5% proparacaine hydrochloride were applied topically for local anesthesia. After conforming the proper depth of anesthesia, the rabbit was placed onto a stage for position adjustment. The rabbit's eye was covered with sterile ultrasound gel to provide conductive medium between the eye and the acoustic wave for the IOP experiment. To obtain a higher IOP, the rabbit eye was carefully proposed, and a sterile latex drape with an aperture was put through the globe to maintain the proptosis. Eye proptosis in rabbits typically increases the IOP to ~50 mmHg. All procedures were reviewed and approved by the Institutional Animal Care and Use Committee at the University of California, Irvine, under protocol #AUP-19-042.

5.2.2 Imaging Results

(1) Phase Stability Quantification

To measure the phase stability of our SS-OCE$_{CP}$ system, a 1.0-mm microscope slide was placed at the focus of the objective lens to generate an autocorrelation interference by the back-reflected light from the front and back surfaces of the slide. In our SS-OCE$_{COV}$ counterpart, a gold mirror was placed at the focus of the objective lens; to generate an OCT interference signal with the same frequency as SS-OCE$_{CP}$, the length of the reference arm was adjusted by 1.40 mm to offset the zero OPD. In both cases, 5000 A-lines were acquired sequentially. Figure 5.13 (a) and (b) show the overlaid interference fringes (n = 5000) from SS-OCE$_{COV}$ and SS-OCE$_{CP}$, respectively. Temporal shifting is much more severe in SS-OCE$_{COV}$, which infers a better timing stability in SS-OCE$_{CP}$. For temporal analysis, the timing information of each zero-crossing was obtained through linear interpolation (blue and red dashed boxes in Figure 5.13 (a) and (b), respectively), and the standard deviation of the timing variation corresponds to the phase stability of the system. For SS-OCE$_{COV}$, the standard deviation was calculated to be 940 ps whereas that of SS-OCE$_{CP}$ was 35 ps. The corresponding histograms are shown in Figure 5.13 (c). In addition, the

phase stabilities of SS-OCE$_{COV}$ and SS-OCE$_{CP}$ were determined by calculating the standard deviation of the phase angle at the peak in the frequency domain which were 175 mrad and 4.2 mrad, respectively, demonstrating a >40-fold phase stability improvement in SS-OCE$_{CP}$ compared to SS-OCE$_{COV}$.

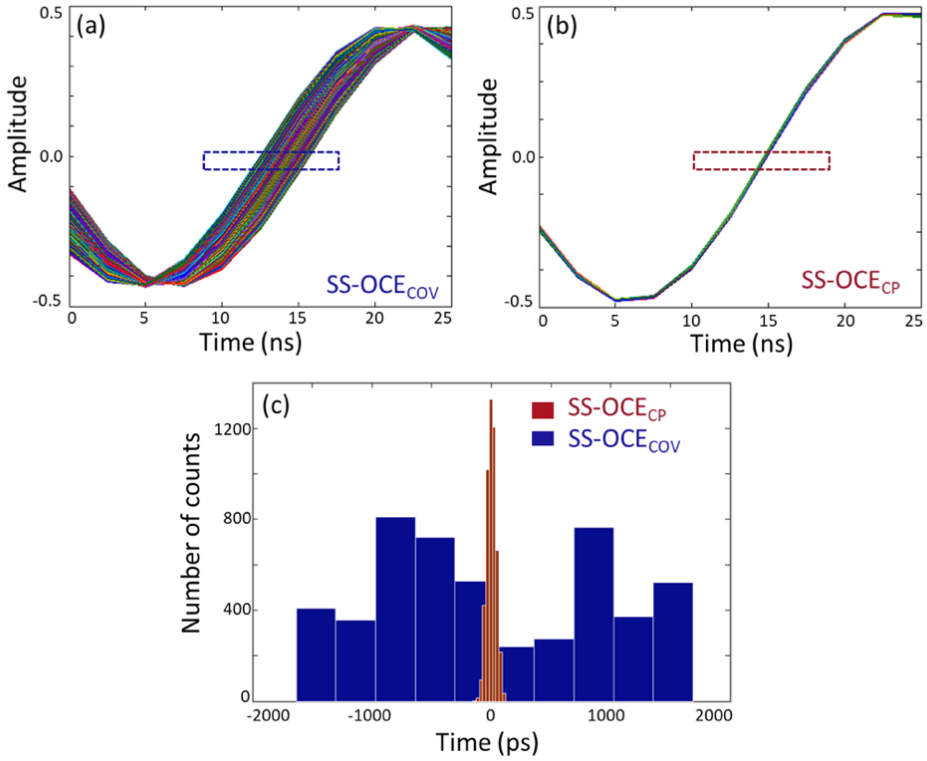

Figure 5.13 Phase stability quantification. Overlaid 5000 interference fringes obtained using (a) SS-OCE$_{COV}$ and (b) SS-OCE$_{CP}$. (c) Timing consistency at zero-crossings.

(2) Enhanced SNR

Since the 3-mm wedged window generates two OCT images in different frequency domains, these two OCT images can be averaged to enhance the SNR, further improving the phase stability. Figure 5.14(a) shows the OCT images of the phantom obtained via SS-OCE$_{CP}$; the top and bottom images are the interference signals generated by the back-reflected light from the back and front window surface, respectively, with the backscattered light from the phantom. The high intensity horizontal line between the two OCT images is the interference signal from the two

surfaces of the window. The two images are separated by ~3.4 mm. By averaging the two images, the SNR was improved from 73 and 71 dB to 76 dB, or approximately a 3-dB improvement [Figure 5.14 (b)]. The enhanced SNR through averaging is also reflected on the Doppler OCT images. Figure 5.14 (c) shows the pair of Doppler images obtained via SS-OCE$_{CP}$, and Figure 5.14 (d) shows the averaged result, demonstrating the reduced noise floor and hence improved SNR.

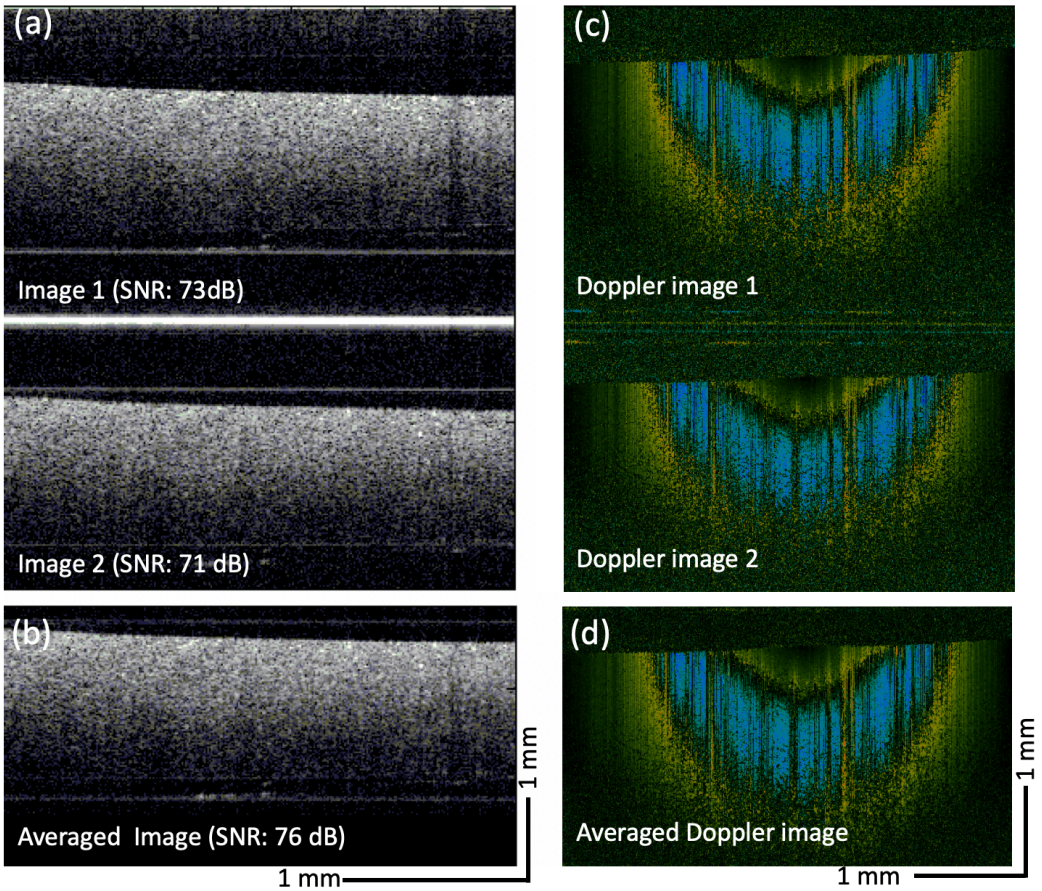

Figure 5.14 SNR quantification. (a) and (b): Original and averaged OCT images, respectively. (c) and (d): Original and averaged Doppler OCT images, respectively.

(3) Phantom Experiment

After demonstrating the improved SNR and phase stability of the SS-OCE_{CP} system, elastograms of the phantom obtained using both SS-OCE_{COV} and SS-OCE_{CP} were compared. The time-lapse Doppler images of SS-OCE_{COV} and SS-OCE_{CP} are shown in Figure 5.15(a-d) and Figure 5.15 (e-h), respectively. While the outward propagation of the spherical elastic waves was observed in both cases, the SS-OCE_{CP} result reveals a more pronounced boundary between the upward (yellow) and downward (blue) displacement, denoted by white * in Figure 5.15. In addition, this displacement boundary is better maintained in the deeper region when imaged using SS-OCE_{CP} [same white * in Figure 5.15 (b) and (f)]. Since the deeper region of the image is encoded in the higher frequency components of the interference signal, a higher phase stability is necessary for revealing detailed information in those regions. This is further exemplified by the less phase stable SS-OCE_{COV} in which the displacement boundary is more difficult to be demarcated [Figure 5.15 (a-d)]. Figure 5.15 (i) and (j) show the spatiotemporal images from SS-OCE_{COV} and SS-OCE_{CP} at the depths indicated by the white arrows in Figure 5.15 (a) and (e), respectively. The significantly reduced noise floor can be visualized in the SS- OCE_{CP} image [Figure 5.15 (j)]. Propagation speed of elasticity wave and Young's modulus of the phantom are shown in Figure 5.16.

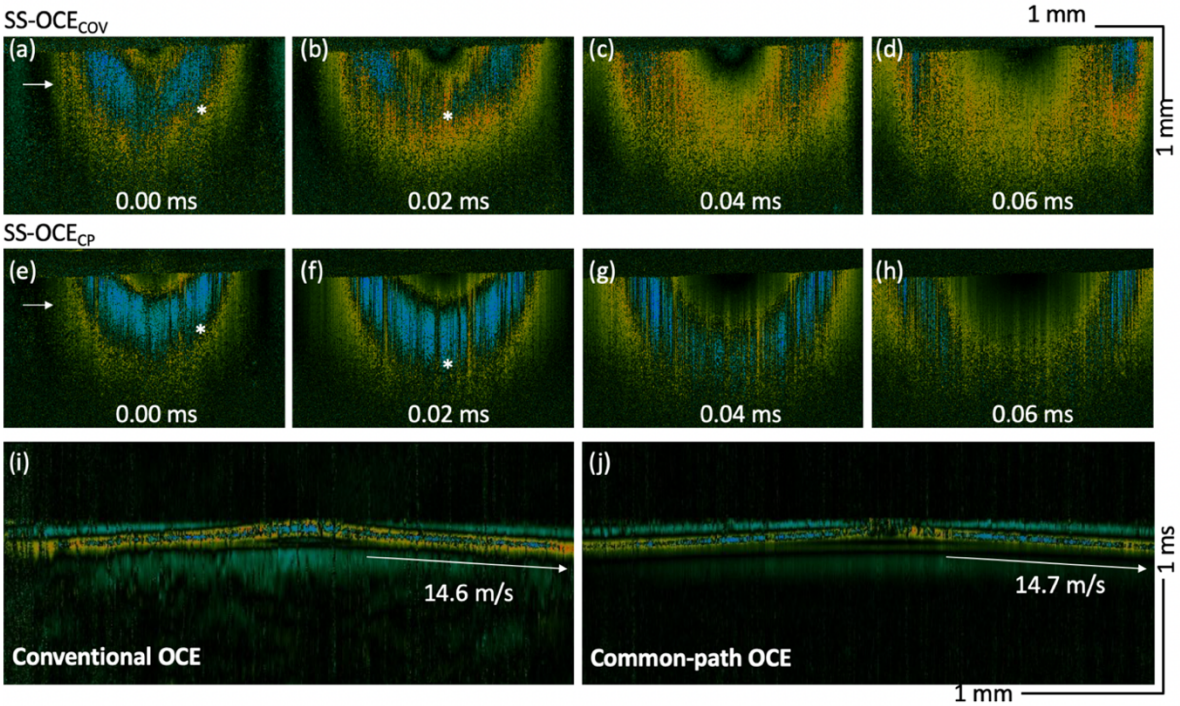

Figure 5.15 Elastic wave in the silicone phantom. Time-lapse Doppler OCT B-scans obtained using (a-d) SS-OCE$_{COV}$ and (e-h) SS-OCE$_{CP}$. (i) and (j) Spatiotemporal Doppler OCT at a depth indicated by white arrows in (a) and (e), respectively.

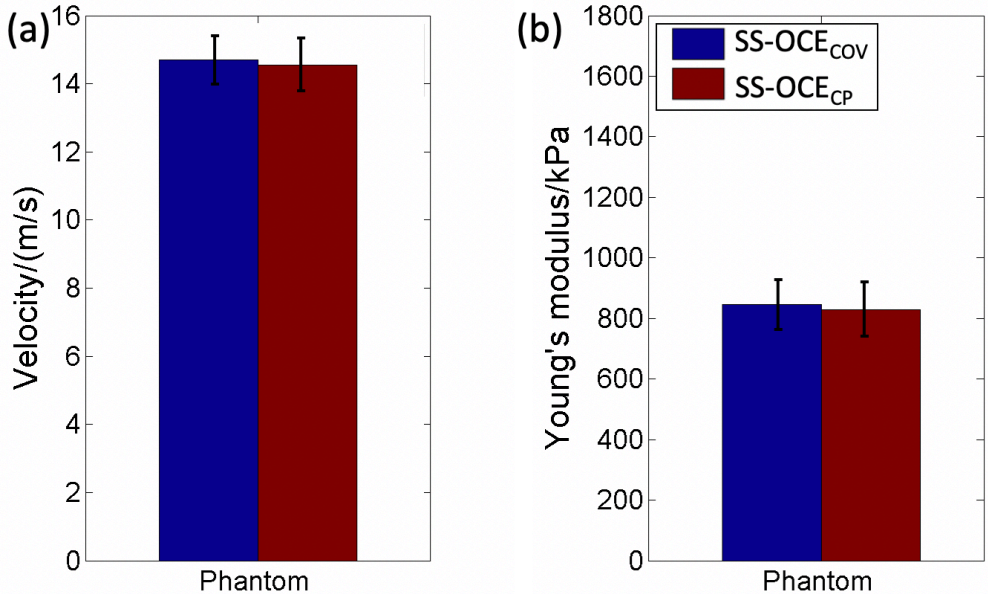

Figure 5.16 Velocity and Young's modulus quantification of phantom.

(4) *In vivo* Rabbit Experiment

We further verified the performance of the proposed SS-OCE$_{CP}$ system in a rabbit model. Figure 5.17 (a-d) and Figure 5.17 (e-h) show the time-lapse Doppler OCT B-scans of rabbit cornea obtained using SS-OCE$_{COV}$ and SS-OCE$_{CP}$, respectively. In these figures, an elastic wave that propagates outwards from the center can be visualized. Figure 5.17 (i) and (j) show the corresponding spatiotemporal images and propagation speed from the two OCE systems at the depths indicated by the white arrows in Figure 5.17 (a) and (e). The propagation speed of the elasticity wave and Young's modulus of the cornea are shown in Figure 5.18. The results concur with the phantom experiment, demonstrating the enhanced phase stability of SS-OCE$_{CP}$ that allows for observing more pronounced displacement boundary, improved SNR in the deeper region, and reduced background noise.

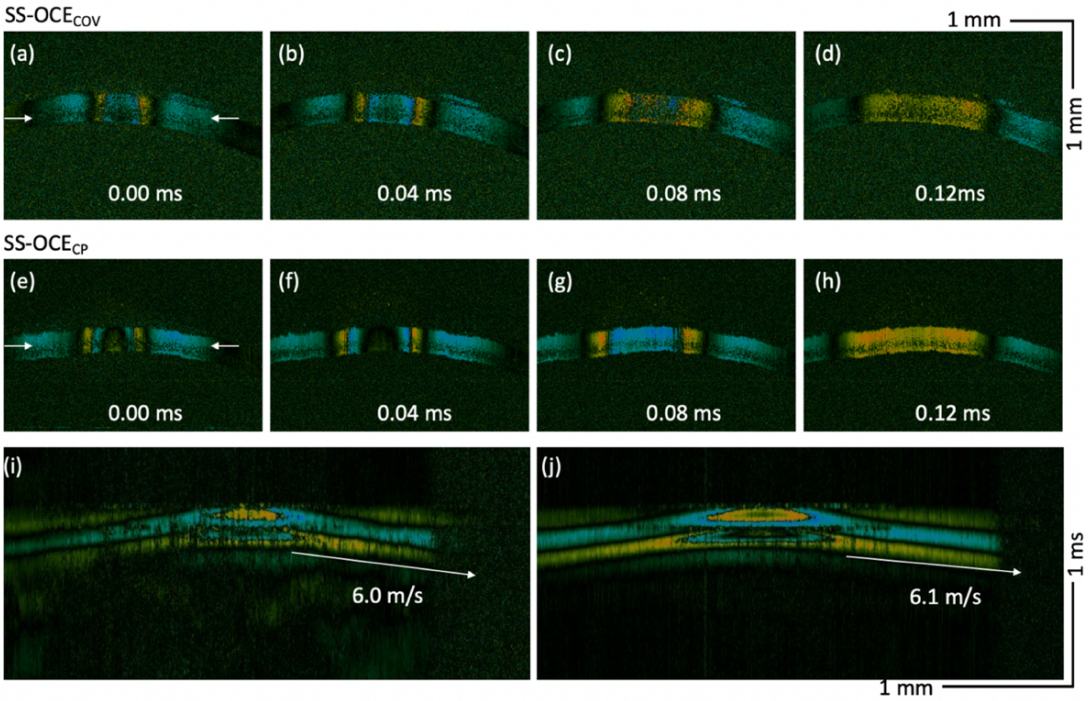

Figure 5.17 Elastic wave in rabbit cornea. (a)-(d) Time-lapse Doppler OCT B-scans from SS-OCECOV system. (e)-(h) Time-lapse Doppler OCT B-scans from Common-path OCE system. (i) and (j) Spatiotemporal Doppler OCT at a depth indicated by white arrows in (a) and (e), respectively.

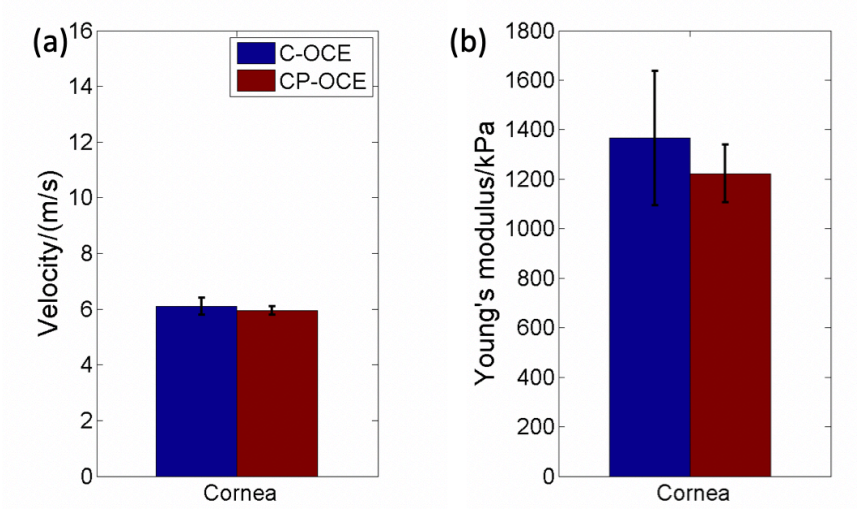

Figure 5.18 Velocity and Young's modulus quantification of rabbit cornea.

A highly phase stable OCE system can detect smaller displacements with improved accuracy. To investigate the influence of generated ARF amplitude on the phase information retrieval, we applied 3 different levels of ARF amplification reducing from 800 mV to 400 mV using the same rabbit cornea model. In all cases, SS-OCE$_{CP}$ provided a better visualization of elastic wave propagation compared to SS-OCE$_{COV}$. In the 800-mV SS-OCE$_{COV}$ case, phase error was observed at a time point of 0.12 ms in [Figure 5.19 (a)]. When applying 600 mV amplification to SS-OCE$_{COV}$, although the bidirectional wave propagation can be identified in the center at a time point of 0 ms [Figure 5.19 (d)], only one direction of displacement was observed at 0.04 ms [Figure 5.19 (c)]. A moderately poorer SNR was also observed in the 400-mV SS-OCE$_{COV}$ [Figure 5.19 (a) versus Figure 5.19 (b)]. The corresponding spatiotemporal Doppler OCT images are shown in Figure 5.20.

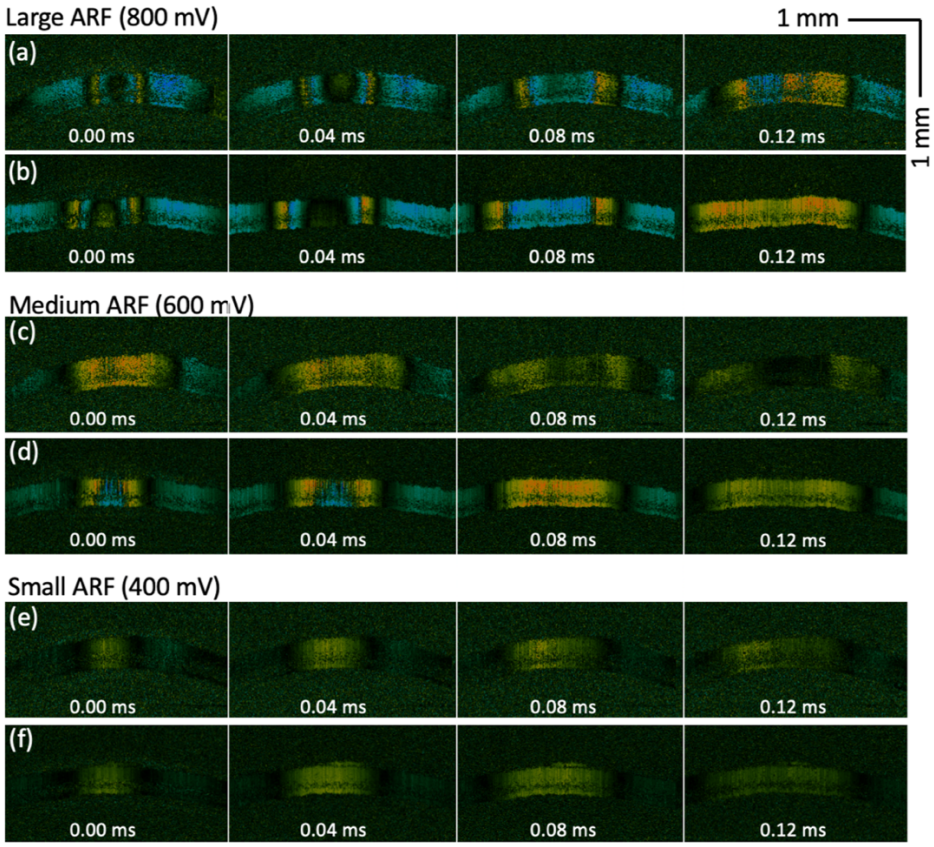

Figure 5.19 Time-lapse Doppler OCT B-scans from SS-OCE$_{COV}$ and SS-OCE$_{CP}$ system with different ARF. (a), (c), and (e) Time-lapse Doppler OCT B-scans from SS-OCE$_{COV}$ system with large, medium, and small ARF, respectively. (b), (d), and (f) Time-lapse Doppler OCT B-scans from SS-OCE$_{CP}$ system with large, medium, and small ARF, respectively.

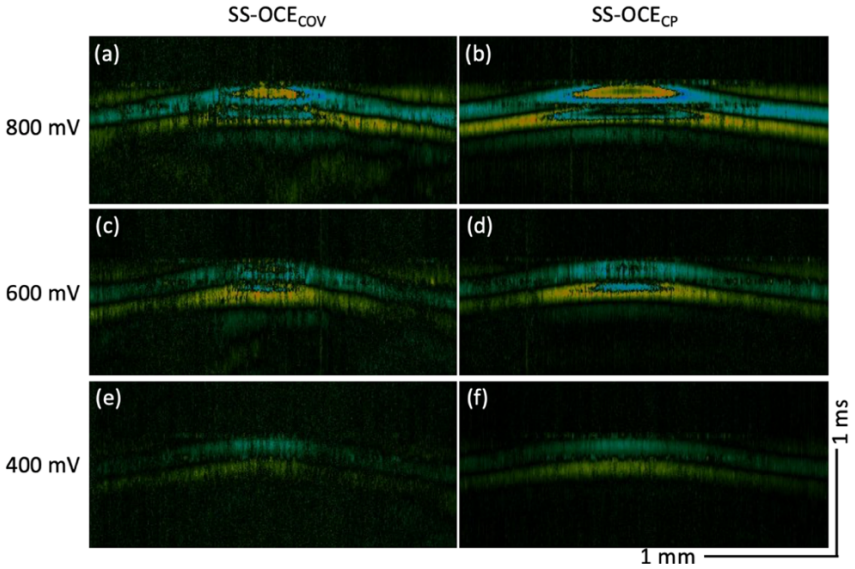

Figure 5.20 Spatiotemporal Doppler OCT of the cornea with different ARF. (a), (c), and (e) B-scans from SS-OCE$_{COV}$ excited with large, medium, and small ARF, respectively. (b), (d), and (f) B-scans from SS-OCE$_{CP}$ excited with large, medium, and small ARF, respectively.

Lastly, we tested the change in elastic wave velocity in *in vivo* rabbit cornea with normal and high intraocular pressure (IOP) to further verify the capability of SS-OCE$_{CP}$. A positive correlation between corneal elasticity and IOP has been previously reported, and our results (shown in Figure 5.21 and Figure 5.22) demonstrating the same correlation agree well with the previous study [209].

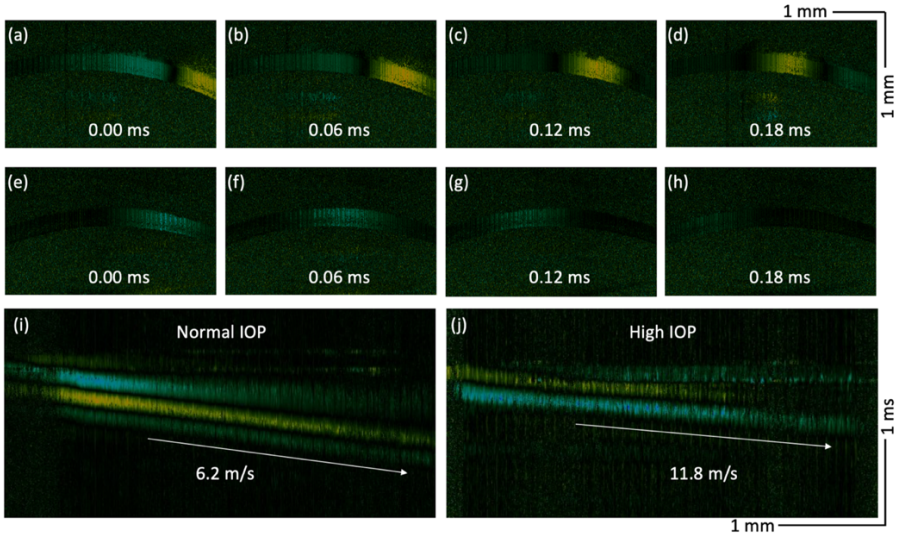

Figure 5.21 *In vivo* IOP experiment in a rabbit model

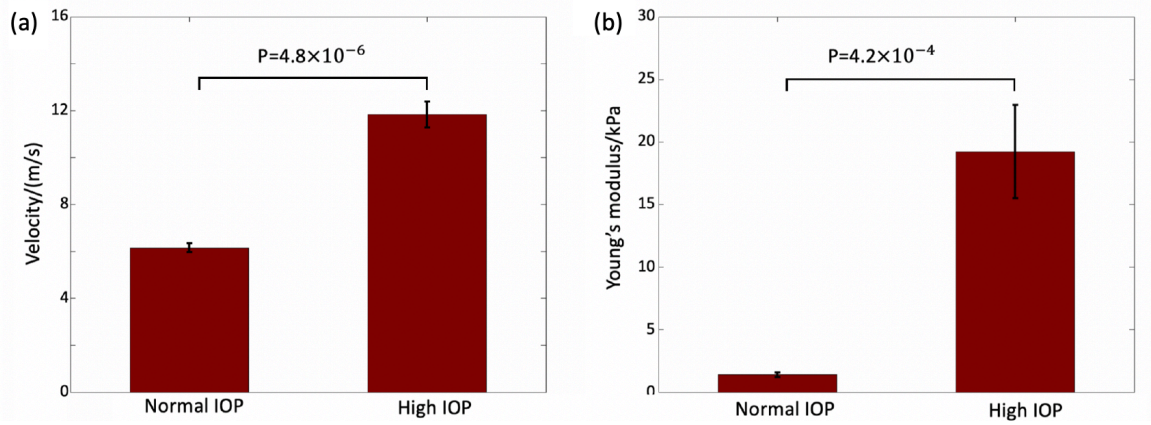

Figure 5.22 Velocity and Young's modulus of cornea with different IOP from SS-OCE$_{CP}$.

5.2.3 Conclusion

OCE benefits from OCT, providing the ability to measure biological tissue with micrometer spatial resolution and subnanometer displacement sensitivity. The static operation principle of SD-OCT contributes to its wide use in OCE. However, recent advancements in SS-OCT has proven its utility in OCE, especially with the advantages of enhanced imaging range, depth, speed, increased SNR, and reduced phase washout. The phase stability of SS-OCT can be improved through optical and electrical optimization, but reducing the phase fluctuation in a conventional SS-OCT setup is fundamentally challenging as the reference and sample signals must travel through different optical paths. We have previously demonstrated a method to optimize the electrical components in a SS-OCT system to achieve high phase stability [336], and in this study, we employed a common-path configuration to further attain the peak performance of SS-OCE. This was accomplished by enhancing SNR through averaging, minimizing time jittering by adjusting electrical delay, and reducing fluctuation of OPD via common-path configuration. The resulting SS-OCE_{CP} demonstrated a phase stability of 4.2 mrad which is not only a specification measurement in system characterization but also a realistic phase performance achieved during experiments. In addition to the 40-fold improvement of phase stability over SS-OCE_{COV}, SS-OCE_{CP} also showed a 10% increase in imaging SNR, all without the need of external stabilization or extravagant post-processing.

The phase performance of our SS-OCE_{CP} was first validated using a tissue-mimicking silicone phantom. The improved phase stability was reflected by the more pronounced displacement boundary of the elastic wave when compared to SS-OCE_{COV}. We repeated the experiment using an *in vivo* rabbit corneal model to further demonstrate the improved capability of SS-OCE_{CP} to retrieve precise phase information for elasticity quantification. The results from

the IOP experiment are also supported by reported studies [209]. Additionally, the improved displacement sensitivity provided by SS-OCE$_{CP}$ can reduce the minimal ARF for inducing detectable tissue displacement which is essential for future clinical translation.

Although we have demonstrated the superior performance of SS-OCE$_{CP}$, there are a few design improvements that can be implemented. First, in the proposed optical configuration, the reference signals are generated by the front and back surfaces of the 3-mm wedged window. In order to achieve optimal SNR, the travel distance of the detection beam from the scan lens to the first surface of the window must be constant to provide a uniform back-reflected signal; even a slight deviation will cause variation in OPD and back-reflected power during scanning, resulting in reduced SNR. For applications that require scanning of a larger area, a scan lens that provides a larger field of view should be used. Furthermore, for 3-dimensional OCE, a 4f optical corrector can be incorporated into the scanning design to ensure a constant entrance pupil and OPD.

In addition, we have previously demonstrated a confocal alignment between the OCT detection beam and the ARF excitation via a coaxial configuration for high excitation efficiency [187, 210]. A confocal/coaxial setup can improve the ease of use and reduce the form factor of the sample arm, further facilitating the translation of this technology to clinical use. In our current SS-OCE$_{CP}$ design, the wedged window prevents such a confocal setup as the ARF will be attenuated by the window. Alternatively, the wedged window can be fabricated using an optically and acoustically transparent material, such as Pebax® and low-density polyethylene [5, 337]. With such a window, a ring-shaped ultrasound transducer can be inserted between the scan lens and the window for excitation, allowing the OCT detection beam to travel through the center of the transducer for imaging.

Finally, the light source of the SS-OCE$_{CP}$ system is a vertical-cavity surface-emitting laser with an internal MZI that provides the k-clock signal at ~400 MHz, allowing for an imaging range ~11 mm in standard OCT or ~5.5 mm when utilizing the proposed averaging method that enhances the SNR by 10%. While a 5.5 mm-imaging range may be enough in many applications, a long imaging range can be achieved through doubling the k-clock frequency by building an external circuit or through dual edge sampling provided by certain waveform digitizers. A custom-built external k-clock can also be considered. Alternatively, an acousto-optic modulator can be incorporated to shift the frequency of the interferometer signal in order to take advantage of the full bandwidth of the frequency [1]. With respect to achieving a better penetration depth, swept-source lasers with a longer center wavelength, such as 1.7 μm, can be utilized [61].

In summary, we have reported the first OCE system based on SS-OCT with a common-path configuration. A phase stability of 4.2 mrad was obtained, and the feasibility and the performance of our SS-OCE$_{CP}$ system have been tested and validated using a phantom and *in vivo* rabbit model. This highly phase stable system can practically quantify displacement in the subnanometer range, and we believe that it has great potential in other applications that require precision phase measurement, such as flowmetry [6], vibrometry [338], and molecular imaging [339].

Chapter 6 –Optical Coherence Angiogram

In recent decades, imaging techniques, such as high frequency ultrasound (US) imaging, magnetic resonance imaging (MRI), confocal microscopy (CM), multiphoton tomography (MPT) and optical coherence tomography (OCT), have been developed for improving the diagnostic accuracy of skin cancer [118-130]. Despite diagnostic advantages, *in vivo* real time imaging allow dynamic visualization that plays an important role in imaging guide surgery when histopathological examinations are time consuming. Among them, OCT uses low-coherence light to capture two- and three-dimensional (3D) structural images down to skin depths of ~ 1- 2.00 mm with a spatial resolution of 3 to 15 μm, which can supplement current imaging methods and, therefore, has become an attractive research tool for dermatology. In addition, Doppler OCT and OCT angiography (OCTA) have been developed to visualize the vascular network and tumor angiogenesis [131, 132]. Furthermore, OCTA, as a functional augmentation of OCT, allows for the visualization of cutaneous microvasculature via the detection of fluctuations in amplitude and/or phase of sequential OCT signal with high resolution and sensitivity. It offers an extension to the structural rendering of the skin, providing more critical information toward accurate cancer diagnosis (e.g. vascular density and blood flow rate) because vascular formation and angiogenesis are key indicators of tumor development and progression [6, 7, 156-159, 340, 341]. Finally, the recent advances in spatial resolution, imaging speed, and probe design make OCT an attractive clinical tool for skin cancer diagnostics, margin delineation, and therapy monitoring. Most commercial OCT devices for skin imaging, such as Vivosight®, Callisto®, and NITID®, use a light source with a wavelength centered at 1.3 μm for image acquisition which has limited imaging depth. In spite of this limitation, studies on various skin diseases using OCT devices revealed an

increased diagnostic accuracy when dermatologists apply OCT as a supplement to routine clinical work [342-345].

To further optimize the performance of OCT devices, several studies have reported that 1.7-micron OCT devices with a light source centered at 1.7 μm demonstrated improved penetration depth by up to ~25% through *ex vivo* or *in vivo* tests [61, 346, 347]. In our study, we developed a 1.7-micron OCT and OCTA system and extended its capability to characterize skin lesions by visualizing both morphology and vasculature in the deeper layer of the skin. We imaged different types of human skin lesions *in vivo* and described the features of the OCT and OCTA images.

6.1 Methods

(1) System setup

The schematic diagram of the developed OCT and OCTA system is presented in Figure 6.1. The system is powered by a 1.7 μm-centered wavelength swept-source laser. The output light from the laser source is split by a 90:10 optical fiber coupler where 90% of the light is propagated to the sample arm (handheld probe) and the remaining 10% to the reference arm, which consists of a collimator, lens, and mirror. The backscattered light from the sample and the back-reflected reference beam generates the interference signal in the 50:50 optical fiber coupler which is then delivered to the balanced photodetector. In the handheld probe, a dual-axis galvanometer and a scan lens were applied for 3D OCT imaging. To make sure the imaging target is placed within the depth of focus, a threaded adapter was connected to the probe where the distance between the target and the probe can be easily adjusted with rotation of the adapter.

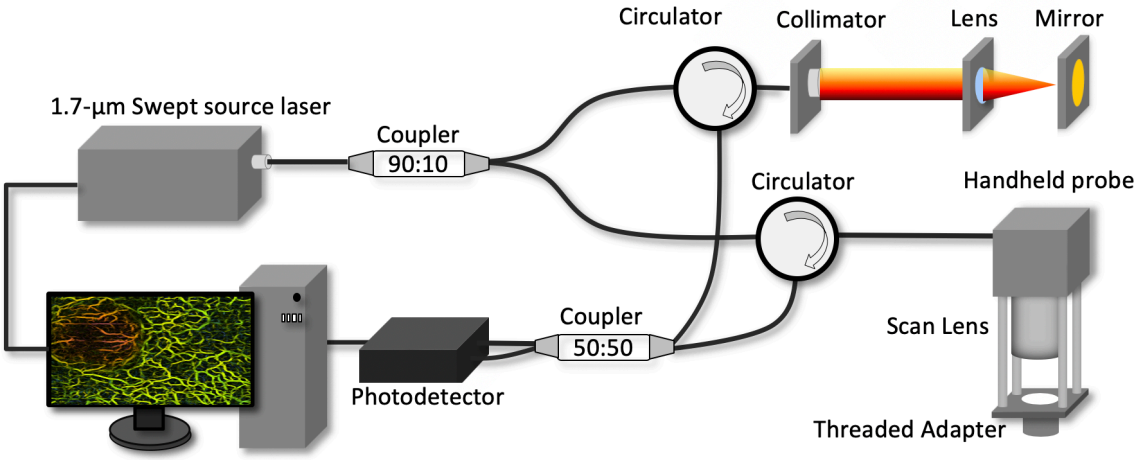

Figure 6.1 System setup of 1.7-micron OCT/OCTA system.

(2) Scan protocol and OCTA algorithm

OCTA requires multiple images in sequence at the same position to reveal the portion with fluctuations. Here, an inter-frame scanning protocol is applied in which consequent 6 cross-sectional B-scans (M=6) are acquired at the same position and compared to extract vascular information, shown in Figure 6.2. This protocol has a longer time interval ΔT of ~ 5.6 ms as it utilizes the slow scan (Galvo Y) of the scanning apparatus which is able to provide high sensitivity for microvasculature. An intensity based Doppler variance algorithm [equation (6.1)] is utilized to capture the fluctuation caused by blood flow to form Doppler OCT images. Then Doppler OCT images are resliced along depth direction and then processed by a 2D low pass filter and a Hessian based Frangi Vesselness filter [348] to generate and enhance blood vessel networks at different depth, shown in Figure 6.2 (c).

$$\sigma^2 = 1 - \frac{2 \times \sum_{m=1}^{M-1}(|F_m| \times |F_{m+1}|)}{\sum_{m=1}^{M-1}|F_m|^2 + \sum_{m=1}^{M-1}|F_{m+1}|^2} \tag{6.1}$$

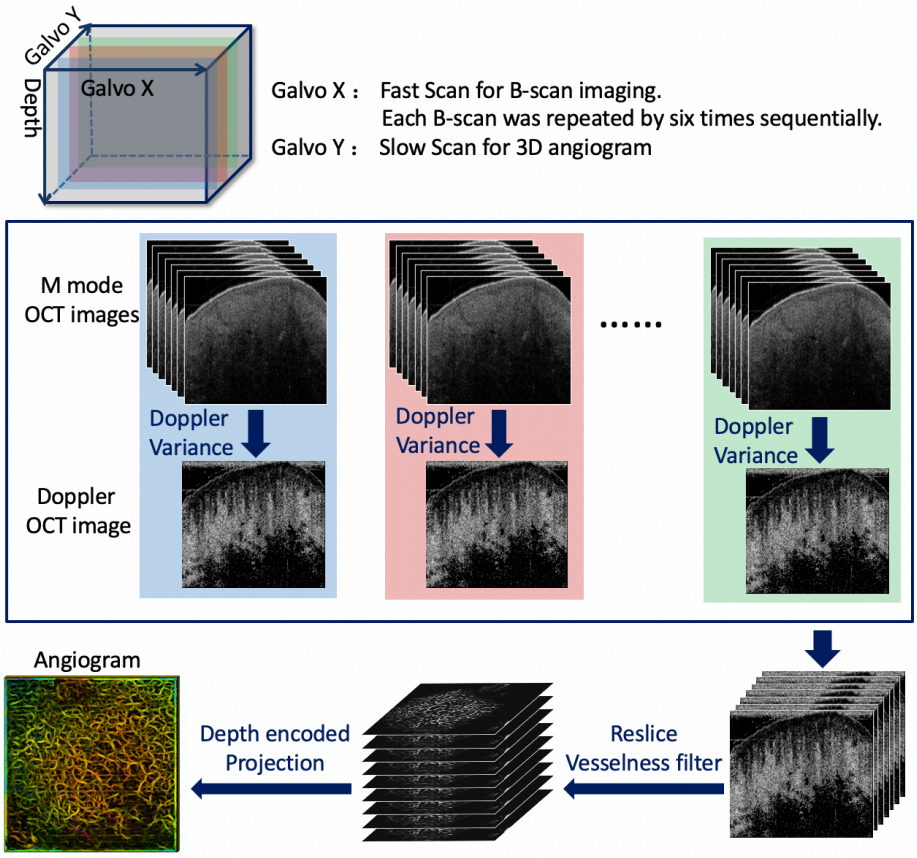

Figure 6.2 Scan protocol and OCTA angiogram.

6.2 Imaging Results

This was a prospective pilot study to evaluate skin tumors using 1.7-micron OCT/OCTA technology. Protocol was approved by the Institutional Review Board and patients were recruited from the Department of Dermatology at the University of California, Irvine (UCI). The handheld probe was sterilized before imaging. Patients with various types of skin tumors diagnosed by a dermatologist were referred. A single operator performed all imaging to minimize operator variability. Single image acquisition took 30 seconds to complete. Six subjects were involved in this study where the skin with an area of 5 mm × 5 mm was imaged. 3D and cross-sectional OCT images that allow for the visualization of both overall and detailed morphologies were obtained. In addition, Doppler variance algorithm was applied to reconstruct the vasculature of the skin. To

quantify the morphology and vasculature, the thickness of the epidermis as well as the density of the vasculature were calculated.

(1) Healthy human palm

Figure 6.3 (a)-(c) show representative 3D OCT images, 2D depth color encoded vasculature, and a 3D rendering of co-registered OCT and angiography (X-Y plane), respectively. Figure 6.3 (d)-(k) are the cross-sectional OCT images (Y-Z plane) at different longitudinal positions along X axis. Dermal-epidermal junction (DEJ) of the skin which is determined by both OCT and Doppler OCT images was labeled by a dashed green line in Figure 6.3 (d). Homogeneous vascular patterns and well-defined layer architecture can be visualized from the angiogram and OCT images. Healthy skin is supplied with a rich vascular network. The vessel density in this case is ~54%, and the average thickness of the epidermis is ~ 200 μm.

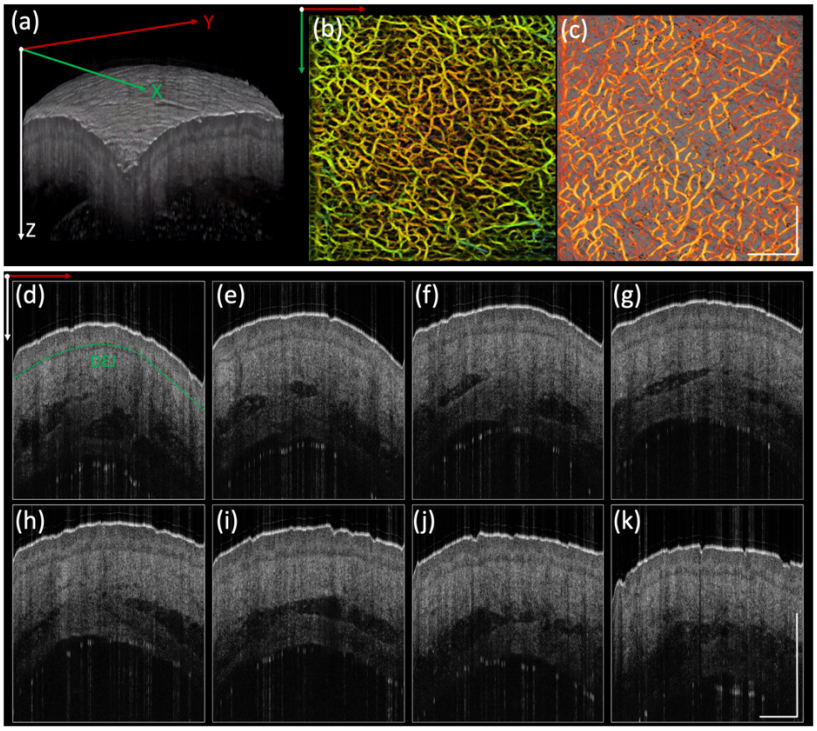

Figure 6.3 Healthy palm. (a) 3D OCT image. (b) Depth encoded angiogram where red to green represent shallow to deep depths. (c) Co-registered OCT image and angiogram projection on Y-X plane. (d)-(k) Cross-sectional OCT images on Y-Z plane from different positions along X direction. DEJ: dermal-epidermal junction, indicated by green dashed line. Scale bar: 1mm.

(2) Solar lentigo

OCT and Doppler angiography of a solar lentigo on the back of a hand are shown in Figure 6.4. The DEJ can be clearly defined, indicated by the green dashed line in Figure 6.4 (d). The thickness of epidermis is ~ 80 µm. Figure 6.4 (b) and (c) show 2D depth-encoded angiography and a co-registered rendering of OCT image and angiography where a homogenous valvular pattern with a density of ~52% was identified.

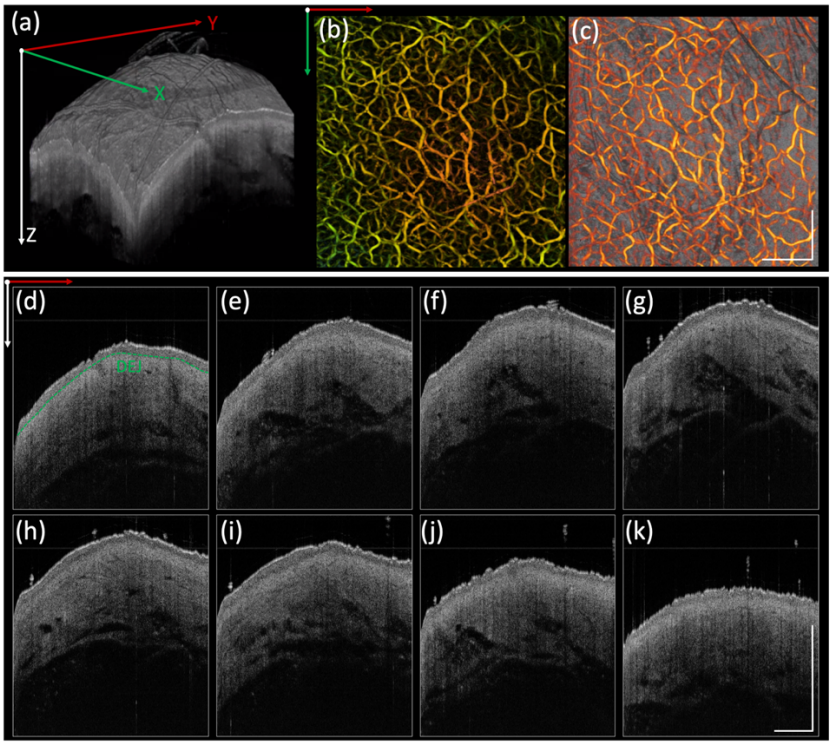

Figure 6.4 Solar lentigo. (a) 3D OCT image. (b) Depth encoded angiogram where red to green represent shallow to deep depths. (c) Co-registered OCT image and angiogram projection on Y-X plane. (d)-(k) Cross-sectional OCT images on Y-Z plane from different positions along X direction. DEJ: dermal-epidermal junction, indicated by green dashed line. Scale bar: 1mm.

(3) Seborrheic keratosis

OCT and angiography of a SK on the back of a hand are presented in Figure 6.5. The lesion [on the right of the dashed white line in Figure 6.5 (b)] has a rough, verrucous surface, which can be appreciated in the 3D rendering in Figure 6.5 (a). OCT cross-sections exhibit decreased and

nonhomogeneous signal intensity. The epidermis of lesions (thickness: ~ 197 μm) was thicker than that of normal skin on the back of the hand. According to the angiogram [Figure 6.5 (b) and (c)], the vascular densities of the two skin profiles, the SK itself (right) and surrounding skin (left), [separated by white dashed line in Figure 6.5 (b)], were ~52% and ~58%.

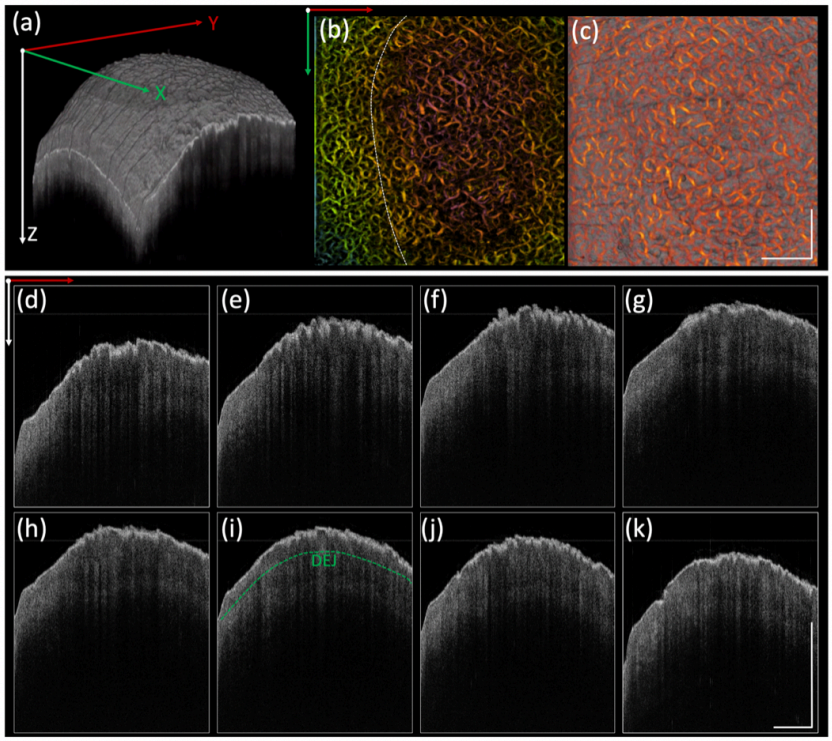

Figure 6.5 Seborrheic keratosis. (a) 3D OCT image. (b) Depth encoded angiogram where red to green represent shallow to deep depths. (c) Co-registered OCT image and angiogram projection on Y-X plane. (d)-(k) Cross-sectional OCT images on Y-Z plane from different positions along X direction. DEJ: dermal-epidermal junction, indicated by green dashed line. Scale bar: 1mm.

(4) Cherry angioma

A cherry angioma was scanned with OCT and is presented in Figure 6.6. In the 3D OCT rendering [Figure 6.6 (a)], a protruding lesion can be clearly identified. From the corresponding angiogram, it exhibits a clustered vascular pattern with a density of ~63%, which is much higher than that of adjacent tissue (density: ~52%). The DEJ is labeled in Figure 6.6 (d) and (h). The epidermis thickness of the angioma ~ 43 μm, which is thinner than that of adjacent tissue

(epidermis thickness: ~56 μm). In addition, another feature of the angioma is decreased OCT intensity in contrast to that of adjacent tissue.

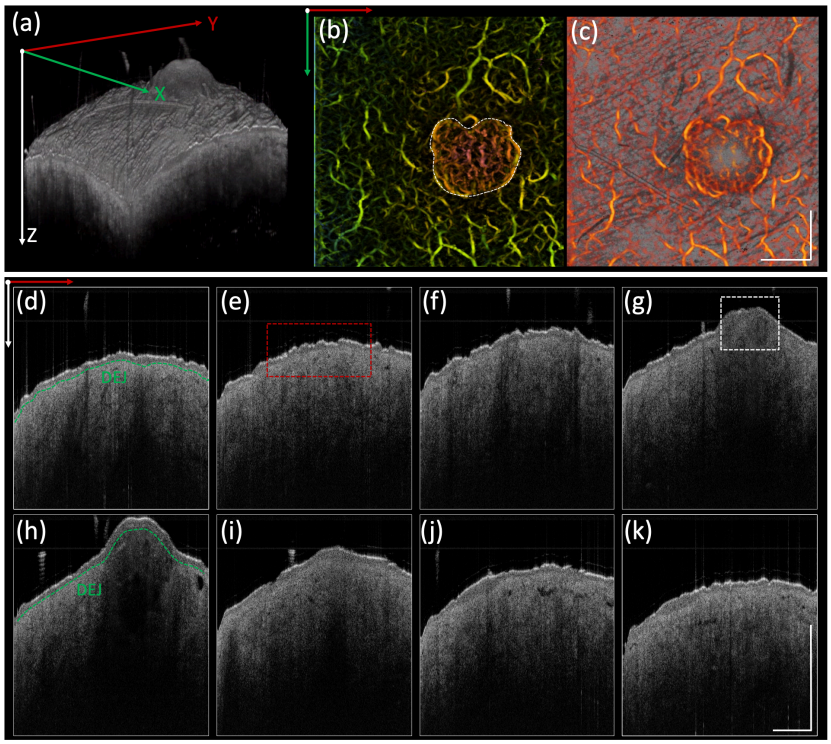

Figure 6.6 Cherry angioma. (a) 3D OCT image. (b) Depth encoded angiogram where red to green represent shallow to deep depths. (c) Co-registered OCT image and angiogram projection on Y-X plane. (d)-(k) Cross-sectional OCT images on Y-Z plane from different positions along X direction. DEJ: dermal-epidermal junction, indicated by green dashed line. White dashed box: angioma. Red dashed box: normal tissue. Scale bar: 1mm.

(5) Dermal nevus

OCT images and angiography of a dermal nevus on the back are shown in Figure 6.7. Similar to the gross superficial structure of an angioma, a protruding lesion is identified in the 3D OCT image [Figure 6.7 (a)]. Regarding the angiogram, the vessel density (~53%) of the lesion was similar to that of the adjacent skin (density: 49%). In the cross-sectional OCT images, the DEJ was labeled in Figure 6.7 (d) and (e). The epidermal thickness of this dermal nevus was found to be ~123 μm which was higher than that of the adjacent skin (~76 μm). In addition, another feature of

the dermal nevus was slightly decreased OCT intensity from the tissue under the DEJ in contrast to that of the adjacent tissue.

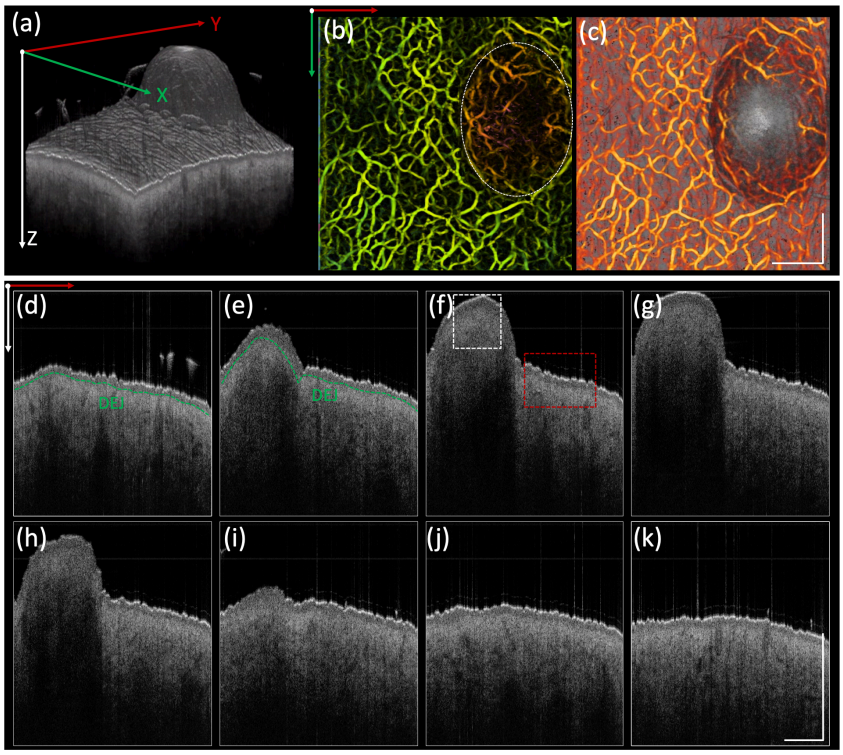

Figure 6.7 Dermal nevus. (a) 3D OCT image. (b) Depth encoded angiogram where red to green represents shallow to deep depths. (c) Co-registered OCT image and angiogram projection on Y-X plane. (d)-(k) Cross-sectional OCT images on Y-Z plane from different positions along X direction. DEJ: dermal-epidermal junction, indicated by green dashed line. Scale bar: 1mm. White dashed box: dermal nevus. Red dashed box: normal skin.

(6) Actinic keratosis

Results of OCT scans of an actinic keratosis on the back of the hand are shown in Figure 6.8. In the 3D rendering [Figure 6.8 (a)], two protruding lesions can be clearly visualized, which exhibit decreased vessel density (43%) compared to that of adjacent tissue (56%), shown in Figure 6.8 (b) and (c). The overall angiography of the lesion exhibited a dense, tortuous, reticular vascular network. In the cross-sectional OCT images, the DEJ is indicated by a green dashed line in Figure 6.8 (j), which is more irregularly shaped when compared to that of previous cases with varied epidermal thicknesses in a wide range from 91 to 225 μm.

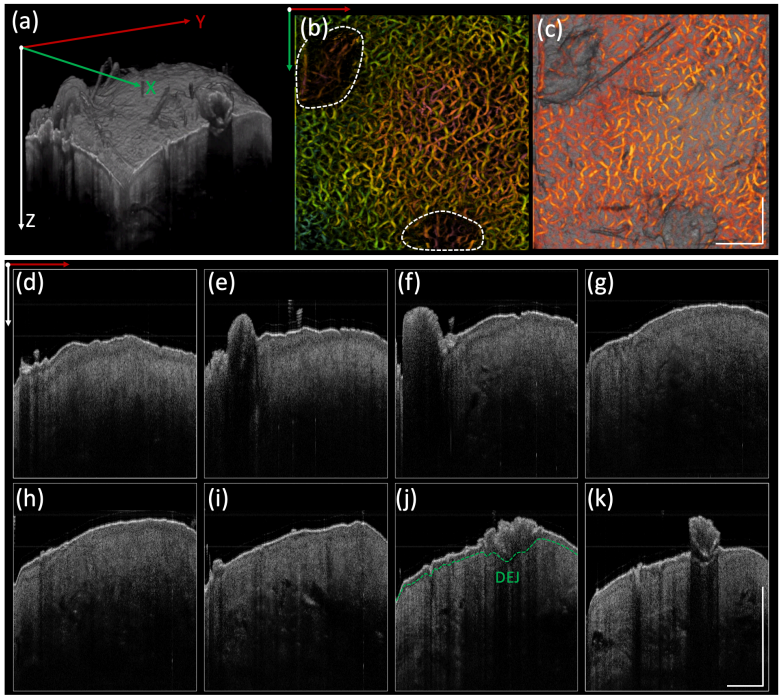

Figure 6.8 Actinic keratosis. (a) 3D OCT. (b) Depth encoded angiogram where red to green represent shallow to deep depths. (c) Co-registered OCT image and angiogram projection on Y-X plane. (d)-(k) Cross-sectional OCT images on Y-Z plane from different positions along X direction. DEJ: dermal-epidermal junction, indicated by green dashed line. Scale bar: 1mm.

6.5 Conclusion

OCTA, as a functional extension of OCT, provides the ability to visualize vascular morphology down to a skin depth of ~ 1-2 mm with spatial resolution on the level of micrometers. Recent studies have demonstrated the utility of 1.3 μm OCT/OCTA in dermatology and its increased diagnostic accuracy [342]. Increasing the center wavelength to 1.7 μm in OCT has permitted the visualization of skin morphology at greater skin depths. In this paper, we developed a 1.7-micron OCT/OCTA system and further explored its feasibility in dermatology.

We tested the system *in vivo* on six subjects with different skin conditions, including healthy skin, solar lentigo, seborrheic keratosis, cherry angioma, dermal nevus, and actinic keratosis. Each case was described in terms of structure and vascular morphology of the skin as interpreted via OCT/OCTA. The results indicated that 1.7-micron OCT/OCTA can provide more comprehensive information as a supplement to dermoscopy. While the proposed 1.7-micron OCT/OCTA system is a promising *in vivo* imaging method for characterization of skin cancer, a few challenges still need be addressed in order to successfully translate this technology for clinical applications.

Six subjects were involved in our feasibility study. While different features were presented in each case, objective quantitative analysis was lacking. To establish diagnostic criteria (typical features in skin architecture and vascular morphology), more subjects with different conditions need to be studied and analysed statistically. Furthermore, the influence from both intrinsic and extrinsic factors, such as different body locations and age, on the thickness of the epidermis as well as the density and morphology of blood vessels likely introduces more variability. To further improve accuracy, normal adjacent tissue should be imaged for each patient as a control, and the

epidermal thickness and vessel morphology could be used as comparisons to lesional or diseased tissue.

In our study, the epidermal thickness and vessel morphology were described for the characterization of various skin lesions. To further improve the accuracy, more parameters should be investigated to quantify the changes in structure, vascular morphology, and chemical composition based on OCT and OCTA images. For example, vascular tortuosity that is closely associated with the progression of basal cell carcinoma could be quantified to characterize the tissue. Additionally, the measurement of reflectivity and attenuation coefficient could provide a quantitative analysis regarding the skin's physical alterations.

In summary, we have reported on a 1.7-micron OCT/OCTA system for characterization of benign and cancerous skin lesions. The feasibility and performance of our system were tested and validated *in vivo* in human subjects. The proposed system has the capability of providing more structural and vascular information at greater skin depths than previous OCT systems, and we believe it has great potential to bring new insights in diagnosis as well as better management of skin cancer.

Chapter 7 – Summary

7.1 Summary

This Ph.D. dissertation presented the development of four endoscopic imaging systems, one microscopic OCTA system, and two microscopic OCE imaging systems, and applied them in cardiology, gastroenterology, dermatology, and ophthalmology with the aim of providing a powerful tool in clinical diagnosis and therapeutic monitoring [55, 61, 64, 77, 207, 275, 298, 337, 341, 346, 349, 350]. The theoretical approach, system and probe design, and experimental research have been discussed in detail.

7.1.1 Intravascular Imaging for Characterization of Atherosclerosis

Ruptured atherosclerotic plaques are the main cause of acute coronary events. Early detection and characterization of vulnerable plaques are the first and necessary step in preventing lethal consequences and for selecting proper interventional techniques. First, we presented a novel IVOCT system with a 1.7 μm center wavelength swept light source that can readily penetrate deeper into tissue because of the longer wavelength and allow for better identification of plaques due to the lipid absorption spectrum at 1.7 μm [61]. Using this system, we have imaged a human coronary artery to evaluate the performance of the novel OCT system and verified the results by hematoxylin and eosin (H&E) histology. The significantly improved imaging depth and better identification sensitivity suggest that the 1.7 μm OCT system holds great potential that can be further translated for *in vivo* applications of atherosclerosis characterization.

Furthermore, to achieve a complete assessment of atherosclerotic plaque, IVOCT is insufficient due to limited information, and therefore, several imaging methods are often performed in sequence. To address this issue, we presented a tri-modality imaging system and fully integrated tri-modality probe for intravascular imaging [55]. The tri-modality imaging system is able to simultaneously acquire optical coherence tomography (OCT), ultrasound (US), and fluorescence imaging. Moreover, for fluorescence imaging, we used the FDA-approved indocyanine green (ICG) dye as a contrast agent to target lipid-loaded macrophages. We conducted imaging of a male New Zealand white rabbit to evaluate the performance of the tri-modality system. In addition, tri-modality images of rabbit aortas were correlated with hematoxylin and eosin (H&E) histology to check the measurement accuracy. The fully integrated miniature tri-modality probe, together with the use of ICG dye, suggest that the system has great potential for providing a more accurate assessment of vulnerable plaques in clinical applications.

7.1.2 Multimodal Endoscopic Imaging in Gastrointestinal Tract

Colonoscopy (i.e., white light endoscopy) is the gold standard for colorectal and GI examinations, and suspicious regions are further biopsied to rule out cancer. Accuracy is limited due to small sample numbers. In recent decades, optical endoscopes (such as fluorescence and OCT) and endoscopic ultrasound have been applied in order to provide additional information. Similar to cardiology, several imaging modalities are often performed in sequence to obtain more information for accurate diagnosis which causes increased procedure time, risk, and cost. To address this issue, we developed two dual modality endoscopic imaging systems that allow for simultaneous visualization of vascular network and morphology for a better characterization of colorectal cancer.

First, we combined OCT and ICG-based NIRF together to enable a high-resolution visualization of both vasculature and microstructure [77, 298]. An *in vivo* animal study was performed using a rat with colorectal cancer. The co-registered OCT and NIR fluorescence images allowed the identification and differentiation of normal colon, hyperplastic polyp, adenomatous polyp, and adenocarcinoma, demonstrating the potential to provide a new clinical tool to advance gastroenterology practice.

To achieve a fully non-invasive diagnosis, we developed a high speed integrated endoscopic PA and US imaging system which is able to obtain morphological tissue information and vasculature of the GI tract simultaneously at a high imaging speed up to 50 frames/s without the need of any contrast agent [64]. *In vivo* animal studies confirmed the performance of our imaging system for evaluating the GI tract. To further improve its capability, we reported on a high sensitivity dual modality PA/US imaging system using a single-element ultrasonic transducer fabricated with PMN-33%PT/epoxy 1-3 composite. We compared the performance of our system with conventional PA/US imaging systems [337]. Phantom and *in vivo* rat experiments demonstrated an enhanced sensitivity of our imaging system over conventional systems.

7.1.3 Microscopic Optical Coherence Elastography in Ophthalmology

The crystalline lens and cornea comprise the eye's optical system for focusing light in human vision. The changes in biomechanical properties of the lens and cornea are closely associated with common diseases, including presbyopia and cataract. OCE is an emerging functional imaging technique that quantifies the elasticity of biological tissue by using Doppler optical coherence tomography (OCT) to measure the local tissue displacement as a function of applied stress [182, 193]. Compared with conventional elastography (e.g., magnetic resonance

elastography, ultrasound elastography, and Brillouin microscopy), OCE possesses micron-level resolution and an axial displacement sensitivity on the order of subnanometers and, therefore, has become an attractive research tool for ophthalmology.

Currently, most *in vivo* elasticity studies using OCE of the anterior eye focus on the measurement of the cornea while lens measurement remains challenging. In our study, we developed an ARF-OCE system to quantify the elasticities of the cornea and the lens, simultaneously [207]. The system was tested through first *ex vivo* then *in vivo* experiments using a rabbit model. The elasticities of corneal and lens tissue in an excised normal whole-globe and a cold cataract model were measured to reveal that cataractous lenses have a higher Young's modulus. Simultaneous *in vivo* elasticity measurements of lens and cornea were performed in a rabbit model to demonstrate the correlations between elasticity and intraocular pressure and between elasticity and age. To the best of our knowledge, we demonstrated the first *in vivo* imaging of elasticity of both lens and cornea using ARF-OCE, thereby providing a potential powerful clinical tool to advance ophthalmic research in disorders affecting the lens and the cornea.

Furthermore, we developed an ultrahigh sensitive OCT to further improve the capability of ARF-OCE [350]. The phase stability of an optical coherence elastography (OCE) system is the key determining factor for achieving a precise elasticity measurement, and it can be affected by the signal-to-noise ratio (SNR), timing jitters in the signal acquisition process, and fluctuations in the optical path difference (OPD) between the sample and reference arms. In this study, we developed an OCE system based on swept-source optical coherence tomography (SS-OCT) with a common-path configuration (SS-OCE$_{CP}$). Our system has a phase stability of 4.2 mrad without external stabilization or extensive post-processing, such as averaging. This phase stability allows us to detect a displacement as small as ~300 pm. A common-path interferometer was incorporated

by integrating a 3-mm wedged window into the SS-OCT system to provide intrinsic compensation for polarization and dispersion mismatch as well as to minimize phase fluctuations caused by the OPD variation. The wedged window generates two reference signals that produce two OCT images, allowing for averaging to improve the SNR. Furthermore, the electrical components are optimized to minimize the timing jitters and prevent edge collisions by adjusting the delays among the trigger, k-clock and signal, utilizing a high-speed waveform digitizer, and incorporating a high-bandwidth balanced photodetector. We validated the SS-OCE$_{CP}$ performance in a tissue-mimicking phantom and an *in vivo* rabbit model, and the results demonstrated a significantly improved phase stability compared to that of conventional SS-OCE. To the best of our knowledge, we demonstrated the first SS-OCE$_{CP}$ system which possesses high phase stability and can be utilized to significantly improve the sensitivity of elastography.

7.1.4 1.7-micron OCT/OCT Angiogram in Dermatology

OCT/OCTA is a non-invasive diagnostic method that offers real-time visualization of the layered architecture and vascular morphology of the skin *in vivo*, which has been widely used in dermatological clinical and research settings for characterization of benign and cancerous skin lesions. Most commercial skin imaging OCT devices apply a light source with a wavelength centered at 1.3 μm for imaging skin with limited imaging depth. To further extend the capability, we developed a 1.7-micron OCT/OCTA system that allows for a visualization of both morphology and microvasculature in the deeper layers of the skin. Using this imaging system, we imaged human skin with different benign lesions and described the corresponding features of both structure and vasculature. The significantly improved imaging depth and additional functional information suggest that the 1.7-micron OCTA system has great potential to advance both

dermatological clinical and research settings for characterization of benign and cancerous skin lesions.

7.2 Future Directions

7.2.1 Intravascular Imaging

Ruptured atherosclerotic plaques are the main cause of acute coronary events which are of lethal consequence [351-355]. The first line of defense against such events not only relies on early detection but also accurate characterization of plaques. It has been demonstrated that the stability of a plaque is highly associated with its morphology, chemical composition, and biomechanical properties [44, 356-363]. Structurally, the thickness of a fibrous cap is a reliable indicator of plaque vulnerability [43, 44]. Chemically, intra-lesion lipid density and cholesterol content have been shown to be correlated with vulnerability [44, 292, 364]. Biomechanically, shifting in local tissue elasticity is also one of the key indicators as the stress in a fibrous cap is altered by its thickness and macrophage infiltration [360-363]. More importantly, tissue elasticity can be used for identifying plaque type based on the composition-dependent biomechanical property of the plaque. Comprehensive plaque evaluation, particularly for detecting vulnerable plaques at the earliest stage, must incorporate the quantification of these structural, chemical, and biomechanical properties in situ. Specifically, an ideal imaging method should possess a spatial resolution capable of resolving fibrous cap detail, imaging depth sufficient for assessing plaque burden and vessel remodeling, and biomechanical sensitivity adequate for determining tissue composition and mechanical properties.

In Chapter 3, we demonstrated a tri-modality intravascular imaging system that enables the visualization of both structural imaging and chemical composition. However, the mechanical properties are still lacking. As the next step, we are aiming to develop a multimodal intravascular imaging system that combines OCT, US, and shear-wave OCE (OCE_{SW}) for studying and

characterizing plaque vulnerability. The proposed system, IVOCT-US-OCE$_{SW}$, is built upon ARF-OCE technology (introduced in Chapter 5). First, the IVOCT-US-OCE$_{SW}$ system will feature a 4-MHz, 1.7-μm swept-source laser for an improved penetration depth that allows OCT and OCE to assess deeper features of a plaque. The rapid repetition rate of the laser will also enable B-M mode scanning with single-shot excitation thus achieving high-speed OCE$_{SW}$ that greatly reduces the procedure time and hence minimizes light and acoustic radiation force (ARF) exposures. In addition to visualizing the displacement based on compressional waves for quantifying biomechanical properties [14, 105, 106], OCE$_{SW}$ is incorporated to provide direct, accurate, and quantitative elasticity measurements by eliminating the need for calibration as well as the influence of phase washout. Furthermore, a dual ultrasonic setup will be utilized for US imaging and ARF excitation separately, maintaining high resolution of US while providing sufficient ARF for OCE$_{SW}$. To attain the optimal imaging speed for OCT, US, and OCE$_{SW}$, the imaging probe will also feature a dual scanning scheme incorporating both proximal and distal mechanisms which can operate simultaneously at different speeds.

(1) System setup:

The schematic diagram of the proposed IVOCT-US-OCE$_{SW}$ is presented in Figure 7.1. The system is powered by a 1.7-μm center wavelength swept-source laser which will have a repetition rate of 4 MHz. The output light from the laser source is split by a 90:10 optical fiber coupler where 90% of the light is propagated to the sample arm (imaging probe) and the remaining 10% to a retroreflector "compensation arm" with adjustable optical power. Since the common-path configuration is utilized to achieve high phase stability, the reference arm is achieved through reflecting a small portion of light by the angled distal end of the GRIN fiber. The backscattered light from the sample and the back-reflected reference beam generate an interference signal which

is then delivered to one channel of the balanced photodetector. The signal from the compensation arm is collected by the other channel of the photodetector to offset the undesired DC component in the interferogram that lowers the SNR and causes phase washout. A computer workstation with two high-performance graphic processing units will be used for image processing and real-time display. A US pulser/receiver will be used to generate acoustic waves and receive and amplify the returning US signals for IVUS. To provide the ARF for tissue excitation, a function generator is synchronized with the λ trigger from the laser to generate an 18-MHz sine wave (duration: 20 μs) that is then amplified to drive the ultrasound transducer.

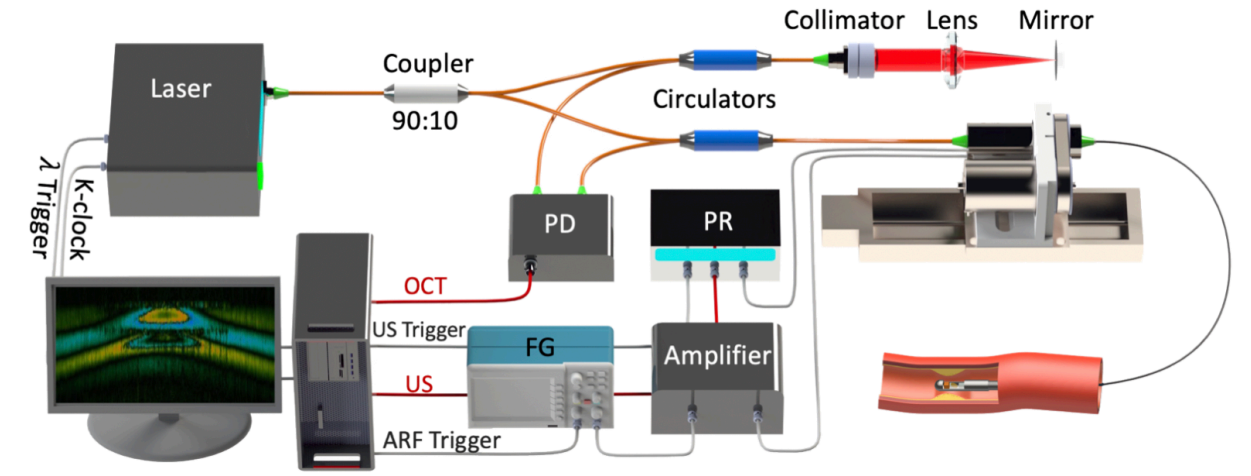

Figure 7.1 Schematic of the proposed intravascular system. FG: function generator. PD: photodetector. PR: pulser/receiver.

(2) Trimodal intravascular imaging probe and dual-rotation scan

Figure 7.2 (a) presents the schematic diagram of the proposed imaging probe. The imaging and the pushing transducer (45-MHz and 18-MHz center frequency, respectively) are diametrically aligned, facing away from each other. The optical sub-probe is interposed between the two transducers. To minimize the probe dimension, a graded-index (GRIN) fiber with the same diameter as the single mode fiber (SMF) is fused at the end of the SMF to allow focused

illumination. The emitting light from the GRIN fiber is then reflected by a rod mirror attached onto the shaft of a micromotor that can operate at 4,900 revolutions per second (rps). In order to achieve a high phase stability for accurate OCE_{SW} measurement, a common-path configuration is incorporated in the optical sub-probe. This is achieved by polishing the distal end of the GRIN fiber at a specific angle to partially reflect the illumination light which acts as the reference arm. This configuration provides a highly stable phase by minimizing the fluctuation of optical path difference between the sample and reference arms. Furthermore, the polarization and the dispersion mismatch can be intrinsically compensated for to enhance the axial resolution and signal-to-noise ratio (SNR).

The reported highest imaging speed of IVOCT currently is 5,600 fps [365]. In conventional IVUS-OCT design where a single scanning scheme is utilized, the imaging speed of OCT is confined by US. Because of the slow propagation speed of acoustic waves, the imaging speed of modern IVUS is limited to ~100 fps (30 fps in typical clinical practices). To bridge the speed gap between IVOCT and IVUS imaging, we will implement dual-rotation radial scan in which OCT is driven by a high-speed micromotor (distal fast scan) while US imaging and ARF pushing are steered through a torque coil by a rotary joint device (proximal slow scan). As such, the rotations of the optical and acoustic path can be separately controlled, achieving simultaneous but variable scanning operation. More importantly, this mechanism allows for the B-M scanning protocol because the pushing duration is substantially shorter than the period of the slow scan such that the ARF excitation with respect to its own rotation is considered static. To achieve proximal scanning, the entire probe is rotated at 100 rps through connection to a rotary joint device in which an optical rotary joint with a mercury slip ring is driven by a motor to enable rotation of the probe,

shown in Figure 7.2 (b). Combined with the micromotor operating at 4,900 rps, the proposed IVOCT will acquire OCT images at 5,000 fps.

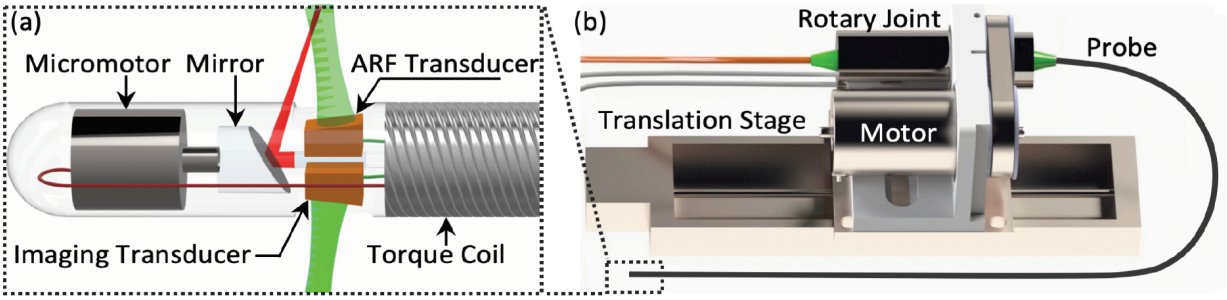

Figure 7.2 Schematic of (a) IVOCT-US-OCE$_{SW}$ probe and (b) rotary joint.

In summary, the future goal is to develop a multimodal intravascular imaging system that simultaneously performs OCT, US, and OCE$_{SW}$ and to ready this technology for clinical applications. This will enhance clinicians' ability to identify vulnerable lesions, tailor interventional therapy, and monitor disease progression. More importantly, it will be a powerful tool that provides a quantitative means to benchmark and evaluate new medical devices and therapies.

7.2.2 Single-Shot ARF-OCE$_{SW}$ for Ophthalmology

OCE possesses micron-level resolution and an axial displacement sensitivity on the order of a few nanometers, and it has been widely applied in ophthalmology to provide quantitative assessment of tissue biomechanical properties. However, in most cases, a repeated and relative strong ARF is necessary to accurately reconstruct the elastic wave propagation, and such force elongates the exposure of the tissue to the excitation source (including acoustic and light) as well as exceeds the ophthalmic mechanical index (MI) safety standard of 0.23 approved by the Food and Drug Administration [106, 187, 207]. In Chapter 5, we introduced an ultrahigh sensitivity

OCE system which is able to scale down the single excitation ARF by at least 1 order of magnitude while maintaining sufficient signal-to-noise ratio (SNR), and this may potentially limit the required ARF to be within the safety MI. As a next step, we proposed a single-shot ARF-OCE_{SW} system to further reduce the total exposure time of excitation using Fourier domain mode locking (FDML) lasers which are able to provide a laser repetition rate in the MHz range. The rapid repetition rate of the laser will also enable B-M mode scanning with single-shot excitation, achieving high-speed OCE_{SW} that greatly reduces the procedure time and hence minimizing the light and acoustic radiation force (ARF). Furthermore, the proposed single-shot ARF-OCE_{SW} system has the capability to minimize artifacts induced by bulk motion of the body.

(1) System design

A schematic of the single-shot ARF-OCE_{SW} system is demonstrated in Figure 7.3. In contrast to the schematic of ARF-OCE discussed in Section 5.1.1, there are two main improvements. First, an ultra-fast 1,060±50 nm FDML laser with a scan repetition rate of 2.8 MHz will be the light source of the system which enables B-M mode scanning with single-shot excitation. In addition, a coaxial alignment between OCT illumination light and acoustic radiation force is applied which is able to improve the ease of use and reduce the form factor of the sample arm, further facilitating the translation of this technology to clinical use.

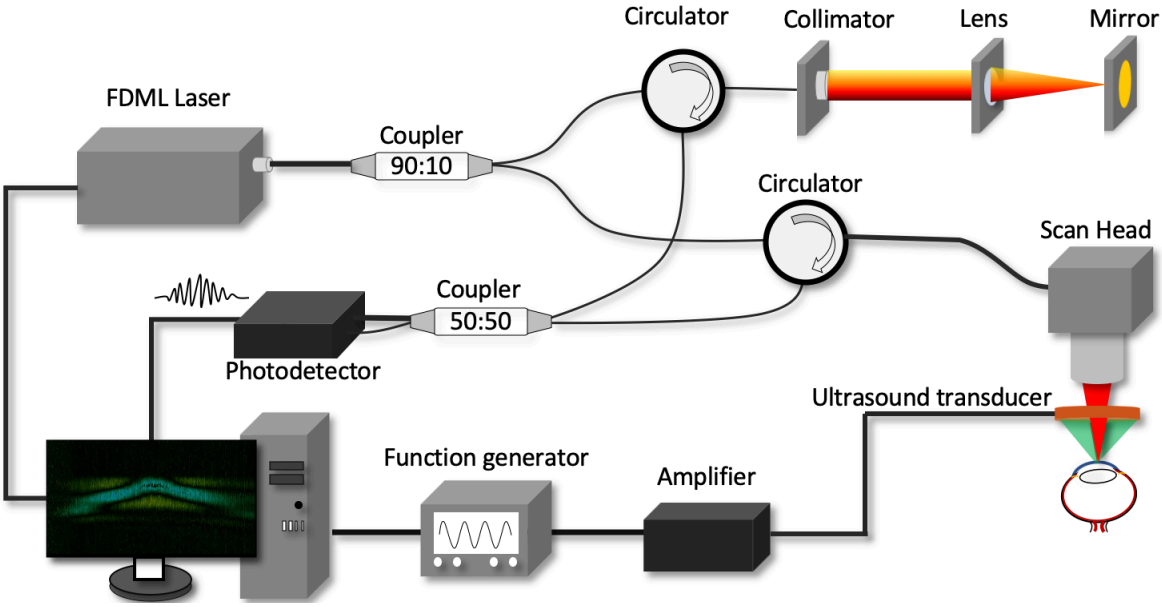

Figure 7.3 Schematic of ARF-OCE$_{SW}$ system. FDML: Fourier domain mode locking.

(2) Scanning protocol

The propagation velocity of the elastic wave provides a direct measurement of the biomechanical property as pre-calibration or the knowledge of applied force is not needed to convert the displacement to elasticity. To visualize the elastic wave propagation in real time, a B-M mode protocol will be applied. At each lateral position along the slow scan direction, sequential cross-sectional OCT images (fast scan X) will be acquired to record phase change over time (one B-M mode). After one B-M mode data acquisition, the slow scanner moves the detection beam to the next lateral position, and the same B-M mode scan is repeated for reconstructing 3-D elastic wave propagation. The scanning protocol is summarized in Figure 7.4. The ARF transducer will be excited at the beginning of the first B-M mode.

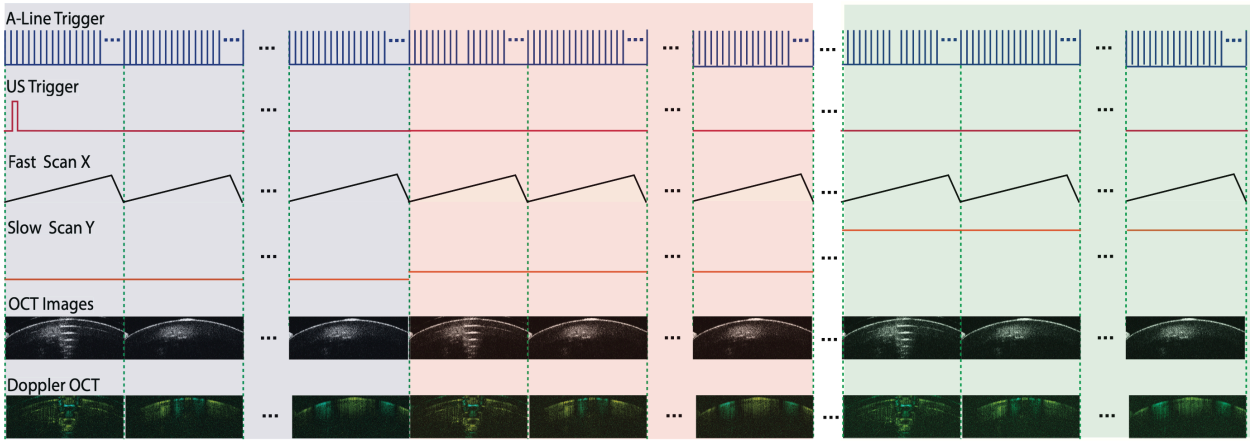

Figure 7.4 Scanning protocol

In summary, the future study will center on the design, construction, and evaluation of the single-shot OCE system with confocal acoustic radiation force excitation (confocal ARF-OCE). The single-shot ARF-OCE will have the capability to spatially map localized tissue elasticity in a large field of view, allowing for probing biomechanical properties at the tissue level. Compared to its conventional counterparts, the proposed system delivers optical and acoustic energy that is under the exposure limit and therefore can be safely translated to clinical applications.

References

[1] J. Jing, J. Zhang, A.C. Loy, B.J. Wong, Z. Chen, High-speed upper-airway imaging using full-range optical coherence tomography, J Biomed Opt 17(11) (2012) 110507.

[2] M.A. Calfon, A. Rosenthal, G. Mallas, A. Mauskapf, R.N. Nudelman, V. Ntziachristos, F.A. Jaffer, In vivo near infrared fluorescence (NIRF) intravascular molecular imaging of inflammatory plaque, a multimodal approach to imaging of atherosclerosis, J Vis Exp (54) (2011).

[3] A.M. Altman, J. Bankson, N. Matthias, J.V. Vykoukal, Y.H. Song, E.U. Alt, Magnetic resonance imaging as a novel method of characterization of cutaneous photoaging in a murine model, Arch Dermatol Res 300(5) (2008) 263-7.

[4] X.D. Wang, Y.J. Pang, G. Ku, X.Y. Xie, G. Stoica, L.H.V. Wang, Noninvasive laser-induced photoacoustic tomography for structural and functional in vivo imaging of the brain, Nat Biotechnol 21(7) (2003) 803-806.

[5] J.M. Yang, K. Maslov, H.C. Yang, Q. Zhou, K.K. Shung, L.V. Wang, Photoacoustic endoscopy, Opt Lett 34(10) (2009) 1591-3.

[6] Y. Zhao, Z. Chen, C. Saxer, S. Xiang, J.F. de Boer, J.S. Nelson, Phase-resolved optical coherence tomography and optical Doppler tomography for imaging blood flow in human skin with fast scanning speed and high velocity sensitivity, Opt Lett 25(2) (2000) 114-6.

[7] G. Liu, Z. Chen, Advances in Doppler OCT, Chinese Optics Letters 11(1) (2013).

[8] J. Zhu, Y. Qu, T. Ma, R. Li, Y. Du, S. Huang, K. Kirk Shung, Q. Zhou, Z. Chen, Imaging and characterizing shear wave and shear modulus under orthogonal acoustic radiation force excitation using OCT Doppler variance method, Optics letters 40(9) (2015) 2099-102.

[9] V. Hoang, J. Grounds, D. Pham, S. Virani, I. Hamzeh, A.M. Qureshi, N. Lakkis, M. Alam, The Role of Intracoronary Plaque Imaging with Intravascular Ultrasound, Optical Coherence Tomography, and Near-Infrared Spectroscopy in Patients with Coronary Artery Disease, Curr Atheroscler Rep 18(9) (2016) 57.

[10] H.G. Bezerra, M.A. Costa, G. Guagliumi, A.M. Rollins, D.I. Simon, Intracoronary optical coherence tomography: a comprehensive review clinical and research applications, JACC Cardiovasc Interv 2(11) (2009) 1035-46.

[11] D. Huang, E.A. Swanson, C.P. Lin, J.S. Schuman, W.G. Stinson, W. Chang, M.R. Hee, T. Flotte, K. Gregory, C.A. Puliafito, Optical coherence tomography, Science 254(5035) (1991) 1178-81.

[12] Y. Qu, T. Ma, Y. He, M. Yu, J. Zhu, Y. Miao, C. Dai, P. Patel, K.K. Shung, Q. Zhou, Z. Chen, Miniature probe for mapping mechanical properties of vascular lesions using acoustic radiation force optical coherence elastography, Sci Rep 7(1) (2017) 4731.

[13] Wenjuan Qi, Rui Li, Teng Ma, Jiawen Li, K. Kirk Shung, Qifa Zhou, Z. Chen, Resonant acoustic radiation force optical coherence elastography, Appl Phys Lett. 103(10) (2013) 103704.

[14] Wenjuan Qi, Ruimin Chen, Lidek Chou, Gangjun Liu, Jun Zhang, Qifa Zhou, Z. Chen., Phase-resolved acoustic radiation force optical coherence elastography, J Biomed Opt 17(11) (2012) 110505.

[15] Wenjuan Qi, Rui Li, Teng Ma, K. Kirk Shung, Qifa Zhou, Z. Chen, Confocal acoustic radiation force optical coherence elastography using a ring ultrasonic transducer, Appl. Phys. Lett. 104 (2014) 123702.

[16] S. Karlsson, E. Anesäter, K. Fransson, P. Andell, J. Persson, D. Erlinge, Intracoronary near-infrared spectroscopy and the risk of future cardiovascular events, Open Heart 6(1) (2019) e000917.

[17] R.D. Madder, S. VanOosterhout, D. Klungle, A. Mulder, M. Elmore, J.M. Decker, D. Langholz, T.F. Boyden, J. Parker, J.E. Muller, Multimodality Intracoronary Imaging With Near-Infrared Spectroscopy and Intravascular Ultrasound in Asymptomatic Individuals With High Calcium Scores, Circ Cardiovasc Imaging 10(10) (2017).

[18] T. Hara, F.A. Jaffer, Intravascular NIRF Molecular Imaging Approaches in Coronary Artery Disease, Curr Cardiovasc Imaging Rep 9 (2016).

[19] Z. Piao, T. Ma, J. Li, M.T. Wiedmann, S. Huang, M. Yu, K. Kirk Shung, Q. Zhou, C.S. Kim, Z. Chen, High speed intravascular photoacoustic imaging with fast optical parametric oscillator laser at 1.7 mum, Applied physics letters 107(8) (2015) 083701.

[20] Y. Cao, J. Hui, A. Kole, P. Wang, Q. Yu, W. Chen, M. Sturek, J.X. Cheng, High-sensitivity intravascular photoacoustic imaging of lipid-laden plaque with a collinear catheter design, Scientific reports 6 (2016) 25236.

[21] M. Wu, A. Fw van der Steen, E. Regar, G. van Soest, Emerging Technology Update Intravascular Photoacoustic Imaging of Vulnerable Atherosclerotic Plaque, Interv Cardiol 11(2) (2016) 120-123.

[22] T. Sawada, J. Shite, H.M. Garcia-Garcia, T. Shinke, S. Watanabe, H. Otake, D. Matsumoto, Y. Tanino, D. Ogasawara, H. Kawamori, H. Kato, N. Miyoshi, M. Yokoyama, P.W. Serruys, K. Hirata, Feasibility of combined use of intravascular ultrasound radiofrequency data analysis and optical coherence tomography for detecting thin-cap fibroatheroma, Eur Heart J 29(9) (2008) 1136-46.

[23] M. Michail, P.W. Serruys, R. Stettler, T. Crake, R. Torii, E. Tenekecioglu, Y. Zeng, Y. Onuma, A. Mathur, C.V. Bourantas, Intravascular multimodality imaging: feasibility and role in the evaluation of coronary plaque pathology, Eur Heart J Cardiovasc Imaging 18(6) (2017) 613-620.

[24] C.V. Bourantas, F.A. Jaffer, F.J. Gijsen, G. van Soest, S.P. Madden, B.K. Courtney, A.M. Fard, E. Tenekecioglu, Y. Zeng, A.F.W. van der Steen, S. Emelianov, J. Muller, P.H. Stone, L. Marcu, G.J. Tearney, P.W. Serruys, Hybrid intravascular imaging: recent advances, technical considerations, and current applications in the study of plaque pathophysiology, Eur Heart J 38(6) (2017) 400-412.

[25] A.J. Lusis, Atherosclerosis, Nature 407(6801) (2000) 233-41.

[26] C. Weber, H. Noels, Atherosclerosis: current pathogenesis and therapeutic options, Nat Med 17(11) (2011) 1410-22.

[27] C. Stefanadis, C. Antoniou, D. Tsiachris, P. Pietri, Coronary Atherosclerotic Vulnerable Plaque: Current Perspectives, Journal of the American Heart Association 6(3) (2017).

[28] J. Silva Marques, F.J. Pinto, The vulnerable plaque: current concepts and future perspectives on coronary morphology, composition and wall stress imaging, Rev Port Cardiol 33(2) (2014) 101-10.

[29] A.V. Finn, Y. Chandrashekhar, J. Narula, Vulnerable plaques: from PROSPECT to Prospects... J. Am. coll. Cardiol. Img. 5 (2012) 334-6.

[30] M.J. Bom, D.J. van der Heijden, E. Kedhi, J. van der Heyden, M. Meuwissen, P. Knaapen, S.A.J. Timmer, N. van Royen, Early Detection and Treatment of the Vulnerable Coronary Plaque: Can We Prevent Acute Coronary Syndromes?, Circ Cardiovasc Imaging 10(5) (2017).

[31] A. Sharma, A. Arbab-Zadeh, Detection of the Vulnerable Coronary Atherosclerotic Plaque-Promises and Limitations, Current Cardiovascular Imaging Reports 10(9) (2017).

[32] J.L. Fleg, G.W. Stone, Z.A. Fayad, J.F. Granada, T.S. Hatsukami, F.D. Kolodgie, J. Ohayon, R. Pettigrew, M.S. Sabatine, G.J. Tearney, S. Waxman, M.J. Domanski, P.R. Srinivas, J. Narula, Detection of high-risk atherosclerotic plaque: report of the NHLBI Working Group on current status and future directions, JACC Cardiovasc Imaging 5(9) (2012) 941-55.

[33] R.A. Swallow, I.A. Court, A.L. Calver, N.P. Curzen, The limitations of coronary angiography: identification of a critical coronary stenosis using intravascular ultrasound, Int J Cardiol 106(1) (2006) 123-5.

[34] S.E. Nissen, Limitations of computed tomography coronary angiography, J Am Coll Cardiol 52(25) (2008) 2145-7.

[35] F. Prati, [Coronary computed tomography angiography in coronary heart disease: clinical applications and limitations], G Ital Cardiol (Rome) 20(7) (2019) 409-416.

[36] S.E. Nissen, P. Yock, Intravascular ultrasound: novel pathophysiological insights and current clinical applications, Circulation 103 (2001) 604 –16.

[37] G.S. Mintz, N.J. Weissman, Intravascular Ultrasound in the Drug-Eluting Stent Era(2006), Journal of the American College of Cardiology 48 (2006) 421.

[38] J. Bermejo, J. Botas, E. Garcia, J. Elizaga, J. Osende, J. Soriano, M. Abeytua, J.L. Delcan, Mechanisms of residual lumen stenosis after high-pressure stent implantation: a quantitative coronary angiography and intravascular ultrasound study, Circulation 98 (1998) 112-8.

[39] C. Hanekamp, J. Koolen, J. Pijls, H. Michels, H. Bonnier, Comparison of quantitative coronary angiography, intravascular ultrasound, and coronary pressure measurement to assess optimum stent deployment, Circulation 99 (1999) 1015-21.

[40] M. Cilingiroglu, J.H. Oh, B. Sugunan, N.J. Kemp, J. Kim, S. Lee, H.N. Zaatari, D. Escobedo, S. Thompson, T.E. Milner, M.D. Feldman, Detection of vulnerable plaque in a murine model of athereosclerosis with optical coherence tomography, Catheter. Cardiovasc. Interv. 67(6) (2006) 915-923.

[41] G.J. Tearney, I.K. Jang, B.E. Bouma, Optical coherence tomography for imaging vulnerable plaque, J. Biomed. Opt. 11(2) (2006) 021002.

[42] M. Villiger, A. Karanasos, J. Ren, N. Lippok, M. Shishkov, G. van Soest, S. Nadkarni, E. Regar, B. Bouma, Intravascular polarization sensitive optical coherence tomography in human patients, 2016 Conference on Lasers and Electro-Optics (Cleo) (2016).

[43] T. Sawada, J. Shite, G.-G.H. M., T. Shinke, S. Watanabe, H. Otake, D. Matsumoto, T. Y., D. Ogasawara, H. Kawamori, H. Kato, N. Miyoshi, M. Yokoyama, P.W. Serruys, K.I. Hirata, Feasibility of combined use of intravascular ultrasound radiofrequency data analysis and optical coherence tomography for detecting thin-cap fibroatheroma, European Heart Journal 29 (2008) 1136-46.

[44] R. Puri, M.I. Worthley, S.J. Nicholls, Intravascular imaging of vulnerable coronary plaque: current and future concepts, Nat Rev Cardiol 8(3) (2011) 131-9.

[45] F. Bray, J. Ferlay, I. Soerjomataram, R.L. Siegel, L.A. Torre, A. Jemal, Global cancer statistics 2018: GLOBOCAN estimates of incidence and mortality worldwide for 36 cancers in 185 countries, CA: a cancer journal for clinicians 68(6) (2018) 394-424.

[46] B.W. Stewart, C. Wild, International Agency for Research on Cancer, World Health Organization, World cancer report 2014.

[47] Wikipedia contributors, Endoscopy, Wikipedia, The Free Encyclopedia, 2019. https://en.wikipedia.org/w/index.php?title=Endoscopy&oldid=933326143.

[48] S.J. Winawer, S.D. Leidner, S.I. Hajdu, P. Sherlock, Colonoscopic biopsy and cytology in the diagnosis of colon cancer, Cancer 42(6) (1978) 2849-53.

[49] A. Gado, B. Ebeid, A. Abdelmohsen, A. Axon, Improving the Yield of Histological Sampling in Patients With Suspected Colorectal Cancer During Colonoscopy by Introducing a Colonoscopy Quality Assurance Program, Gastroenterology research 4(4) (2011) 157-161.

[50] J.C. van Rijn, J.B. Reitsma, J. Stoker, P.M. Bossuyt, S.J. van Deventer, E. Dekker, Polyp miss rate determined by tandem colonoscopy: a systematic review, Am J Gastroenterol 101(2) (2006) 343-50.

[51] T.H. Tsai, O.O. Ahsen, H.C. Lee, K. Liang, M. Figueiredo, Y.K. Tao, M.G. Giacomelli, B.M. Potsaid, V. Jayaraman, Q. Huang, A.E. Cable, J.G. Fujimoto, H. Mashimo, Endoscopic optical coherence angiography enables 3-dimensional visualization of subsurface microvasculature, Gastroenterology 147(6) (2014) 1219-21.

[52] G.C. Harewood, Assessment of clinical impact of endoscopic ultrasound on rectal cancer, Am J Gastroenterol 99(4) (2004) 623-7.

[53] K. Iseki, M. Tatsuta, H. Iishi, N. Sakai, H. Yano, S. Ishiguro, Effectiveness of the near-infrared electronic endoscope for diagnosis of the depth of involvement of gastric cancers, Gastrointest Endosc 52(6) (2000) 755-62.

[54] S. Yuan, C.A. Roney, J. Wierwille, C.W. Chen, B. Xu, G. Griffiths, J. Jiang, H. Ma, A. Cable, R.M. Summers, Y. Chen, Co-registered optical coherence tomography and fluorescence molecular imaging for simultaneous morphological and molecular imaging, Phys Med Biol 55(1) (2010) 191-206.

[55] Y. Li, J. Jing, Y. Qu, Y. Miao, B. Zhang, T. Ma, M. Yu, Q. Zhou, Z. Chen, Fully integrated optical coherence tomography, ultrasound, and indocyanine green-based fluorescence tri-modality system for intravascular imaging, Biomedical optics express 8(2) (2017) 1036-1044.

[56] D. Mascagni, L. Corbellini, P. Urciuoli, G. Di Matteo, Endoluminal ultrasound for early detection of local recurrence of rectal cancer, The British journal of surgery 76(11) (1989) 1176-80.

[57] T.S. Kirtane, M.S. Wagh, Endoscopic Optical Coherence Tomography (OCT): Advances in Gastrointestinal Imaging, Gastroenterology Research and Practice (2014).

[58] T. Kubo, T. Akasaka, Optical coherence tomography imaging: current status and future perspectives : Current and future developments in OCT, Cardiovasc Interv Ther 25(1) (2010) 2-10.

[59] V.X. Yang, S.J. Tang, M.L. Gordon, B. Qi, G. Gardiner, M. Cirocco, P. Kortan, G.B. Haber, G. Kandel, I.A. Vitkin, B.C. Wilson, N.E. Marcon, Endoscopic Doppler optical coherence tomography in the human GI tract: initial experience, Gastrointestinal endoscopy 61 (2006) 879-90.

[60] N. Iftimia, A.K. Iyer, D.X. Hammer, N. Lue, M. Mujat, M. Pitman, R.D. Ferguson, M. Amiji, Fluorescence-guided optical coherence tomography imaging for colon cancer screening: a preliminary mouse study, Biomed Opt Express 3(1) (2012) 178-91.

[61] Y. Li, J. Jing, E. Heidari, J. Zhu, Y. Qu, Z. Chen, Intravascular Optical Coherence Tomography for Characterization of Atherosclerosis with a 1.7 Micron Swept-Source Laser, Sci Rep 7(1) (2017) 14525.

[62] G.J. Ughi, H. Wang, E. Gerbaud, J.A. Gardecki, A.M. Fard, E. Hamidi, P. Vacas-Jacques, M. Rosenberg, F.A. Jaffer, G.J. Tearney, Clinical Characterization of Coronary Atherosclerosis With Dual-Modality OCT and Near-Infrared Autofluorescence Imaging, JACC Cardiovasc Imaging 9(11) (2016) 1304-1314.

[63] J. Mavadia, J. Xi, Y. Chen, X. Li, An all-fiber-optic endoscopy platform for simultaneous OCT and fluorescence imaging, Biomed Opt Express 3(11) (2012) 2851-9.

[64] Y. Li, Z.K. Zhu, J.C. Jing, J.J. Chen, A.E. Heidari, Y.M. He, J. Zhu, T. Ma, M.Y. Yu, Q.F. Zhou, Z.P. Chen, High-Speed Integrated Endoscopic Photoacoustic and Ultrasound Imaging System, Ieee J Sel Top Quant 25(1) (2019).

[65] Y. Li, R. Lin, C. Liu, J. Chen, H. Liu, R. Zheng, X. Gong, L. Song, In vivo photoacoustic/ultrasonic dual-modality endoscopy with a miniaturized full field-of-view catheter, Journal of biophotonics (2018) e201800034.

[66] B.A. Standish, K.K. Lee, A. Mariampillai, N.R. Munce, M.K. Leung, V.X. Yang, I.A. Vitkin, In vivo endoscopic multi-beam optical coherence tomography, Phys Med Biol 55(3) (2010) 615-22.

[67] V.X. Yang, S.J. Tang, M.L. Gordon, B. Qi, G. Gardiner, M. Cirocco, P. Kortan, G.B. Haber, G. Kandel, I.A. Vitkin, B.C. Wilson, N.E. Marcon, Endoscopic Doppler optical coherence tomography in the human GI tract: initial experience, Gastrointest Endosc 61(7) (2005) 879-90.

[68] Z. Chen, T.E. Milner, D. Dave, J.S. Nelson, Optical Doppler tomographic imaging of fluid flow velocity in highly scattering media, Optics letters 22(1) (1997) 64-6.

[69] A.M.D. Lee, K. Ohtani, C. MacAulay, A. McWilliams, T. Shaipanich, V.X.D. Yang, S. Lam, P. Lane, In vivo lung microvasculature visualized in three dimensions using fiber-optic color Doppler optical coherence tomography, J Biomed Opt 18(5) (2013).

[70] J.T. Alander, I. Kaartinen, A. Laakso, T. Patila, T. Spillmann, V.V. Tuchin, M. Venermo, P. Valisuo, A review of indocyanine green fluorescent imaging in surgery, Int J Biomed Imaging 2012 (2012) 940585.

[71] C.J. Gostout, S.L. Jacques, Infrared video imaging of subsurface vessels: a feasibility study for the endoscopic management of gastrointestinal bleeding, Gastrointest Endosc 41(3) (1995) 218-24.

[72] S.Y. Kim, S.J. Myung, Optical molecular imaging for diagnosing intestinal diseases, Clin Endosc 46(6) (2013) 620-6.

[73] T. Kimura, N. Muguruma, S. Ito, S. Okamura, Y. Imoto, H. Miyamoto, M. Kaji, E. Kudo, Infrared fluorescence endoscopy for the diagnosis of superficial gastric tumors, Gastrointest Endosc 66(1) (2007) 37-43.

[74] L.V. Wang, S. Hu, Photoacoustic tomography: in vivo imaging from organelles to organs, Science 335(6075) (2012) 1458-62.

[75] J. Yao, K.I. Maslov, L.V. Wang, In vivo photoacoustic tomography of total blood flow and potential imaging of cancer angiogenesis and hypermetabolism, Technology in cancer research & treatment 11(4) (2012) 301-7.

[76] J. Li, X. Li, D. Mohar, A. Raney, J. Jing, J. Zhang, A. Johnston, S. Liang, T. Ma, K.K. Shung, S. Mahon, M. Brenner, J. Narula, Q. Zhou, P.M. Patel, Z. Chen, Integrated IVUS-OCT for real-time imaging of coronary atherosclerosis, JACC. Cardiovascular imaging 7(1) (2014) 101-3.

[77] Y. Li, Z. Zhu, J.J. Chen, J.C. Jing, C.H. Sun, S. Kim, P.S. Chung, Z. Chen, Multimodal endoscopy for colorectal cancer detection by optical coherence tomography and near-infrared fluorescence imaging, Biomed Opt Express 10(5) (2019) 2419-2429.

[78] T.H. Tsai, C.L. Leggett, A.J. Trindade, A. Sethi, A.F. Swager, V. Joshi, J.J. Bergman, H. Mashimo, N.S. Nishioka, E. Namati, Optical coherence tomography in gastroenterology: a review and future outlook, J Biomed Opt 22(12) (2017) 1-17.

[79] I.S. Nash, P.R. Greene, C.S. Foster, Comparison of mechanical properties of keratoconus and normal corneas, Experimental eye research 35(5) (1982) 413-24.

[80] H.A. Weeber, G. Eckert, F. Soergel, C.H. Meyer, W. Pechhold, R.G. van der Heijde, Dynamic mechanical properties of human lenses, Experimental eye research 80(3) (2005) 425-34.

[81] R. Navarro, The Optical Design of the Human Eye: a Critical Review, J Optom 2(1) (2009) 3–18.

[82] R. Michael, A.J. Bron, The ageing lens and cataract: a model of normal and pathological ageing, Philosophical transactions of the Royal Society of London. Series B, Biological sciences 366(1568) (2011) 1278-92.

[83] K.R. Heys, S.L. Cram, R.J. Truscott, Massive increase in the stiffness of the human lens nucleus with age: the basis for presbyopia?, Molecular vision 10 (2004) 956-63.

[84] A. Glasser, M.A. Croft, P.L. Kaufman, Aging of the human crystalline lens and presbyopia, International ophthalmology clinics 41(2) (2001) 1-15.

[85] B. Gilmartin, The aetiology of presbyopia: a summary of the role of lenticular and extralenticular structures, Ophthalmic & physiological optics : the journal of the British College of Ophthalmic Opticians 15(5) (1995) 431-7.

[86] C. de Freitas, M. Ruggeri, F. Manns, A. Ho, J.M. Parel, In vivo measurement of the average refractive index of the human crystalline lens using optical coherence tomography, Optics letters 38(2) (2013) 85-7.

[87] M. Adhi, J.S. Duker, Optical coherence tomography--current and future applications, Current opinion in ophthalmology 24(3) (2013) 213-21.

[88] S.A. Read, M.J. Collins, D.R. Iskander, B.A. Davis, Corneal topography with Scheimpflug imaging and videokeratography: comparative study of normal eyes, Journal of cataract and refractive surgery 35(6) (2009) 1072-81.

[89] M. Tavakoli, P. Hossain, R.A. Malik, Clinical applications of corneal confocal microscopy, Clinical ophthalmology 2(2) (2008) 435-45.

[90] M.D. Twa, J. Li, S. Vantipalli, M. Singh, S. Aglyamov, S. Emelianov, K.V. Larin, Spatial characterization of corneal biomechanical properties with optical coherence elastography after UV cross-linking, Biomed Opt Express 5(5) (2014) 1419-27.

[91] S. Wang, K.V. Larin, Optical coherence elastography for tissue characterization: a review, Journal of biophotonics 8(4) (2015) 279-302.

[92] S. Wang, K.V. Larin, Noncontact depth-resolved micro-scale optical coherence elastography of the cornea, Biomed Opt Express 5(11) (2014) 3807-21.

[93] Z. Han, J. Li, M. Singh, C. Wu, C.H. Liu, R. Raghunathan, S.R. Aglyamov, S. Vantipalli, M.D. Twa, K.V. Larin, Optical coherence elastography assessment of corneal viscoelasticity with a modified Rayleigh-Lamb wave model, Journal of the mechanical behavior of biomedical materials 66 (2017) 87-94.

[94] M.A. Kirby, I. Pelivanov, S. Song, L. Ambrozinski, S.J. Yoon, L. Gao, D. Li, T.T. Shen, R.K. Wang, M. O'Donnell, Optical coherence elastography in ophthalmology, Journal of biomedical optics 22(12) (2017) 1-28.

[95] M. Singh, J. Li, Z. Han, R. Raghunathan, A. Nair, C. Wu, C.H. Liu, S. Aglyamov, M.D. Twa, K.V. Larin, Assessing the effects of riboflavin/UV-A crosslinking on porcine corneal mechanical anisotropy with optical coherence elastography, Biomed Opt Express 8(1) (2017) 349-366.

[96] A. Sarvazyan, T.J. Hall, M.W. Urban, M. Fatemi, S.R. Aglyamov, B.S. Garra, An Overview of Elastography - an Emerging Branch of Medical Imaging, Current medical imaging reviews 7(4) (2011) 255-282.

[97] J. Vappou, Magnetic resonance- and ultrasound imaging-based elasticity imaging methods: a review, Critical reviews in biomedical engineering 40(2) (2012) 121-34.

[98] S. Besner, G. Scarcelli, R. Pineda, S.H. Yun, In Vivo Brillouin Analysis of the Aging Crystalline Lens, Investigative ophthalmology & visual science 57(13) (2016) 5093-5100.

[99] Y. Feng, E.H. Clayton, Y. Chang, R.J. Okamoto, P.V. Bayly, Viscoelastic properties of the ferret brain measured in vivo at multiple frequencies by magnetic resonance elastography, Journal of biomechanics 46(5) (2013) 863-70.

[100] X. Zhang, Q. Wang, Z. Lyu, X. Gao, P. Zhang, H. Lin, Y. Guo, T. Wang, S. Chen, X. Chen, Noninvasive assessment of age-related stiffness of crystalline lenses in a rabbit model using ultrasound elastography, Biomed Eng Online 17(1) (2018) 75.

[101] G. Scarcelli, P. Kim, S.H. Yun, In vivo measurement of age-related stiffening in the crystalline lens by Brillouin optical microscopy, Biophysical journal 101(6) (2011) 1539-45.

[102] S.H. Yun, D. Chernyak, Brillouin microscopy: assessing ocular tissue biomechanics, Current opinion in ophthalmology 29(4) (2018) 299-305.

[103] K. Wang, B.K. Pierscionek, Biomechanics of the human lens and accommodative system: Functional relevance to physiological states, Progress in retinal and eye research (2018).

[104] Jiang Zhu, Xingdao He, Z. Chen, Acoustic radiation force optical coherence elastography for elasticity assessment of soft tissues, Applied Spectroscopy Reviews (2018).

[105] Y. Qu, T. Ma, Y. He, J. Zhu, C. Dai, M. Yu, S. Huang, F. Lu, K.K. Shung, Q. Zhou, Z. Chen, Acoustic Radiation Force Optical Coherence Elastography of Corneal Tissue, IEEE journal of selected topics in quantum electronics : a publication of the IEEE Lasers and Electro-optics Society 22(3) (2016).

[106] Y. Qu, Y. He, A. Saidi, Y. Xin, Y. Zhou, J. Zhu, T. Ma, R.H. Silverman, D.S. Minckler, Q. Zhou, Z. Chen, In Vivo Elasticity Mapping of Posterior Ocular Layers Using Acoustic Radiation Force Optical Coherence Elastography, Invest Ophthalmol Vis Sci 59(1) (2018) 455-461.

[107] J. Zhu, J. Yu, Y. Qu, Y. He, Y. Li, Q. Yang, T. Huo, X. He, Z. Chen, Coaxial excitation longitudinal shear wave measurement for quantitative elasticity assessment using phase-resolved optical coherence elastography, Optics letters 43(10) (2018) 2388-2391.

[108] J. Zhu, Y. Miao, L. Qi, Y. Qu, Y. He, Q. Yang, Z. Chen, Longitudinal shear wave imaging for elasticity mapping using optical coherence elastography, Applied physics letters 110(20) (2017) 201101.

[109] J. Zhu, L. Qi, Y.S. Miao, T. Ma, C.X. Dai, Y.Q. Qu, Y.M. He, Y.W. Gao, Q.F. Zhou, Z.P. Chen, 3D mapping of elastic modulus using shear wave optical micro-elastography, Sci Rep-Uk 6 (2016).

[110] H.W. Rogers, M.A. Weinstock, S.R. Feldman, B.M. Coldiron, Incidence Estimate of Nonmelanoma Skin Cancer (Keratinocyte Carcinomas) in the U.S. Population, 2012, JAMA Dermatol 151(10) (2015) 1081-6.

[111] H.W. Rogers, M.A. Weinstock, S.R. Feldman, B.M. Coldiron, Incidence Estimate of Nonmelanoma Skin Cancer (Keratinocyte Carcinomas) in the US Population, 2012, Jama Dermatol 151(10) (2015) 1081-1086.

[112] M.K. Tripp, M. Watson, S.J. Balk, S.M. Swetter, J.E. Gershenwald, State of the science on prevention and screening to reduce melanoma incidence and mortality: The time is now, CA: a cancer journal for clinicians (2016).

[113] E.A. Levin, Mortality rate from skin cancer, California medicine 83(6) (1955) 443-5.

[114] All Cancers Estimated Incidence, Mortality and Prevalence of All Cancers (excluding non-melanoma skin cancer) in 2012, Journal of the National Cancer Institute 109(9) (2017).

[115] J. Baldwin, A.E. Janitz, J. Erb-Alvarez, C. Snider, J.E. Campbell, Prevalence and Mortality of Melanoma in Oklahoma Among Racial Groups, 2000-2008, The Journal of the Oklahoma State Medical Association 109(7-8) (2016) 311-316.

[116] P. Carli, V. De Giorgi, E. Crocetti, F. Mannone, D. Massi, A. Chiarugi, B. Giannotti, Improvement of malignant/benign ratio in excised melanocytic lesions in the 'dermoscopy era': a retrospective study 1997-2001, The British journal of dermatology 150(4) (2004) 687-92.

[117] M.E. Vestergaard, P. Macaskill, P.E. Holt, S.W. Menzies, Dermoscopy compared with naked eye examination for the diagnosis of primary melanoma: a meta-analysis of studies performed in a clinical setting, The British journal of dermatology 159(3) (2008) 669-76.

[118] M.R.N. Avanaki, A. Hojjat, A.G. Podoleanu, Investigation of computer-based skin cancer detection using optical coherence tomography, J Mod Optic 56(13) (2009) 1536-1544.

[119] C.A. Banzhaf, L. Themstrup, H.C. Ring, M. Mogensen, G.B.E. Jemec, Optical coherence tomography imaging of non-melanoma skin cancer undergoing imiquimod therapy, Skin Res Technol 20(2) (2014) 170-176.

[120] R.L. Bard, High-Frequency Ultrasound Examination in the Diagnosis of Skin Cancer, Dermatologic clinics 35(4) (2017) 505-511.

[121] C. Clark, O. Markowitz, Confirmation of Non-Melanoma Skin Cancer Clearance Using Optical Coherence Tomography Imaging, Laser Surg Med 45(4) (2013) 281-281.

[122] L.F. di Ruffano, J. Dinnes, J.J. Deeks, N. Chuchu, S.E. Bayliss, C. Davenport, Y. Takwoingi, K. Godfrey, C. O'Sullivan, R.N. Matin, H. Tehrani, H.C. Williams, S. Bayliss, N. Chuchu, C. Davenport, J. Deeks, J. Dinnes, L.F. di Ruffano, K. Godfrey, R. Matin, C. O'Sullivan, Y. Takwoingi, H. Williams, R. Abbott, B. Aldridge, O. Bassett, S.A. Chan, A. Durack, M. Fawzy, A. Gulati, J. Moreau, L. Patel,

D. Saleh, D. Thompson, K.Y. Wong, L. Johnston, H. Tehrani, F. Bath-Hextall, J. Bowling, S.T. Cheung, C. Fleming, M. Gardiner, A. Jain, S. O'Connell, P. Lawton, J. Lear, M. Leeflang, R. Motley, P. Nathan, J. Newton-Bishop, M. Payne, R. Robinson, S. Rodwell, J. Schofield, N. Shroff, H. Tehrani, Z. Traill, F. Walter, A. Webster, C.S.C.D. Test, Optical coherence tomography for diagnosing skin cancer in adults, Cochrane Db Syst Rev (12) (2018).

[123] J. Dinnes, J. Bamber, N. Chuchu, S.E. Bayliss, Y. Takwoingi, C. Davenport, K. Godfrey, C. O'Sullivan, R.N. Matin, J.J. Deeks, H.C. Williams, G. Cochrane Skin Cancer Diagnostic Test Accuracy, High-frequency ultrasound for diagnosing skin cancer in adults, The Cochrane database of systematic reviews 12 (2018) CD013188.

[124] F. Farnetani, A. Scope, R.P. Braun, S. Gonzalez, P. Guitera, J. Malvehy, M. Manfredini, A.A. Marghoob, E. Moscarella, M. Oliviero, S. Puig, H.S. Rabinovitz, I. Stanganelli, C. Longo, C. Malagoli, M. Vinceti, G. Pellacani, Skin Cancer Diagnosis With Reflectance Confocal Microscopy Reproducibility of Feature Recognition and Accuracy of Diagnosis, Jama Dermatol 151(10) (2015) 1075-1080.

[125] U. Goyal, Y. Kim, H.A. Tiwari, R. Witte, B. Stea, A pilot study of ultrasound-guided electronic brachytherapy for skin cancer, Journal of contemporary brachytherapy 7(5) (2015) 374-80.

[126] K. Koenig, In vivo multiphoton tomography of skin cancer, Melanoma Res 26 (2016) E116-E117.

[127] K. Konig, Skin Cancer-Diagnostics with the new Method of Multiphoton Tomography (MPT), J Dtsch Dermatol Ges 15 (2017) 61-61.

[128] A. Levine, K. Wang, O. Markowitz, Optical Coherence Tomography in the Diagnosis of Skin Cancer, Dermatologic clinics 35(4) (2017) 465-+.

[129] M. Mogensen, G.B.E. Jemec, Diagnosis of non-melanoma skin cancer with Optical Coherence Tomography, J Invest Dermatol 126 (2006) S47-S47.

[130] A. Zemtsov, J. Reed, L. Dixon, Magnetic-Resonance-Imaging Evaluation Helps to Delineate a Recurrent Skin-Cancer Present under the Skin Flap, J Dermatol Surg Onc 18(6) (1992) 508-511.

[131] G. Liu, W. Jia, J.S. Nelson, Z. Chen, In vivo, high-resolution, three-dimensional imaging of port wine stain microvasculature in human skin, Lasers Surg Med 45(10) (2013) 628-32.

[132] H.S. Chen, C.H. Liu, W.C. Wu, H.J. Tseng, Y.S. Lee, Optical Coherence Tomography Angiography of the Superficial Microvasculature in the Macular and Peripapillary Areas in Glaucomatous and Healthy Eyes, Invest Ophthalmol Vis Sci 58(9) (2017) 3637-3645.

[133] J. Schmitt, Optical coherence tomography (OCT): A review, Ieee Journal of Selected Topics in Quantum Electronics 5(4) (1999) 1205-1215.

[134] Optical Coherence Tomography, 2nd edition ed., Springer2015.

[135] A.F. Fercher, C.K. Hitzenberger, W. Drexler, G. Kamp, H. Sattmann, In vivo optical coherence tomography, Am J Ophthalmol 116(1) (1993) 113-4.

[136] E.A. Swanson, J.A. Izatt, M.R. Hee, D. Huang, C.P. Lin, J.S. Schuman, C.A. Puliafito, J.G. Fujimoto, In vivo retinal imaging by optical coherence tomography, Opt Lett 18(21) (1993) 1864-6.

[137] A. Rollins, S. Yazdanfar, M. Kulkarni, R. Ung-Arunyawee, J. Izatt, In vivo video rate optical coherence tomography, Opt Express 3(6) (1998) 219-29.

[138] R. Leitgeb, C. Hitzenberger, A. Fercher, Performance of fourier domain vs. time domain optical coherence tomography, Opt Express 11(8) (2003) 889-94.

[139] M. Choma, M. Sarunic, C. Yang, J. Izatt, Sensitivity advantage of swept source and Fourier domain optical coherence tomography, Opt Express 11(18) (2003) 2183-9.

[140] Z. Chen, Y. Zhao, J. de Boer, J. Nelson, IEEE, Functional optical coherence tomography: technology and applications, Leos 2000 - Ieee Annual Meeting Conference Proceedings, Vols. 1 & 2 (2000) 268-268.

[141] J. Fujimoto, IEEE, Optical coherence tomography: Technology and applications, 2002 Ieee/leos International Conference on Optical Mems, Conference Digest (2002) 147-148.

[142] W. Drexler, J. Fujimoto, Optical Coherence Tomography: Technology and Applications, Optical Coherence Tomography: Technology and Applications (2008) 1-1346.

[143] A. FERCHER, C. HITZENBERGER, G. KAMP, S. ELZAIAT, MEASUREMENT OF INTRAOCULAR DISTANCES BY BACKSCATTERING SPECTRAL INTERFEROMETRY, Optics Communications 117(1-2) (1995) 43-48.

[144] R. Huber, M. Wojtkowski, J. Fujimoto, Fourier Domain Mode Locking (FDML): A new laser operating regime and applications for optical coherence tomography, Optics Express 14(8) (2006) 3225-3237.

[145] B.E. Bouma, S.H. Yun, B.J. Vakoc, M.J. Suter, G.J. Tearney, Fourier-domain optical coherence tomography: recent advances toward clinical utility, Curr Opin Biotechnol 20(1) (2009) 111-8.

[146] W. Drexler, J.G. Fujimoto, Optical Coherence Tomography: Technology and Applications, 2 ed., Springer2015.

[147] J.F. de Boer, B. Cense, B.H. Park, M.C. Pierce, G.J. Tearney, B.E. Bouma, Improved signal-to-noise ratio in spectral-domain compared with time-domain optical coherence tomography, Opt Lett 28(21) (2003) 2067-9.

[148] R.C. Youngquist, S. Carr, D.E. Davies, Optical coherence-domain reflectometry: a new optical evaluation technique, Opt Lett 12(3) (1987) 158-60.

[149] J. Ballif, R. Gianotti, P. Chavanne, R. Wälti, R.P. Salathé, Rapid and scalable scans at 21 m/s in optical low-coherence reflectometry, Opt Lett 22(11) (1997) 757-9.

[150] C.B. Su, Achieving variation of the optical path length by a few millimeters at millisecond rates for imaging of turbid media and optical interferometry: a new technique, Opt Lett 22(10) (1997) 665-7.

[151] G.J. Tearney, B.E. Bouma, J.G. Fujimoto, High-speed phase- and group-delay scanning with a grating-based phase control delay line, Opt Lett 22(23) (1997) 1811-3.

[152] R. Huber, M. Wojtkowski, K. Taira, J. Fujimoto, K. Hsu, Amplified, frequency swept lasers for frequency domain reflectometry and OCT imaging: design and scaling principles, Opt Express 13(9) (2005) 3513-28.

[153] E. Azimi, B. Liu, M.E. Brezinski, Real-time and high-performance calibration method for high-speed swept-source optical coherence tomography, J Biomed Opt 15(1) (2010) 016005.

[154] C.K. Hitzenberger, A. Baumgartner, W. Drexler, A.F. Fercher, Dispersion effects in partial coherence interferometry: implications for intraocular ranging, J Biomed Opt 4(1) (1999) 144-51.

[155] J.P. Marfice, O.R. Baiocchi, Dispersion approximation using higher-order Taylor series terms, Appl Opt 26(19) (1987) 4043-5.

[156] Z. Chen, T.E. Milner, S. Srinivas, X. Wang, A. Malekafzali, M.J. van Gemert, J.S. Nelson, Noninvasive imaging of in vivo blood flow velocity using optical Doppler tomography, Opt Lett 22(14) (1997) 1119-21.

[157] G. Liu, L. Chou, W. Jia, W. Qi, B. Choi, Z. Chen, Intensity-based modified Doppler variance algorithm: application to phase instable and phase stable optical coherence tomography systems, Opt Express 19(12) (2011) 11429-40.

[158] Y. Wang, D. Huang, Y. Su, X.S. Yao, Two-dimensional phase unwrapping in Doppler Fourier domain optical coherence tomography, Opt Express 24(23) (2016) 26129-26145.

[159] J. Zhu, X. He, Z. Chen, Current challenges and solutions of Doppler optical coherence tomography and angiography for neuroimaging, Apl Photonics 3(12) (2018).

[160] J.A. Izatt, M.D. Kulkarni, S. Yazdanfar, J.K. Barton, A.J. Welch, In vivo bidirectional color Doppler flow imaging of picoliter blood volumes using optical coherence tomography, Opt Lett 22(18) (1997) 1439-41.

[161] Z. Chen, Y. Zhao, S. Srinivas, J. Nelson, N. Prakash, R. Frostig, Optical Doppler Tomography, IEEE Journal of Selected Topics in Quantum Electronics 5(4) (1999) 1134-1141.

[162] Z. Chen, T.E. Milner, X. Wang, S. Srinivas, J.S. Nelson, Optical Doppler tomography: imaging in vivo blood flow dynamics following pharmacological intervention and photodynamic therapy, Photochem Photobiol 67(1) (1998) 56-60.

[163] J.S. Nelson, K.M. Kelly, Y. Zhao, Z. Chen, Imaging blood flow in human port-wine stain in situ and in real time using optical Doppler tomography, Arch Dermatol 137(6) (2001) 741-4.

[164] Y. Zhao, K. Brecke, H. Ren, Z. Ding, J. Nelson, Z. Chen, Three-dimensional reconstruction of in vivo blood vessels in human skin using phase-resolved optical Doppler tomography, Ieee Journal of Selected Topics in Quantum Electronics 7(6) (2001) 931-935.

[165] Y. Zhao, Z. Chen, C. Saxer, Q. Shen, S. Xiang, J.F. de Boer, J.S. Nelson, Doppler standard deviation imaging for clinical monitoring of in vivo human skin blood flow, Opt Lett 25(18) (2000) 1358-60.

[166] H. Ren, K.M. Brecke, Z. Ding, Y. Zhao, J.S. Nelson, Z. Chen, Imaging and quantifying transverse flow velocity with the Doppler bandwidth in a phase-resolved functional optical coherence tomography, Opt Lett 27(6) (2002) 409-11.

[167] L. Yu, Z. Chen, Doppler variance imaging for three-dimensional retina and choroid angiography, J Biomed Opt 15(1) (2010) 016029.

[168] Y. Jia, O. Tan, J. Tokayer, B. Potsaid, Y. Wang, J. Liu, M. Kraus, H. Subhash, J. Fujimoto, J. Hornegger, D. Huang, Split-spectrum amplitude-decorrelation angiography with optical coherence tomography, Optics Express 20(4) (2012) 4710-4725.

[169] Y. Huang, Q. Zhang, M.R. Thorell, L. An, M.K. Durbin, M. Laron, U. Sharma, G. Gregori, P.J. Rosenfeld, R.K. Wang, Swept-source OCT angiography of the retinal vasculature using intensity differentiation-based optical microangiography algorithms, Ophthalmic Surg Lasers Imaging Retina 45(5) (2014) 382-9.

[170] Y. Jia, S.T. Bailey, D.J. Wilson, O. Tan, M.L. Klein, C.J. Flaxel, B. Potsaid, J.J. Liu, C.D. Lu, M.F. Kraus, J.G. Fujimoto, D. Huang, Quantitative optical coherence tomography angiography of choroidal

neovascularization in age-related macular degeneration, Ophthalmology 121(7) (2014) 1435-44.

[171] T.E. de Carlo, A. Romano, N.K. Waheed, J.S. Duker, A review of optical coherence tomography angiography (OCTA), Int J Retina Vitreous 1 (2015) 5.

[172] I. Gorczynska, J.V. Migacz, R.J. Zawadzki, A.G. Capps, J.S. Werner, Comparison of amplitude-decorrelation, speckle-variance and phase-variance OCT angiography methods for imaging the human retina and choroid, Biomed Opt Express 7(3) (2016) 911-42.

[173] E.J. Lee, K.M. Lee, S.H. Lee, T.W. Kim, OCT Angiography of the Peripapillary Retina in Primary Open-Angle Glaucoma, Invest Ophthalmol Vis Sci 57(14) (2016) 6265-6270.

[174] A. Rabiolo, F. Gelormini, R. Sacconi, M.V. Cicinelli, G. Triolo, P. Bettin, K. Nouri-Mahdavi, F. Bandello, G. Querques, Comparison of methods to quantify macular and peripapillary vessel density in optical coherence tomography angiography, PLoS One 13(10) (2018) e0205773.

[175] A.C. Werner, L.Q. Shen, A Review of OCT Angiography in Glaucoma, Semin Ophthalmol 34(4) (2019) 279-286.

[176] A. Mariampillai, B.A. Standish, E.H. Moriyama, M. Khurana, N.R. Munce, M.K. Leung, J. Jiang, A. Cable, B.C. Wilson, I.A. Vitkin, V.X. Yang, Speckle variance detection of microvasculature using swept-source optical coherence tomography, Opt Lett 33(13) (2008) 1530-2.

[177] J. Zhu, B. Zhang, L. Qi, L. Wang, Q. Yang, Z. Zhu, T. Huo, Z. Chen, Quantitative angle-insensitive flow measurement using relative standard deviation OCT, Appl Phys Lett 111(18) (2017) 181101.

[178] L. An, J. Qin, R.K. Wang, Ultrahigh sensitive optical microangiography for in vivo imaging of microcirculations within human skin tissue beds, Opt Express 18(8) (2010) 8220-8.

[179] B. Park, M.C. Pierce, B. Cense, S.H. Yun, M. Mujat, G. Tearney, B. Bouma, J. de Boer, Real-time fiber-based multi-functional spectral-domain optical coherence tomography at 1.3 microm, Opt Express 13(11) (2005) 3931-44.

[180] J. Fingler, D. Schwartz, C. Yang, S.E. Fraser, Mobility and transverse flow visualization using phase variance contrast with spectral domain optical coherence tomography, Opt Express 15(20) (2007) 12636-53.

[181] C.L. Chen, R.K. Wang, Optical coherence tomography based angiography [Invited], Biomed Opt Express 8(2) (2017) 1056-1082.

[182] J. Schmitt, OCT elastography: imaging microscopic deformation and strain of tissue, Opt Express 3(6) (1998) 199-211.

[183] W. Qi, R. Li, T. Ma, K. Kirk Shung, Q. Zhou, Z. Chen, Confocal acoustic radiation force optical coherence elastography using a ring ultrasonic transducer, Appl Phys Lett 104(12) (2014) 123702.

[184] W. Qi, R. Li, T. Ma, J. Li, K. Kirk Shung, Q. Zhou, Z. Chen, Resonant acoustic radiation force optical coherence elastography, Appl Phys Lett 103(10) (2013) 103704.

[185] W. Qi, R. Chen, L. Chou, G. Liu, J. Zhang, Q. Zhou, Z. Chen, Phase-resolved acoustic radiation force optical coherence elastography, J Biomed Opt 17(11) (2012) 110505.

[186] H. Zhang, C. Wu, M. Singh, A. Nair, S. Aglyamov, K. Larin, Optical coherence elastography of cold cataract in porcine lens, J Biomed Opt 24(3) (2019) 1-7.

[187] Y. He, Y. Qu, J. Zhu, Y. Zhang, A. Saidi, T. Ma, Q. Zhou, Z. Chen, Confocal Shear Wave Acoustic Radiation Force Optical Coherence Elastography for Imaging and Quantification of the In Vivo Posterior Eye, Ieee Journal of Selected Topics in Quantum Electronics 25(1) (2019).

[188] C. Wu, S.R. Aglyamov, Z. Han, M. Singh, C.H. Liu, K.V. Larin, Assessing the biomechanical properties of the porcine crystalline lens as a function of intraocular pressure with optical coherence elastography, Biomed Opt Express 9(12) (2018) 6455-6466.

[189] V.S. De Stefano, M.R. Ford, I. Seven, W.J. Dupps, Live human assessment of depth-dependent corneal displacements with swept-source optical coherence elastography, PLoS One 13(12) (2018) e0209480.

[190] Y. Qu, Y. He, Y. Zhang, T. Ma, J. Zhu, Y. Miao, C. Dai, M. Humayun, Q. Zhou, Z. Chen, Quantified elasticity mapping of retinal layers using synchronized acoustic radiation force optical coherence elastography, Biomed Opt Express 9(9) (2018) 4054-4063.

[191] M.A. Kirby, I. Pelivanov, S. Song, Ł. Ambrozinski, S.J. Yoon, L. Gao, D. Li, T.T. Shen, R.K. Wang, M. O'Donnell, Optical coherence elastography in ophthalmology, J Biomed Opt 22(12) (2017) 1-28.

[192] J. Li, S. Wang, M. Singh, S. Aglyamov, S. Emelianov, M. Twa, K. Larin, Air-pulse OCE for assessment of age-related changes in mouse cornea in vivo, Laser Physics Letters 11(6) (2014).

[193] B. Kennedy, P. Wijesinghe, D. Sampson, The emergence of optical elastography in biomedicine, Nature Photonics 11(4) (2017) 215-221.

[194] S.L. Owens, Indocyanine green angiography, Br J Ophthalmol 80(3) (1996) 263-6.

[195] R.V. Agrawal, J. Biswas, D. Gunasekaran, Indocyanine green angiography in posterior uveitis, Indian J Ophthalmol 61(4) (2013) 148-59.

[196] J. Micheels, B. Alsbjorn, B. Sorensen, Laser doppler flowmetry. A new non-invasive measurement of microcirculation in intensive care?, Resuscitation 12(1) (1984) 31-9.

[197] M.D. Stern, Laser Doppler velocimetry in blood and multiply scattering fluids: theory, Appl Opt 24(13) (1985) 1968.

[198] N. Handa, R. Fukunaga, A. Uehara, H. Etani, S. Yoneda, K. Kimura, T. Kamada, Echo-Doppler velocimeter in the diagnosis of hypertensive patients: the renal artery Doppler technique, Ultrasound Med Biol 12(12) (1986) 945-52.

[199] A. Rege, N.V. Thakor, K. Rhie, A.P. Pathak, In vivo laser speckle imaging reveals microvascular remodeling and hemodynamic changes during wound healing angiogenesis, Angiogenesis 15(1) (2012) 87-98.

[200] A. Nadort, K. Kalkman, T.G. van Leeuwen, D.J. Faber, Quantitative blood flow velocity imaging using laser speckle flowmetry, Sci Rep 6 (2016) 25258.

[201] Z. Ding, Y. Zhao, H. Ren, J. Nelson, Z. Chen, Real-time phase-resolved optical coherence tomography and optical Doppler tomography, Opt Express 10(5) (2002) 236-45.

[202] Y. Zhao, Z. Chen, Z. Ding, H. Ren, J.S. Nelson, Real-time phase-resolved functional optical coherence tomography by use of optical Hilbert transformation, Opt Lett 27(2) (2002) 98-100.

[203] E. Pijewska, I. Gorczynska, M. Szkulmowski, Computationally effective 2D and 3D fast phase unwrapping algorithms and their applications to Doppler optical coherence tomography, Biomed Opt Express 10(3) (2019) 1365-1382.

[204] M.A. Schofield, Y. Zhu, Fast phase unwrapping algorithm for interferometric applications, Opt Lett 28(14) (2003) 1194-6.

[205] G. Liu, A.J. Lin, B.J. Tromberg, Z. Chen, A comparison of Doppler optical coherence tomography methods, Biomed Opt Express 3(10) (2012) 2669-80.

[206] R. Muthupillai, R.L. Ehman, Magnetic resonance elastography, Nat Med 2(5) (1996) 601-3.

[207] Y. Li, J. Zhu, J. Chen, J. Yu, Z. Jin, Y. Miao, A. Browne, Q. Zhou, Z. Chen, Simultaneously imaging and quantifying in vivo mechanical properties of crystalline lens and cornea using optical coherence elastography with acoustic radiation force excitation, APL Photonics 4(10) (2019) 106104.

[208] S. Es'haghian, K.M. Kennedy, P. Gong, Q. Li, L. Chin, P. Wijesinghe, D.D. Sampson, R.A. McLaughlin, B.F. Kennedy, volumetric quantitative micro-elastography of human skin, Biomed Opt Express 8(5) (2017) 2458-2471.

[209] L. Ambrozinski, S. Song, S. Yoon, I. Pelivanov, D. Li, L. Gao, T. Shen, R. Wang, M. O'Donnell, Acoustic micro-tapping for non-contact 4D imaging of tissue elasticity, Scientific Reports 6 (2016).

[210] J. Zhu, J. Yu, Y. Qu, Y. He, Y. Li, Q. Yang, T. Huo, X. He, Z. Chen, Coaxial excitation longitudinal shear wave measurement for quantitative elasticity assessment using phase-resolved optical coherence elastography, Optics Letters 43(10) (2018) 2388-2391.

[211] L. Wang, Photoacoustic Imaging and Spectroscopy, 1st ed., CRC Press 2009.

[212] W. Wei, X. Li, Q.F. Zhou, K.K. Shung, Z.P. Chen, Integrated ultrasound and photoacoustic probe for co-registered intravascular imaging, Journal of biomedical optics 16(10) (2011).

[213] Y. Yuan, S. Yang, D. Xing, Preclinical photoacoustic imaging endoscope based on acousto-optic coaxial system using ring transducer array, Opt Lett 35(13) (2010) 2266-8.

[214] X.R. Ji, K.D. Xiong, S.H. Yang, D. Xing, Intravascular confocal photoacoustic endoscope with dual-element ultrasonic transducer, Optics express 23(7) (2015) 9130-9136.

[215] J.M. Yang, K. Maslov, H.C. Yang, Q.F. Zhou, K.K. Shung, L.H.V. Wang, Photoacoustic endoscopy, Opt Lett 34(10) (2009) 1591-1593.

[216] L.V. Wang, Photoacoustic Imaging and Spectroscopy, Taylor & Francis/CRC Press Boca Raton, Florida, 2009.

[217] Y. Li, X. Gong, C. Liu, R. Lin, W. Hau, X. Bai, L. Song, High-speed intravascular spectroscopic photoacoustic imaging at 1000 A-lines per second with a 0.9-mm diameter catheter, J Biomed Opt 20(6) (2015) 065006.

[218] H.F. Zhang, K. Maslov, G. Stoica, L.V. Wang, Functional photoacoustic microscopy for high-resolution and noninvasive in vivo imaging, Nat Biotechnol 24(7) (2006) 848-51.

[219] H. Fang, K. Maslov, L.V. Wang, Photoacoustic Doppler effect from flowing small light-absorbing particles, Phys Rev Lett 99(18) (2007) 184501.

[220] J. Yao, K.I. Maslov, Y. Zhang, Y. Xia, L.V. Wang, Label-free oxygen-metabolic photoacoustic microscopy in vivo, J Biomed Opt 16(7) (2011) 076003.

[221] P.C. Beard, T.N. Mills, Characterization of post mortem arterial tissue using time-resolved photoacoustic spectroscopy at 436, 461 and 532 nm, Physics in medicine and biology 42(1) (1997) 177-198.

[222] X. Li, W. Wei, Q.F. Zhou, K.K. Shung, Z.P. Chen, Intravascular photoacoustic imaging at 35 and 80 MHz, Journal of biomedical optics 17(10) (2012).

[223] H. Crazzolara, W. Vonmuench, C. Rose, U. Thiemann, K.K. Haase, M. Ritter, K.R. Karsch, Analysis of the Acoustic Response of Vascular Tissue Irradiated by an Ultraviolet-Laser Pulse, J Appl Phys 70(3) (1991) 1847-1849.

[224] J. Hui, Y. Cao, Y. Zhang, A. Kole, P. Wang, G. Yu, G. Eakins, M. Sturek, W. Chen, J.X. Cheng, Real-time intravascular photoacoustic-ultrasound imaging of lipid-laden plaque in human coronary artery at 16 frames per second, Sci Rep 7(1) (2017) 1417.

[225] R. Bitton, R. Zemp, J. Yen, L.V. Wang, K.K. Shung, A 3-D high-frequency array based 16 channel photoacoustic microscopy system for in vivo micro-vascular imaging, IEEE Trans Med Imaging 28(8) (2009) 1190-7.

[226] J. Staley, P. Grogan, A.K. Samadi, H. Cui, M.S. Cohen, X. Yang, Growth of melanoma brain tumors monitored by photoacoustic microscopy, J Biomed Opt 15(4) (2010) 040510.

[227] S. Hu, K. Maslov, V. Tsytsarev, L.V. Wang, Functional transcranial brain imaging by optical-resolution photoacoustic microscopy, J Biomed Opt 14(4) (2009) 040503.

[228] W. Song, Q. Wei, T. Liu, D. Kuai, J.M. Burke, S. Jiao, H.F. Zhang, Integrating photoacoustic ophthalmoscopy with scanning laser ophthalmoscopy, optical coherence tomography, and fluorescein angiography for a multimodal retinal imaging platform, J Biomed Opt 17(6) (2012) 061206.

[229] H.F. Zhang, K. Maslov, M.L. Li, G. Stoica, L.V. Wang, In vivo volumetric imaging of subcutaneous microvasculature by photoacoustic microscopy, Opt Express 14(20) (2006) 9317-23.

[230] K.J. Rowland, J. Yao, L. Wang, C.R. Erwin, K.I. Maslov, L.V. Wang, B.W. Warner, Immediate alterations in intestinal oxygen saturation and blood flow after massive small bowel resection as measured by photoacoustic microscopy, J Pediatr Surg 47(6) (2012) 1143-9.

[231] J. Zhang, S. Yang, X. Ji, Q. Zhou, D. Xing, Characterization of lipid-rich aortic plaques by intravascular photoacoustic tomography: ex vivo and in vivo validation in a rabbit atherosclerosis model with histologic correlation, J Am Coll Cardiol 64(4) (2014) 385-90.

[232] M. Wu, G. Springeling, M. Lovrak, F. Mastik, S. Iskander-Rizk, T. Wang, H.M. van Beusekom, A.F. van der Steen, G. Van Soest, Real-time volumetric lipid imaging in vivo by intravascular photoacoustics at 20 frames per second, Biomed Opt Express 8(2) (2017) 943-953.

[233] J. Hui, Q. Yu, T. Ma, P. Wang, Y. Cao, R.S. Bruning, Y. Qu, Z. Chen, Q. Zhou, M. Sturek, J.X. Cheng, W. Chen, High-speed intravascular photoacoustic imaging at 1.7 μm with a KTP-based OPO, Biomed Opt Express 6(11) (2015) 4557-66.

[234] Y. Li, X.J. Gong, C.B. Liu, R.Q. Lin, W. Hau, X.S. Bai, L. Song, High-speed intravascular spectroscopic photoacoustic imaging at 1000 A-lines per second with a 0.9-mm diameter catheter, J Biomed Opt 20(6) (2015).

[235] H. Yabushita, B.E. Bouma, S.L. Houser, H.T. Aretz, I.K. Jang, K.H. Schlendorf, C.R. Kauffman, M. Shishkov, D.H. Kang, E.F. Halpern, G.J. Tearney, Characterization of human atherosclerosis by optical coherence tomography, Circulation 106(13) (2002) 1640-5.

[236] J. Yin, H.C. Yang, X. Li, J. Zhang, Q. Zhou, C. Hu, K.K. Shung, Z. Chen, Integrated intravascular optical coherence tomography ultrasound imaging system, J Biomed Opt 15(1) (2010) 010512.

[237] G.J. Tearney, H. Yabushita, S.L. Houser, H.T. Aretz, I.K. Jang, K.H. Schlendorf, C.R. Kauffman, M. Shishkov, E.F. Halpern, B.E. Bouma, Quantification of macrophage content in atherosclerotic plaques by optical coherence tomography, Circulation 107(1) (2003) 113-119.

[238] J.G. Fujimoto, S.A. Boppart, G.J. Tearney, B.E. Bouma, C. Pitris, M.E. Brezinski, High resolution in vivo intra-arterial imaging with optical coherence tomography, Heart 82(2) (1999) 128-133.

[239] G.J. Tearney, S. Waxman, M. Shishkov, B.J. Vakoc, M.J. Suter, M.I. Freilich, A.E. Desjardins, W.Y. Oh, L.A. Bartlett, M. Rosenberg, B.E. Bouma, Three-Dimensional Coronary Artery Microscopy by Intracoronary Optical Frequency Domain Imaging, Jacc-Cardiovasc Imag 1(6) (2008) 752-761.

[240] G.J. Tearney, M.E. Brezinski, B.E. Bouma, S.A. Boppart, C. Pitris, J.F. Southern, J.G. Fujimoto, In vivo endoscopic optical biopsy with optical coherence tomography, Science 276(5321) (1997) 2037-2039.

[241] M. Abran, B.E. Stahli, N. Merlet, T. Mihalache-Avram, M. Mecteau, E. Rheaume, D. Busseuil, J.C. Tardif, F. Lesage, Validating a bimodal intravascular ultrasound (IVUS) and near-infrared fluorescence (NIRF) catheter for atherosclerotic plaque detection in rabbits, Biomed Opt Express 6(10) (2015) 3989-3999.

[242] J.W. Li, T. Ma, D. Mohar, E. Steward, M.Y. Yu, Z.L. Piao, Y.M. He, K.K. Shung, Q.F. Zhou, P.M. Patel, Z.P. Chen, Ultrafast optical-ultrasonic system and miniaturized catheter for imaging and characterizing atherosclerotic plaques in vivo, Sci Rep-Uk 5 (2015).

[243] C.L. Tsai, J.C. Chen, W.J. Wang, Near-infrared Absorption Property of Biological Soft Tissue Constituents,, Journal of Medical and Biological Engineering 21 (2001) 7-14.

[244] J.C. Jing, L.D. Chou, E.C. Su, B.J.F. Wong, Z.P. Chen, Anatomically correct visualization of the human upper airway using a high-speed long range optical coherence tomography system with an integrated positioning sensor, Sci Rep-Uk 6 (2016).

[245] J. Zhu, Y.Q. Qu, T. Ma, R. Li, Y.Z. Du, S.H. Huang, K.K. Shung, Q.F. Zhou, Z.P. Chen, Imaging and characterizing shear wave and shear modulus under orthogonal acoustic radiation force excitation using OCT Doppler variance method, Opt Lett 40(9) (2015) 2099-2102.

[246] A.P. Schroeder, E. Falk, Vulnerable and dangerous coronary plaques, Atherosclerosis 118 Suppl (1995) S141-9.

[247] A.V. Finn, M. Nakano, J. Narula, F.D. Kolodgie, R. Virmani, Concept of vulnerable/unstable plaque, Arterioscler Thromb Vasc Biol 30(7) (2010) 1282-92.

[248] H. Garcia-Garcia, M. Costa, P. Serruys, Imaging of coronary atherosclerosis: intravascular ultrasound, European Heart Journal 31(20) (2010) 2456-2469C.

[249] T. Wang, W. Wieser, G. Springeling, R. Beurskens, C. Lancee, T. Pfeiffer, A. van der Steen, R. Huber, G. van Soest, Intravascular optical coherence tomography imaging at 3200 frames per second, Optics Letters 38(10) (2013) 1715-1717.

[250] J.G. Fujimoto, S.A. Boppart, G.J. Tearney, B.E. Bouma, C. Pitris, M.E. Brezinski, High resolution in vivo intra-arterial imaging with optical coherence tomography, Heart 82(2) (1999) 128-33.

[251] C. Vinegoni, I. Botnaru, E. Aikawa, M.A. Calfon, Y. Iwamoto, E.J. Folco, V. Ntziachristos, R. Weissleder, P. Libby, F.A. Jaffer, Indocyanine green enables near-infrared fluorescence imaging of lipid-rich, inflamed atherosclerotic plaques, Sci Transl Med 3(84) (2011) 84ra45.

[252] J. Jing, J. Li, X. Li, J. Yin, J. Zhang, K. Hoang, P. Patel, Q. Zhou, Z. Chen, J. Izatt, J. Fujimoto, V. Tuchin, Advances in a fully integrated intravascular OCT-Ultrasound system for cardiovascular imaging, Optical Coherence Tomography and Coherence Domain Optical Methods in Biomedicine Xvi 8213 (2012).

[253] T. Ma, J. Li, J. Jing, X. Li, P. Patee, K. Shung, Z. Chen, Q. Zhou, Real-time Co-registered IVUS-OCT Catheter for Atherosclerotic Plaque Identification, 2013 Ieee International Ultrasonics Symposium (Ius) (2013) 769-772.

[254] X. Li, J. Li, J. Jing, T. Ma, S. Liang, J. Zhang, D. Mohar, A. Raney, S. Mahon, M. Brenner, P. Patel, K.K. Shung, Q. Zhou, Z. Chen, Integrated IVUS-OCT Imaging for Atherosclerotic Plaque Characterization, IEEE J Sel Top Quantum Electron 20(2) (2014) 7100108.

[255] M. Abran, G. Cloutier, M.H. Cardinal, B. Chayer, J.C. Tardif, F. Lesage, Development of a photoacoustic, ultrasound and fluorescence imaging catheter for the study of atherosclerotic plaque, IEEE Trans Biomed Circuits Syst 8(5) (2014) 696-703.

[256] S. Liang, T. Ma, J. Jing, X. Li, J. Li, K.K. Shung, Q. Zhou, J. Zhang, Z. Chen, Trimodality imaging system and intravascular endoscopic probe: combined optical coherence tomography, fluorescence imaging and ultrasound imaging, Opt Lett 39(23) (2014) 6652-5.

[257] Y. Yang, X. Li, T. Wang, P.D. Kumavor, A. Aguirre, K.K. Shung, Q. Zhou, M. Sanders, M. Brewer, Q. Zhu, Integrated optical coherence tomography, ultrasound and photoacoustic imaging for ovarian tissue characterization, Biomed Opt Express 2(9) (2011) 2551-61.

[258] S. Liang, T. Ma, J. Jing, X. Li, J. Li, K. Shung, Q. Zhou, J. Zhang, Z. Chen, Trimodality imaging system and intravascular endoscopic probe: combined optical coherence tomography, fluorescence imaging and ultrasound imaging, Optics Letters 39(23) (2014) 6652-6655.

[259] M. Calfon, A. Rosenthal, G. Mallas, A. Mauskapf, R. Nudelman, V. Ntziachristos, F. Jaffer, In vivo Near Infrared Fluorescence (NIRF) Intravascular Molecular Imaging of Inflammatory Plaque, a Multimodal Approach to Imaging of Atherosclerosis, Jove-Journal of Visualized Experiments (54) (2011).

[260] H.P. Brecht, R. Su, M. Fronheiser, S.A. Ermilov, A. Conjusteau, A.A. Oraevsky, Whole-body three-dimensional optoacoustic tomography system for small animals, Journal of biomedical optics 14(6) (2009).

[261] J.M. Yang, R. Chen, C. Favazza, J. Yao, C. Li, Z. Hu, Q. Zhou, K.K. Shung, L.V. Wang, A 2.5-mm diameter probe for photoacoustic and ultrasonic endoscopy, Optics express 20(21) (2012) 23944-53.

[262] J.M. Yang, C. Favazza, R. Chen, J. Yao, X. Cai, K. Maslov, Q. Zhou, K.K. Shung, L.V. Wang, Simultaneous functional photoacoustic and ultrasonic endoscopy of internal organs in vivo, Nat Med 18(8) (2012) 1297-1302.

[263] C. Li, J.M. Yang, R. Chen, C.H. Yeh, L. Zhu, K. Maslov, Q. Zhou, K.K. Shung, L.V. Wang, Urogenital photoacoustic endoscope, Opt Lett 39(6) (2014) 1473-1476.

[264] J.M. Yang, C. Favazza, R. Chen, J. Yao, X. Cai, K. Maslov, Q. Zhou, K.K. Shung, L.V. Wang, Simultaneous functional photoacoustic and ultrasonic endoscopy of internal organs in vivo, Nat Med (2012).

[265] ANSI Standard Z136.1, (2000).

[266] G. Ku, B.D. Fornage, X. Jin, M. Xu, K.K. Hunt, L.V. Wang, Thermoacoustic and photoacoustic tomography of thick biological tissues toward breast imaging, Technology in cancer research & treatment 4(5) (2005) 559-66.

[267] R. Ansari, E.Z. Zhang, A.E. Desjardins, P.C. Beard, All-optical forward-viewing photoacoustic probe for high-resolution 3D endoscopy, Light Sci Appl 7 (2018) 75.

[268] S.J. Mathews, C. Little, C.D. Loder, R.D. Rakhit, W. Xia, E.Z. Zhang, P.C. Beard, M.C. Finlay, A.E. Desjardins, All-optical dual photoacoustic and optical coherence tomography intravascular probe, Photoacoustics 11 (2018) 65-70.

[269] G. Wissmeyer, M.A. Pleitez, A. Rosenthal, V. Ntziachristos, Looking at sound: optoacoustics with all-optical ultrasound detection, Light Sci Appl 7 (2018) 53.

[270] Z. Chen, S. Yang, Y. Wang, D. Xing, Noncontact broadband all-optical photoacoustic microscopy based on a low-coherence interferometer, Applied Physics Letters 106(4) (2015).

[271] Z. Guo, G. Li, S.L. Chen, Miniature probe for all-optical double gradient-index lenses photoacoustic microscopy, J Biophotonics 11(12) (2018) e201800147.

[272] G. Li, Z. Guo, S.L. Chen, Miniature all-optical probe for large synthetic aperture photoacoustic-ultrasound imaging, Opt Express 25(21) (2017) 25023-25035.

[273] C. Sheaff, S. Ashkenazi, An All-optical Thin-film High-frequency Ultrasound Transducer, 2011 Ieee International Ultrasonics Symposium (Ius) (2011) 1944-1947.

[274] S. Preisser, W. Rohringer, M. Liu, C. Kollmann, S. Zotter, B. Fischer, W. Drexler, All-optical highly sensitive akinetic sensor for ultrasound detection and photoacoustic imaging, Biomed Opt Express 7(10) (2016) 4171-4186.

[275] Y. Li, R. Lin, C. Liu, J. Chen, H. Liu, R. Zheng, X. Gong, L. Song, In vivo photoacoustic/ultrasonic dual-modality endoscopy with a miniaturized full field-of-view catheter, Journal of biophotonics 11(10) (2018) e201800034.

[276] Z. Guo, Y. Li, S.L. Chen, Miniature probe for in vivo optical- and acoustic-resolution photoacoustic microscopy, Optics letters 43(5) (2018) 1119-1122.

[277] A.B. Karpiouk, B. Wang, S.Y. Emelianov, Development of a catheter for combined intravascular ultrasound and photoacoustic imaging, Rev Sci Instrum 81(1) (2010) 014901.

[278] J.M. Yang, C. Li, R. Chen, Q. Zhou, K.K. Shung, L.V. Wang, Catheter-based photoacoustic endoscope, J Biomed Opt 19(6) (2014) 066001.

[279] J.M. Yang, C. Li, R. Chen, B. Rao, J. Yao, C.H. Yeh, A. Danielli, K. Maslov, Q. Zhou, K.K. Shung, L.V. Wang, Optical-resolution photoacoustic endomicroscopy in vivo, Biomedical optics express 6(3) (2015) 918-32.

[280] K. Jansen, M. Wu, A.F. van der Steen, G. van Soest, Photoacoustic imaging of human coronary atherosclerosis in two spectral bands, Photoacoustics 2(1) (2014) 12-20.

[281] X. Bai, X. Gong, W. Hau, R. Lin, J. Zheng, C. Liu, C. Zeng, X. Zou, H. Zheng, L. Song, Intravascular optical-resolution photoacoustic tomography with a 1.1 mm diameter catheter, PLoS One 9(3) (2014) e92463.

[282] D. VanderLaan, A.B. Karpiouk, D. Yeager, S. Emelianov, Real-Time Intravascular Ultrasound and Photoacoustic Imaging, IEEE Trans Ultrason Ferroelectr Freq Control 64(1) (2017) 141-149.

[283] Q. Zhou, K.H. Lam, H. Zheng, W. Qiu, K.K. Shung, Piezoelectric single crystals for ultrasonic transducers in biomedical applications, Progress in materials science 66 (2014) 87-111.

[284] Q. Zhou, E.L. Gottlieb , L. Sun, L.M. Cannata, H. Ameri, M.S. Humayun, H. Pengdi, K.K. Shung, PMN-PT single crystal, high-frequency ultrasonic needle transducers for pulsed-wave Doppler application, IEEE Trans. Ultrason., Ferroelect., Freq. Contr. 54 (2007) 668-75.

[285] G.Z.C.a.I.Y.S. Qing Guo, Measurements of Piezoelectric Coefficient d33 of Lead Zirconate Titanate Thin Films Using a Mini Force Hammer, J. Vib. Acoust 135(1) (2013).

[286] K.B. Kim, D.K. Hsu, B. Ahn, Y.G. Kim, D.J. Barnard, Fabrication and comparison of PMN-PT single crystal, PZT and PZT-based 1-3 composite ultrasonic transducers for NDE applications, Ultrasonics 50(8) (2010) 790-7.

[287] K.K.S.M.C.F. Zhou, Piezoelectric materials for high frequency medical imaging applications: A review, Journal of Electroceramics 19(1) (2007).

[288] P. Sun, Q.F. Zhou, B.P. Zhu, D.W. Wu, C.L. Hu, J.M. Cannata, J. Tian, P.D. Han, G.F. Wang, K.K. Shung, Design and Fabrication of PIN-PMN-PT Single-Crystal High-Frequency Ultrasound Transducers, Ieee T Ultrason Ferr 56(12) (2009) 2760-2763.

[289] H. Pahlevaninezhad, A.M. Lee, G. Hohert, S. Lam, T. Shaipanich, E.L. Beaudoin, C. MacAulay, C. Boudoux, P. Lane, Endoscopic high-resolution autofluorescence imaging and OCT of pulmonary vascular networks, Opt Lett 41(14) (2016) 3209-12.

[290] A.M. Winkler, P.F. Rice, J. Weichsel, J.M. Watson, M.V. Backer, J.M. Backer, J.K. Barton, In vivo, dual-modality OCT/LIF imaging using a novel VEGF receptor-targeted NIR fluorescent probe in the AOM-treated mouse model, Mol Imaging Biol 13(6) (2011) 1173-82.

[291] A.R. Tumlinson, L.P. Hariri, U. Utzinger, J.K. Barton, Miniature endoscope for simultaneous optical coherence tomography and laser-induced fluorescence measurement, Appl Opt 43(1) (2004) 113-21.

[292] H. Yoo, J.W. Kim, M. Shishkov, E. Namati, T. Morse, R. Shubochkin, J.R. McCarthy, V. Ntziachristos, B.E. Bouma, F.A. Jaffer, G.J. Tearney, Intra-arterial catheter for simultaneous microstructural and molecular imaging in vivo, Nat Med 17(12) (2011) 1680-4.

[293] H.L. Wang, X.X. Li, B.W.C. Tse, H.T. Yang, C.A. Thorling, Y.X. Liu, M. Touraud, J.B. Chouane, X. Liu, M.S. Roberts, X.W. Liang, Indocyanine green-incorporating nanoparticles for cancer theranostics, Theranostics 8(5) (2018) 1227-1242.

[294] S. Yoneya, T. Saito, Y. Komatsu, I. Koyama, K. Takahashi, J. Duvoll-Young, Binding properties of indocyanine green in human blood, Investigative ophthalmology & visual science 39(7) (1998) 1286-90.

[295] J.C. Delong, J.M. Chakedis, A. Hosseini, K.J. Kelly, S. Horgan, M. Bouvet, Indocyanine green (ICG) fluorescence-guided laparoscopic adrenalectomy, J Surg Oncol 112(6) (2015) 650-653.

[296] R.H. Shen, Y. Zhang, T. Wang, Indocyanine Green Fluorescence Angiography and the Incidence of Anastomotic Leak After Colorectal Resection for Colorectal Cancer: A Meta-analysis, Dis Colon Rectum 61(10) (2018) 1228-1234.

[297] J.M. Amos-Landgraf, L.N. Kwong, C.M. Kendziorski, M. Reichelderfer, J. Torrealba, J. Weichert, J.D. Haag, K.S. Chen, J.L. Waller, M.N. Gould, W.F. Dove, A target-selected Apc-mutant rat kindred enhances the modeling of familial human colon cancer, Proc Natl Acad Sci U S A 104(10) (2007) 4036-41.

[298] Y. Li, J. Jing, J. Yu, B. Zhang, T. Huo, Q. Yang, Z. Chen, Multimodality endoscopic optical coherence tomography and fluorescence imaging technology for visualization of layered architecture and subsurface microvasculature, Optics letters 43(9) (2018) 2074-2077.

[299] S. Wang, K.V. Larin, Shear wave imaging optical coherence tomography (SWI-OCT) for ocular tissue biomechanics, Optics letters 39(1) (2014) 41-4.

[300] Z. Han, S.R. Aglyamov, J. Li, M. Singh, S. Wang, S. Vantipalli, C. Wu, C.H. Liu, M.D. Twa, K.V. Larin, Quantitative assessment of corneal viscoelasticity using optical coherence elastography and a modified Rayleigh-Lamb equation, Journal of biomedical optics 20(2) (2015) 20501.

[301] M.R. Ford, W.J. Dupps, Jr., A.M. Rollins, R.A. Sinha, Z. Hu, Method for optical coherence elastography of the cornea, Journal of biomedical optics 16(1) (2011) 016005.

[302] S. Vantipalli, J. Li, M. Singh, S.R. Aglyamov, K.V. Larin, M.D. Twa, Effects of Thickness on Corneal Biomechanical Properties Using Optical Coherence Elastography, Optometry and vision science : official publication of the American Academy of Optometry 95(4) (2018) 299-308.

[303] M.D. Twa, G.P. Lan, M. Singh, K. Larin, In-vivo human corneal elasticity imaging: a phase sensitive optical coherence elastography method, Investigative ophthalmology & visual science 58(8) (2017).

[304] C. Wu, S.R. Aglyamov, Z.L. Han, M. Singh, C.H. Liu, K.V. Larin, Assessing the biomechanical properties of the porcine crystalline lens as a function of intraocular pressure with optical coherence elastography, Biomed Opt Express 9(12) (2018) 6455-6466.

[305] C. Wu, S.R. Aglyamov, H. Zhang, K.V. Larin, Measuring the elastic wave velocity in the lens of the eye as a function of intraocular pressure using optical coherent elastography, Quantum Electron+ 49(1) (2019) 20-24.

[306] Z. Chen, T.E. Milner, S. Srinivas, T. Lindmo, D. Dave, J.S. Nelson, Optical Doppler tomography for noninvasive imaging of in vivo blood flow, 1997, pp. 112-18.

[307] Z. Chen, Optical Doppler tomography, in: V.V. Tuchin (Ed.), Coherent-Domain Optical Methods for Biomedical Diagnostics, Environmental and Material Science, Kluwer Academic Publishers, Boston, 2004, pp. 315-40.

[308] C. Li, G. Guan, F. Zhang, G. Nabi, R.K. Wang, Z. Huang, Laser induced surface acoustic wave combined with phase sensitive optical coherence tomography for superficial tissue characterization: a solution for practical application, Biomed Opt Express 5(5) (2014) 1403-19.

[309] S. Reiss, G. Burau, O. Stachs, R. Guthoff, H. Stolz, Spatially resolved Brillouin spectroscopy to determine the rheological properties of the eye lens, Biomed Opt Express 2(8) (2011) 2144-2159.

[310] A.S. Vilupuru, A. Glasser, Optical and biometric relationships of the isolated pig crystalline lens, Ophthal Physl Opt 21(4) (2001) 296-311.

[311] M. Tanter, D. Touboul, J.L. Gennisson, J. Bercoff, M. Fink, High-Resolution Quantitative Imaging of Cornea Elasticity Using Supersonic Shear Imaging, IEEE transactions on medical imaging 28(12) (2009) 1881-1893.

[312] J. Kampmeier, B. Radt, R. Birngruber, R. Brinkmann, Thermal and biomechanical parameters of porcine cornea, Cornea 19(3) (2000) 355-363.

[313] M. Singh, J. Li, S. Vantipalli, S. Wang, Z. Han, A. Nair, S.R. Aglyamov, M.D. Twa, K.V. Larin, Noncontact Elastic Wave Imaging Optical Coherence Elastography for Evaluating Changes in

Corneal Elasticity Due to Crosslinking, IEEE journal of selected topics in quantum electronics : a publication of the IEEE Lasers and Electro-optics Society 22(3) (2016).

[314] L. Ambrozinski, S.Z. Song, S.J. Yoon, I. Pelivanov, D. Li, L. Gao, T.T. Shen, R.K.K. Wang, M. O'Donnell, Acoustic micro-tapping for non-contact 4D imaging of tissue elasticity, Scientific reports 6 (2016).

[315] C. Wu, Z. Han, S. Wang, J. Li, M. Singh, C.H. Liu, S. Aglyamov, S. Emelianov, F. Manns, K.V. Larin, Assessing age-related changes in the biomechanical properties of rabbit lens using a coaligned ultrasound and optical coherence elastography system, Investigative ophthalmology & visual science 56(2) (2015) 1292-300.

[316] T. Nelson, J. Fowlkes, J. Abramowicz, C. Church, Ultrasound Biosafety Considerations for the Practicing Sonographer and Sonologist, Journal of Ultrasound in Medicine 28(2) (2009) 139-150.

[317] S. Song, W. Wei, B.Y. Hsieh, I. Pelivanov, T.T. Shen, M. O'Donnell, R.K. Wang, Strategies to improve phase-stability of ultrafast swept source optical coherence tomography for single shot imaging of transient mechanical waves at 16 kHz frame rate, Appl Phys Lett 108(19) (2016) 191104.

[318] A. Szkulmowska, M. Szkulmowski, A. Kowalczyk, M. Wojtkowski, Phase-resolved Doppler optical coherence tomography - limitations and improvements, Optics Letters 33(13) (2008) 1425-1427.

[319] J.U. Kang, J.H. Han, X. Liu, K. Zhang, Common-Path Optical Coherence Tomography for Biomedical Imaging and Sensing, J Opt Soc Korea 14(1) (2010) 1-13.

[320] A.B. Vakhtin, D.J. Kane, W.R. Wood, K.A. Peterson, Common-path interferometer for frequency-domain optical coherence tomography, Appl Opt 42(34) (2003) 6953-8.

[321] K.M. Tan, M. Mazilu, T.H. Chow, W.M. Lee, K. Taguichi, B.K. Ng, W. Sibbett, C.S. Herrington, C.T. Brown, K. Dholakia, In-fiber common-path optical coherence tomography using a conical-tip fiber, Opt Express 17(4) (2009) 2375-84.

[322] G. Lan, M. Singh, K.V. Larin, M.D. Twa, Common-path phase-sensitive optical coherence tomography provides enhanced phase stability and detection sensitivity for dynamic elastography, Biomed Opt Express 8(11) (2017) 5253-5266.

[323] N. Leartprapun, R.R. Iyer, G.R. Untracht, J.A. Mulligan, S.G. Adie, Photonic force optical coherence elastography for three-dimensional mechanical microscopy, Nat Commun 9(1) (2018) 2079.

[324] A. Ahmad, J. Kim, N.A. Sobh, N.D. Shemonski, S.A. Boppart, Magnetomotive optical coherence elastography using magnetic particles to induce mechanical waves, Biomed Opt Express 5(7) (2014) 2349-61.

[325] Y.Q. Qu, Y.H. He, J. Jing, Characterization of oviduct ciliary beat frequency using real time phase resolved Doppler spectrally encoded interferometric microscopy, Biomedical Optics Express 10(10) (2019) (In press).

[326] H.C. Hendargo, R.P. McNabb, A.H. Dhalla, N. Shepherd, J.A. Izatt, Doppler velocity detection limitations in spectrometer-based versus swept-source optical coherence tomography, Biomed Opt Express 2(8) (2011) 2175-88.

[327] J.F. de Boer, R. Leitgeb, M. Wojtkowski, Twenty-five years of optical coherence tomography: the paradigm shift in sensitivity and speed provided by Fourier domain OCT [Invited], Biomed Opt Express 8(7) (2017) 3248-3280.

[328] S. Song, J. Xu, R.K. Wang, Long-range and wide field of view optical coherence tomography for in vivo 3D imaging of large volume object based on akinetic programmable swept source, Biomed Opt Express 7(11) (2016) 4734-4748.

[329] M. Tsai, Y. Lee, Y. Yao, C. Kung, F. Chang, J. Lee, Quantitative Phase Imaging With Swept-Source Optical Coherence Tomography for Optical Measurement of Nanostructures, Ieee Photonics Technology Letters 24(8) (2012) 640-642.

[330] M. Razani, A. Mariampillai, C. Sun, T.W. Luk, V.X. Yang, M.C. Kolios, Feasibility of optical coherence elastography measurements of shear wave propagation in homogeneous tissue equivalent phantoms, Biomed Opt Express 3(5) (2012) 972-80.

[331] R.K. Manapuram, S.R. Aglyamov, F.M. Monediado, M. Mashiatulla, J. Li, S.Y. Emelianov, K.V. Larin, In vivo estimation of elastic wave parameters using phase-stabilized swept source optical coherence elastography, J Biomed Opt 17(10) (2012) 100501.

[332] M. Singh, J. Li, Z. Han, S. Vantipalli, C.H. Liu, C. Wu, R. Raghunathan, S.R. Aglyamov, M.D. Twa, K.V. Larin, Evaluating the Effects of Riboflavin/UV-A and Rose-Bengal/Green Light Cross-Linking of the Rabbit Cornea by Noncontact Optical Coherence Elastography, Invest Ophthalmol Vis Sci 57(9) (2016) OCT112-20.

[333] J. Zhu, Y. Qu, T. Ma, R. Li, Y. Du, S. Huang, K.K. Shung, Q. Zhou, Z. Chen, Imaging and characterizing shear wave and shear modulus under orthogonal acoustic radiation force excitation using OCT Doppler variance method, Opt Lett 40(9) (2015) 2099-102.

[334] Z. Zhi, W. Qin, J. Wang, W. Wei, R.K. Wang, 4D optical coherence tomography-based micro-angiography achieved by 1.6-MHz FDML swept source, Opt Lett 40(8) (2015) 1779-82.

[335] J. Zhang, B. Rao, L. Yu, Z. Chen, High-dynamic-range quantitative phase imaging with spectral domain phase microscopy, Opt Lett 34(21) (2009) 3442-4.

[336] S. Moon, Z. Chen, Phase-stability optimization of swept-source optical coherence tomography, Biomed Opt Express 9(11) (2018) 5280-5295.

[337] Y. Li, G. Lu, J.J. Chen, J.C. Jing, T. Huo, R. Chen, L. Jiang, Q. Zhou, Z. Chen, PMN-PT/Epoxy 1-3 composite based ultrasonic transducer for dual-modality photoacoustic and ultrasound endoscopy, Photoacoustics 15 (2019) 100138.

[338] S. Choi, K. Sato, T. Ota, F. Nin, S. Muramatsu, H. Hibino, Multifrequency-swept optical coherence microscopy for highspeed full-field tomographic vibrometry in biological tissues, Biomed Opt Express 8(2) (2017) 608-621.

[339] S. Makita, Y. Yasuno, Detection of local tissue alteration during retinal laser photocoagulation of ex vivo porcine eyes using phase-resolved optical coherence tomography, Biomed Opt Express 8(6) (2017) 3067-3080.

[340] M. Lupu, C. Caruntu, M.I. Popa, V.M. Voiculescu, S. Zurac, D. Boda, Vascular patterns in basal cell carcinoma: Dermoscopic, confocal and histopathological perspectives, Oncol Lett 17(5) (2019) 4112-4125.

[341] Y. Li, J. Chen, Z. Chen, Advances in Doppler Optical Coherence Tomography and Angiography, Translational Biophotonics e201900005 (2019).

[342] M. Ulrich, T. von Braunmuehl, H. Kurzen, T. Dirschka, C. Kellner, E. Sattler, C. Berking, J. Welzel, U. Reinhold, The sensitivity and specificity of optical coherence tomography for the assisted diagnosis of nonpigmented basal cell carcinoma: an observational study, Br J Dermatol 173(2) (2015) 428-35.

[343] J. Olsen, L. Themstrup, N. De Carvalho, M. Mogensen, G. Pellacani, G.B. Jemec, Diagnostic accuracy of optical coherence tomography in actinic keratosis and basal cell carcinoma, Photodiagnosis Photodyn Ther 16 (2016) 44-49.

[344] O. Markowitz, M. Schwartz, E. Feldman, A. Bienenfeld, A.K. Bieber, J. Ellis, U. Alapati, M. Lebwohl, D.M. Siegel, Evaluation of Optical Coherence Tomography as a Means of Identifying Earlier Stage Basal Cell Carcinomas while Reducing the Use of Diagnostic Biopsy, J Clin Aesthet Dermatol 8(10) (2015) 14-20.

[345] M. Mogensen, T.M. Joergensen, B.M. Nürnberg, H.A. Morsy, J.B. Thomsen, L. Thrane, G.B. Jemec, Assessment of optical coherence tomography imaging in the diagnosis of non-melanoma skin cancer and benign lesions versus normal skin: observer-blinded evaluation by dermatologists and pathologists, Dermatol Surg 35(6) (2009) 965-72.

[346] Y. Li, N.T. Sudol, Y. Miao, J.C. Jing, J. Zhu, F. Lane, Z. Chen, 1.7 micron optical coherence tomography for vaginal tissue characterization in vivo, Lasers Surg Med 51(2) (2019) 120-126.

[347] U. Sharma, E.W. Chang, S.H. Yun, Long-wavelength optical coherence tomography at 1.7 microm for enhanced imaging depth, Opt Express 16(24) (2008) 19712-23.

[348] D.-J. Kroon, Hessian based Frangi Vesselness filter 2020. https://www.mathworks.com/matlabcentral/fileexchange/24409-hessian-based-frangi-vesselness-filter.

[349] Y. Li, Z. Chen, Multimodal intravascular photoacoustic and ultrasound imaging, Biomedical Engineering Letters 8(2) (2018) 193-201.

[350] Y. Li, S. Moon, J.J. Chen, Z. Zhu, Z. Chen, Ultrahigh-sensitive optical coherence elastography, Light Sci Appl 9 (2020) 58.

[351] Troels Thim, Mette Kallestrup Hagensen, David Wallace-Bradley, Juan F. Granada, Greg L. Kaluza, Ludovic Drouet, William P. Paaske, Hans Erik Bøtker, E. Falk, Unreliable Assessment of Necrotic Core by Virtual Histology Intravascular Ultrasound in Porcine Coronary Artery Disease, Circulation 3 (2010) 384-391.

[352] J. Narula, H.W. Strauss, Imaging of unstable atherosclerotic lesions, Eur J Nucl Med Mol I 32(1) (2005) 1-5.

[353] C. Weber, H. Noels, Atherosclerosis: current pathogenesis and therapeutic options, Nat Med 17(11) (2011) 1410-1422.

[354] R. Virmani, F.D. Kolodgie, A.P. Burke, A.V. Finn, H.K. Gold, T.N. Tulenko, S.P. Wrenn, J. Narula, Atherosclerotic plaque progression and vulnerability to rupture - Angiogenesis as a source of intraplaque hemorrhage, Arterioscl Throm Vas 25(10) (2005) 2054-2061.

[355] J. Narula, H.W. Strauss, The popcorn plaques, Nat Med 13(5) (2007) 532-534.

[356] R. Virmani, F.D. Kolodgie, A.P. Burke, A.V. Finn, H.K. Gold, T.N. Tulenko, S.P. Wrenn, J. Narula, Atherosclerotic plaque progression and vulnerability to rupture: angiogenesis as a source of intraplaque hemorrhage, Arterioscler Thromb Vasc Biol 25(10) (2005) 2054-61.

[357] J. Narula, H.W. Strauss, Imaging of unstable atherosclerotic lesions, Eur J Nucl Med Mol Imaging 32(1) (2005) 1-5.

[358] P.R. Moreno, R.A. Lodder, K.R. Purushothaman, W.E. Charash, W.N. O'Connor, J.E. Muller, Detection of lipid pool, thin fibrous cap, and inflammatory cells in human aortic atherosclerotic plaques by near-infrared spectroscopy, Circulation 105(8) (2002) 923-7.

[359] F.D. Kolodgie, A.P. Burke, A. Farb, H.K. Gold, J. Yuan, J. Narula, A.V. Finn, R. Virmani, The thin-cap fibroatheroma: a type of vulnerable plaque: the major precursor lesion to acute coronary syndromes, Curr Opin Cardiol 16(5) (2001) 285-92.

[360] R.A. Baldewsing, J.A. Schaar, C.L. de Korte, F. Mastik, P.W. Serruys, A.F. van der Steen, Intravascular Ultrasound Elastography: A Clinician's Tool for Assessing Vulnerability and Material Composition of Plaques, Stud Health Technol Inform 113 (2005) 75-96.

[361] C.L. de Korte, A.F. van der Steen, Intravascular ultrasound elastography: an overview, Ultrasonics 40(1-8) (2002) 859-65.

[362] C.L. de Korte, M.J. Sierevogel, F. Mastik, C. Strijder, J.A. Schaar, E. Velema, G. Pasterkamp, P.W. Serruys, A.F. van der Steen, Identification of atherosclerotic plaque components with intravascular ultrasound elastography in vivo: a Yucatan pig study, Circulation 105(14) (2002) 1627-30.

[363] J.D. Allen, K.L. Ham, D.M. Dumont, B. Sileshi, G.E. Trahey, J.J. Dahl, The development and potential of acoustic radiation force impulse (ARFI) imaging for carotid artery plaque characterization, Vasc Med 16(4) (2011) 302-11.

[364] S. Waxman, F. Ishibashi, J.E. Muller, Detection and treatment of vulnerable plaques and vulnerable patients: novel approaches to prevention of coronary events, Circulation 114(22) (2006) 2390-411.

[365] T. Wang, T. Pfeiffer, E. Regar, W. Wieser, H. van Beusekom, C. Lancee, G. Springeling, I. Krabbendam, A. van der Steen, R. Huber, G. van Soest, Heartbeat OCT: in vivo intravascular megahertz-optical coherence tomography, Biomedical Optics Express 6(12) (2015) 5021-5032.